Electrografting of Thin Films on Engineering Alloys for Advanced Joining Processes

Dissertation

submitted by

Belma Duderija, née Beglerović, M.Sc.,

born in Mostar,

BiH

in fulfilment of requirements for the degree of

Doctor of Science (Dr. rer. nat.)

at the University Paderborn

Faculty of Science

Department of Chemistry

at the chair of Prof. Dr.-Ing. Guido Grundmeier

Technical and Macromolecular Chemistry (TMC)

Examination board:

Chair	Prof. Dr. Sabine Fechner
First examiner	Prof. Dr.-Ing. Guido Grundmeier
Second examiner	Prof. Dr. rer. nat. Wolfgang Bremser
Third examiner	Jun. Prof. Dr. Nieves Lopez Salas

Day of examination: 09.07.2024

Printed and published with the approval of the examination board.

I, Belma Duderija, born on February 25, 1992, in Mostar (BiH), solemnly affirm that I am the author of the dissertation entitled *"Electrografting of thin films on engineering alloys for advanced joining processes"* conducted under the guidance of Professor Dr.-Ing. Guido Grundmeier. I have duly acknowledged and referenced all the resources and literature sources employed in this research. Additionally, I affirm that this thesis has not been presented in a comparable or identical format to any other examination authority.

Paderborn, 02.05.2024

Belma Duderija

Acknowledgements

First and foremost, I would like to express my deepest appreciation to Prof. Dr.-Ing. Guido Grundmeier for granting me the opportunity to embark on my doctoral journey under his supervision. My perspective on contemporary science has been significantly influenced by the availability of advanced laboratory equipment within the department and the opportunity to unleash creativity across multiple projects. I am profoundly thankful for entrusting me with this and other projects, and for the unwavering support in every conceivable manner, even during times with unforeseen challenges.

Additionally, I extend my deep gratitude to Dr. Alejandro Orive for his remarkable support, engaging discussions, and for consistently serving as a supervisor and valuable colleague throughout this journey.

Next, I extend my thanks to Prof. Dr. rer. nat. Wolfgang Bremser and Jun. Prof. Dr. Nieves Lopez Salas for agreeing to be the examiners.

A doctoral dissertation is never the work of a single individual but a result of collective efforts and support. Therefore, I would like to express my gratitude to all my colleagues at TMC for fostering a pleasant atmosphere during my time in the department and highlight the invaluable support I received from Dr. Juan Carlos Calderon for his assistance with electrochemical methods, Dr. Christoph Ebbert for his support in resolving technical issues, Dr. Markus Voigt for discussions on the interpretation of XPS data, Dr. Mike Bobert, Claudia Altmiks, and Thomas Arens for their support in handling organizational tasks, Gissela Jünnemann-Held for her fruitful support in the labs, and Dr. Teresa de los Arcos de Pedro for her attentiveness and proofreading the Thesis.

Furthermore, I would like to thank Prof. Dr.-Ing. Werner Homberg and Dr. Christian Schmidt for the great collaboration within the ECUF-Project, Nadine Buitkamp for performing the SEM measurements and the German Research Foundation (DFG) for their funding support.

Finally, my deepest thanks go to my husband Semir Duderija, my parents, stepparents and my whole family for their boundless love and support they gave me throughout this journey. Your encouragement has been my motivation, and your unwavering endurance in not giving up has made this achievement possible. Thank you!

List of publications

Publication included in this thesis:

(1) **B. Duderija**, A. González-Orive, H.C. Schmidt, J.C. Calderón, I. Hordych, H.J. Maier, W. Homberg, G. Grundmeier, Electrografting of BTSE: Zn films for advanced steel-aluminum joining by plastic deformation. Journal of Advanced Joining Processes 2022;7:1100137.

(2) **B. Duderija,** F. Sahin, D. Meinderik, J.C. Calderón, H.C. Schmidt, W. Homberg, G. Grundmeier, A. González-Orive, Electrografting of Acrylic acid on steel for enhanced joining by plastic deformation. Journal of Advanced Joining Processes 2024;9:100181.

Other Publication:

(3) **B. Duderija,** A. González-Orive, C. Ebbert, V. Neßlinger, A. Keller, G. Grundmeier, Electrode Potential-Dependent Studies of Protein Adsorption on Ti6Al4V Alloy. Molecules 2023;28(13):5109.

(4) H.C. Schmidt, W. Homberg, A.G. Orive, G. Grundmeier, **B. Duderija,** I. Hordych, S. Herbst, F. Nürnberger, H.J. Maier , Joining of blanks by cold pressure welding : Incremental rolling and strategies for surface activation and heat treatment. Materialwissenschaft Und Werkstofftechnik 2019;50:924–939.

(5) Giner, B. Torun, Y. Han, **B. Duderija**, D. Meinderink, A.G. Orive, M.T. de los Arcos de Pedro, C. Weinberger, M. Tiemann, H.-J. Schmid, G. Grundmeier, Water adsorption and capillary bridge formation on silica micro-particle layers modified with perfluorinated organosilane monolayers. Applied Surface Science 2019;475:873–879.

(6) R. Hajiraissi, M. Hanke, A. Gonzalez Orive, **B. Duderija**, U.Hofmann, Y.Zhang, G. Grundmeier, A. Keller, Effect of Terminal Modifications on the Adsorption and Assembly of hIAPP. ACS Omega 2019;4:2469-2660;20-29.

(7) R. Hajiraissi, M. Hanke, Y. Yang, **B. Duderija**, A. Gonzalez Orive, G. Grundmeier, A. Keller, Adsorption and Fibrillization of Islet Amyloid Polypeptide at Self-Assembled Monolayers Studied by QCM-D, AFM, and PM-IRRAS. Langmuir 2018;34:3517–3524.

Summary

Adhesive bonding of dissimilar materials, such as steel and aluminum, has gained significant interest in in recent decades, particularly in industries like automotive, aircraft, construction materials, and microelectronics due to numerous advantages, including enhanced failure resistance and reduced weight. In lightweight construction, adhesive bonds are used to join metallic surfaces with other metals, polymeric or composite materials. Thanks to recent advancements in this field, various processes and methods have been developed for joining similar and dissimilar metals such as cold pressure welding (CPW).

CPW involves welding metallic sheets through plastic deformation induced by high deformation forces and reduction ratios. This process extrudes virgin metallic material through cracked oxide layers, creating metal-to-metal bonds between the welded surfaces. CPW does not require solder or high temperatures, making it an economical and suitable method for welding hybrid metal combinations. Given their potential for lightweight construction and various technological applications, steel/aluminum combinations are considered highly promising hybrid joints.

Effective conditioning of metal surfaces is crucial for the success of the CPW process. In this context, the improvement of interfacial adhesion in metal/metal joints formed through CPW entails in surface conditioning and modifying metals at the metal-oxide interface using thin molecule-based layers. Specifically, electrografting offers the possibility for the deposition of very thin organic films by means of the formation of strong molecule-substrate bonds.

Built upon these insights, this thesis focuses on the electrochemical modification of DC04 steel surfaces using of 1,2-bis (triethoxysilyl) ethane (BTSE) and poly(acrylic acid) (PAA) and Zinc (Zn) doped BTSE/ PAA nanocomposite thin films with the aim of enhancing interfacial adhesion to aluminum after CPW. The modified low-alloy DC04 plates were employed in the CPW process and joined with Aluminum, EN-AW-1050A , to create dissimilar metal joints. Subsequently, joint specimens underwent a thermal annealing step at 200 ºC or400 °C.

Surface chemical state and morphological features of the BTSE and PAA thin films formed on the DC04 steel surface were characterized through complementary analytical surface techniques such as AFM, FE-SEM, PM-IRRAS, and XPS.

Additionally, the electron transfer properties of both BTSE and PAA films with and without Zn particles were assessed using cyclic voltammetry (CV).

Corrosion resistance properties of the as-formed thin films on steel alloys were studied through potentiodynamic polarization curves (LSV) and electrochemical impedance spectroscopy (EIS).

Finally, tensile shear testing measurements of steel/aluminum specimens were performed to demonstrate the bonding strength of the as-prepared aluminum-steel joints. A fracture analysis was carried out by field-emission scanning electron microscopy (FE-SEM) and energy dispersive X-ray spectroscopy (EDX) characterization of fractured DC04 and EN-AW-1050A H11 specimens.

Summary (German)

Die Klebeverbindung unterschiedlicher Materialien, wie Stahl und Aluminium, hat in den letzten Jahrzehnten erhebliches Interesse in Branchen wie Automobilbau, Flugzeugbau, Bauwesen und Mikroelektronik geweckt. Dies resultiert aus zahlreichen Vorteilen wie einer gesteigerten Ausfallfestigkeit und einem reduzierten Gewicht. Insbesondere im Leichtbau werden Klebeverbindungen genutzt, um metallische Oberflächen mit anderen Metallen, polymeren Materialien oder Verbundwerkstoffen zu verbinden. Durch neuartige Fortschritte wurden verschiedene Prozesse und Methoden für die Verbindung von Metallen entwickelt, darunter das Kaltumformen (cold pressure welding, CPW).

CPW beinhaltet das Verschweißen metallischer Bleche durch plastische Deformation, die durch hohe Verformungskräfte und Reduktionsverhältnisse induziert wird. Dabei wird reines metallisches Material durch rissige Oxidschichten extrudiert, wodurch Metall-zu-Metall-Bindungen zwischen den verschweißten Oberflächen entstehen. CPW erfordert weder Löten noch hohe Temperaturen, was es zu einer wirtschaftlichen und geeigneten Methode für das Verschweißen von Hybridmetallkombinationen macht. Aufgrund des Potenzials für Leichtbaukonstruktionen und verschiedenste technologische Anwendungen gelten Stahl/Aluminium-Kombinationen als äußerst vielversprechende Hybridverbindungen.

Eine effektive Vorbehandlung der Metalloberflächen ist entscheidend für den Erfolg des CPW-Prozesses. Hierbei umfasst die Verbesserung der grenzflächenmäßigen Haftung in Metall/Metall-Verbindungen, die durch CPW entstehen, die Oberflächenbehandlung und Modifikation von Metallen an der Metall-Oxid-Grenzfläche unter Verwendung von dünnen molekularbasierten Schichten. Insbesondere ist das Graften eine elektrochemische Technik, die Möglichkeit zur Abscheidung sehr dünner organischer Filme durch starke Molekül-Substrat-Bindungen bietet.

Ausgehend von diesen Erkenntnissen fokussiert sich diese Arbeit auf die elektrochemische Modifikation von DC04-Stahloberflächen mittels 1,2-bis (triethoxysilyl) ethane (BTSE) und Polyacrylsäure (PAA) sowie Zink (Zn)-dotierte BTSE/PAA-Nanokomposit-Dünnschichten mit dem Ziel, die grenzflächenmäßige Haftung an Aluminium nach CPW zu verbessern. Die modifizierten DC04 Proben wurden im CPW-Prozess eingesetzt und mit Aluminium, EN-AW-1050A , zu unähnlichen Metallverbindungen gepresst. Anschließend wurden die Verbindungsmuster einer thermischen Glühbehandlung bei 200 °C und 400 °C unterzogen.

Die oberflächenchemische Zusammensetzung und die morphologischen Merkmale der BTSE- und PAA-Dünnschichten auf der DC04-Stahloberfläche wurden mithilfe von ergänzenden analytischen Oberflächentechniken wie AFM, FE-SEM, PM-IRRAS und XPS charakterisiert.

Zusätzlich wurden die elektrochemischen Eigenschaften sowohl der BTSE- als auch der PAA-Filme mit und ohne Zinkpartikel mithilfe von zyklischer Voltammetrie (CV) untersucht. Die Korrosionsbeständigkeit der gebildeten dünnen Filme auf Stahllegierungen wurde durch potentiodynamische Polarisationskurven (LSV) und elektrochemische Impedanzspektroskopie (EIS) analysiert.

Abschließend wurden Zugversuche an Stahl/Aluminium-Mustern durchgeführt, um die Haftfestigkeit der Aluminium-Stahl-Verbindungen zu bestimmten, gefolgt mit der FE-SEM-Charakterisierung der gezogenen DC04- und EN-AW-1050A Oberflächen.

Table of Contents

1

Introduction

In this chapter, the study is introduced through a structured progression, starting with an exploration of the background and context. Subsequently, the research motivation, objectives, and steps are delineated, emphasizing their significance. The chapter concludes by outlining the specific inquiries that will be addressed through the thesis and referencing the layout of the Thesis.

The modification of metal surfaces and metallic oxides using organic and inorganic molecules has garnered significant attention over the years due to its potential to alter their inherent interfacial properties. In this context, various molecules containing diverse functional groups are well-documented for their ability to form self-assembled monolayers on a wide range of metallic oxide surfaces. Notably, functional groups like phosphonates, carboxylates, silanol, and amines are known to exhibit strong binding affinity with surfaces such as copper, steel, aluminum oxide, and zinc oxide. Particularly, the study of adhesion properties of steel has gained significant relevance in surface science. Various surface treatments have been proposed to enhance the adhesive properties of steel surfaces, including metal/metal oxide deposition [1], plasma activation [2], acidic etching [3], and the adsorption of thin organic layers that promote adhesion [4]. It is established that organosilanes can create thin films that are covalently bonded to hydroxyl-rich metallic oxide surfaces [5-8]. Indeed, the grafting of alkoxysilanes has been successfully accomplished on various substrates, including gold, glass, aluminum, iron oxide, among others.

Adhesion promotion is also an important aspect when using organosilanes as molecules for enhancing the joining of dissimilar metals. Organosilanes are bi-functional hybrid compounds containing silicon atoms bonded to organic groups, typically consisting of functional groups such as alkoxy, amino, or epoxy groups. These functional groups play a vital role in promoting adhesion between metal surfaces through various mechanisms. They form chemical bonds with metal surfaces through interactions such as covalent bonding or coordination bonding. This bonding mechanism allows the organosilane molecules to anchor firmly onto the metal surfaces, creating a strong interface between dissimilar metals. Similarly, poly acrylic acid (PAA) is beneficial for adhesion between two metals. It contains carboxylic acid (-COOH) functional groups along its polymer chain. These groups can interact with metal surfaces through chemical bonding, such as hydrogen bonding or coordination bonding, promoting adhesion between the polymer and the metal. PAA can be tailored to specific requirements by adjusting its molecular weight, polymerization conditions, and functional group density. This versatility allows for the optimization of adhesion properties to suit different metal surfaces and joining processes. A seminal study by Huser et al., demonstrated the formation of thin films using different organosilanes on a minimally reactive stainless steel 316L surface [9]. Similarly, Hoppe et al., showcased the effectiveness of a self-assembled multilayer of metacryloxypropyltrimethoxysilane (MPTS) chemisorbed onto an oxide-free copper surface through Cu-S bonds, resulting in a significant enhancement of shear strength in copper/aluminum welded joints [10]. This approach necessitated an additional step, involving the heating of the prepared welded samples to 200 ºC, to facilitate the condensation of silanol groups present in the MPTS layer with the hydroxyl-rich aluminum oxo-hydroxide surface [11].

Interestingly, the deposition and chemisorption of organosilane-based films, such as BTSE, can also be accomplished through electrochemical methods, as determined by Mandler, Walcarius, and Collinson [12-14]. For example, electrografting is an electrochemical technique that enables the deposition of very thin organic films through strong molecule-substrate bonds. It is typically a cathodic process, and it can be applied to metallic and semiconducting surfaces without the hindrance of oxide formation [15, 16]. However, due to the highly negative potential required for this reaction, it is typically conducted in organic solvents like acetonitrile and dimethylformamide, since in in aqueous solutions the reaction occurs at more cathodic potentials than the hydrogen evolution reaction (HER) [17, 18]. Nonetheless, there is an interest to perform these reactions in aqueous solutions to align with the principles of green chemistry in industrial applications. According to Cécius et al., even water molecules can

diffuse to the electrode surface and hydrogen radicals formed therein can sustain film growth by extending polymerization to closer micelles [19]. Preliminary studies from Schmidt et al. showed promising results for the use of thin organic layers as an adhesion-promoting layer [20,21]. Further, Bauer et al. have employed a straightforward electrochemical procedure involving the grafting and polymerization of acrylic acid (AA) into thin films of poly (acrylic acid) (PAA) on carbon fibers and mild-alloy steel to enhance interfacial adhesion to model epoxy resins [22]. Notably, the electrografting of AA molecules and subsequent polymerization into PAA on various substrates have demonstrated exceptional performance [23-29]. Palacin and colleagues employed the electrochemical reduction of aryl diazonium salts and subsequent grafting of aryl radicals to initiate the radical polymerization of an aryl-vinylic copolymer covalently bound to the steel substrate [23]. In this case, the presence of a surfactant is required to form an emulsion containing the diazonium salt and the vinylic monomers. Additionally, Sabbatini and colleagues reported PAA formation on Ti6Al4V substrates through cathodic electropolymerization from acidic aqueous solutions containing AA and persulfate ions [30]. The electroreduction of the latter at cathodic potentials generates sulfate radicals at the metal oxide solid-liquid interface, which are responsible for initiating the radical polymerization of AA monomers in solution. This approach has been successfully employed by researchers such as Katz, Hernández, and Willner for the preparation of PAA-based organic layers for various applications [31-33].

Within this framework, the electrografting of 1,2-bis(triethoxysilyl)ethane (BTSE) and AA-containing aqueous solutions incorporating Zn^{2+} ions onto conductive DC04 steel surfaces were proposed in order to enhance adhesion between the as-modified steel surfaces and aluminum after CPW. So far, none of these approaches have been previously associated with the enhancement of adhesion-promoting purposes, so that, the efficiency of such processes remains an open question. This thesis focuses on the fundamental investigations and molecular understanding of electrochemical grafting of thin BTSE and PAA films on technically relevant surfaces like stainless steel and its application and efficiency in advanced joining processes with aluminum via CPW.

1.1 Motivation and scientific approach

The primary areas of focus in fundamental research and industries, particularly within the automotive and aerospace sectors, are centered on the pursuit of lightweight structures. One of the most pressing issues involves reducing fuel consumption and minimizing CO_2 emissions from combustion processes. Hence, there is a significant emphasis on reducing the overall mass, such as that of vehicles and aircraft [34]. The concept of minimizing total mass aligns with the idea of hybrid construction [35]. Lightweight materials like aluminum and magnesium offer favorable strength-to-weight ratios when combined with steel, enabling the design of hybrid structures that are both strong and lightweight. However, magnesium alloys exhibit poor formability at room temperature, creating an ongoing trade-off between reducing weight (or fuel consumption) and energy efficiency. In this context, steel and aluminum hybrid constructions offer a compelling solution for achieving lightweight yet durable structures in various engineering applications. By combining the strengths of both materials, engineers can optimize performance while minimizing weight. Within recent advancements in the field of hybrid construction, numerous processes and techniques have emerged for joining metals of similar or dissimilar nature. One notable example is the joining of two metal components or metal components via cold pressure welding (CPW) [36-38]. CPW is a form of joining that involves welding of metallic sheets through plastic deformation induced by applying high deformation forces and reduction ratios. This process relies on the extrusion of pristine metallic material through cracked oxide or bifunctional molecules layers via plastic deformation where metal-to-metal bonds are established between the welded metallic surfaces [39,40]. Therefore, it is crucial to identify optimized surface treatments for materials of interest before effectively joining modified multi-materials with enduring properties (see Figure 1-1).

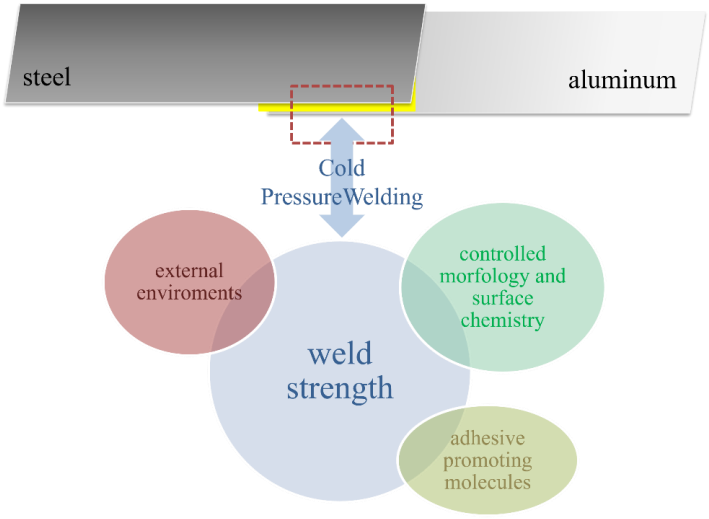

Figure 1-1: Schematic illustration depicting factors that influence weld strength following cold pressure welding.

Comprehending the chemical, mechanical, and molecular properties, particularly the adhesion mechanisms at material interfaces, is imperative for the long-term stability of lightweight constructions [41–43]. The selection of optimally matched materials, along with potential pre-treatment methods such as deposition of nanostructures or application of adhesion-promoting thin films with corrosion-inhibiting properties, continues to present challenges in both the lightweight construction industry and scientific research. Recent research has delved into the influence of surface preparation and thermal annealing on the weld strength when connecting galvanized steel with aluminum specimens via CPW [44]. Altering metal interfaces with bifunctional molecules capable of binding to dissimilar metal oxide surfaces have the potential to significantly impact the bonding strength of the welded specimens [10]. Ensuring proper condition of metal surfaces is essential for CPW. In this regard, recent contributions from Grundmeier et al. have effectively addressed surface activation, electrochemical roughening, and temperature treatments of the specimens to enhance the strength of the welded joints [20,21, 45-49]. Given that steel-aluminum combinations are regarded as among the most intriguing hybrid joints due to their potential for lightweight construction and various technological applications [11], this study introduces an electrochemical approach for the modification of steel surfaces with i) bis-1,2-(triethoxysilyl) ethane BTSE and ii) poly acrylic acid (PAA) based thin films to enhance the strength of the welded joints after CPW.

Figure 1-2 illustrates the stepwise processes conducted in this thesis, involving surface activation using BTSE and PAA (I) followed by thin film characterization (II), CPW (III) and tensile testing (IV).

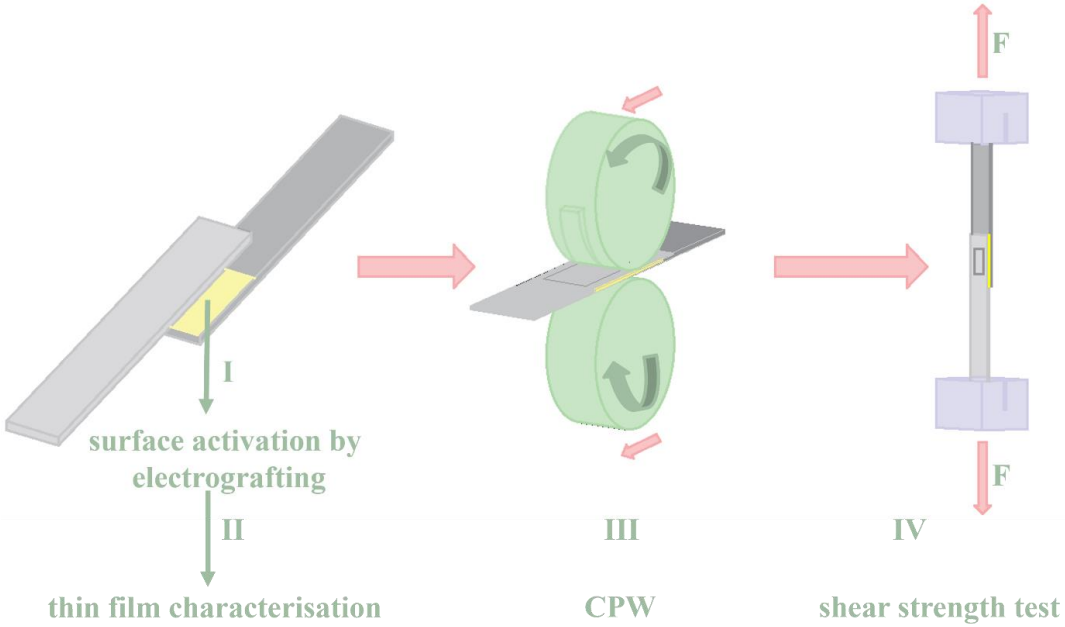

Figure 1-2: Graphical illustration of the four processes conducted in this thesis.

Firstly, aluminum surfaces were modified via pickling, while two distinct electrochemical grafting procedures were conducted on DC04 surfaces that underwent polishing and solvent cleaning:

1. grafting of BTSE thin films and BTSE thin films containing Zn^{2+} ions.
2. grafting of poly PAA thin films, derived from acrylic acid (AA) molecules, and aqueous solutions containing Zn^{2+} ions.

In the following text, specifically in the content of Chapter 4, the as modified surfaces are referred to as BTSE and BTSE:Zn, PAA and PAA:Zn, respectively.

Secondly, the investigation of the as-prepared BTSE and PAA thin films on DC04 steel alloy involved the characterization of surface chemical composition and morphological features of the resulting BTSE and PAA thin films formed on steel alloy.

The characterization of the as-modified CD04 and pickled aluminum was conducted using complementary analytical surface techniques such as AFM, FE-SEM, PM-IRRAS, and XPS, revealing the formation of densely packed BTSE and PAA films firmly adhered to the steel surface.

Thirdly, these as-modified low-alloy DC04 steel specimens were employed for CPW due to their anticipated deformability, joining them with aluminum, EN-AW-1050A , to create dissimilar metal joints. Further, a thermal annealing process at 200ºC or 400°C was performed on the joint specimens.

Fourthly, the electrochemical properties of both BTSE, PAA films and BTSE, PAA films containing Zn particles were evaluated by CV. Additionally, the corrosion resistance properties of these films were examined using LSV and EIS.

Finally, the study included tensile shear testing measurements of modified steel/aluminum joint specimens followed by the FE-SEM characterisation of fractured DC04 and EN AW-1050A H11 sheets.

In this context, the following questions where discussed:

1) What is the importance of electrochemical technologies for surface activation in press welding processes?
2) What is the mechanism by which BTSE and PAA graft to the surface of DC04 steel?
3) What are the corrosion protection properties of BTSE and PAA thin films formed on the surface of DC04 steel, and how does the presence of Zn particles in BTSE and PAA thin films affect their corrosion protection properties?

4) How do BTSE and PAA thin films formed on DC04 steel surfaces affect the joining between as-modified steel and aluminum via CPW, and how does the presence of Zn particles affect the bond strength?

1.2 Thesis layout

This thesis comprises 9 chapters, where *Chapter 1* serves as an introduction, providing background information, outlining the study objectives, and offering an overview of the entire thesis. *Chapter 2* delves into the current state of the research, providing an extensive literature review. *Chapter 3* outlines the basic principles of the experimental methods employed in the Thesis providing a detailed description of the experimental setup, including specifications of the samples, chemicals, and methods used in the study. *Chapter 4* presents the experimental results and discussion of the research. *Chapter 5* outlines a summary of the dissertation and study findings, following by the outlook for future developments in *Chapter 6*. Lastly, *Chapter 7, 8 and 9* outline the Supporting Information, List of References and Attachments, respectively.

2

State of the Art

In this chapter, a broad array of topics exploring the fundamental concepts of adhesion mechanisms at metal and oxide interfaces is presented. Subsequently, it delves into the basic concepts of electrografting, specifically focusing on the electrografting processes involving organosilanes and acrylates. Further, it displays an overview of the microstructure and mechanical properties of the low alloyed steel and aluminum utilized in this research. The chapter then proceeds to discuss techniques for joining through plastic deformation. Finally, it concludes by describing the foundational aspects of analytical methods applied to surface and interface analysis, electrochemical analysis, macroscopic and adhesion tests conducted within this research.

2.1 Basic concepts of adhesion mechanisms at metal and oxide interfaces

Comprehending the molecular adhesion mechanisms at oxide interfaces is crucial for achieving efficient and durable connections in manufacturing engineering, as outlined in DIN 8593 [N1], particularly in the context of lightweight constructions. The enhancement of macroscopic, microscopic, molecular, and atomic interactions between two components involved in bonding, such adhesive and a metallic substrate (adherends), stands out as a vital aspect in the production of enduring joins [50].

This holds significant relevance in the context of this thesis, as the adhesive properties of two different organic thin films formed on steel were explored with the objective to facilitate joining with aluminium through cold pressure welding (CPW).

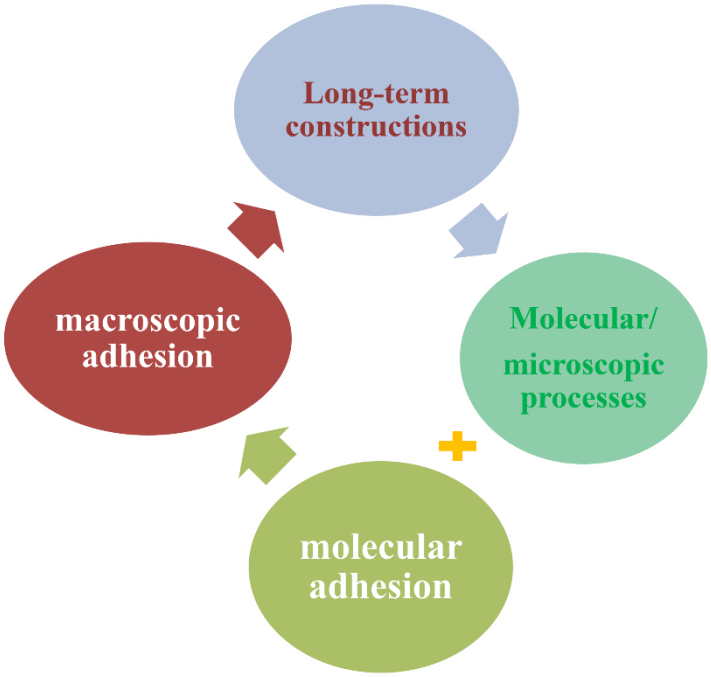

Figure 2-1: Schematic of connections between microscopic and molecular interfacial adhesion processes and macroscopic adhesion which is crucial for optimizing long-term constructions.

In the assessment of joint strength between two systems, it becomes crucial to identify failures at the weakest point contributing to adhesion [50]. Various adhesion failures may occur, including cohesive failures within the adhesives or component parts. A more complex scenario involves the rupture of harnessed structures in the vicinity of the interface [50]. Precisely determining the component (adhesive, adhesion-promoting molecules, or nanostructures) where the failure initiates or occurs is often challenging. Consequently, establishing connections between molecular and microscopic processes and macroscopically measured adhesion forces, as depicted in Figure 2-1, becomes crucial. To establish a fundamental comprehension of the macroscopically measurable adhesion force, it is important to analyze the interfacial regions. Various "classes" of adhesion mechanisms, often termed "adhesion theories," have been identified, as noted by Ebnesajjad et al. [50], along with relevant literature [51,52]. Based on that classification, the general categorization of adhesion mechanisms is shown in Figure 2-2. It is based in mechanical, physical, and chemical driving forces and causes.

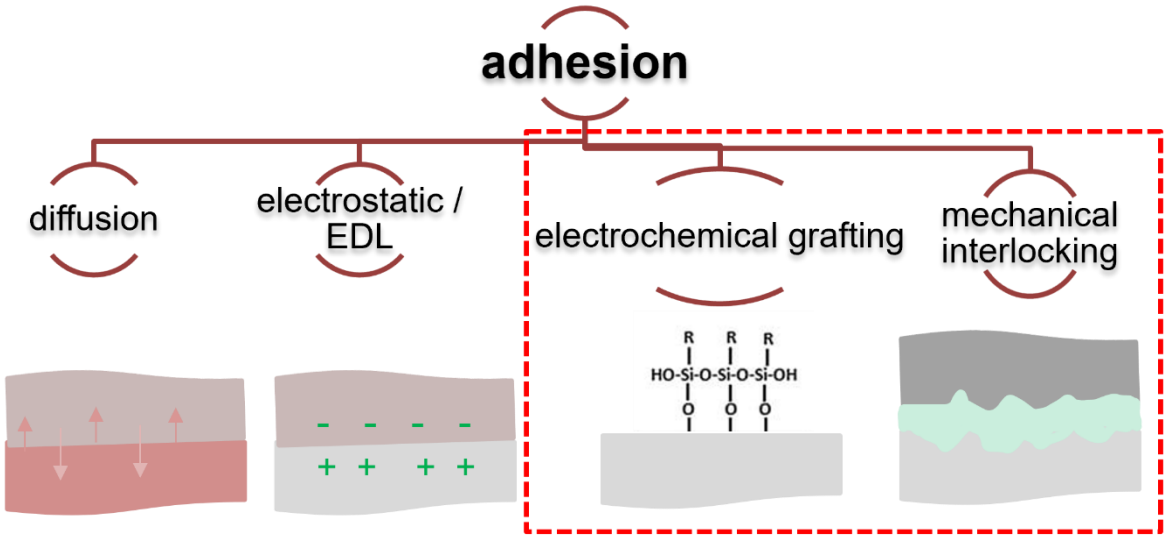

Figure 2-2: Theoretical adhesion mechanism (based on Ebnesajjad et al. [50])

A thorough comprehension of all the outlined adhesion mechanisms is crucial for optimizing the performance of interfacial bonding and cohesive properties. Furthermore, it is important to mention that wettability and morphology significantly influence adsorption properties in the realm of adhesion [50, 54, 55]. The chemical and physical foundations underlying these phenomena are associated with various adsorption and binding processes, as outlined in Figure 2-3.

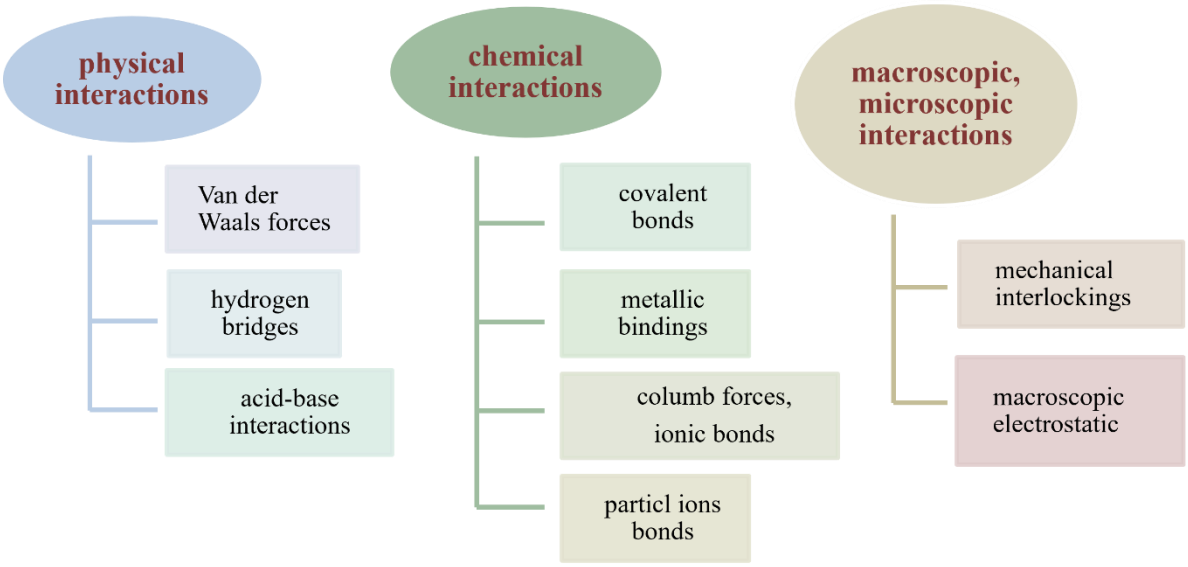

Figure 2-3. Classification of basic adhesion mechanisms and binding forces (based on literature [51,52]).

Determining the precise adhesion mechanism along with their corresponding interactions is challenging. Additionally, there are overlapping features and properties among all adhesion mechanisms since real interfaces usually involve a combination of different mechanisms [53]. However, thorough understanding of all the adhesion mechanisms outlined in Figure 2-3 is

crucial for optimizing the performance of interfacial bonding and cohesive properties. In the context of this thesis, the interaction between surface reactions and mechanical interlocking is crucial for the efficiency of cold pressure welding between modified DC04 steel and aluminum, thus impacting the integrity of the final joint. Further explanation of both the mechanical interlocking and surface reactions, as well as the importance of electrostatic double-layer, will be provided in the following subchapters.

2.1.1 Electrostatic double-layer (EDL)

The hydration of metal ions from metals in water-based electrolytes can lead to charged metal surfaces. Positively and negatively charged ions interact electrostatically with surfaces, leading surfaces to adsorb or repel ions, thereby creating an electric field. The accumulated counter ions, forming distinct layers on the surface, are collectively known as the "electric double layer" (EDL) [56]. Various models have been developed to elucidate the complex adsorption states and layers within the EDL. Helmholtz initially proposed an adsorbed layer of counter ions where ions adhere to oppositely charged positions, resembling a molecular layer akin to a plate capacitor, termed the "Helmholtz layer" [56]. Gouy and Chapman expanded upon this model by accounting for the thermal fluctuation of ions, introducing an extended diffuse layer, with a thickness of microns, much wider than the double layer, formed during deposition by the consumption of a particular species. This allowed counter ions to transition from the charged surface into the diffuse layer [56]. Otto Stern, a Nobel laureate in physics in 1943, integrated both Helmholtz's and the diffuse layer theory into his "Stern layer" model, which features an inner Stern layer and an outer diffuse layer or Gouy layer from the Gouy-Chapman model (see Figure 2-4).

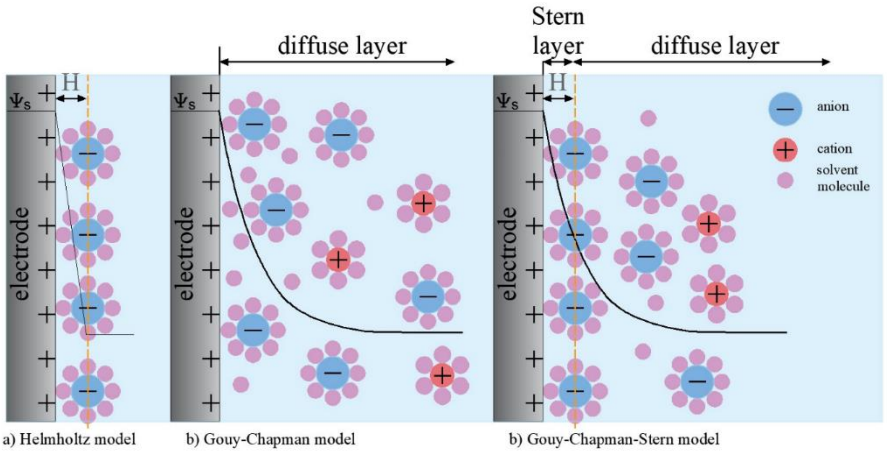

Figure 2-4: Graphical illustration of the fundamental structure of electric double layer according to Stern model (drawing based on Butt et al. [56]).

In the model of "Stern layer", the Poisson-Boltzmann statistic for mobile ions in the coordinate normal to the plane x in the diffuse layer, assuming an infinitely extended planar surface, can be expressed with equation 2-1[56]:

$$\frac{d^2\Psi}{dx^2} = \frac{c_0 e}{\varepsilon\varepsilon_0} \cdot \left(exp\left(\frac{e\Psi(x)}{k_B T}\right) - exp\left(-\frac{e\Psi(\mathrm{x})}{k_B T}\right)\right) \qquad (2-1)$$

where c_0 represents the bulk concentration, e the elementary charge constant, ε the relative permittivity, ε_0 the vacuum permittivity, k_B the Boltzmann's constant, T the temperature, and $\psi(x)$ the potential dependent on the distance x from the surface with $\psi_0 = \psi(x = 0)$ defined as surface potential. The surface potential ψ_0 is identified in Figure 2-4a as the inner Helmholtz plane (IHP) and encompasses the permanently adsorbed ions and water molecules, illustrated as circles with their dipole moments. Regarding charged surfaces, the zeta potential ζ serves as a characteristic parameter for describing interfacial processes. The EDL results from specifically adsorbed ions that are bounded to the surface. Consequently, certain adlayers on the surface create a shear plane at a specific distance from the surface, where the ions begin to exhibit mobility. In this area the zeta potential ζ is measurable and represents the hydrodynamic interfacial region [57]. At low potentials in the range of $e|\psi| << k_B T$ (at $RT\,\psi \leq 25\ mV$), equation 1-4 is commonly referred as "linearized Poisson-Boltzmann equation" 2-2:

$$\Psi(x) = C_1 \cdot \exp\left(-\frac{x}{\lambda_D}\right) + C_2 \cdot exp\left(\frac{x}{\lambda_D}\right) \qquad (2-2)$$

where constants C_1 and C_2 are expressed as $C_1 = \Psi_0$ and $C_2 = 0$. Assuming that the potential at the surface x= *0* has a surface potential of Ψ_0 and that for infinitely large distances *x*, the potential will be *0*, the equation 2-2 can be written as 2-3:

$$\Psi(x) = \Psi_o \cdot \exp\left(-\frac{x}{\lambda_D}\right) \qquad (2-3)$$

where λ_D represents the Debye length. The Debye length is the length at which the potential ψ has decreased to *1/e* of its original value (with *e* as the Euler's number) and it is given by the following equation 2-4:

$$\lambda_D = \sqrt{\frac{\varepsilon\varepsilon_0 k_B T}{e^2 I}} \qquad (2-4)$$

where I is the ionic strength in particles per m^3. In fact, the adhesion force depends on the surface potential.

In typical scenarios, it is observed that the electrostatic double layer force undergoes an exponential decrease concerning the ratio of distance x to the Debye length λ_D. Additionally, it is applicable in the context of the DLVO (Derjaguin, Landau, Verwey, and Overbeek) theory, particularly when considering the attractive van der Waals forces [56].

2.1.2 Mechanical interlocking

Mechanical interlocking can play a role at both macroscopic and nanoscopic scales, involving a mechanical connection between two solid phases. For instance, when a cured polymer encounters a metallic substrate, the polymer chains can interlock with the pores, gaps, cracks, or fractures of the metallic component [50]. This interaction leads to an increase in the overall adhesion force in the direction of the interlocking. It is noteworthy in this case to perform a measurement of surface roughness and specific surface area, which provides insights into the potential for mechanical interlocking. While these factors may offer indications, it is important to note that strong adherence can still occur even in the case of flat or smooth substrates [50, 52]. The chemical surface chemistry plays a crucial role in determining the performance and properties of interfacial adhesion. However, in the realm of surface engineering, the most prevalent adhesion mechanism relies on mechanical interlocking within well-defined layers and (nano-)structures, leading to an increased contact surface area and improved macroscopic adhesion performance which is particularly intriguing for CPW. Therefore, several methods for the pretreatment of metal alloys and oxides have been established, including mechanical techniques such as blasting with alumina grit or glass beads [58], ultrasonication [59,60], chemical treatments [61,62] and electrochemical treatments like surface roughening and electrografting. Furthermore, in the context of macroscopic adhesion involving metal oxides in lightweight constructions and adhesive bonding, aluminum materials with well-defined oxide surfaces are indispensable [61,63].

As highlighted earlier, electrografting is a pivotal aspect of this thesis. Its significance lies in the application of performing thin layers of BTSE and PAA thin based layers on the surface of low-alloyed DC04 steel. This process serves to activate the surface for subsequent cold-pressure welding procedures, where the as-modified steel specimens are joined with aluminum to enhance the welding process. Further details regarding this electrografting process and its fundamentals will be elucidated in the upcoming subchapter.

2.2 Fundamentals of Electrografting

Electrografting can be described as an electrochemical process that initiates the deposition of organic and organometallic films on surfaces. In this process, a singular, typically Faradaic electrochemical reaction is linked to various non-Faradaic chemical reactions, resulting in the creation of a film. This innovative technology is applicable to surfaces with varying degrees of conductivity, including both conducting and semiconducting surfaces. Electrografting is a broad term encompassing grafting processes driven by electric energy. Its origins trace back to the early nineteenth century, marked by Luigi Valentino Brugnatelli's pioneering use of Volta's battery for electrodeposition [64,65]. As an electrochemical process, it adheres to the principles of electrochemistry: each electrochemical reaction must not only adhere to mass balance but also to charge balance. Formulated by Faraday in 1833, the two laws governing mass and charge balance in electrochemical reactions are significant [66]. The first law asserts that the number of moles n produced or consumed in an electrochemical reaction is directly proportional to the charge Q flowing through the circuit [66]. The second law states that the mass m of different substances formed by the flow of the same charge is proportional to the molar mass M divided by the oxidation state of the species z [66]. The two laws can be summarized by equation 2-5 [66]:

$$m = \frac{A \cdot Q}{zF} \qquad (2-5)$$

where Q is the total charge ($i \cdot t$) flowing through the electrochemical cell during the process of interest, and the Faraday constant $F = 95.485\ C/mol$. Electrochemical deposition of metals is driven by electrochemical reactions, capitalizing on the notable contrast in solubility between the two redox states of the deposit [66].

As a simple illustration, Fe^{3+} undergoes reduction on the cathode (equation 2-6), leading to its deposition due to the limited solubility of the resulting neutral metal atoms in aqueous solutions [66].

$$Fe^{2+}_{(aq)} + 2^- \rightarrow Fe_{(s)} \qquad (2-6)$$

Most metals can undergo electrochemical deposition from aqueous or non-aqueous solutions, as well as molten salts. Non-aqueous systems become imperative when the redox potential of the metal ions is considerably more negative than the reduction of water (equation 2-7). Clearly, the presence of water hinders electrochemical deposition at negative potentials, primarily because of the substantial evolution of hydrogen (equation 2-8) [66].

$$2H_20_{(l)} + 2e^- \rightarrow H_{2(g)} + 2OH^-_{(aq)} \qquad (2-7)$$

$$2H^+ + 2e^- \rightarrow H_{2(g)} \qquad (2-8)$$

Assigning a redox potential $E(H^+/H_2)=0$ under standard conditions (standard hydrogen electrode, (SHE)) the equilibrium potential of any other redox reaction can be defined by experimentally measuring the potential difference between the SHE and the electrode under study [67]. The concentration-dependent electrode potential for redox reactions is determined using the Nernst equation [68]. In Pourbaix diagrams, the thermodynamic stability of metal-electrolyte systems is illustrated based on the Nernst equation with respect to pH [68].

Concurrently, the electrochemical grafting of various organic and inorganic substances, other than metals, are also well-established methods. Electrografting enables the deposition of ultra-thin organic films through robust molecule-substrate bonds. The control of the film thickness and compositions is achieved by manipulating electrochemical parameters, such as potential, time, and current density, electrolyte compositions involving different concentrations, simultaneous use of various monomers, pH, and solvent [68-71]. Given its typically cathodic nature, it can be employed on metallic and semiconducting surfaces without being constrained by oxide formation. In this context, electrochemical methods for coating conductive materials with polymers or silanes have garnered significant scientific attention. The use of grafted polymers, produced through electrochemically induced polymerization, holds considerable potential for diverse applications, making it a compelling avenue for future research [72].

One significant area of application lies in corrosion protection, utilizing the hindering and blocking properties of polymer layers on metallic components with complex geometries.

For instance, Sabbatini's group demonstrated the successful electropolymerization of poly(acrylic acid) films on titanium substrates, opening possibilities for physiological coatings with anti-corrosion and bioactive properties [73]. To provide a comprehensive understanding of the electrografting mechanisms, it is crucial to delve into the formation of deposits.

A model elucidating the electrodeposition process entails i) the initial step of a solvated ion traversing the diffusion layer, followed by ii) the loosening of the solvation sheath through electron transfer with the electrode, resulting in adsorption as the second step. The third step iii) involves surface diffusion and incorporation into an energetically favorable site.

The deposition sites can be either punctual or extended surface defects, such as vacancies or kinks, generally referred to as nucleation sites.

These nucleation sites facilitate the development of nuclei (islands) that undergo evolution into grains, forming compact deposits that grow atop the electrode surface [74].

A general mechanism of electrodeposit formation on the surface of an electrolyte is shown in Figure 2-5.

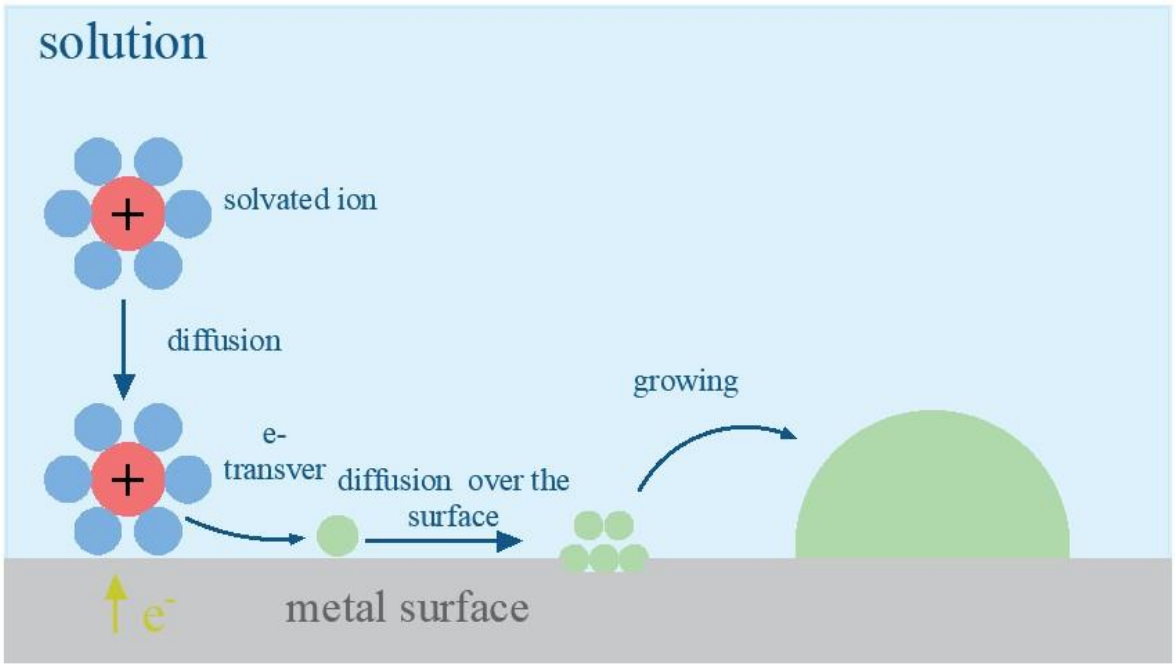

Figure 2-5: Graphical illustration of a general mechanism for electrodeposit formation on the surface of an electrolyte (drawing based on [74]).

The localized increase in current amplifies the deposition rate, promoting further growth of the asperities and consequently leading to an overall augmentation in the roughness of the electrodeposited layer [74].

Within the electrolyte bulk, mass transport is primarily driven by migration, an ionic motion mechanism induced by the presence of an applied electric field. In the electrochemical cell, the potential drop generates an electric field, significantly more intense in regions near the surface of the electrodes but sufficiently strong in the electrolyte bulk to facilitate ion migration toward the diffusion layer.

Thus, a significant mechanism of mass transport involves convection. Here, the ion migration occurs in an uncontrolled manner due to natural density gradients, which are caused by concentration and temperature fluctuations.

However, convection can also be controlled by different methods, such as mechanically stirring the electrolyte [74]. The following subchapter delves into the fundamentals of electrochemical grafting of BTSE and PAA on metal surface in order to provide a comprehensive understanding of the electrografting process and its significance for surface activation.

2.2.1 Electrografting of bis-1,2-(triethoxysilyl) ethane (BTSE)

Organosilanes are hybrid compounds featuring organic groups like methoxy or ethoxy attached to silicon atoms. They may also include additional functional groups, such as amines or epoxides, aimed at enhancing adhesion to metal surfaces [75-77]. They hold appeal for various industrial applications as they serve not only as adhesion promoters but also as corrosion barriers for many metals and alloys [78-81]. The processing of functional materials involving silanes and organosilanes falls within the realm of "sol-gel." The ultimate characteristics of the synthesized protective coatings rely on factors such as precursor chemistry, temperature, solution pH, molar ratios of reactants, solvent composition, water content, and catalyst presence [82,83]. Various sol-gel materials are produced based on the silane precursors used, offering distinct functionalities tailored to modify surface properties for specific applications. Moreover, silane treatments represent an easily applicable, cost-effective, and environmentally friendly option [84].

As described by Woo et.al [85], the sol-gel synthesis typically involves two steps:

1. *Hydrolysis*
2. *Condensation*

The first step involves the hydrolysis of siloxane groups to silanols in mildly acidic conditions, while the second step entails the condensation of the generated silanol groups, catalyzed by the controlled increase in pH induced by the electrode in its vicinity, completing the chemisorption process [85].

Bis-1,2-(triethoxysilyl) ethane (BTSE) $(H_5C_2O)_3–Si–(CH_2)_2–Si–(OC_2H_5)_3$ is an organosilane molecule containing six ethoxy groups. For the ideal linear structure, the hydrolysis of the ethoxy groups to generate functional silanol groups requires the addition of water. Since water and alkoxysilanes are immiscible, solvents such as alcohol are normally used as a homogenizing medium [86]. The hydrolysis reaction of BTSE is complex, but it can be expressed simply as [86]:

$$X - Si - O - CH_3 \; + \; H_2O \rightarrow X - Si - OH + \; CH_3CH_2OH \qquad (2-9)$$

Even while in solution, hydrolyzed molecules can undergo additional reactions to form dimers, trimers, and larger species through condensation. The condensation reaction can be outlined as following equation 2-10 [86]:

$$X - Si - OH \; + \; HO - Si - X \rightarrow \; X - Si - O - Si - X + \; H_2O \qquad (2-10)$$

Applications of electrochemical methods for sol-gel syntheses have experienced rapid development in recent years. The initial work by Woo et al. [85] may be the earliest report on the electrodeposition of silane films, primarily focusing on improving adhesive performance. Subsequently, Mandler's group [87] and van Ooij's group [88] have explored this technique for the anti-corrosion treatment of metals. Their findings indicate that silane films prepared at specific cathodic potentials exhibit higher corrosion resistance compared to those obtained through conventional dip-coating methods. In previous studies of Hu et al., various silane films, such as BTSE [89] and dodecyltrimethoxysilane (DTMS) [90, 91], were electrodeposited on aluminum alloys. Mandler and co-workers presented a novel approach of one pot sol-gel synthesis by electrochemically generating the condensation catalyst. This method is rooted in the "two-step" sol-gel preparation procedure [12], where the initial hydrolysis of a metal alkoxide occurs at a low pH, followed by polycondensation of the hydrolyzed monomer at a

higher pH. The separation of these steps is feasible because hydrolysis is rapid under acidic conditions, while condensation is enhanced in alkaline solutions which is dictated by the relative electron-withdrawing or donating power of –OH versus –OR groups [89,90] and it is minimally affected by other carbon-bonded substituents. The hydrolysis is headed by protonation of the alkoxy group [89]. In both acid- and base-catalyzed systems, during hydrolysis, the alkoxy group is replaced with the hydroxyl group on a pentacoordinate transition state of Silicon (Si). Figure 2-6 shows the acid- and base-catalyzed hydrolysis of silicon alkoxides [92].

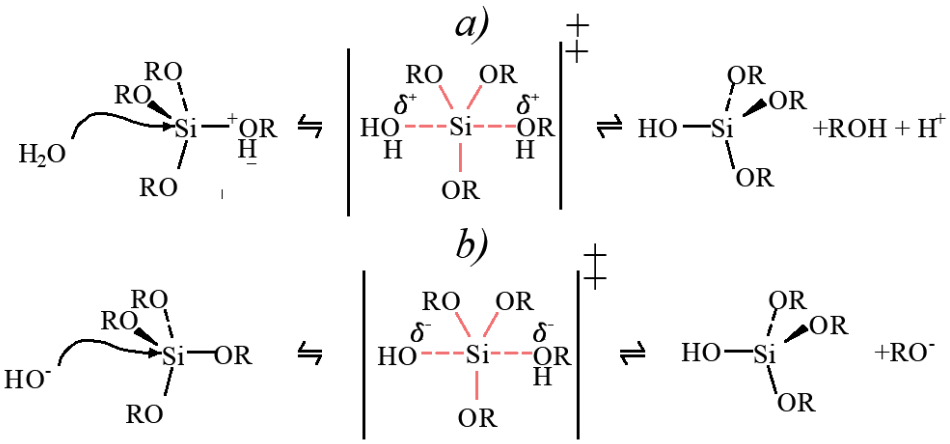

Figure 2-6: Acid- a) and b) base-catalyzed hydrolysis of silicon alkoxides (drawing based on Schnepp et al. [92])

The pH dependency of the hydrolysis and condensation of alkoxysilanes presented in Figure 2-7 [93]. When the reactions are base-catalyzed, gelation is fast due to the high rate of condensation, while, in acid-catalyzed reactions, the rate of hydrolysis is high with slow gelation [94].

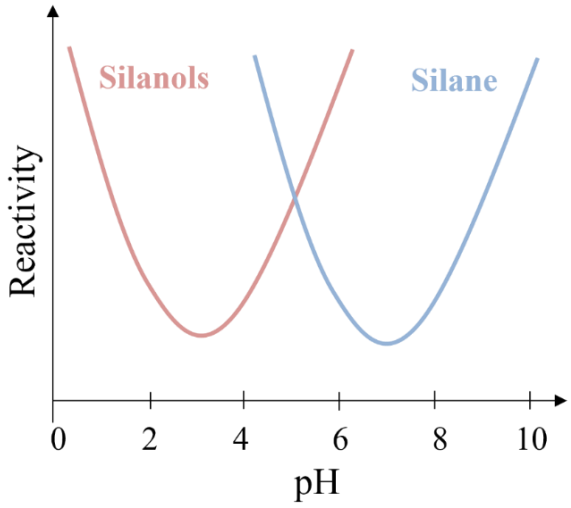

Figure 2-7: The pH dependency of the hydrolysis and condensation of alkoxysilanes (drawing based on Weissenbach et al. [93])

Pu et al. [94] examined the kinetics of hydrolysis and condensation for BTSE in a water–ethanol solution. The research showed that the hydrolysis rate reached a minimum at pH = 7, with rates increasing both at pH values lower and higher than 7. Additionally, they observed that hydrolysis was significantly faster than condensation at pH values lower than 4.5, while condensation was faster in the pH range of 4.5–9.0. At pH values near 4.5, the difference between hydrolysis and condensation rates tended to be small.

According to the developed methodology of Mandler and co-workers [12], a localized increase in pH near the electrode surface is induced by applying a constant negative potential to the electrode surface. Thus, they [12] also proposed the pH increase by reducing protons, such as nitrates, simply by adding $NaNO_3$ to the solution, a method that has not been previously utilized to improve sol-gel condensation and deposition. The generation of OH^- at the interfacial surface increases the pH in the vicinity of the electrode and catalyzes the poly-condensation between silanols. The organo-silane aggregates in solution have a surface potential caused by the charge-determining ions [12, 87].

Consequently, a silane-based thin film can be attached to the surface electrode by the deposition of the positively charged silane-particles after a sufficiently negative potential is applied forming a covalent bond to the metal surface (see Figure 2-8).

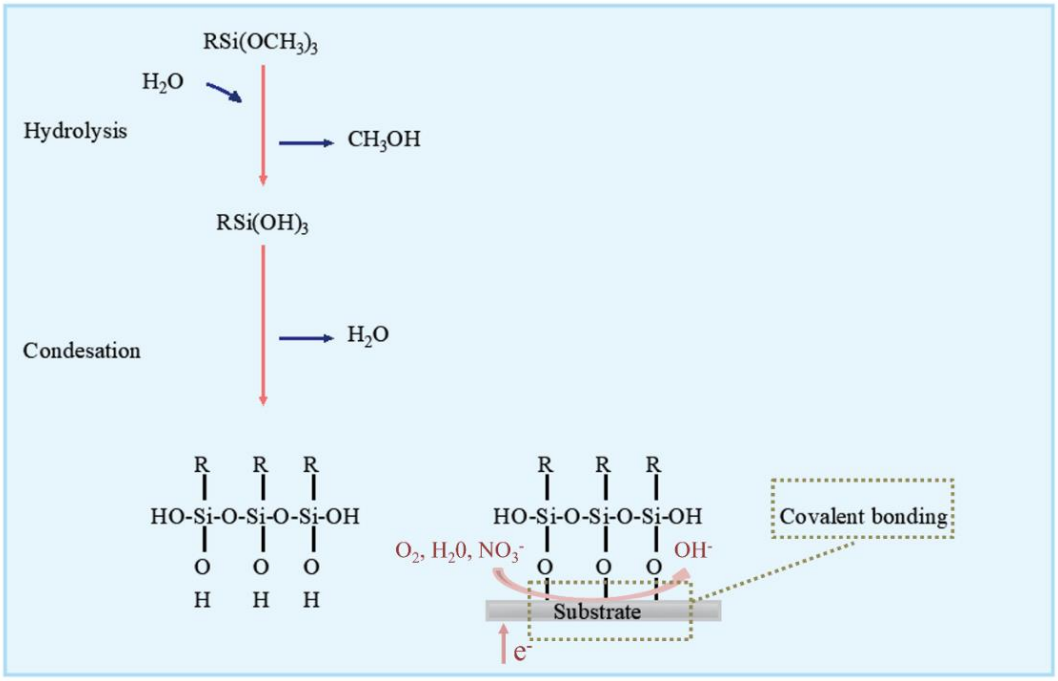

Figure 2-8: Electrochemical grafting silanols to the metal surfaces (drawing based on Hu et al. [89,90] including literature in there).

2.2.2 Electrografting of polyacrylic acid (PAA)

The electrografting of acryic acid (AA) molecules and subsequent polymerization into polyacrylic acid (PAA) on various substrates have demonstrated exceptional performance [23-29]. Due to the highly negative potential required for this reaction, it is typically not feasible to carry out the process in aqueous solutions, as it occurs at more cathodic potentials than the hydrogen evolution reaction (HER) [17, 18]. Consequently, the process is commonly conducted in organic solvents like acetonitrile (ACN) and dimethylfuran (DMF). However, in line with the principles of green chemistry for industrial applications, there is a desire to operate in aqueous solutions. Several approaches have been proposed. One involves designing vinylic monomers with an alkyl chain and a cationic functional group, along with the acrylic moiety [18, 19]. In this approach, micellization and adsorption onto the electrode surface can occur in the aqueous solution. Upon cathodic charging of the electrode, a bilayer of these molecules is organized at the solid-liquid interface, with the cationic head groups oriented towards the electrode. Subsequently, the acrylic groups in this double layer are reduced and grafted to the electrode (step 1) as radical species initiating the polymerization reaction (step 2). According to the authors, even with water molecules diffusing to the electrode surface, hydrogen radicals formed therein can sustain film growth by extending polymerization to closer micelles (step 3) [19]. A second approach, suggested by Palacin and colleagues, elegantly involves the electrochemical reduction of aryl diazonium salts and the subsequent grafting of aryl radicals to initiate the radical polymerization of an aryl-vinylic copolymer covalently bound to the steel substrate [27]. Here, the presence of a surfactant is required for emulsion formation containing the diazonium salt and vinylic monomers. A third approach, reported by Sabbatini and co-workers, involves the cathodic electropolymerization of PAA on Ti6Al4V substrates from acidic aqueous solutions containing AA and persulfate ions [30]. The electroreduction of persulfate at cathodic potentials generates sulfate radicals at the metal oxide solid-liquid interface, initiating the radical polymerization of AA monomers in solution. In a recent study, Bauer et al. employed a straightforward electrochemical procedure, involving the grafting of polyacrylic acid (PAA) thin films on carbon fibers and mild-alloy steel, to significantly enhance interfacial adhesion with model epoxy resins [22].

However, the utilization of electropolymerization with acrylic acid for depositing adhesion-promoting thin coatings remains an open field. Additionally, it is crucial to discern how the deposited coating interacts with the outer layers of the metallic oxide, a dependence strongly influenced by the deposition method and conditions.

In Figure 3-9, polymer-surface interactions are depicted, showing distinct covalent grafting of the polymers onto the surface. Depending on the polymer and its deposition process, different structures of the resulting polymer layer emerge.

The polymer density on the surface, influenced by factors such as polymer length, impacts the two distinct states of grafted polymers: the "mushroom" like deposition and "brush" state, as explained in the preceding paragraph for physisorbed polymers. Another intriguing aspect is the growth mechanism of grafted polymers.

In principle, two different mechanisms are possible: the direct coupling reaction of two functional groups (marked with "y" and "z" in Figure 2-9) or polymerization directly initiating at the surface containing some starting points or "nucleation" points [15,94].

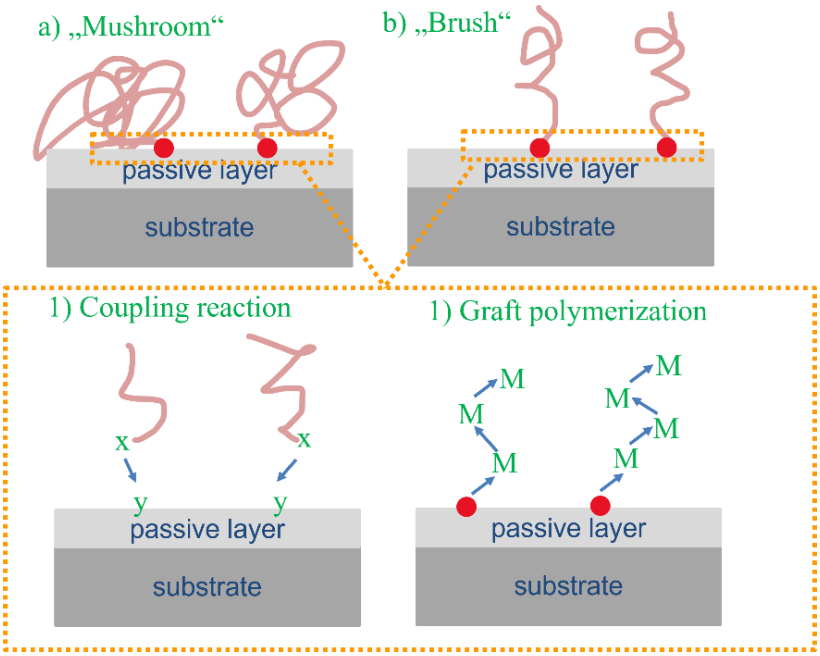

Figure 2-9: Electrochemically grafted polymers showing a) the “mushroom”-like state and b) the “brush”. Both a) and b) could be generated via a “direct coupling reaction” or a “graft polymerization” with monomers (drawing based on Butt et al. [56] and Uyama et al. [95]).

As an example of grafting poly (acrylic acid) on an oxide surface, Barroso-Bujans et al. explored the grafting of PAA on aluminum using free radical polymerization and chemical vapor deposition of acrylic acid with thermal polymerization [96]. Electrochemically initiated polymerization relies on a transfer reaction induced by the polarization of the working electrode, typically the metal substrate.

The electropolymerization of AA is facilitated by the high chemical reactivity of commonly used monomers. For instance, the initiation of AA can be initiated by metallic center such as zinc cations [97] or copper cations [98,99].

In general, there are two methods , for the generation of reactive species on the surface of the working electrodes: an electron transfer from either a radical-anionic species or anionic species of the AA monomer [100]. Anionic species exhibit high instability when reacting with other molecules like water or acids. Additionally, radicals can react with oxygen, giving them a biradical character and forming stable species. To prevent the cessation of the reaction, it is imperative to establish oxygen-free conditions.

The precise mechanisms of the reaction, particularly the initiation at the interface, remain open questions and are heavily reliant on the entire system and experimental conditions, especially the employed monomers [101-103].

2.3 Microstructure and mechanical properties of low alloyed steel and aluminum

2.3.1 DC04 steel alloy

Deep drawing steels such as DC04 steel alloy play a crucial role in the automotive industry, finding applications in vehicle bodies, fenders, floor panels, and door panels. Depending on their specific use, these steels must exhibit diverse mechanical properties, including high yield strength, tensile strength, and considerable fracture strain [104].

The varied demands in terms of mechanical properties have led to the development of a wide range of materials over the decades. Figure 2-10 illustrates different types of steels commonly used in automotive applications, categorized based on their fracture strains and strengths. The figure highlights the challenge of achieving a combination of high strengths and high fracture strains [105].

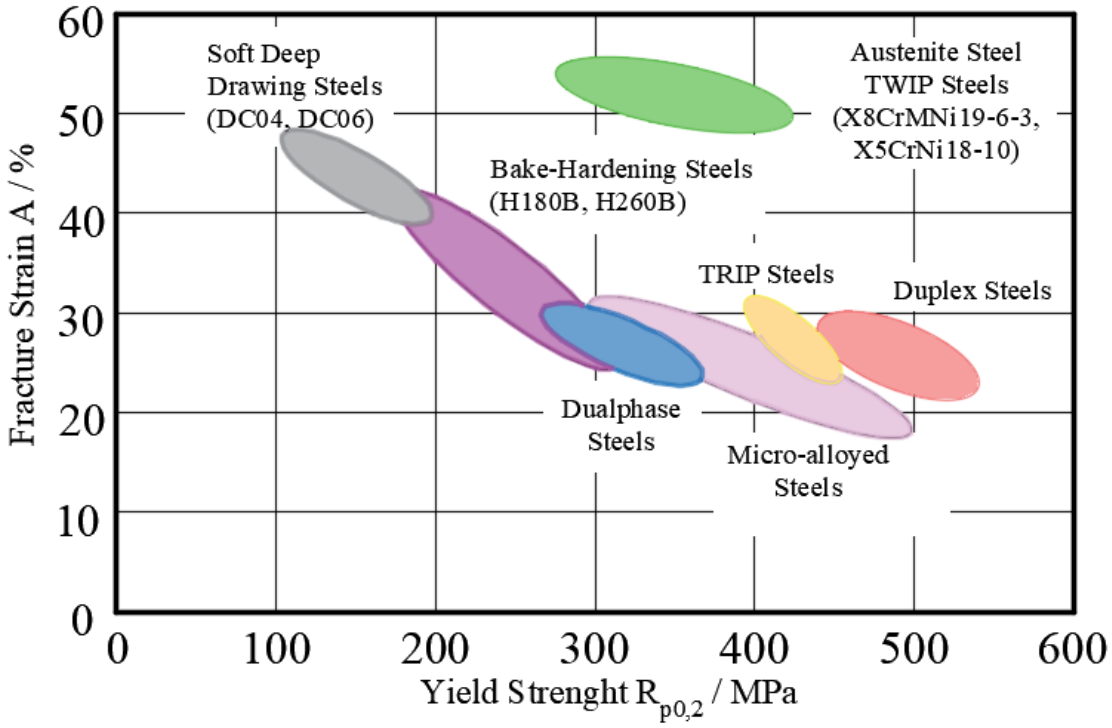

Figure 2-10. Illustration of different types of steels commonly used in automotive applications, categorized based on their fracture strains and strengths (drawing based on Steinbeck et.al [105]).

The chemical composition of the DC04 steel EN 1.0338 is detailed in Table 2-1, and the Standard mechanical properties, Yield point (R_e); Yield strength ($R_{p\ 0.2}$); Ultimate Strength ($R_{m)}$ and Elongation (A), are presented in Table 2-2.

Table 2-1: The weight percentage composition of EN-1030 DC04 steel alloy (wt.%) [106].

Fe	C	Mn	P	S
≤ 99.5	≤ 0.1	≤ 0.45	≤ 0.03	≤ 0.03

Table 2-2: Standard properties of the DC04 steel sheets [N2].

Norm designation	short form	R_e / MPa	$R_{p0.2}$ / MPa	R_m / MPa	A / %
DC04 1.0338	St	210	-	270-350	38

DC04 steel is a low alloyed deep drawing steel that has the same crystal structure as α-Fe. It was extracted from the production chain after the cold rolling process [104]. Figure 2-11 shows the grain morphologies of the alloy.

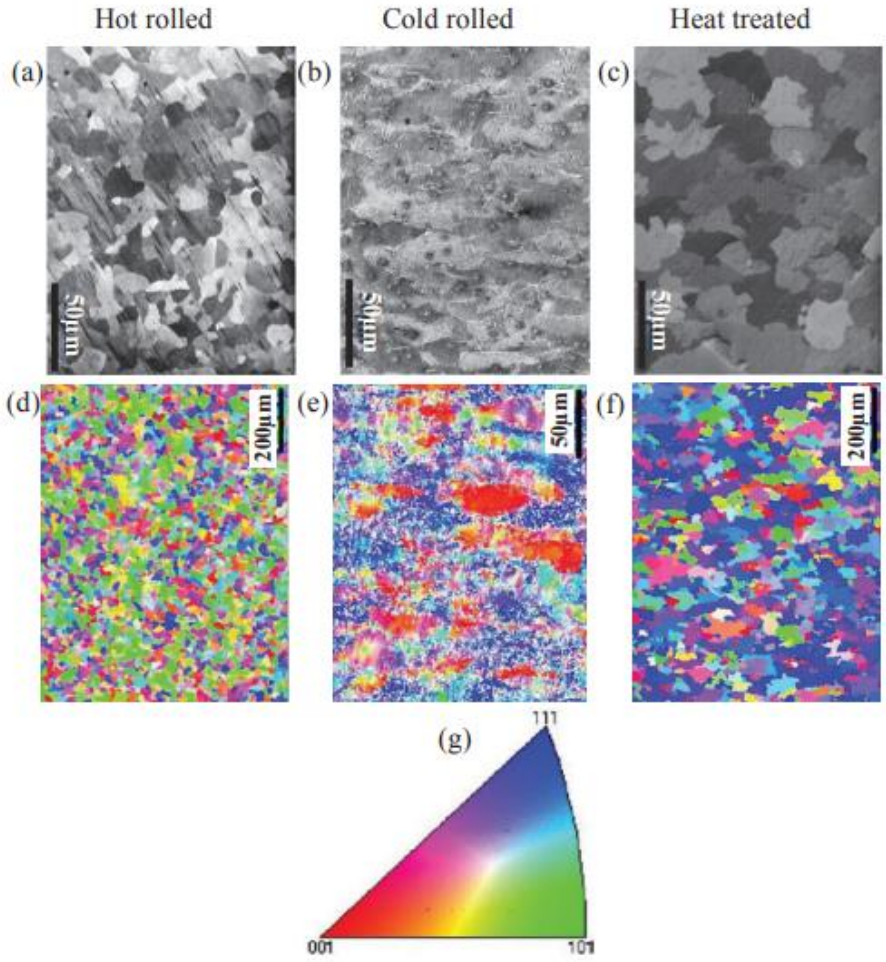

Figure 2-11: FIB and EBSD scan images of cold rolled DC04 steel. Reprinted from Ref. [104] (Open access under the CC-BY-NC-ND 3.0 DE license.)

Schreijäg et al. have studied the grain morphology of the hot and cold rolled DC04 material via SEM-FIB and showed that cold rolled DC04 material Figure 2-11b has strong <111> and <001> fiber texture components whereby the <111> fibers have a higher intensity than the <001>. The orientations of the fibers are preferentially aligned along the rolling direction [104]. The SEM images of the cold rolled DC04 steel show a grain morphology that is elongated along the rolling direction showing several undetected points (white pixels) which are visible in the Electron Backscatter Diffraction (EBSD) scan. The white pixels are a result of a distorted diffraction patterns that cannot be identified by the EBSD software. Distorted patterns may occur due to multiple crystal orientations at one data acquisition point or due to smeared out diffraction patterns in highly deformed regions [104]. Since the orientations vary

within the grains it can be assumed that the grains were strongly deformed during the cold rolling process [104].

2.3.2 EN-AW-1050A H 111 Aluminium alloy

Aluminum stands out as the lightest metal among common metals, with a density of 2700 kg·m³, nearly three times less than that of steel. The density of aluminum alloys falls within the range of 2600 to 2800 kg·m³ [107]. Practical experience has demonstrated that a structure made from an aluminum alloy can be up to 50% lighter than its counterpart crafted from mild steel or stainless steel. This consideration accounts for factors such as the modulus of elasticity (one-third of that for steel) and the fatigue limits of structures, whether welded or bolted, constructed using aluminum alloys [107].

Aluminum, like steel, comes in various alloys and forms. EN AW-1050A, characterized by its minimum 99.5% aluminum purity, displays modest strength characteristics. Nevertheless, the elevated purity contributes positively to the material's physical attributes, including thermal and electrical conductivity. Moreover, EN AW-1050A demonstrates exceptional cold-forming capabilities and resistance to atmospheric corrosion. Recognized for its weldability, the material is employed in various applications, serving as a deep-drawn, pressed, and sheet-formed component. It also finds utility in roles like a light reflector or electrical conductor [107]. The chemical composition of the EN AW-1050A aluminum alloy [108] is detailed in Table 2-3, while the standard mechanical properties, yield point (R_e); yield stress ($R_{p\ 0.2}$); ultimate strength ($R_{m)}$ and elongation (A), are presented in Table 2-4.

Table 2-3: Weight percentage composition of EN-AW-1050A aluminum alloy (wt.%) [13].

Al	Fe	Si	Cu	Mn	Mg	Zn	Ti
≤ 99.5	≤ 0.5	≤ 0.25	≤ 0.05	≤ 0.05	≤ 0.05	≤ 0.07	≤ 0.05

Table 2-4: Standard properties of the of EN-AW-1050A aluminum sheets [N3].

Norm designation	short form	R_e / MPa	$R_{p0.2}$ / MPa	R_m / MPa	A / %
EN-AW-1050A	Al	-	20	65-95	22

The microstructure of a material serves as a key indicator of its inherent properties. Material characteristics are notably influenced by the volume fraction of inclusions and the grain size.

Alterations to the microstructure take place throughout various processes, including homogenization, annealing, preheating, as well as solution heat treatment and precipitation heat treatment [109].

Figure 2-12 illustrates a representative TEM micrograph of EN-AW-1050A aluminum alloy published by Kurzydłowski et al. [109] alongside the grain size distribution of the as-deformed material. The microstructure showcases an ultrafine grain structure with an average grain equivalent diameter of 300 nm. The grains exhibit minimal dislocations and possess a relatively equiaxial shape. Grain orientation analyses indicate that the grains align either with the <111> or <100> direction parallel to the extrusion direction, as depicted in an insert within the micrograph. Kurzydłowski et al. studied the grain boundary misorientation distribution showing that the calculated fraction of high angle grain boundaries (HAGB), defined as those with a misorientation angle was greater than 15, is 72% [109]. This, along with the bimodal distribution of misorientations, aligns with findings from other investigations on severely deformed aluminum alloys [110–112].

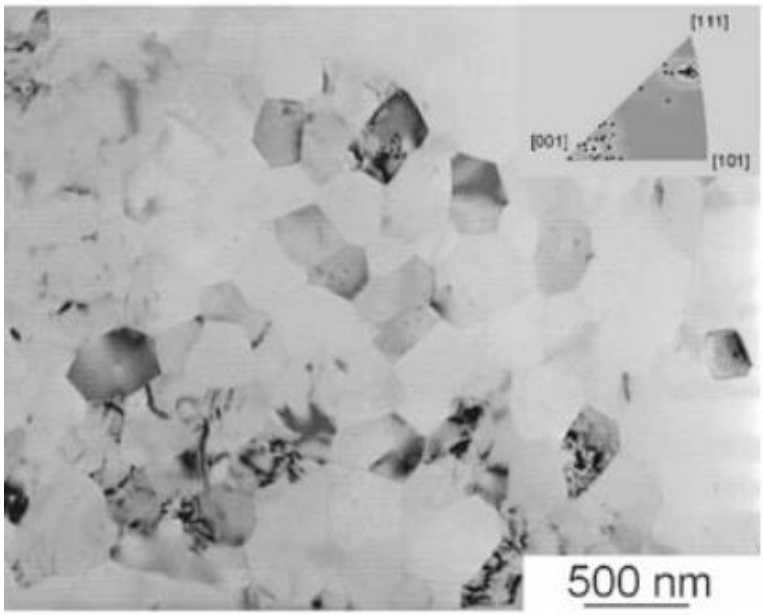

Figure 2-12: TEM micrograph and grain size distribution of EN-AW-1050A aluminum alloy. (Reprinted with permission from Ref. [109]. Copyright @ 2024, Springer Nature).

As previously mentioned, aluminum and its alloys EN AW-1050A demonstrates resistance to atmospheric corrosion. In this context, the formation of a thin oxide layer, approximately 5 nm thick, contributes to the passivation of aluminum materials against corrosion within the pH range of 4.5 to 8.5 [113]. This characteristic might be unexpected, considering that

aluminum, with a reduction potential of -1.67 V, is inherently a less reactive metal. Despite its cathodic potential, which suggests aluminum should be prone to oxidation, the reality is that aluminum exhibits remarkable stability. This stability is credited to the spontaneous formation of aluminum oxide in an oxidizing environment, as indicated by the following equation 2-11 [113]:

$$2Al + \frac{3}{2}O_2 \rightarrow Al_2O_3 \qquad (2-11)$$

The spontaneous reaction of aluminum with oxygen, resulting in the formation of a stable and dense passivating oxide layer, is driven by a free energy of -1.67 kJ/mol. Given its amphoteric nature, aluminum exhibits reactivity in both acidic and alkaline environments. The passivation range of aluminum is depicted in the subsequent Pourbaix diagram (see Figure 2-13) [113].

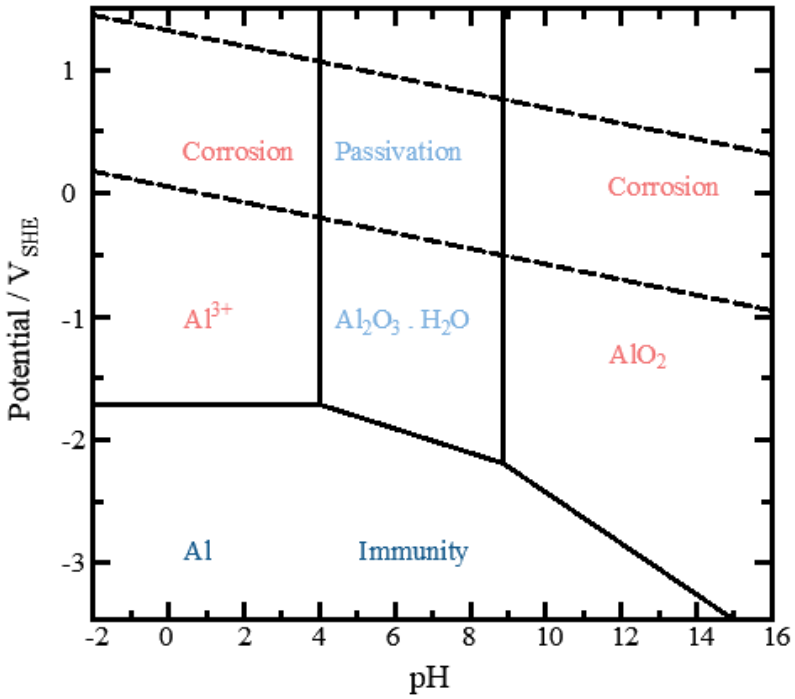

Figure 2-13: Pourbaix diagram of Aluminum (drawing based on [113])

To elucidate aluminum passivation, it is essential to consider the stability of the oxide layer and the dissolution rate of aluminum, both of which depend on the pH level. The dissolution rate is directly impacted by the stability of the oxide. In acidic pH ranges, aluminum reacts with substances like hydrochloric acid (HCl), leading to an increase in the dissolution rate with higher concentrations. Conversely, aluminum does not undergo a reaction with nitric acid

(HNO_3), making it a frequently employed option due to its oxidizing properties for enhancing the strength of the oxide layer [114,115].

Within the framework of this thesis, the pickling of aluminum in NaOH was undertaken to create a meticulously defined oxide layer. This step played a pivotal role in ensuring the success of the subsequent Cold pressure welding (CPW), a subject that will be further explored in the forthcoming subchapter focusing on the importance of surface treatments in CPW.

2.4 Joining by plastic deformation

2.4.1. General aspects

Transportation vehicles like airplanes and automobiles are constructed from an extensive array of mechanical components, manufactured through diverse production methods. Automobiles typically incorporate 10,000–30,000 parts, while aircraft boast millions of components [116]. A prevailing trend in the manufacturing of these products involves a simultaneous increase in both the quantity of parts and their intricacy, often incorporating novel combinations of dissimilar materials [116]. In the manufacturing processes welding, adhesive bonding, and mechanical fastening are commonly employed for assembling two metal parts. Welding typically involves using an external heat source to melt material at the interface and create the joining. Although welding is widespread, its high operating temperatures can impact the quality, precision, and reliability of the assembled parts. In the other hand, joints created with adhesives or mechanical joining often lack the strength of welded joints. In manufacturing, plastic deformation is commonly employed in forming processes to shape mechanical parts and manipulate their mechanical properties.

Beyond its typical application in shaping, plastic deformation can also serve as a method to join parts with adequate ductility, eliminating the need for an external heat source as in fusion welding.

The processes for joining through plastic deformation can be conveniently categorized into two groups [116]:

1) *Metallurgical joining:*

- *cold welding by rolling, extrusion, forging, etc.,*

- *friction welding,*
- *friction-stir welding,*
- *resistance welding, etc.*

2) *Mechanical joining:*

- *self-pierce riveting,*
- *mechanical clinching,*
- *joining by forming*
    - *hydroforming,*
    - *electromagnetic forming, and*
    - *incremental forming.*
- *fastening*
    - *hemming,*
    - *seaming, and*
    - *staking.*

In mechanical joining through plastic deformation, interfacial pressure and interlocking are employed without relying on thermal effects. The pressure persists at the interface even after unloading resulting in the mechanical joining of the workpieces. Unlike metallurgical joining processes, the contacting surfaces in mechanical joining processes are not bonded, eliminating the need for breaking up oxide films and elevating interfacial temperature. In these mechanical joining processes, plastic deformation is precisely controlled to generate the required pressure and interlocks [116].

Mechanical joints find broader applications and are frequently stronger than those from mechanical fastening methods [117]. As products like aircraft and cars become larger and more complex, there is an increasing demand for new functional processes to join mechanical parts. Using plastic deformation for joining parts has the potential to offer improved accuracy, reliability, and environmental safety, opening avenues for designing new products by joining dissimilar materials [116]. Mori et al. have reviewed the recent developments and progress in joining processes using plastic deformation [116].

However, joining by plastic deformation has its advantages and disadvantages compared to fusion welding which are collected in the Table 2-5.

Table 2-5: Advantages and disadvantages of CPW compared to fusion welding.

Advantages	Disadvantages
➢ diverse material compatibility ➢ reduced distortion, embrittlement, and tensile residual stress ➢ high process reliability and streamlined quality control ➢ environmental safety	➢ mainly joints that overlap ➢ geometrical unevenness of joining ➢ difficulty in correction and repair ➢ lacking standardization and calculation methods

2.4.2 Cold pressure welding

Cold welding, also referred to as cold pressure welding (CPW), is a solid-state welding procedure typically conducted at room temperature below the recrystallization temperature. This technique is among the earliest forms of welding, with historical roots (hammer welding) tracing back to around 1000 b.c.[118]. The method allows the joining of numerous metals, including challenging dissimilar combinations like Al–Cu, Al–Fe, and Al–Ti, which cannot be achieved through fusion welding. In-depth insights into the fundamental aspects of cold welding can be found in comprehensive reviews by Milner et al. [119], Bay et al. [120], and Li et al. [117]. The formation of a metallic bond requires interaction between surfaces on an atomic level, i.e., at a distance of a few angstroms (1-2 Å [121]). At this distance, both ionic bonding (Coulomb force) and van der Waals bonding are significant. Regardless of the type of bond between the surfaces, they require “clean” metallic surfaces. However, under normal atmospheric conditions, adsorption layers, such as those formed from absorbed gases, develop naturally on all metals [116]. Such layers hinder the formation of a press-welding joint which will be further explained in relevance of surface treatments in section 2.4.5.

Durst et al. have reported experiments on PCW of stainless steel (18-8 CrNi) and mercury in liquid nitrogen [122]. Hofmann and Ruge measured nearly the same shear strength for aluminum joints made at temperatures of -150 °C and -50 °C as at room temperature [123]. There also seems to be no direct dependency on time, as indicated by the wide range of press welding processes in the field of high-speed forming.

Press welding connections can be established even with process times of a few microseconds [124]. Lu et al. observed the CPW of single-crystal gold wires in the transmission electron microscope (TEM) and reported a complete welding 1.5 s after welding [125]. Bay developed a model of the structure of press welding joints based on the assumptions of the so called “film theory”, which will be explained in more detail in the following section.

From his studies, a relationship between the bond strength of press welding connections and the nominal tensile strength of the material was derived [126]. In his investigations, Bay initially focused on roll-bonded composites of aluminum, whose surfaces were pretreated and activated by mechanical brushing. In the context of this thesis CPW was performed via incremental rolling tool.

Bay et al. [126] defined the exposed surface Y as the reference quantity (Surface Exposure) since only the newly exposed surface during deformation can form a press welding joint (equation 2-12):

$$Y = \frac{A_1 - A_0}{A_1} \qquad (2-12)$$

where A_0 and A_1 are the initial and final interface areas, respectively.

For the formation of press welding joint between surfaces, Bay et al. [126] divided the surface into two parts: surface covered with a native oxide or absorption layer (F, film), and surface additionally covered (C, cover layer), as generated, for example, during mechanical brushing. The failure of the surface during deformation depends therefore on the condition of the surface, where Bay et al. [126] distinguished between two failure mechanisms: failure of the native oxide and absorption layers and failure of the cover layer. Figure 2-14 shows the schematic representation of the three steps leading to the formation of press welding joints between two surfaces.

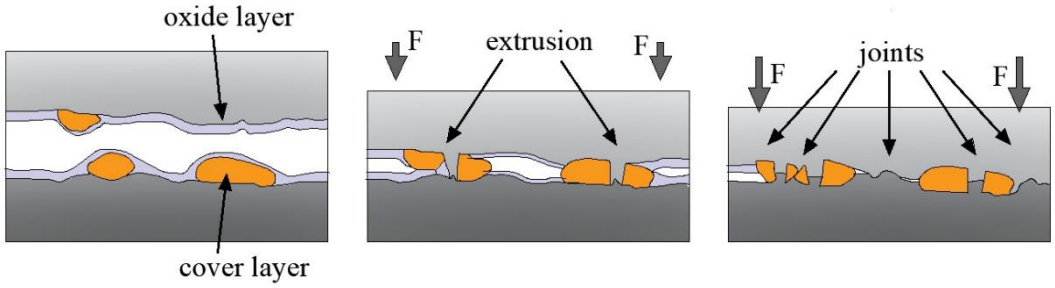

Figure 2-14: Schematic representation of the three steps leading to the formation of press welding joints between two surfaces (drawing based on Bay et al. [126]).

Drawing on metallographic investigations based on Bay et al., a continuum mechanics model has been formulated to predict the bond strength in the cold welding of two identical

materials. This model correlates bond strength with normal pressure and surface exposure, which is described by the following equation 2-13 [126]:

.

$$\frac{\sigma_b}{\sigma_0} = (1-\beta)Y\frac{p-p_E}{\sigma_0} + \beta\frac{Y-Y'}{1-Y'}\cdot\frac{p}{\sigma_0} \qquad (2-13)$$

where σ_B is the bond strength, σ_0 the flow stress of the material after deformation, p the normal pressure on base metal surfaces, p_E the pressure required to extrude through cracks of the cover layer and Y_0 the threshold surface exposure for the contaminant film.

The initial component in equation 2-12 signifies the impact on bond strength originating from the region where the brittle cover layer fractures. This is applicable in regions where either one or both mating surfaces possess a brittle cover layer, as indicated by following equation 2-14:

$$\beta = \varphi \cdot f^2 \qquad (2-14)$$

where φ is the fraction of film layer.

Drawing upon fundamental investigations regarding the impact of hydrostatic pressure on the ductility of the cover layer [127], the model was subsequently extended by Zhang et al. [121].
To encompass cold welding of dissimilar metals by incorporating several additional influences:

- *differentiation between joining partners with varying strength (hard, soft)*
- *contact between different surface conditions*
- *mechanical properties of the cover layers (ductility G)*
- *surface portions of different cover layers and their combinations (γ), and*
- *ratio between crack width and layer thickness.*

This description is based on the equilibrium between bond strength σ_b and the normal pressure at the junction where, according to Conrad and Rice, the bond strength between ideally pure and active surfaces is equal to the contact pressure during welding [128].
The bond strength is calculated as the sum of the four partial strengths:

- *with cover layer,*
- *without cover layer (film),*

- *a cover layer only on the soft joining partner, and*
- *a cover layer only on the hard joining partner.*

Here, the ductility of the cover layer G is defined through the true exposed surface Ψ. This is determined by the new surface A_l, subtracting the area still covered by a cover layer A_c (covered). Therefore, $G = 1$ represents a ductile, and $G = 0$ represents a brittle cover layer [127].

It is very important to highlight that the two descriptions by Bay and Zhang have been derived from a multitude of results, and the developed conceptual model for the formation of press welding joints is acknowledged as empirical [129]. However, their application requires an elaborate parameterization through a series of experiments. The so-called Freiberg model is described as an extension of the models by Bay and Zhang. It consists of a significantly more complex simulation system, where the rolling process and surface contact, along with their mechanics, are depicted in detail [129, 130].

2.4.3 Cold pressure welding by incremental rolling

Metal welding, as defined by DIN EN ISO 2080, involves the "application of a metal coating onto another metal through mechanical manufacturing processes" [N4]. The various welding processes can be distinguished by the achievable layer thickness including explosion welding, which has a maximum of 200 mm, hot rolling welding, with a maximum of 55 mm, cold rolling welding, with a maximum of 6 mm, weld overlay, involving several millimeters, and electroplating, with a thickness of a few micrometers [131-133].

Roll welding involves distinguishing between cold and hot roll welding. If the material pairing demonstrates sufficient ductility, cold rolling can be applied. Hot rolling is used to increase the ductility of solid materials or to equalize the flow stress of significantly different materials. In the present day, nearly all technically relevant materials can be manufactured in combination as a clad composite [134]. This process allows for the processing of both thin sheets and entire slabs. In industrial applications, roll-welding composite materials are utilized when the properties of a base material can be enhanced in terms of mechanical, thermal, or chemical resistance by overlay materials, without the need to switch to a generally more expensive base material [135]. Instances of this include applying copper on steel to enhance electrical conductivity (in electronics), utilizing stainless steel on steel for corrosion protection (in chemical apparatus), or employing pure aluminum on aluminum alloys for

improved corrosion resistance (in aerospace). The array of applications spans from button cells (comprising copper/stainless steel/nickel) and lithium-ion batteries (comprising copper/nickel) to foils for catalysts (comprising aluminum/stainless steel), façade elements (comprising copper/steel), and household items (comprising copper/stainless steel) [134].

The application scope also encompasses transition metals to forestall galvanic corrosion on electrical contacts (steel/aluminum) [134]. The assembly of a welding composite through press welding connections occurs under substantial pressure and adequate deformation of the joining partners or their surfaces within the rolling gap. Within the rolling gap, it is imperative to establish the requisite conditions to subsequently achieve a fully integrated and load-bearing composite.

Rolling, categorized under bulk forming in accordance with DIN 8583 [N5], is characterized as a continuous pressure forming process [136]. The basic configuration of the forming zone in the rolling gap is depicted in Figure 2-15.

The material traverses the rolling gap with a decrease in height Δh. Essential factors in describing the rolling process encompass the relative draft ε_h, the roll angle α, the bite angle α_e, the pressed length l_d and friction coefficient μ [136].

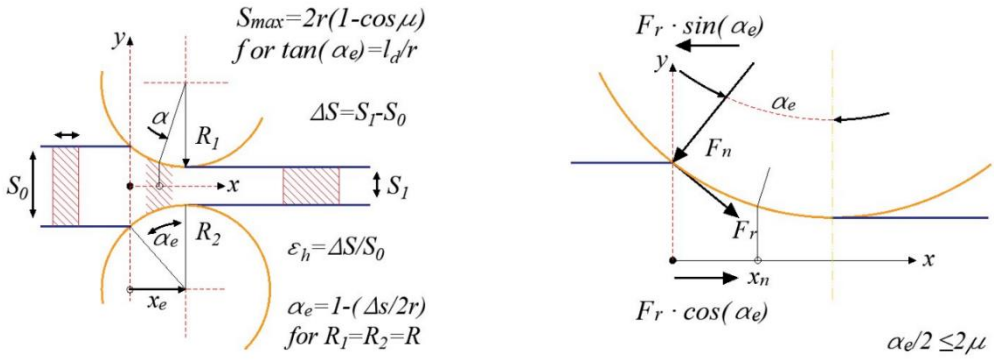

Figure 2-15: Graphical illustration of the rolling gap main configuration a) and the acting forces b) (drawing based on Lange [136]).

To facilitate the material's independent advancement into the rolling gap, it is essential to fulfill both the gripping and pulling conditions. In general, for the gripping condition with Coulomb friction, equation 2-15 [136] is relevant:

$$F_n \sin \alpha_e \leq \mu F_n \cos \alpha_e \qquad (2-15)$$

For relatively small drafts the equation can be expressed as $\alpha_e \leq \mu$. Similar to the gripping condition, the pulling condition ($\alpha \leq 2\mu$) is established, with forces acting in the middle of the rolling gap ($2\alpha=\alpha_{e1/2}$). To extend the operational range for larger drafts, Lange suggests the following measures [136]:

- *increase of the surface roughness ($\mu\uparrow$),*
- *larger roller diameter ($\alpha_e\downarrow$),*
- *reduce of the draft in the inlet by tapering the material,*
- *pushing or pulling the strip.*

Over the years, roll welding has taken diverse directions and broadened its scope to encompass new applications or cladding platforms.

Building upon the foundation of basic overlay welding, further possibilities for cladding forms have emerged [137].

Roll welding with intermediate layers represents a process variation where an extremely thin intermediate layer is inserted between the cladding partners. The purpose of this intermediary is to establish a bond with metals that either lack or have insufficient bonding surfaces with each other. Moreover, it allows for the use of materials that can form an alloy with one or both welding partners. For instance, Knauscher discusses the utilization of nickel [138].

The incorporation of separating layers in roll welding enables the deliberate prevention of connection formation. Kleiner et al., for example, employed a graphite suspension as a separating agent, applied through screen printing [139]. These partially connected sheets find applications primarily in subsequent processes like Internal high-pressure sheet metal forming (Innen-Hochdruck-Blechumformung (IHU)). In [139], the production of car body components is explored, and Rubanox SA, as of now, engages in the production of various products, including heat exchangers and evaporator plates, utilizing roll cladding with separating layers [140]. Figure 2-16 shows the schematic structure of the rolling gap in the roll cladding of a soft (w) and hard (h) material, according to [141].

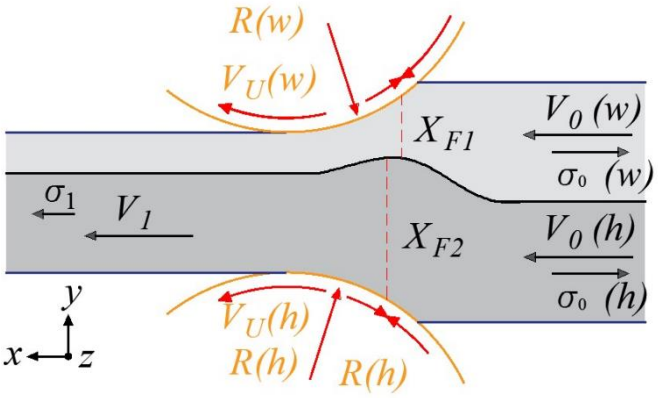

Figure 2-16: Schematic illustration of the rolling gap structure in the roll cladding of a soft (w) and hard (h) material, according to (drawing based on Trumble et al. [141]).

In this context, an incremental approach for joining through deformation was performed. Figure 2 -17shows a schematic representation of the incremental rolling concept developed by Schmidt et al. [48]. The fundamental notion revolves around the gradual deformation of sheet-shaped metallic materials. The forming tool seamlessly integrates a rolling motion with the deformation of the joining partners as it approaches, initiating a cohesive joining process. The entire roller can either be eccentrically mounted for executing the deformation or work with a shaping element on the roller surface.

The simultaneous deformation aims to establish a friction welding connection between the surfaces of the joining partners. After "setting" such a joining point, the tool undergoes repositioning, leading to the establishment of a second joining point. This approach facilitates the creation of diverse joint locations through a suitable process regime, ranging from point-shaped and linear to curved joint contours. The construction of a friction welding connection typically demands a substantial degree of deformation [48]. To mitigate the required minimum deformation, surface activation becomes crucial. The exploration of electrochemical technologies holds substantial promise and is, therefore, a focal point of investigation in this thesis.

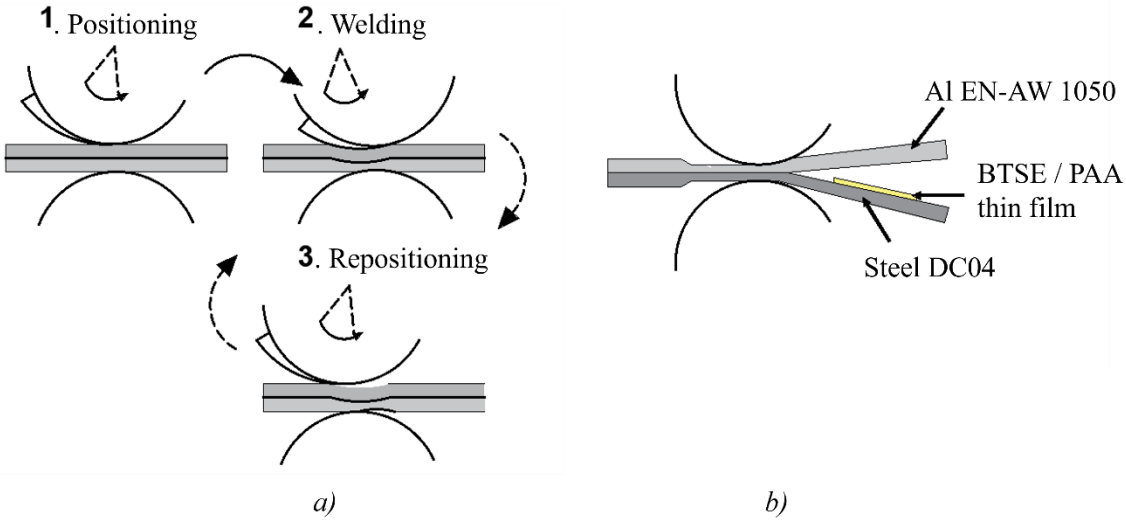

Figure 2-17. Illustration depicting the incremental rolling of sheets and their electrochemical surface activation: a) sequential steps in the joining process through incremental rolling for a linear joint; b) Activation of surfaces using electrochemical methods (drawing based on Schmidt [48]).

2.4.4 Relevance of surface treatments

> "When a plate of gold shall be bonded with a plate of silver or joined thereto, it is necessary to beware of three things of dust of wind, and of moisture: for if any come between the gold and silver, they may not be joined together…"
>
> Extract from "On the Properties of Things"- John Trevisa's Translation of "Bartholomew Anglicus De Proprietatibus Rerum" AD 1323 d.c. [142]

Recognition of the important role that surfaces play in technology has been longstanding. Cold welding in the atmosphere is consistently linked to contaminated surfaces that cannot adhere to each other unless there is sufficient surface exposure to fracture the surface film. Figure 2-18 shows a metal surface in an oxygen-containing atmosphere [143].

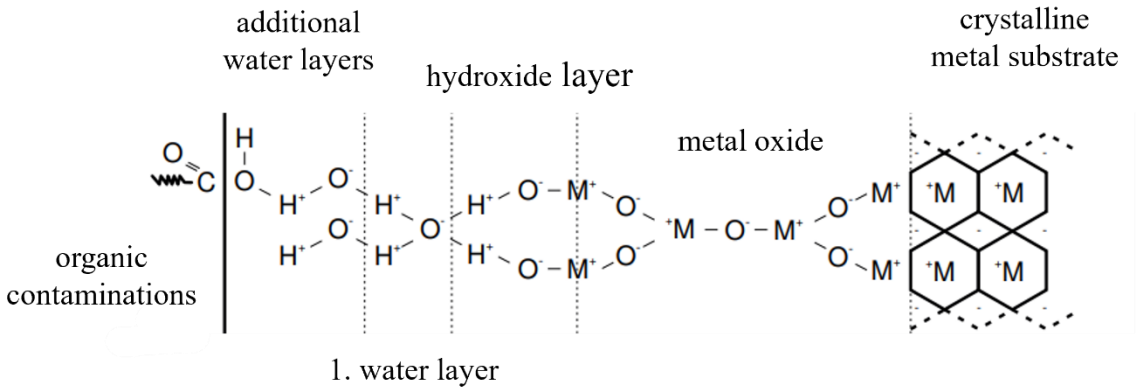

Figure 2-18: Schematic illustration of a metal surface in an oxygen-containing atmosphere (drawing based on Bobzin [143]).

Surface preparation before cold welding is thus a fundamental parameter that governs the mechanisms of bond formation. Various methods have been explored in the literature, such as those by Vaidyanath and Milner [151], Clemmensen et al. [154], and Schey [146]. Most authors suggest that degreasing followed by scratch-brushing with a rotating steel brush is the most effective treatment [116, 144,145, 149, 150]. Experimental studies by Wittman [147] and Ulmer et al. [148] suggest that the normal pressure on the weld interface significantly influences weld strength. This explains why different weld strengths are achieved at the same surface exposure in different processes.

The methods of surface preparation can be categorized into three groups:

1. chemical / electrochemical cleaning,
2. mechanical cleaning, brushing/ polishing, and
3. establishing a thin surface coating.

1.Chemical / electrochemical cleaning

Chemical procedures like pickling are highly efficient in cleansing metal surfaces, covering the entire treated surface in contrast to mechanical activation. However, they may leave behind reaction by-products, necessitating neutralization.

The efficacy of the cleaning process might decrease due to potential "contamination" from the neutralization solution. Even solvent cleaning is conducted prior to brushing [135] to prevent recontamination and avoid impeding the bonding process between surfaces [151].

Electrochemical techniques present significant potential as activation technology, further enhancing the weldability of metals in press welding. Electrochemical surface treatment methods, such as electroplating, enable the targeted and localized processing of metal surfaces

(selective electroplating). This encompasses cleaning through surface removal or dissolution (electropolishing), the deposition or formation of protective layers (electrodeposition), and the precise modification of surfaces through electrolysis. Electrochemical processes, thus, amalgamate various potential benefits for activating sheet metal surfaces. They operate uniformly or selectively, material-specifically, and in a controlled manner [48].

The potential of electrochemical treatments has been primarily explored for applying additional protective layers of third metals. Bay investigated the press welding behaviour during roll cladding of aluminum with a nickel coating [126] and observed that the nickel coating influenced the failure behaviour of the protective layers favourably. Positive properties of a nickel coating have been noted in studies on press welding of electrical components [152, 153]. Dubolazov et al. attribute the brittle properties of the nickel coating to hydrogen ingress (composite of Kovar steel and copper) [153]. Scanning electron microscope images (SEM) in [154] illustrate how the protective layer on the surface tears open, exposing pure aluminum. In the research by Clemensen [145] the nickel coating could achieve the same composite strength and threshold value as pretreatment by mechanical brushing. A significant advantage of a nickel coating lies in the time-independent quality of the pretreatment. Koike et al. indicate a durability of four months for the nickel coating in high humidity without compromising weldability [155]. Likewise, subjecting steel surfaces to electrochemical cycling led to an enhancement in the bond strength between steel and aluminum during the welding process [39]. Ebbert et al. demonstrated that electrochemically reducing the native oxide layer on copper specimens, results in a significant increase in surface roughness with achieving higher levels of weld strength [40].

2.Mechanical cleaning, brushing/ polishing

The studies of Bay et al. [120] have unveiled that utilizing scratch brushing results in a surface that is, in part, composed of a relatively thick, hard, and brittle cover layer (approximately 20 mm), and in part, a surface solely covered by a contaminant film of oxides and water vapor. Bonding in these regions takes place when the contaminant film, which is in the order of 10–100 nm. Experimental investigations were conducted on the cold welding of surfaces that had been scratch brushed. Analysis of the welds under an optical microscope [156] led to the hypothesis that the fundamental bonding mechanism results from the fracture of surface layers, exposing clean metal surfaces that weld upon subsequent contact. Subsequent studies of fractured cold welds in SEM confirmed this hypothesis [157], emphasizing the paramount importance of surface preparation before cold welding. Scratch brushing as a surface preparation method produces a hard, brittle surface layer that fractures under expansion. As shown in Figure 2-19, with significant surface expansion, the virgin material is exposed, extruding through the cracks in the surface layer to meet the similarly exposed surface area from the opposing metal [23].

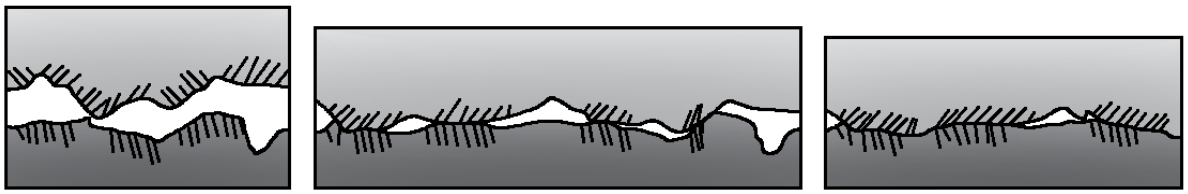

Figure 2-19: Schematic illustration of a model for bonding mechanism in cold welding with a) Scratch brushed surface; b) extrusion of virgin material and c) bonding (drawing based on Bay et al. [120])

3.Establishing a thin surface coating

The modification of metallic surfaces using electrochemical to form thin surface coatings is extensively applied in various industrial procedures. This encompasses traditional electroplating for the application of metal coatings (enhancing surface properties through deposition) to electropolishing, which involves cleaning and refining through material removal.

Electrochemical surface pretreatments can be categorized into three types based on their effects[158]:

1. Active coatings that inherently contribute to bond strength.
2. Passive coatings that enhance bond strength, either minimally or through an additional process step (e.g., diffusion annealing).
3. Modifications that bring about a change in the atomic surface structure through cleaning or activation.

Jensen et al. illustrated a single instance of active coatings, specifically in the realm of friction welding. This involves a coating that is expelled during the forming process, causing the destruction of the surface layers [158]. This methodology can be linked to the use of interlayers, where a soft layer functions as an adhesive due to the absence of bond formation between the primary joining partners, often due to insufficient deformation. The practical implementation of active metal coatings is highly challenging and would only be plausible with precious metals. However, even gold, with its ability to form a boundary layer on its surface, does not weld immediately upon contact under normal atmospheric conditions [159]. Consequently, active coatings, primarily metallic ones, are practically unattainable, not only due to cost considerations. Potential solutions lie in organic, bondable layers whose activity is not constrained by elements such as oxygen or nitrogen. These layers could serve as effective adhesion promoters. It's crucial to note that the bonding in this context does not involve a metallic (ionic) bond and is not a consequence of plastic deformation. In this regard, molecules with diverse functional groups are recognized for forming self-assembled monolayers on a wide range of metallic oxide surfaces.
Phosphonates, carboxylates, silanol, and amine groups, for instance, are known to strongly bind to surfaces such as copper, steel, aluminum oxide, and zinc oxide.

However, it is important to highlight that, this thesis specifically investigates the potential of electrochemical surface activation with BTSE and PAA, with known procedures, to improve bond strength in CPW. The emphasis is not on developing new electrochemical processes but rather on examining the effectiveness of existing and modified treatment concepts for CPW.

2.5 Analytical methods for surface and interface analysis

2.5.1 X-ray photoelectron spectroscopy (XPS)

X-ray photoelectron spectroscopy (XPS), which is also often referred as electron spectroscopy for chemical analysis (ESCA), is a spectroscopic method based on the photoelectric effect [161]. This methodology was pioneered by Siegbahn during the 1960s, and in recognition of his contributions, he was honored with the Nobel Prize in 1981 [162]. When solid material surfaces are exposed to high-energy (see Figure 2-20), monochromatic electromagnetic radiation generated by an X-ray source, it comes to emission of electrons from the core energy levels of the constituent elements where energized electrons exit the material near the surface due to a phenomenon referred as photoemission [163].

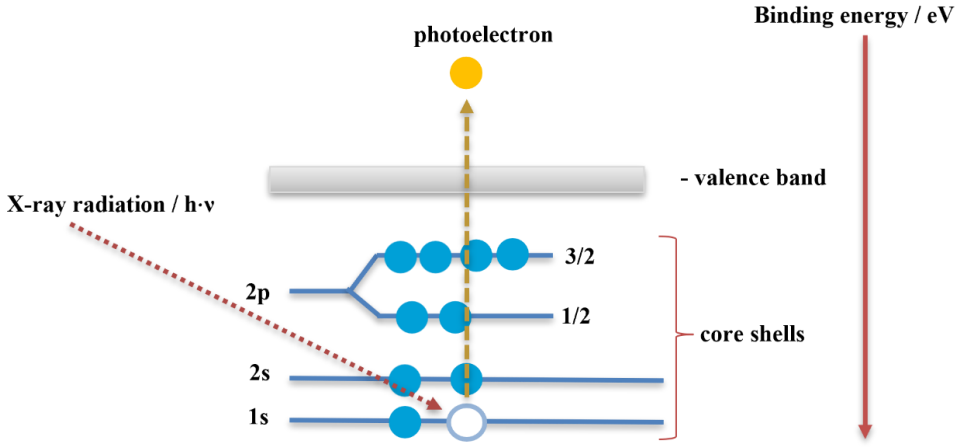

Figure 2-20: Schematic depiction of the photoelectric effect, illustrating the release of a single photoelectron from the inner core shell as a result of X-ray radiation (drawing based on Sabbatini et al. [163])

The photoelectrons that are emitted from the core energy levels have a distinct kinetic energy, E_{kin}, which can be described in the following equation 2-16 [163]:

$$E_{kin} = h \cdot v - E_{BE} - f - K \qquad (2-16)$$

where h represents the Planck's constant, v signifies the frequency of the electromagnetic radiation, E_{BE} represents the binding energy of the electron in the particular orbital of the element, f denotes the work function of the spectrometer, and K is a correction factor [163].

The calculation of the binding energy and kinetic energy is possible by knowing the energy of the primary source X-ray radiation (hν) which is typically 1253.6 eV for Mg Kα or 1486.6 eV for Al Kα [162] and the spectrometer parameters related to the work function *(f)*.

These energies are characteristic for each element and depend on the chemical environment [163,164]. As a result, the presence of attached atoms or molecules causes a shift in the binding energy. The greater the electrostatic attraction between the atom and its electrons, the lower the kinetic energy of the emitted photoelectrons [165]. In addition to the electrons that provide the characteristic peaks in the XPS spectrum which is typically generated by plotting counts per second against either kinetic or binding energy in electron-volts (eV), electrons can also lose energy causing a secondary effect which is the emission of an Auger electron [166]. In the angle-resolved high-resolution XPS (AR-HR-XPS), changing the angle of the sample with respect to the detector direction, can vary the effective sampling depth [164]. In this PhD thesis, AR-HR-XPS measurement was performed using a monochromatic Al Kα (1486.3 eV) X-ray source where the take-off angle of detected photoelectrons was set to 60° in relation to the surface plane to obtain valuable information about the chemical composition of steel surfaces before and after being modified with BTSE and PAA-based thin films.

The approximate sampling depth, d, is given by the equation 2- 17 [164, 165]:

$$d = 3\lambda \cdot \sin\theta \qquad (2-17)$$

where λ is the inelastic mean free path of the photoelectron and θ is the angle between the sample surface and the analyzer (take-off angle). When the angle θ is set at 90°, the sample surface is positioned perpendicularly to the detector's line of acceptance, and the maximum sampling depth is 3λ [164, 165]. As the angle θ is decreased, the sampling depth also diminishes. Figure 2-21 illustrates the AR-HR-XPS measurements with a 60° take-off angle detection.

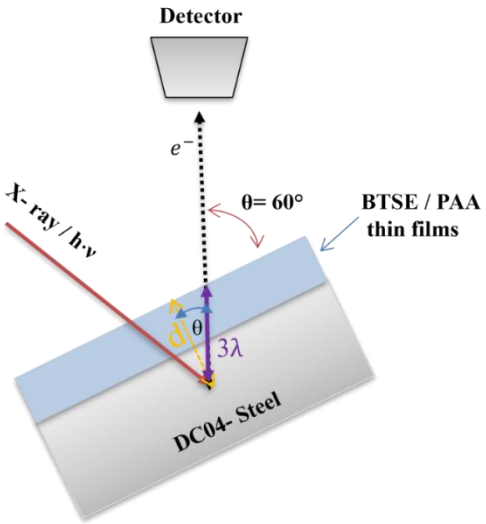

Figure 2-21: Scheme of XPS analysis on DC04 steel substrate modified with a thin BTSE/ PAA layer with a 60° take-off angle detection, (drawing based Bluhm et al. [164]).

2.5.2 Polarization-modulated Fourier-transformed infrared reflection absorption spectroscopy (PM-FT-IRRAS)

Polarization-modulated infrared reflection-absorption spectroscopy (PM-FT-IRRAS) was first introduced by Golden et al. in 1980 [167]. This technique leverages on the selection rules governing the interaction of IR light when it is incident at a shallow angle on a metal substrate [168,169].

In this context, the decomposition of the electric field vector of the electromagnetic infrared radiation wave, as well as its polarization (parallel "p" or perpendicular "s" to the plane of incidence), plays a crucial role which is illustrated in the following Figure 2-22.

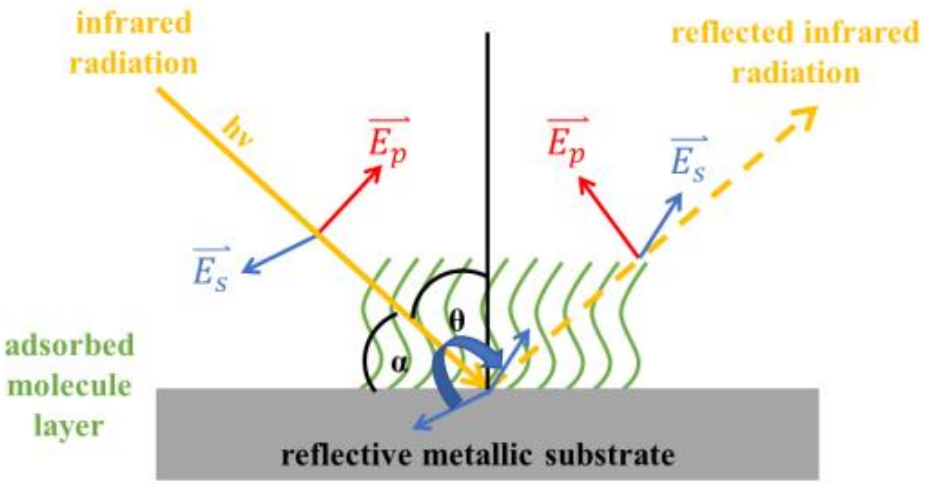

Figure 2-22: Schematic representation of reflected infrared radiation, incorporating the decomposition of the electric field vector (drawing based on Grundmeier et al. [170] and associated literature).

It becomes apparent that the phase change upon reflection remains constant at 180 degrees for perpendicular polarization, while for parallel-polarized light, it varies with the angle of incidence. This causes an increase in electric field intensity for parallel-polarized light, peaking near grazing incidence. In contrast, the electric field intensity for perpendicular-polarized light is minimal at all angles of incidence. Therefore, only light polarized parallel to the plane of incidence reveals information about surface adsorbed species. Gas-phase molecules, with their random orientations, exhibit absorption independent of the electric field vector's orientation.

Grundmeier et al. have described the principle of the selection rule with simply looking at the dipoles oscillating on the surface (see Figure 2-23) [170].

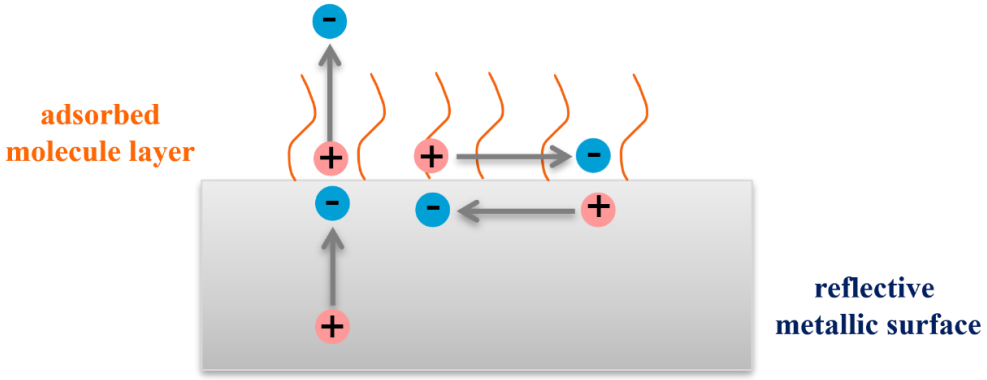

Figure 2-23: Dipole change depending on the orientation (drawing based on based on Grundmeier et al. [170] and associated literature).

The dipole moments can be categorized into two distinct groups:

1. the dipole moments originating from the metal surface referred to as image dipoles and
2. the dipole moments arising from the adsorbates on the surface.

Both groups offset their dipole moments through electrostatic interactions and can align either parallel to each other or perpendicular to the surface plane. This alignment enhances surface sensitivity, particularly at high angles of incidence, as mentioned earlier. In another scenario, where both groups align parallel to the surface plane and parallel to each other, there is a compensation of the infrared active transition dipole moment. This can be exploited by altering the polarization of the infrared radiation in which the surface information obtained from s- and p-polarized IR light differs due to the insensitivity of s-polarized IR light to the angle of incidence, while p-polarized IR light is enhanced. By modulating between the two polarizations from the IR light coming from the Michelson interferometer at a frequency of 50 kHz by using a photoelastic modulator (PEM) made of zinc selenite (ZnS), both the background and the sample can be measured simultaneously [170]. After the Fourier transformation of the measured signal, the averaged spectrum $I_A(\omega)$ and the difference spectrum $I_D(\omega)$ can be calculated using equations 2-18 and 2-19:

$$I_A(\omega) = (Ip + Is) / 2 \qquad (2 - 18)$$

$$I_D(\omega) = (Ip - Is) / 2 \qquad (2-19)$$

where, ω represents the wave number, Ip is the intensity of p-polarized light, and Is is the intensity of s-polarized light. The differential reflectance spectrum can then be calculated using equation 2-20:

$$\frac{\Delta R}{R} = \frac{I_D(\omega)}{I_A(\omega)} \cdot J_2\Phi_0 \qquad (2-20)$$

whit $J_2\Phi_0$ as the second-order Bessel function [170].

The significant advantage of the resulting differential reflectance spectrum lies in its ability to eliminate the requirement for a reference measurement on the atmosphere.

This automated removal of atmospheric effects not only streamlines the process but also enhances the precision of measurements, especially for surface coatings within the monolayer and thin multilayer range [170]. This sets it apart as a more efficient option compared to other IRRAS techniques.

2.5.3 Scanning electron microscope (SEM) and transmission electron microscopy (TEM)

The analysis of material morphologies and their surface characterization can be effectively carried out using a scanning electron microscope, making it an essential technique in the realms of materials science and nanotechnology. During the measurement, a focused electron beam, usually within the energy range of 5-10 keV, scans the surface providing information about microstructure and morphology from the sample leading to the emission of backscattered electrons, secondary electrons, Auger electrons and high energetic radiations: like X-ray with characteristic energies, used for energy disperse microscopy X-ray spectroscopy (EDX) [171,172,173]. These emitted particles are subsequently detected by an electron detector. The interaction between the electron beam and the sample is illustrated in the following Figure 2-24, along with the various detection planes.

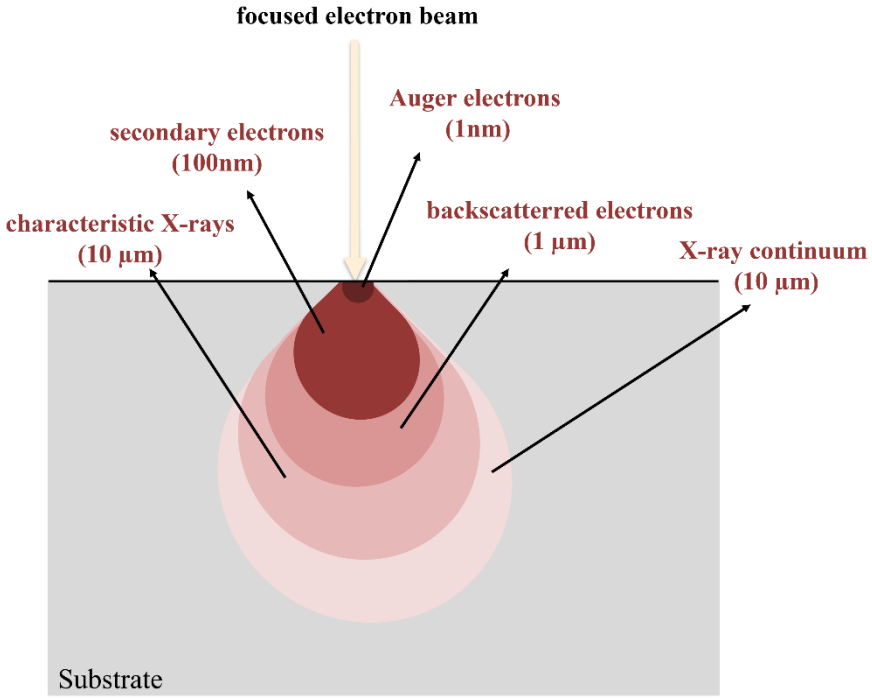

Figure 2-24: Illustration of the various signals generated by the electron beam (drawing based on Subramanian et al. [174]).

The nature of the interaction and its intensity are closely linked to the energy level of the primary electrons. As the energy increases, so does the penetration depth of the primary electrons, as depicted by the "potential bulb" shown by Zhou et al. [172]. For example, an electron source such as a field emission cathode emits electrons due to a high field line density, resulting in a thin electron beam. When an electron from the primary beam strikes the sample, it can create either an elastic collision through electrostatic interaction with the atomic nuclei or an inelastic collision through interaction with the electrons. In this thesis, secondary electrons are captured using both a secondary electron detector and an in-lens/InLens detector. The former collects electrons that scatter to the side of the sample, while the latter is designed to detect electrons emanating directly from the surface normal direction. These electrons have significantly higher kinetic energy due to the elastic nature of their interaction and originate from deeper layers [172]. Consequently, the signals captured by this detector are particularly suitable for examining the topographical features of the sample surface. Furthermore, when coupled with energy-dispersive X-ray spectroscopy (EDX), it enables the evaluation of both surface characteristics and the chemical composition of the analyzed specimen.

2.5.4 Atomic force microscope (AFM)

Atomic Force Microscopy is a highly precise technique for assessing surface topography, which not only provides topographical information but also enables the measurement of adhesive forces. It can be employed for single-molecule spectroscopy to determine the binding forces between individual molecules or as a tool for surface manipulation [175]. The cantilever serves a dual role as a force sensor and actuator, thanks to the piezoelectric transducer that converts electrical signals into mechanical motion. Cantilevers are typically made from pyramidal-shaped Si_3N_4, SiO_2, or Si [176] with a tip radius of 2-10 nm for etched Si and 10-20 to 60 nm for Si_3N_4 tips [177] typically 3 µm in height [178]. The cantilever has a specific spring constant ranging from 0.0006 to 100 N/m. The resonance frequency of the cantilever is chosen based on the application and typically falls within the range of 3 to 500 kHz [177]. The piezoelectric transducer quantifies both attractive and repulsive forces or potential energy between the cantilever and the sample under examination. When the cantilever tip, which is only a few atomic lengths wide, is pressed onto the sample, it facilitates measurements of topographic height. Conversely, when the cantilever tip is withdrawn, it allows for the measurement of the interaction forces between the tip and the sample. The cantilever's movement can be detected with various high-precision methods, including tunneling current measurement, optical laser diffraction, fiber interferometry, and piezoresistive techniques [175,179].

The typical experimental setup of an atomic force microscope (AFM) setup is displayed in Figure 2-25.

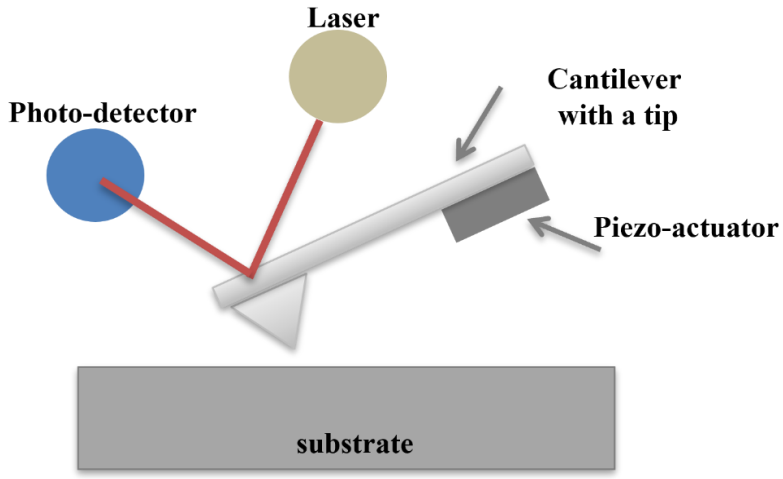

Figure 2-25: Schematic illustration of the experimental setup of an atomic force microscopy (AFM) (drawing based and on Butt et al. [56]).

When the cantilever contacts the sample, in measurements performed on air, it bends in direct proportion to the applied force following Hooke's law:

$$F = -k \cdot x \qquad (2-21)$$

where, k represents the spring constant, and x represents the deflection of the cantilever [56].

The degree of deflection of the cantilever is gauged by directing a laser beam onto the cantilever's top, which then reflects onto a photodiode. To maneuver the tip across the sample surface, a piezoelectric transducer, often constructed from synthetic piezoelectric ceramics, converts electrical signals into mechanical motion.
Additionally, a force-sensing mechanism is required, usually an optical lever used in conjunction with the cantilever, to measure the force between the probe and the sample surface. The attainment of high-resolution topography is realized through feedback control.
When the probe detects an increase in force due to repulsion, it's automatically retracted from the surface. Conversely, when the force decreases, indicative of attraction, the probe approaches the sample surface.
Attractive forces between the cantilever and the sample arise from Van der Waals interactions (VdW), electrostatic forces, and chemical forces. Repulsive forces are explicable through the "hard sphere repulsion" model, the Pauli exclusion principle, and electron-electron Coulombic interactions. Typically, repulsive forces exhibit a very short range and follow either an exponential decay pattern or an inverse power-law relationship with a higher-order dependence on distance. Forces that operate at the atomic level are categorized as either short-range or long-range forces and can manifest as either attraction or repulsion. When the tip nears the surface, the combined interaction forces come into play, encompassing various interactions such as capillary forces, covalent forces, electrostatic forces, shared repulsive interaction forces, and Van der Waals forces [175, 179].

There are three fundamental operating modes in an atomic force microscopy (AFM):

1) *the contact mode,*
2) *the non-contact mode, and*
3) *the intermittent mode (tapping mode).*

The simplest mode is the contact mode, also known as the static mode, which involves scanning the surface with the cantilever in direct contact. The total force is repulsive, encompassing both short-range and long-range forces in the imaging signal.

The cantilever tip is moved across the substrate while maintaining a constant cantilever deflection. Force is determined by measuring cantilever deflection deviations according to Hooke's law, with cantilever movement as the sole controllable parameter. In this mode, both the cantilever tip and the sample may undergo deformation, which can result in potential collision risks. The use of a softer cantilever, significantly softer than the atomic bonds of the substrate, can minimize this risk.

Further, in the non-contact mode the cantilever vibrates near its resonance frequency and is coupled to an actuator for external excitation. The resonance of the cantilever is characterized by its amplitude, phase, and frequency. Interaction with the sample leads to measurable variations in these parameters, and the resulting force is calculated from the recorded signals using a theoretical approach.

The cantilever hovers over the surface during scanning, and the amplitude signal is utilized in feedback control, adjusting the resonance shift to create an image of the substrate.

Finally in the intermittent contact mode, which is also known as tapping mode, the cantilever oscillates cyclically, intermittently contacting the surface and receiving sufficient recovery energy to detach from it. This method, as only used in this thesis, is particularly gentle and allows for the repeated scanning of individual molecules without altering their conformation. Surface measurements in this mode can be conducted using amplitude modulation, controlling either the vibration amplitude or the cantilever phase with a feedback signal while keeping the exit frequency constant. Alternatively, the resonance frequency of the cantilever is measured in frequency modulation mode, producing a change in the excitation frequency directly through a resonance frequency shift. The use of negative feedback allows for adjustments to the frequency or phase of an input signal to a predetermined value, with output signals representing the difference between the collected signal and the preset reference value, generating topographic images [175].

2.6 Electrochemical Analysis

2.6.1 Chronoamperometry

Chronoamperometry is a time-varying method in which a constant potential is applied on the working electrode. The current, monitored over time, undergoes fluctuations due to the diffusion of an analyte from the bulk solution toward the electrode surface.

As a result, chronoamperometry is suitable for analyzing the time relationship between current and diffusion-controlled processes occurring at an electrode, influenced by analyte concentration [181]. It is a highly effective method for quantitatively assessing nucleation and growth mechanisms within an electrodeposition [181-184].

In chronoamperometry, the current is measured versus time as a response to a constant potential pulse. Figure 2-26 illustrates a typical current response in chronoamperometry.

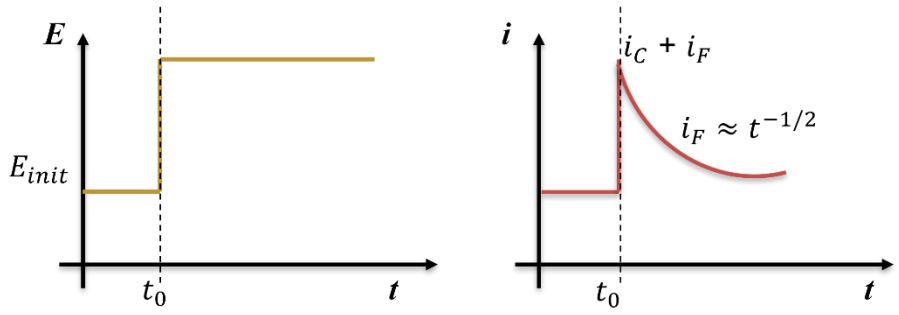

Figure 2-26: Potential-time profile applied during experiment (left), where E_i is an initial potential and E_1 some other potential of interest with the corresponding response of the current due to changes of the potential (right) (drawing based on Inzelt et al. [183]).

The measurement starts with the working electrode's potential held at the initial E (E_{int}). It is then switched to a new potential value, E´, at t_0, and the corresponding current-time response is recorded, as depicted in Figure 2-26. Initially, the current experiences a substantial spike, resulting from the relatively high analyte concentration near the electrode surface. The rate of subsequent charge transfer is then entirely dictated by the mass transport, specifically diffusion, which becomes a progressively decelerating process as a thickening diffusion layer form [183, 183]. In the initial state, the time-dependent behavior of the diffusion-limited current is described by the Cottrell equation:

$$i = z \cdot F \cdot A \cdot D \cdot c_{Red} \sqrt{\frac{D}{\pi \cdot t}} \qquad (2-22)$$

where, the current changes linearly with the reciprocal of the square root of time and *F* is the Faraday's constant, *A* the electrode area (cm^2), *c the* concentration of electroactive species (mol/cm^3), and *D* the diffusion constant for electroactive species (cm^2/s). If other parameters are known, the diffusion coefficient D can be calculated from the slope.

At the potential jump, the measured current is a sum of a capacitive current and a Faradaic current, as the electrochemical double layer also needs to be charged due to the potential change. However, the capacitive current decreases exponentially over time and decreases rapidly, revealing the square root time dependence [184].

As previously mentioned chronoamperometry is a highly effective method for quantitatively assessing nucleation and growth mechanisms within a studied system [185]. In this Thesis chronoamperometry was applied for electrochemical grafting of BTSE and PAA on DC04 steel surfaces.

The evaluation of the nucleation and growth mechanisms of electrodeposited films can be carried out using chronoamperometric curves. The electrodeposition curves exhibit distinctive behaviors as illustrated in Figure 2-27.

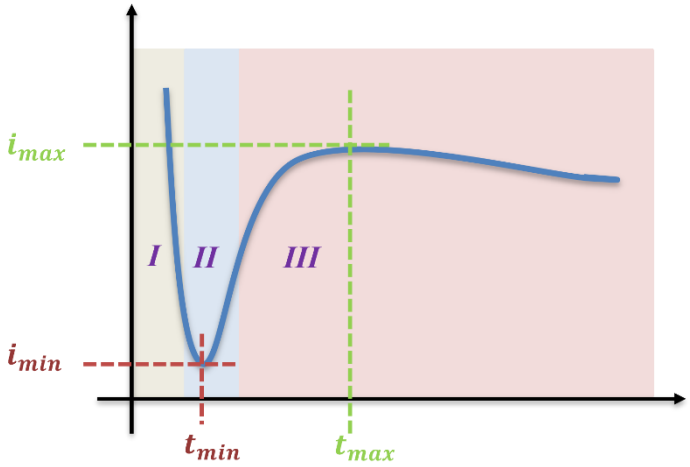

Figure 2-27: Electrodeposition curve presenting different stages of electrodeposition: (I) charge of the electric double layer at the electrode; (II) nucleation/growth; (III) and continuous deposition (drawing based on Bento et al. [185]).

Initially, there is a rapid decrease in current density (*i*) (stage I), indicating the swift development of a double-layer charge on the electrode's surface. Subsequently, after reaching a minimum value, i_{min}, the current density begins to increase and eventually reaches a maximum value, i_{max}, within a certain time frame t_{max}. The increase in *i* during the second

stage (stage II) corresponds to the growth of the film and/or an increase in the number of nuclei.

During this phase, the nuclei start developing diffusion zones around them, and as these zones expand, they overlap, leading to the formation of a linear mass-transfer diffusion zone. Finally, a third stage (stage III) emerges, marked by a decrease in *i* over time, signifying the slow growth rate of the thin film. This is attributed to the linear diffusion of species from the bulk electrolyte to the electrolyte/electrode interface [185,186].

2.6.2 Cyclic voltammetry (CV)

Cyclic voltammetry is one of the most used electrochemical techniques for acquiring qualitative information about electrochemical reactions applied in various fields of research such as batteries, fuel cells, capacitors, and sensors [187-190].

It offers valuable insights into reactions occurring near the electrode surface and the reactivity of electrochemically or chemically active species [187, 188]. In this method, a triangular potential-time profile is applied to the working electrode, resulting in the determination of a current-potential diagram (CV) (see Figure 2-28).

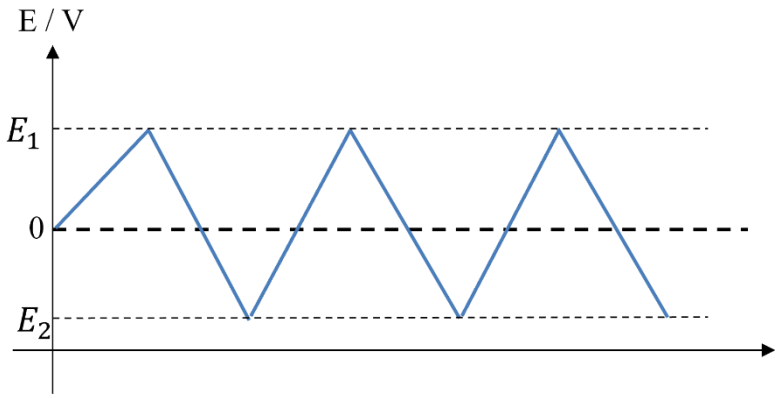

Figure 2-28: Triangular potential-time profile.

The measurement cell comprises a three-electrode arrangement in which the electrodes (working electrode, counter electrode, and reference electrode) are connected to a potentiostat. During the measurement, a potential is applied between the reference electrode and the working electrode, which is first set as the initial potential (*Ei / V*), (open circuit potential (OCP) /resting/equilibrium) at which no apparent external current flows. Then the potential which is carefully selected to span between hydrogen and oxygen evolution increases linearly up, at a constant scan rate, to the upper reversal potential and then decreases

linearly to the lower reversal potential. This process is generally repeat more than three times, by measuring minimally tree CV diagrams [191].

Typically, minimal to no disparities are observed between the first cycle and subsequent cycles. However, any deviations in the response are directly attributed to chemical reactions occurring at the surface interface [192].

By straightforward steady-state measurements, the shape of the CVs is influenced by the diffusion of reactants toward the electrode surface and the ensuing charge-transfer reaction [191, 193].

Due to the sluggish mass transport to the surface, a depletion layer forms at the electrode surface, gradually expanding over time due to the extended distance that molecules must traverse to reach the surface. Consequently, there is a reduction in the mass transport rate, with mass transport serving as the step that limits the rate, culminating in the achievement of a peak maximum [192,193]. Subsequently, there is a swift decline in the concentration of the reacted species, and the diffusion layer expands [191]. Reversing the voltage direction leads to the oxidation of previously reduced species. The concentration of reactants can be determined based on the current peaks, among other characterizations of chemical reactions through the anodic and cathodic peaks [192, 193].

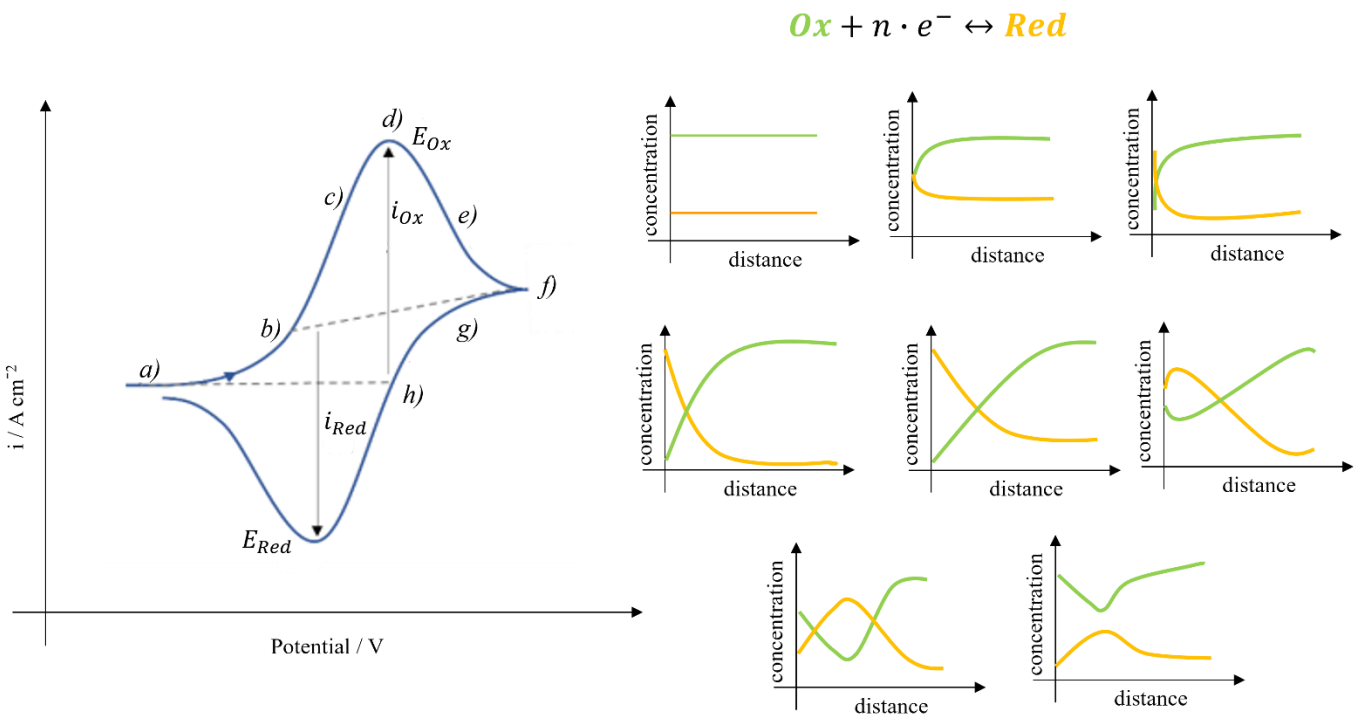

Figure 2-29: A cyclic voltammogram along with the corresponding concentration profiles (drawing based on Bontempelli et al. [193]).

In the context of this Thesis, cyclic voltammetry was employed to characterize the charge transfer barrier capabilities of the BTSE/ PAA and BTSE:Zn/ PAA:Zn thin films.

2.6.3 Linear sweep voltammetry (LSV)

Linear sweep voltammetry (LSV) stands out as a commonly employed voltammetric techniques for investigating redox reactions involving both organic and inorganic compounds. It excels in the capacity to unveil the intricacies of electrochemical processes, all while requiring a relatively modest investment of time and effort in data collection and analysis [194]. LSV is delivering insights not only into the electrochemical aspects inherent to a redox process but also into potential chemical reactions interconnected with charge transfer steps. Furthermore, given that the pertinent responses can be obtained in a matter of milliseconds following electrode stimulation, they prove invaluable for investigating exceedingly rapid reactions and detecting short-lived transient intermediates [194]. In the context of this Thesis LSV was used for evaluating the corrosion resistance of DC04 steel samples. It involves a three-electrode configuration where the sample under examination serves as the working electrode, a gold wire is employed as the counter electrode, and a silver-silver chloride electrode as the reference electrode. The applied potential is linearly changed over time from the initial potential E_i to a final potential E_f [194]. For comprehensive corrosion studies, a quasi-steady-state condition is established first, with the open-circuit potential representing the corrosion potential, which is typically measurement for 30 min before applying the initial potential E_i. In this context, electroactive species are transported to the electrode surface through diffusion [194]. Equation 2-23 provides the instantaneous potential at a specific time, denoted as E_t.

$$E_t = E_i \pm \nu \cdot t \qquad (2-23)$$

where, υ is the chosen scan rate and t is the time. During the time t at which the selected potential is applied, the current is measured, resulting in a current density-potential curve. Based on the current density-potential curves, corrosion current densities and corrosion potentials can be determined using the Butler-Volmer equation. The Redox reactions occurring at the interface between solid and liquid phases, follow the equation 2-24 [191]:

$$Ox + n \cdot e^{-} \leftrightarrow Red \qquad (2-24)$$

The Butler-Volmer equation describes the relationship between the partial current densities of oxidation and reduction reactions as a function of overpotential η and is given by equation (2-25) [195]:

$$i = i_0 \left[\exp\left(\frac{\beta n F}{RT}\eta\right) - exp\left(-\left(\frac{(1-\beta)nF}{RT}\eta\right)\right)\right] \qquad (2-25)$$

where, i represents the current density, i_0 is the exchange current density, β is the symmetry factor, n is the number of electrons, F is the Faraday constant, R is the ideal gas constant, T is the temperature, and η represents the overpotential. It is assumed that the reaction occurs at a specific potential and the mass transport does not result in changes in the concentration at the electrode surface which leads to the formulation of an anodic current and a cathodic current, as presented in equations 2-26 and 2-27 [191].

$$i_{an} = nFc_{ox}\, k_0^{+} \exp\left(\frac{\beta n F}{RT}\eta\right) \qquad (2-26)$$

$$i_{an} = -nFc_{Red}\, k_0^{-} \exp\left(\frac{(1-\beta)nF}{RT}\eta\right) \qquad (2-27)$$

By applying the Nernst equation, the consideration of the forward and backward reactions leads to the Butler-Volmer equation [191]. The two equations describe the respective partial current density at each potential. At the equilibrium potential (OCP), when no current is flowing, the two opposing partial current densities are equal and can be referred to as the exchange current density (i_0). Using these equations, the exchange current density and the transfer coefficients α can be determined by utilizing the Tafel plot [195] (see Figure 2-30).

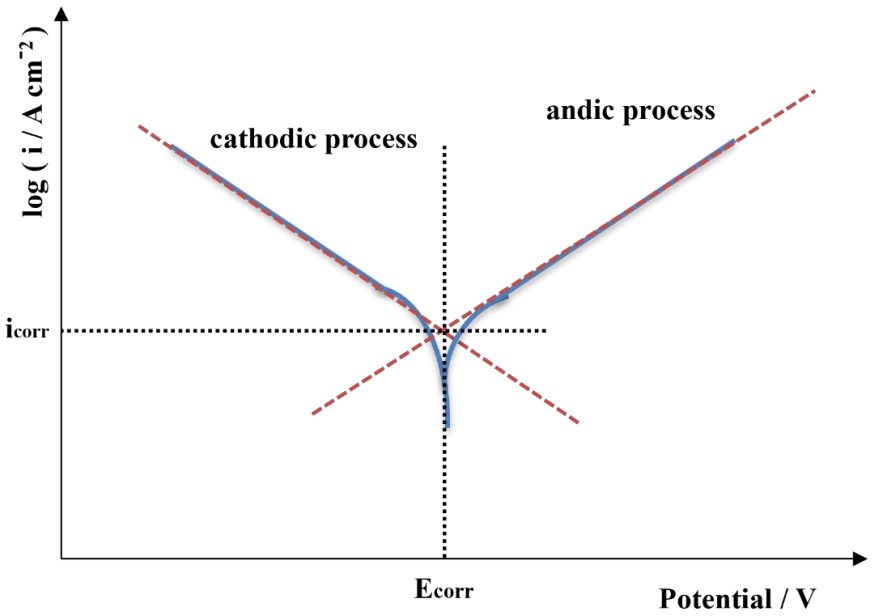

Figure 2-30: A current density-potential curve on a Tafel chart for the determination of corrosion current density and corrosion potential.

The transfer coefficient α is calculated by analyzing the slope of either the cathodic or anodic branch and serves as a valuable parameter for investigating electrode processes kinetically [196]. By applying tangents to the linear segments of the cathodic and anodic branches within this plot, it is possible to determine the corrosion currents and the corrosion potential. This is achieved by extracting the potential and current density at the point where the two axes intersect [195].

2.6.4 Impedance spectroscopy (EIS)

Electrochemical impedance spectroscopy (EIS) allows the investigation of corrosion processes and electrochemical properties of electrodes. It enables the determination of key parameters associated with the electrode's electrochemical reactions, including the charge transfer resistance and electric double-layer capacitance [197-199]. Furthermore, EIS permits the separation of the internal resistance of the cell into components attributed to the positive electrode, negative electrode, and electrolyte [199].

Due to these advantages, EIS is a technique utilized in fundamental research to identify the rate-determining step in electrochemical reactions and in practical applications for characterizing electrochemical devices like batteries and capacitors [199].

It involves applying an alternating voltage (or current) and measuring the resulting current (or voltage). By applying a sinusoidal potential and varying the frequency, it becomes possible to assess the resistance and capacitance components of the electrode [200,201]. The analysis involves considering two periodic waves, one representing the current signal as a function of time and the other representing the potential signal as a function of time. Both waves exhibit identical amplitude and frequency, but they possess a consistent time offset at a particular angle known as the phase angle shift, spanning from 0° to 90°. The voltage signal can be mathematically described as shown in equation 2-28 [201]:

$$E_t = E_0 \sin\ (\omega t) \qquad (2-28)$$

where, E_t symbolizes the potential at time t, E_0 denotes the signal's amplitude, and ω represents the angular frequency. The current at its maximum amplitude experiences a phase shift, as indicated by equation 2-29:

$$I_t = I_0 \sin\ (\omega t + \Phi) \qquad (2-29)$$

where I_t symbolizes the current at time t, I_0 the initial potential and Φ the phase shift.

Based on these two, voltage and current signal, and Ohm's law impedance allows the be determined by following equation 2-30 [201]:

$$Z = \frac{E_t}{I_t} = \frac{E_0 \sin\ (\omega t)}{I_0 \sin\ (\omega t + \Phi)} = Z_0 \frac{\sin\ (\omega t)}{\sin\ (\omega t + \Phi)} \qquad (2-30)$$

where Z_0, signifies the impedance, which comprises components like resistors, capacitors, and inductors.

Impedance Z is a complex function, involving both an imaginary part (Z_{im}) and a real part (Z_{re}). Plotting the imaginary part of impedance against the real part gives rise to the Nyquist plot (see Figure 20-31a). Each point on the plot represents a different frequency. The impedance at various frequencies is depicted through vectors that illustrate the magnitude of the imaginary and real parts of impedance in relation to the phase [201].

Furthermore, the outcomes of EIS measurements can be visualized using the Bode plot (see Figure 2-31b). In this representation, both impedance and phase are graphed against frequency, providing a comprehensive view of the impedance's frequency dependency [201].

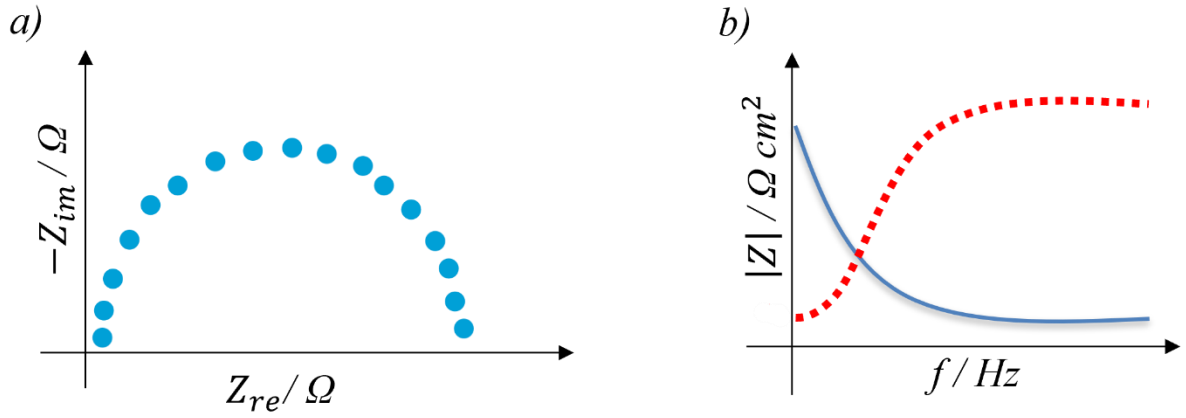

Figure 2-31: Representation of electrochemical impedance measurements using Nyquist plot (left) and Bode plot (right).

2.7 Macroscopic Adhesion Tests

2.7.1 90°-peel-test

The 90° peel test serves as a standardized approach for evaluating the adhesive strength between two pliable materials [202,203]. This method entails the separation of a flexible adherend from a rigid substrate at a 90° angle, inducing the adhesive to peel away from the substrate. Widely employed across diverse industries, this test is a valuable tool for appraising the adhesion characteristics of adhesive bonds and coatings [202,203]. In the context of this thesis, a freestanding epoxy-amine adhesive film is applied to the PAA modified DC04 steel surface and peeled off in strips at a 90° angle from the surface. The required peel-off force can be easily quantified using a force meter, providing an indication of the adhesion performance of joints (see Figure 2-32).

The applied load (p) or force (F) is contingent on the peel angle (β), with the latter consistently set at 90° in all experiments. Peel-off forces are continuously applied to an adhesive film within a brief time segment [203]. For results comparability, peel-off forces in N must be standardized to the width of the detached film, typically yielding units of N/mm [202].

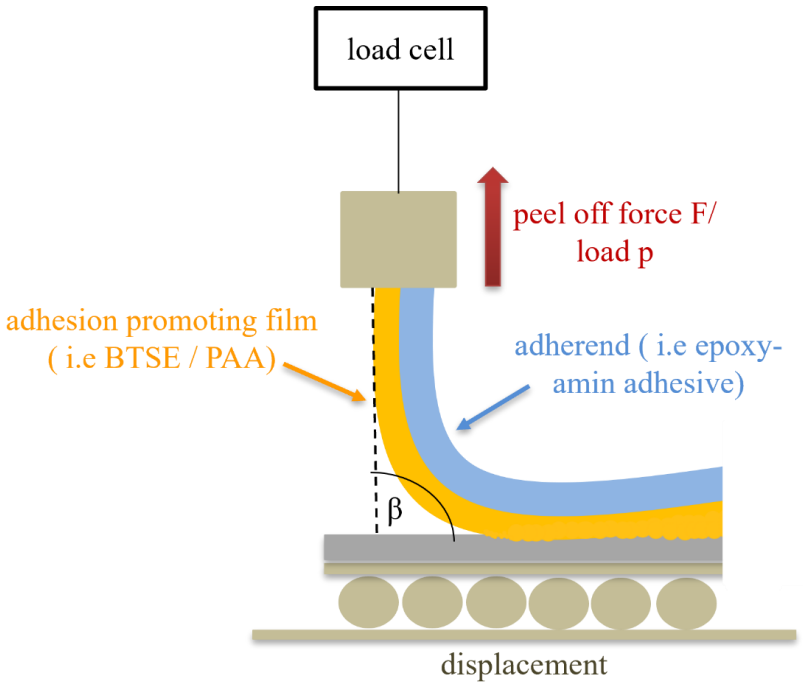

Figure 2-32: Schematic illustration of the peel-test measurement (drawing based on Crocombe and Adams [202]).

2.7.2 Shear test

Lap shear tests, encompassing various configurations such as single lap, double lap, lap-strap, and thick adherend shear tests, are widely employed in adhesive testing [204,205]. The single lap shear test, illustrated in Figure 2-33, is commonly referred to as the thin lap shear test and stands as the most extensively employed approach for generating data on adhesively bonded joints. Numerous standards, such as ISO 4587 and ASTM D 1002, describe variants of this test [204,205]. The single lap test involves bonding together two rectangular adherends (metals), usually 25 mm wide, 100 mm long, and 1.5 to 2.0 mm thick, with an overlap length varying from 12.5 to 25 mm [205]. The shear testing is performed using standard tension/compression mechanical equipment with a suitable pair of self-aligning grips to hold the specimens.

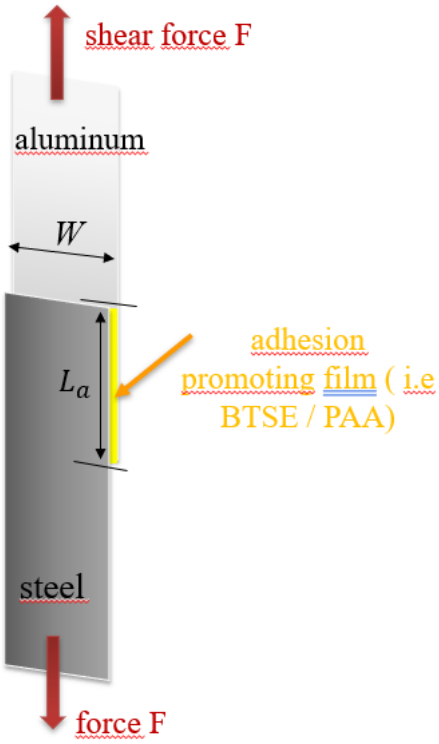

Figure 2-33: Schematic illustration of the shear-test measurement.

The nominal lap-shear strength (LSS_{nom}, in MPa) in a single lap configuration, which was only performed in context of this Thesis, is determined by dividing the maximal applied load/force (F_{max}) by the area (A) of the bonded overlap as indicated by equation 2-31 [206]:

$$LSS_{nom} = \frac{F_{max}}{A} = \frac{F_{max}}{L_a \cdot W} \qquad (2-31)$$

where, F_{max} is the maximal applied load/force, L_a is the overlap length and W the width of the sample. Findings derived from the single lap joint test are notably influenced by the mechanical stiffness of the adherends, as it affects the concentrations of peel stress at the end of the joint [206].

3

Experimental

This chapter presents the experimental segment of the thesis, providing comprehensive details regarding the materials, methods and chemicals utilized in this study, following with an extensive depiction of supplementary interface analytical techniques, electrochemical methods, joining processes, and macroscopic adhesion tests conducted within this research.

3.1 1,2-bis(triethoxysilyl) ethane (BTSE) thin-film deposition

3.1.1 Materials and chemicals

Prior to their usage, he low-alloy DC04 steel and EN-AW-1050A aluminum plates (purchased from Thyssenkrupp and Alumeco Deutschland GmbH, respectively) were solvent cleaned, i.e., ultrasonicated for 15 min. in pure tetrahydrofuran (≥ 98%, Sigma-Aldrich), propan-2-ol (≥ 98%, Sigma-Aldrich), and ethanol (≥ 98%, Sigma-Aldrich). 1,2-bis(triethoxysilyl)ethane (96 %), BTSE, $Zn(NO_3)_2 \cdot 6H_2O$, $NaNO_3$ (99 %), tetrabutylammonium tetrafluoroborate (Bu_4NBF_4), and anhydrous CH_3CN (ACN) were purchased from Sigma-Aldrich.

3.1.2 Surface pre-treatment and electrochemical alteration of the substrate surfaces

To optimize the welding process through plastic deformation, it is essential to eliminate organic and inorganic contaminants while reducing the native oxide layer on specimen surfaces to facilitate metal-to-metal bonding [117]. Accordingly, aluminum EN-AW-1050A substrates underwent immersion in a 10% NaOH aqueous solution at 50 ºC for 2 minutes to remove the native oxide layer [44]. XPS measurements by Hoppe et al. demonstrated a significant reduction in the aluminum oxide layer thickness from 3.8 to 2.1 nm after the surface pickling treatment [44].

Subsequently, the pickled aluminum samples were thoroughly rinsed in Milli-Q water, dried under N_2 flow, while DC04 steel samples were ground with SiC paper (grit size 120, WS Flex, Hermes) for 2 minutes.

The steel samples were then cleaned with Milli-Q water and ethanol, dried under nitrogen flow, and immersed in a 25 $g \cdot L^{-1}$ NaOH (99% from Sigma-Aldrich) aqueous solution at 55°C for 1 minute to achieve a hydroxyl-rich steel surface [208-210].

FE-SEM and AFM images, captured for DC04 and EN-AW-1050A before and after each surface treatment step, are presented in Figures S1, S2, S3, and S4 in the supporting information (SI). Electrochemical measurements were conducted using a three-electrode glass cell setup (see Figure 3-1). The working electrodes were DC04 plates (2 x 7 cm^2), with a gold coil serving as the counter electrode, and a commercial Ag/AgCl reference electrode (3M KCl, Radiometer analytical).

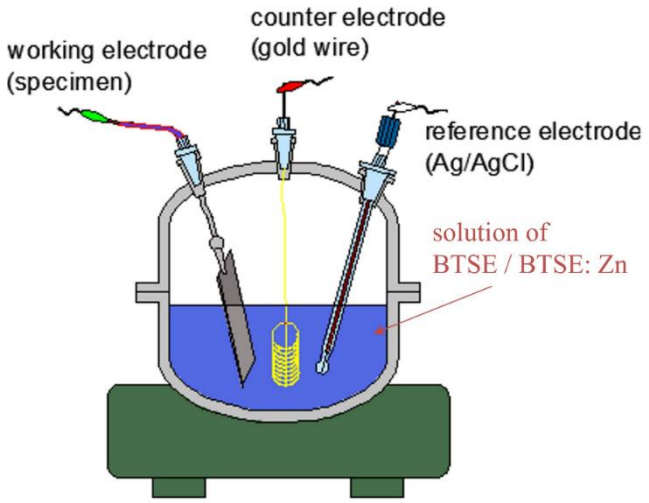

Figure 3-1: Graphical illustration of the three-electrode glass cell setup used for electrografting of BTSE/ BTSE:Zn thin films on DC04 steel.

Chronoamperometry and cyclic voltammetry experiments were performed using a potentiostat, specifically the Reference 600^{TM} from Gamry Instruments.

The electrografting procedure followed the methodology outlined by Mandler et al. [12]. The polycondensation step was carried out in an electrochemical cell by applying a sufficiently negative cathodic potential, leading to an increase in pH in the immediate vicinity of the electrode surface.

This localized pH increase was anticipated to enhance the polycondensation of the newly formed silanol moieties and their subsequent covalent grafting onto the hydroxyl-rich steel surface. As mentioned earlier, the pH increase in the vicinity of the electrode at negative applied potentials is attributed to the emergence of OH^- ions resulting from the overlapping and/or successive electroreduction of H^+ ions (HER), O_2, and NO_3^- ions to NO_2^-.

The organosilane sol-gel precursor was prepared by immersing BTSE into a 75/25 (v/v) ethanol/Milli-Q water solution, resulting in a final BTSE concentration of 2.5% (w/w). The pH was adjusted to 4.5 by adding drops of a 0.1 M CH3COOH (65% Sigma-Aldrich) aqueous solution. This mixture was stirred for 48 hours at 25 ºC in a closed beaker to facilitate hydrolysis.

Subsequently, either $NaNO_3$ or a combination of $NaNO_3$ and $Zn(NO_3)_2{\cdot}6H_2O$ (50 mM) was added to the solution, maintaining a constant final concentration of NO_3^- ions at 0.2 M, to promote the condensation reaction.

Samples modified solely with $NaNO_3$ as the electrolyte in the BTSE organosilane solution are denoted as BTSE, while those modified using the $Zn(NO_3)_2{\cdot}6H_2O$-containing electrolyte are labeled as BTSE:Zn.

For the creation of organosilane-based thin films, the solvent-cleaned DC04 samples, ground to a grit size of 120, were immersed in the previously hydrolyzed BTSE sol-gel precursor solution. A cathodic potential of -1.2 V (vs. Ag/AgCl) was applied for varying immersion times. Subsequently, the organosilane-modified steel samples underwent thorough rinsing in ethanol and Milli-Q water, drying under nitrogen flow, curing in air for 15 minutes at 100 ºC, and storage under vacuum.

3.2 Poly acrylic acid (PAA) thin-film deposition

3.2.1 Materials and chemicals

Prior to their usage, the low-alloy DC04 steel and AL-EN_AW-1050A H111 aluminum plates (purchased from Thyssenkrupp and Alumeco Deutschland GmbH, respectively) were solvent cleaned, i.e., ultrasonicated for 15 min. in pure tetrahydrofuran (≥ 98%, Sigma-Aldrich), propan-2-ol (≥ 98%, Sigma-Aldrich), and ethanol (≥ 98%, Sigma-Aldrich). Acrylic acid (AA) was purchased from Sigma-Aldrich.

3.2.2 Surface pre-treatment and electrochemical alteration of the substrate surfaces

AL-EN-AW-1050A substrates underwent pickling in a 10% NaOH aqueous solution at 50 ºC for 2 minutes to remove the native oxide layer [44]. Subsequently, the pickled aluminum samples were thoroughly rinsed in Milli-Q water and dried under N_2 flow. DC04 steel samples were ground with SiC paper (grit size 120, WS Flex, Hermes) for 2 minutes.

The steel samples were then cleaned with Milli-Q water and ethanol and after dried under nitrogen flow.

The electrografting of acrylic acid (AA) onto steel surfaces utilized a Reference 600™ potentiostat from Gamry Instruments. A constant potential of −1.4 V (vs. Ag/AgCl) was applied to the working electrode in the AA-containing working solution for durations of 5, 10, 15, 30, and 60 seconds through chronoamperometry. Alternatively, polyacrylic acid (PAA) films were prepared by cycling the potential between -1.4 and +0.1 V (vs. Ag/AgCl) for 1, 3, or 5 cycles.

This process employed a three-electrode setup with a potassium chloride-saturated silver/silver chloride reference electrode, steel substrates as the working electrode, and a closely coiled Pt wire inserted in a lugging filled with an aqueous 0.2 M $CaCl_2$ solution (see Figure 3-2).

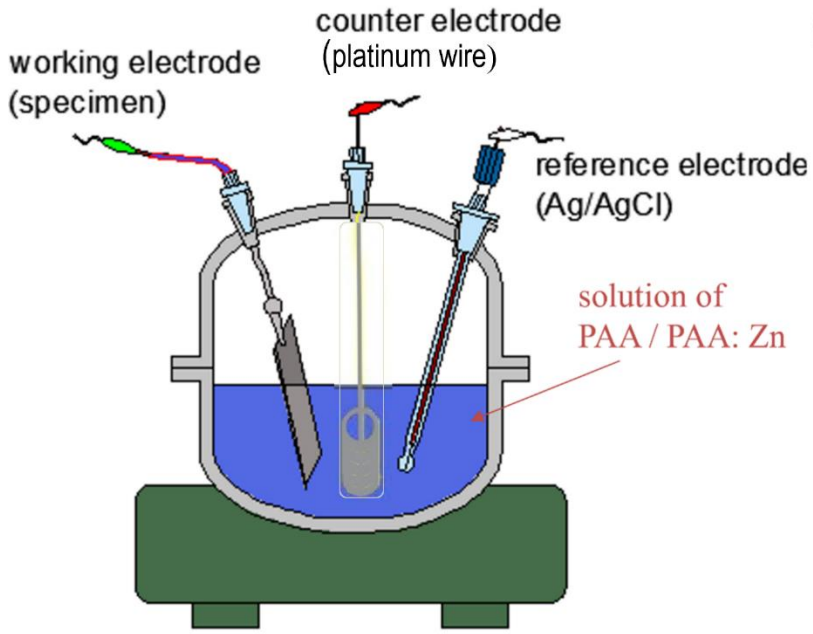

Figure 3-2: Graphical illustration of a three-electrode glass cell setup used for electrografting of PAA / PAA:Zn thin films on DC04 steel.

The 75 mL AA-containing water-based electrolyte for each deposition experiment comprised a 2.0 M AA (monomer) solution with methoxyphenone (inhibitor), 0.2 M zinc chloride (initiator), and 0.04 M N,N′-methylenebisacrylamide (cross-linker) [22, 211]. The pH of the resulting solution was adjusted to 6.0 by adding solid NaOH.

Prior to each deposition, the electrolyte underwent a 20-minute nitrogen purge to maintain oxygen free conditions, preventing the reaction between oxygen and AA radicals, which could stop the electropolymerization reaction and PAA film growth.

Following electrodeposition, the PAA-modified steel samples were rinsed with MiliQ-water. To eliminate embedded zinc species in the polymer, the modified steel substrates were rinsed in an aqueous 0.01 M HCl solution. These DC04-Steel are labeled as PAA, while those not washed with 0.01 M HCl as PAA:Zn.

3.3 BTSE and PAA thin-film characterization

3.3.1 X-ray photoelectron spectroscopy (XPS)

XPS measurements were conducted using an Omicron ESCA+ system (Omicron NanoTechnology GmbH) featuring a hemispherical energy analyzer at a base pressure below <5·10-10 mbar. Survey spectra were recorded at pass energies of 100 eV, while element spectra were recorded at 20 eV. A monochromatic Al Kα (1486.3 eV) X-ray source with a 1mm spot diameter was employed. The take-off angle of the detected photoelectrons was set to 60º in relation to the surface plane. Spectra were internally calibrated to the C1s peak (binding energy, BE = 285 eV). Peak fitting involved a combination of Gaussian (70%) and Lorentzian (30%) distribution. CASA-XPS software was utilized for data analysis. Quantification was conducted by integrating the peaks based on the corresponding relative sensitivity factor (RSF) values, and a Shirley-type background correction was applied.

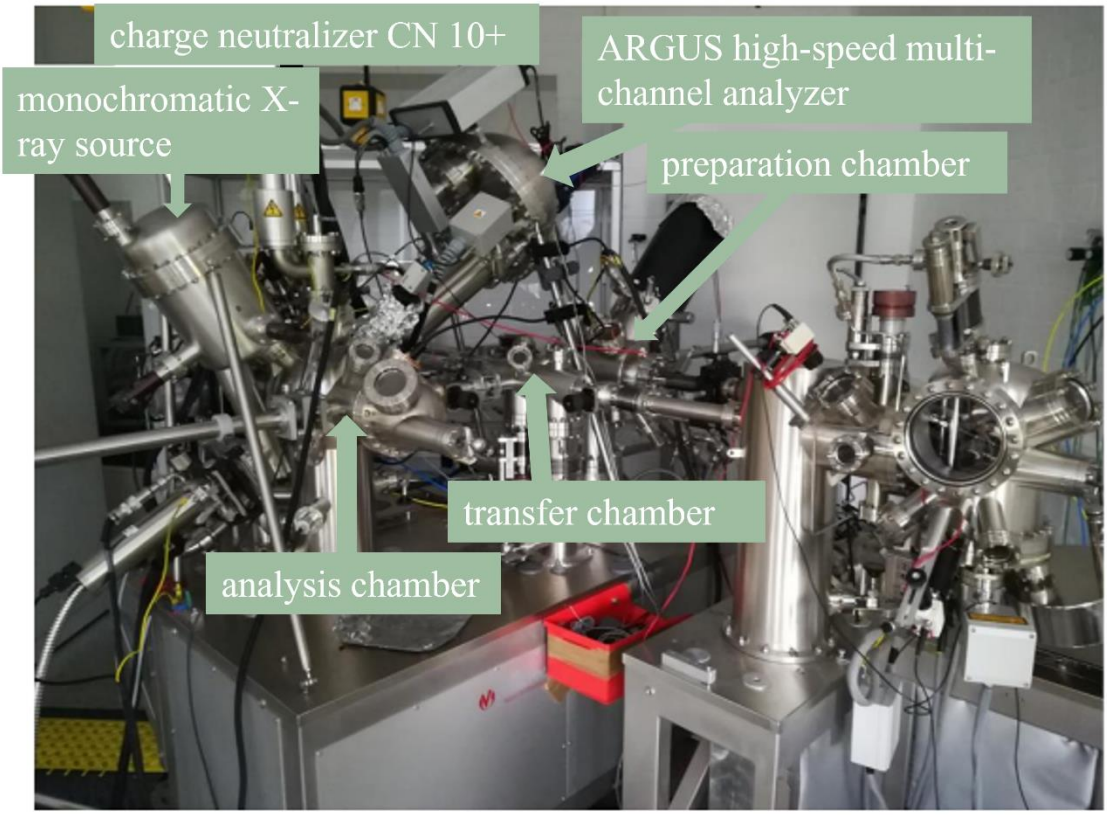

Figure 3-3: X-ray photoelectron spectroscopy analysis tool utilizing an Omicron ESCA+/- System from Omicron NanoTechnology GmbH.

3.3.2 Polarization-modulation infrared reflection-absorption spectroscopy (PM-IRRAS)

PM-IRRAS was employed for the characterization of the deposited organosilane-based thin films. The analysis utilized a Vertex 70 instrument from Bruker Optics Germany, equipped with an external PM-IRRAS setup featuring p-polarization using an aluminum wire grid. The polarization was modulated at 50 kHz with a ZnSe Photo-Elastic-Modulator (PMA50, Bruker Optics Germany) and included a ZnSe lens directed onto a cryogenic mercury cadmium telluride (LN-MCT) detector. The experimental parameters were set with a total of 1024 scans and an energy resolution of 2 cm^{-1}.

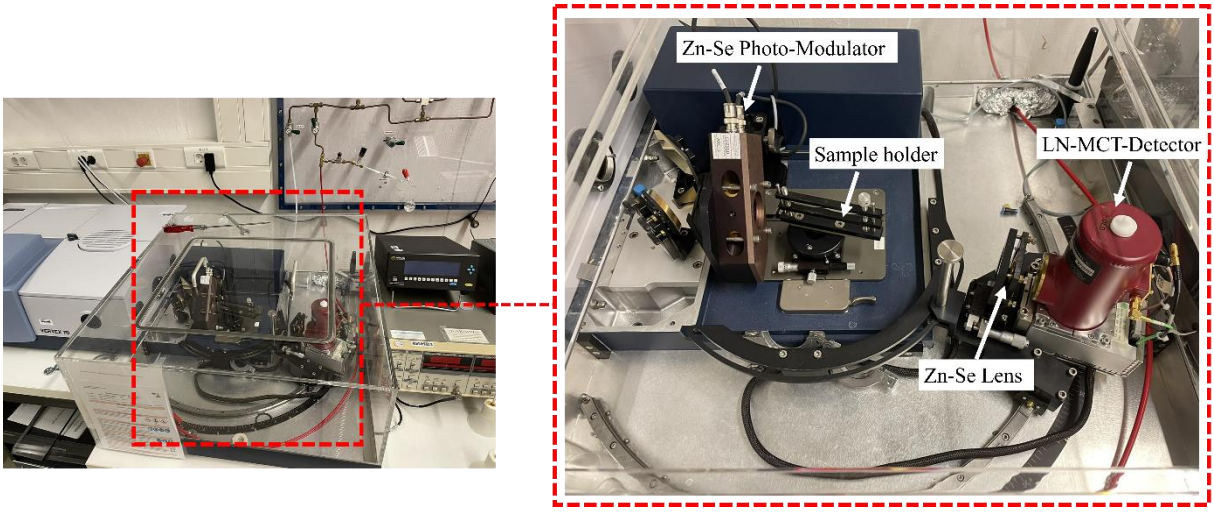

Figure 3-4: Vertex 70 (Bruker) PM-IRRA spectrometer featuring a built-in ZnSe Photo-Elastic Modulator.

3.3.3 Atomic force microscopy (AFM)

AFM imaging was conducted using an MFP-3D-SA instrument (Asylum Research) equipped with an antivibration table and an acoustic enclosure. The imaging was performed in intermittent contact mode under ambient air conditions at a scan rate ranging from 0.5 to 1.2 Hz. For this purpose, HQ:NSC15/AlBS tips (325 kHz and 40 $N \cdot m^{-1}$, nominal radius of 8 nm) and HQ:NSC18/AlBS tips (75 kHz and 2.8 $N \cdot m^{-1}$, nominal radius of 8 nm) obtained from Mikromasch were utilized. Root mean square (RMS) roughness measurements, Rq, were obtained from a minimum of three 10 × 10 μm^2 AFM images captured from different yet equivalent sample areas for each deposition time. These measurements were recorded and considered for statistical analysis.

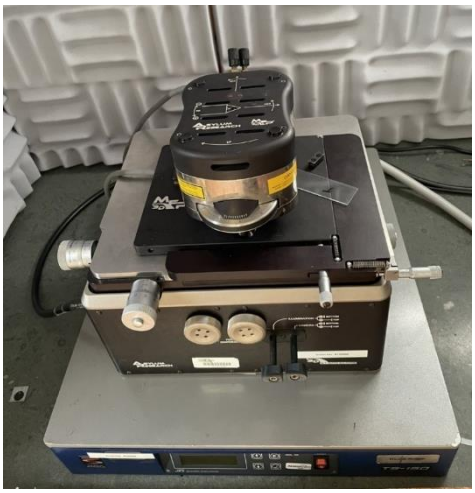

Figure 3-5: MFP-3D-SA AFM Instrument (Asylum Research).

3.3.4 Field-emission scanning electron microscopy (FE-SEM)

Field-emission scanning electron microscopy (FE-SEM) was employed for obtaining SEM images of both the bare substrates and BTSE-based films. The imaging was conducted using a NEON 40 FE-SEM microscope from Carl Zeiss SMT AG, Oberkochen, Germany. This microscope was equipped with both an InLens and a SE2 detector. EDX mapping was carried out with various probe forming convergence semi-angles, each at intervals of 35º, while maintaining a probe voltage of 4 kV. The aperture was set at 120 µm, and the frame size was 256 pixels × 192 pixels. A recording time of 40 ms was applied for each pixel.

Figure 3-6: NEON 40 FE-SEM microscope from Carl Zeiss SMT AG [160].

3.4 Electrochemical characterization of BTSE and PAA thin films

3.4.1 Electrochemical characterization of BTSE thin films

A three-electrode setup cell, connected to a potentiostat Gamry 600TM, was employed for the electrochemical characterization of the substrates. Working electrodes consisted of bare and BTSE-modified DC04 plates (2 cm x 2 cm), while a gold coil served as the counter electrode, and a commercial Ag/AgCl (3 M KCl, Radiometer Analytical) was utilized as the reference electrode. The surface of the samples was exposed to the supporting electrolyte solution, specifically an aerated borate buffer solution (0.2 M H_3BO_3, 0.05 M Na_2SO_4, 0.05 M $Na_2B_4O_7{\cdot}10\ H_2O$, 0.5 M NaCl, pH 8.4).

3.4.1.1 Cyclic voltammetry (CV)

To investigate the charge-transfer properties exhibited by the BTSE films, cyclic voltammetry measurements were carried out in a 0.1 M Bu_4NBF_4-containing acetonitrile (ACN) solution with the presence of an electrochemical redox probe (2 mM of 2,4,6-triphenylpyrylium tetrafluoroborate). Ten consecutives cyclic voltammograms were registered for each sample at a scan rate of 50 $mV{\cdot}s^{-1}$.

3.4.1.2 Linear Sweep Voltammetry (LSV)

Potentiodynamic polarization curves were then recorded after measuring the OCP for 30 minutes. The potential was scanned from -1.0 V (vs. Ag/AgCl) to +1.0 V (vs. Ag/AgCl) at a scan rate of 2 $mV{\cdot}s^{-1}$. The corrosion potential (Ecorr) and corrosion current density (icorr) were obtained from the polarization curves using the Gamry software through Tafel slope extrapolation.

3.4.1.3 Electrochemical Impedance Spectroscopy (EIS)

First, the open circuit potential (OCP) was measured for 30 minutes. Subsequently, electrochemical impedance spectroscopy (EIS) measurements were conducted in a frequency range from 100 kHz to 10 mHz with a signal amplitude perturbation of 10 mV.

3.4.2 Electrochemical characterization of PAA thin films

3.4.2.1 Cyclic voltammetry (CV)

A three-electrode setup, analogue to the one described in previous subchapter, was employed to evaluate the charge transfer/blocking properties of the as-deposited PAA thin films on steel. The assessment was carried out through cyclic voltammetry. In this context, solvent-cleaned and PAA-modified 316L steel samples underwent cycling between +0.2 and -1.0 V (vs. Ag/AgCl) at a scan rate of 0.2 V·s-1. The experiments were conducted in a 2 mM 2,4,6-triphenylthiopyrylium redox probe-containing 0.1 M tetrabutylammonium tetrafluoroborate (TTBAFB) solution in acetonitrile (ACN).

3.4.2.2 Linear Sweep Voltammetry (LSV)

To assess the electrochemical and corrosion-protection capabilities of the PAA layers, potentiodynamic polarization measurements were conducted in a 0.1 M borate buffer (50 mM NaCl) at pH 8.3. The potential was scanned at a sweep rate of 1 mV·s-1 over the range from −0.5 V to 1.0 V vs. open circuit potential (OCP). Before initiating the DC polarization measurements, OCP data were collected for a duration of 20 minutes.

3.4.2.3 Electrochemical Impedance Spectroscopy (EIS)

To further evaluate the electrochemical properties, electrochemical impedance spectroscopy measurements were performed. This involved a frequency range from 100 kHz to 10 mHz with an AC excitation amplitude of ±10 mV vs. OCP. The experiments were conducted in the same 0.1 M borate buffer (50 mM NaCl) at pH 8.3 to provide a comprehensive understanding of the PAA layers' performance.

3.5 Joining by Cold pressure welding

The experimental setup for Cold pressure welding with incremental rolling tool was established at the University of Paderborn in the Department of Forming and Machining Technology (LUF) under the supervision of Prof. Werner Homberg. The setup for incremental rolling features a working roller, propelled in a crank-like manner by a hydraulic cylinder (see Figure 3-7).

Initially set to the starting sheet thickness, the gap between the working roller and the support decreases as the working roller rotates, reaching the desired gap or sheet thickness. All rolling tools are crafted from alloyed tool steel (X38CrMoV5-1 and 42CrMo4) and hardened to a minimum of 50 HRC. The support comprises a sleeve resting on a spherical roller bearing (Type 22315 CAW 33). The roller's rotation angle is gauged by a rotary angle sensor (Type Kübler Sendix 5868), while a proportional valve regulates the hydraulic cylinder's movement based on the set angle (Valve: Parker D1FPB60MB9NB00 12, Cylinder: Differential cylinder 300 10008). The process control adopts an angle-based approach through a programmable National Instruments Compact RIO 9074 controller, equipped with measurement and I/O modules and programmed using National Instruments LabView software.

The hydraulic unit, utilizing a radial piston pump (Type HAWE 6011 R9,8), can deliver an adjustable pressure of up to 300 bar. Throughout this work, specific tool dimensions were consistently applied unless otherwise specified: Working roller radius RW = 30 mm, support radius RA = 88 mm, eccentricity of the working roller Δm = 6 mm. The standard setup for the width of the working roller or the effective web is bW = 7.5 mm. Force measurement was conducted using a force transducer (Type Induk 772B ±500 kN).

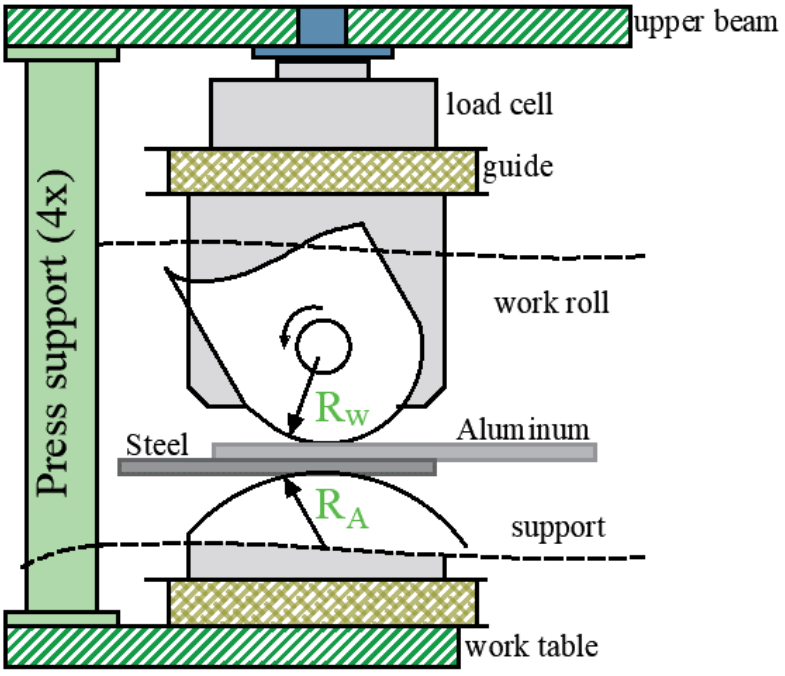

Figure 3-7: Setup of the experimental tool for incremental rolling pressure welding, depicted with a force transducer for the measurement of rolling force (drawing based on Schmidt [16]).

The modified steel and aluminum samples were welded using an incremental rolling tool. The pickled EN-AW1050 H111 aluminum blank (Al) was placed atop the DC04 steel blank, ensuring contact between the rolling tool and the aluminum specimen which increases the deformation within the aluminium blank and leads to comparably higher weld strengths [21]. Subsequently, the steel and aluminum samples, were pressure-welded through incremental rolling at the center of an overlapping length of 30 mm. The process maintained a constant reduction ratio (thickness reduction), denoted as r = 0.67, where the value of r is determined by equation 3-1:

$$r = \frac{(h_0 - h_1)}{h_0} \qquad (3-1)$$

where h_0 and h_1 are the initial and final (after rolling) thicknesses, of the as-formed steel-Al joints [16].

3.6 Mechanical properties of joined steel-aluminum specimens

3.6.1 Shear strength measurements

The strength of the modified aluminum- steel pressure welds was assessed using overlapping shear-test specimens in a Zwick Z100 universal tensile testing machine. The machine was equipped with an automatic mechanical extensometer capable of measuring both longitudinal and transverse elongation. The tests were conducted at a traversal speed of 0.8 mm/s under position control.

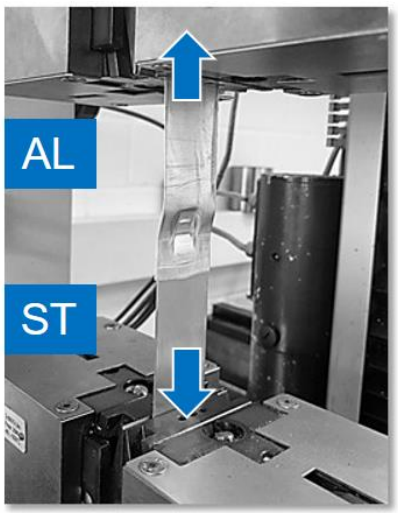

Figure 3-8: The setup for the measurement of the maximum shear force registered for a typical welded aluminum-steel specimen modified with an interlayered BTSE/ PAA thin-film.

3.6.2 90 º Peel-test

A two-component epoxy-amine resin, consisting of 11.2 g epoxy resin (D.E.R 331, a diglycidyl ether of bisphenol A, DOW Chemicals, Midland/USA) and 6.8 g amine hardener (poly(propylene glycol)bis(2-aminopropyl ether), Sigma-Aldrich), was utilized as a model adhesive. After thorough mixing and degassing as outlined elsewhere, the resin was applied onto modified CD04 stainless steel substrates measuring 40 mm x 60 mm x 1 mm [210]. To ensure a controlled film thickness of approximately 150 µm [211], the samples were laterally coated with four stripes of commercial adhesive tape, creating well-defined spacers for the epoxy amine application between the tape walls. Before the application of the adhesive liquid, the samples were stored in a glove box (filled with a mixture of dry air and nitrogen) at room temperature, maintaining a controlled relative humidity of 6.0 ± 3.0%, for 15 minutes to eliminate water layers adsorbed from the atmosphere. Subsequently, the samples were cured at 120 °C for 75 minutes. To quantify the wet deadhesion process, the epoxy-coated PAA-modified DC04 steel samples were exposed to a humid atmosphere (>95% relative humidity) at 40 °C for 24 hours [210, 212]. Peel-tests were performed with a consistent 90º angle relative to the sample surface at a speed of 1 mm/min. This was achieved using a force gauge (model ZP-5, Imada, Tokyo, Japan) and a motorized peel-tester (MV-220 Motorized Test Stand, Imada, Tokyo, Japan) under conditions of ≥ 95% relative humidity and room temperature [213]. For statistical analysis, a minimum of three different samples, prepared under identical experimental conditions, each with 3-4 released adhesive stripes, were used. This approach resulted in a minimum of 10-15 recorded deadhesion values for assessing the bonding properties corresponding to each distinct surface treatment considered in this study.

4

Results and Discussion

In this chapter, the experimental section of the research is delineated, presenting thorough insights into the results and discussions derived from supplementary interface analytical techniques, electrochemical methods, joining processes, and macroscopic adhesion tests conducted within this study. It concludes by proposing a potential mechanism for the joining between modified steel and aluminum via cold pressure welding .

Most of the content in this chapter has been adapted from B. Duderija, A. González-Orive, H.C. Schmidt, J.C. Calderón, I. Hordych, H.J. Maier, W. Homberg, G. Grundmeier, *Electrografting of BTSE: Zn films for advanced steel-aluminum joining by plastic deformation.* Journal of Advanced Joining Processes 2022;7:1100137 and B. Duderija, F. Sahin, D. Meinderik, J.C. Calderón, H.C. Schmidt, W. Homberg, G. Grundmeier, A. González-Orive, *Electrografting of Acrylic acid on steel for enhanced joining by plastic deformation*. Journal of Advanced Joining Processes 2024;9:100181.

4.1 Electrografting of BTSE:Zn films

4.1.1 Specific experimental approach

To decipher the mechanism underlying the sol-gel deposition process on steel, cyclic voltammetry measurements on brushed DC04 substrates immersed in diverse electrolyte-containing aqueous solutions where conducted. The relevant data are depicted in Figure 4-1.

Figure 4-1a shows the electrochemical profile exhibited by DC04 samples after solvent cleaning and 120 grit size grinding in N_2-degassed 0.2 M KCl (black voltammogram) and 0.2 M $NaNO_3$ (red) aqueous solutions. The solution was N_2 purged to subtract the contribution of the O_2 electroreduction occurring in the window potential range of interest.

The voltammograms registered in KCl shows the typical electrochemical profile exhibited by iron electrodes, namely the multiple faradaic processes corresponding to the successive formation and reduction of the differential oxidation state iron oxyhydroxides preceding the *HER* [214,215]. The latter can be expected since DC04 surfaces are mostly iron exposed to the electrolyte. Interestingly, when the background electrolyte is 0.2 M $NaNO_3$, a considerably large net cathodic current with potential onset at -1.15 V (vs. Ag/ AgCl) can be observed for the red voltammogram in Figure 4-1a. By comparison with the voltammogram registered in KCl, the latter can be attributed to the overlapping of the NO_3^- reduction to NO_2^- with *HER*. Consequently, from the measurements shown in Figure 4-1a and the data reported by other authors [216] it is possible to conclude that the overall result of applying a negative enough cathodic potential (in the range of -1.2 V (vs. Ag/ AgCl)) in a NO_3^--containing aqueous solution at pH 4.5 cannot be different from the hydroxyl ion generation in the vicinity of the electrode as a consequence of the overlapping of HER and the reduction reactions of O_2 and NO_3^- [216].

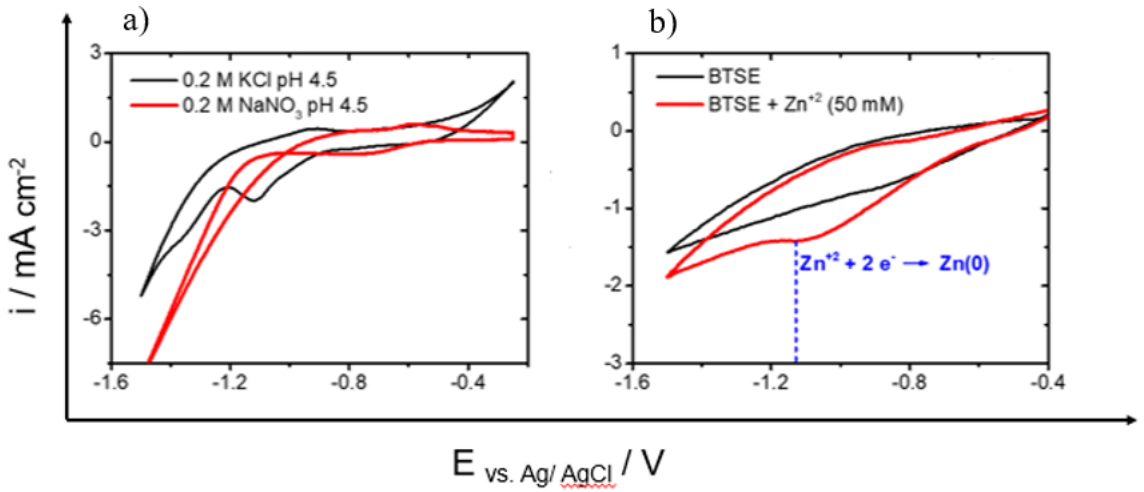

Figure 4-1: Cyclic voltammograms registered for solvent cleaned and freshly 120 grit size grounded DC04 steel substrates at 0.1 $V \cdot s^{-1}$ in a) degassed 0.2 M KCl (black voltammogram) and 0.2 M $NaNO_3$ aqueous solutions at pH 4.5 (red), and in b) a 2.5 % (w/w) BTSE solution-containing 0.20 M $NaNO_3$ (black) and 50 mM of $Zn(NO_3)_2 \cdot 6H_2O$ (red).

Most importantly, when the previously hydrolysed BTSE water/ethanolic solution (pH 4.5) is made 0.2 M in $NaNO_3$, a broad featureless electrochemical response, but exhibiting a net cathodic current preceding HER, can be detected, cf. black voltammogram in Figure 4-1b. As previously stated, this net cathodic current should be attributed to the overlapping of *HER* and the reduction reactions of O_2 and NO_3^-. When 50 mM $Zn(NO_3)_2$ are added to the BTSE containing water/ethanolic solution (but maintaining the concentration of NO_3^- ions, i.e., 0.2 M, constant), a small diffusion-controlled irreversible faradaic peak presumably corresponding to the electroreduction of Zn^{2+} ions to Zn(0) is clearly visible at -1.1 V (vs. Ag/ AgCl). Although not so evident, a small anodic hump can also be identified at -0.85 V (vs. Ag/ AgCl). Indeed, Cruz and co-workers have extensively studied the electrodeposition of Zn at different pH values [217]. According to the authors, the range potential range corresponding to the afore-mentioned peaks registered at pH = 4.5 is broadly matching with the Zn deposition and its ulterior reoxidation [217]. Given the optimal potential range identified from Figure 4-1, BTSE and BTSE:Zn thin films were synthesized on DC04 steel samples using chronoamperometry. Consequently, current density-time curves were recorded for DC04 at -1.2 V (vs. Ag/AgCl), as illustrated in Figure 4-2 . These curves exhibited the typical profile anticipated for electrodeposition processes, featuring instantaneous nucleation followed by diffusion-limited growth, consistent with the Scharifker–Hills model for nucleation and growth [218].

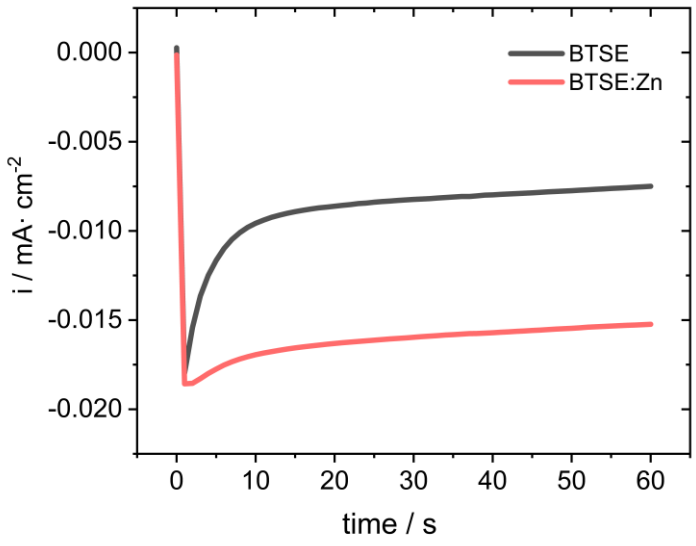

Figure:4-2: Chronoamperometric curves recorded for brushed DC04 specimen at -1.2 V (vs. Ag/AgCl) for a duration of 60 s performed in a 2.5% (w/w) BTSE solution in a 75% (w/w) ethanol/Milli-Q water mixture containing 0.2 M $NaNO_3$ (red line), and 50 mM $Zn(NO_3)_2 \cdot 6H_2O$ (gray line). Based on [258].

Higher diffusion-controlled current densities are observed in the precursor sol-gel solution containing Zn^{2+}, i.e. BTSE: Zn thin film, as depicted by the red chronoammperogram in Figure 4-2 which can be attributed to the co-deposition of metallic Zn nanoparticles [219].

4.1.2 Surface thin film characterization

As mentioned earlier, the surface condition, including solvent cleaning and surface roughening, plays a crucial role in Cold pressure welding (CPW). Subsequently, the results of the surface pre-conditioning of DC04 samples will be presented to elucidate the impact of these treatments on the welding process.

Figure 4-3 displays SEM images of DC04 steel substrates following solvent cleaning, grinding, and NaOH activation. The solvent-cleaned substrates exhibit major lines, defects, and featureless roughness characteristic of the manufacturing process, along with visible grain boundaries (Figure 4-3a). Subsequent polishing (Figure 4-3b) results in the near disappearance of grain boundaries, presenting a more homogeneous surface adorned with parallel polishing lines. No significant differences were detected after the 1 min NaOH activation process (Figure 4-3c).

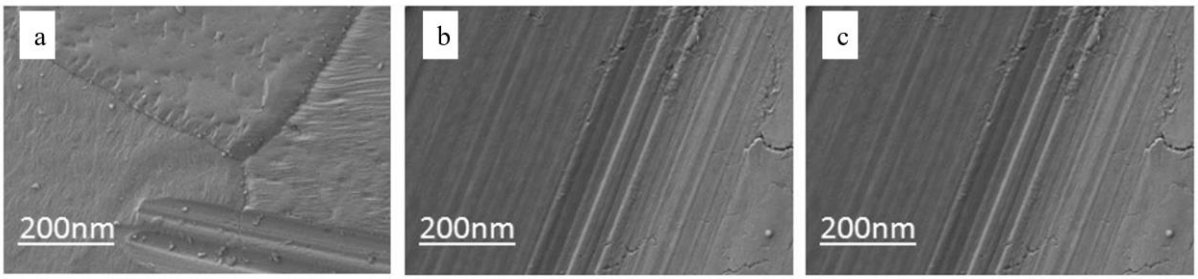

Figure 4-3: SEM images of DC04 steel samples with different surface conditioning processes. Solvent cleaning a); 120 grit size brushing b) and pickling in a 25 g/ L NaOH-containing aqueous solution for 1 min c). Based on [258].

High-resolution FE-SEM and AFM images were captured before and after modifying the activated DC04 steel surfaces with nanocomposite films, namely BTSE and BTSE:Zn. Interestingly, BTSE sol-gel films prepared for short deposition times, specifically for 5 s (Figure 4-4a and 4-4b), exhibited a grain-like structure that allowed the detection of typical features of the underlying steel substrates. This suggests the deposition of a very thin layer.

Characteristic topographic features associated with deposited BTSE:Zn thin films, such as flake-like structures (for 5 s) and amorphous discontinuous deposits (for 60s), were observed in the FE-SEM images presented in Figure 4-4c-f. These features can be attributed to the co-deposition and growth of metallic Zn particles in the nanocomposite films.

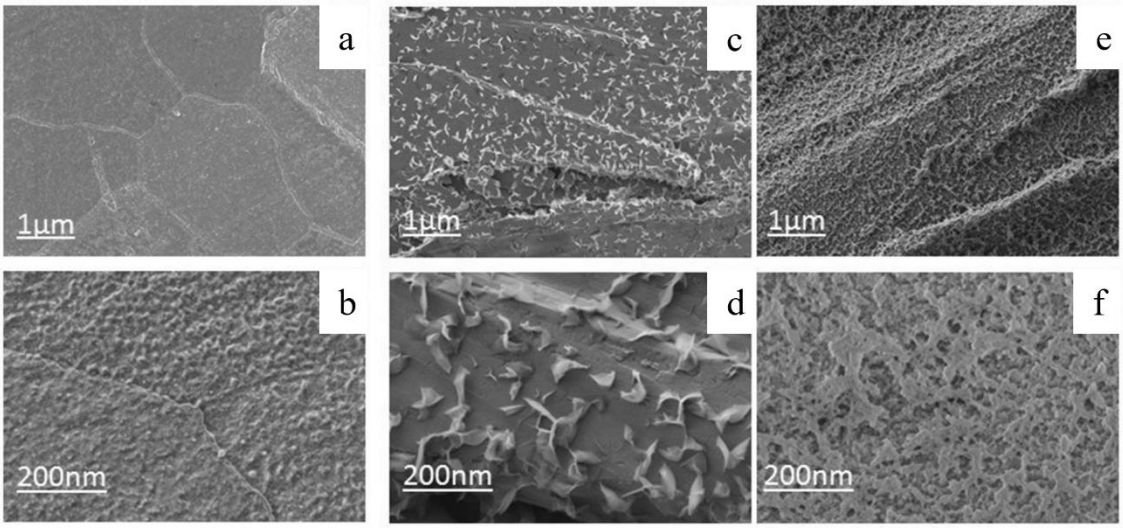

Figure 4-4: FE-SEM images of brushed DC04 steel samples following surface conditioning processes: BTSE modification for 5 s a) and b); BTSE:Zn modification for 5 s c) and d), and BTSE:Zn modification for 60 s e) and f). Based on [258].

AFM measurements were performed to assess the nanoscale topography of the brushed DC04 steel samples before and after being modified with the BTSE and BTSE:Zn layers. In Figure 4-5a, the typical topographic characteristics of an untreated DC04 steel sample reveal a smooth and featureless surface. With a deposition time of 5 s, AFM images depict the development of a sol-gel-based granular electrodeposit, comprising smooth pancake-shaped island structures that uniformly coat the steel substrate. The cracks, rifts, or defects in the film delineate the islands and enable the quantification of the BTSE film thickness. Through cross-sectional profiles, the layer thickness was estimated to be in the range of 3-6 nm. The origin of these cracks can be attributed to the incomplete bidimensional growth of the already formed sol-gel nuclei/islands, a consequence of the short deposition time. Additionally, the occurrence of hydrogen evolution reaction (HER) cannot be ruled out within the applied potential range. As a result, the formation of H_2 bubbles at the solid-liquid interface could contribute to the observed cracked topographic features.

Similar outcomes were observed in the modification of DC04 steel substrates with the BTSE:Zn layer, as depicted in Figure 4-5c. In this case, 3D aggregates of rounded nanoparticles decorating the sol-gel film can be identified.

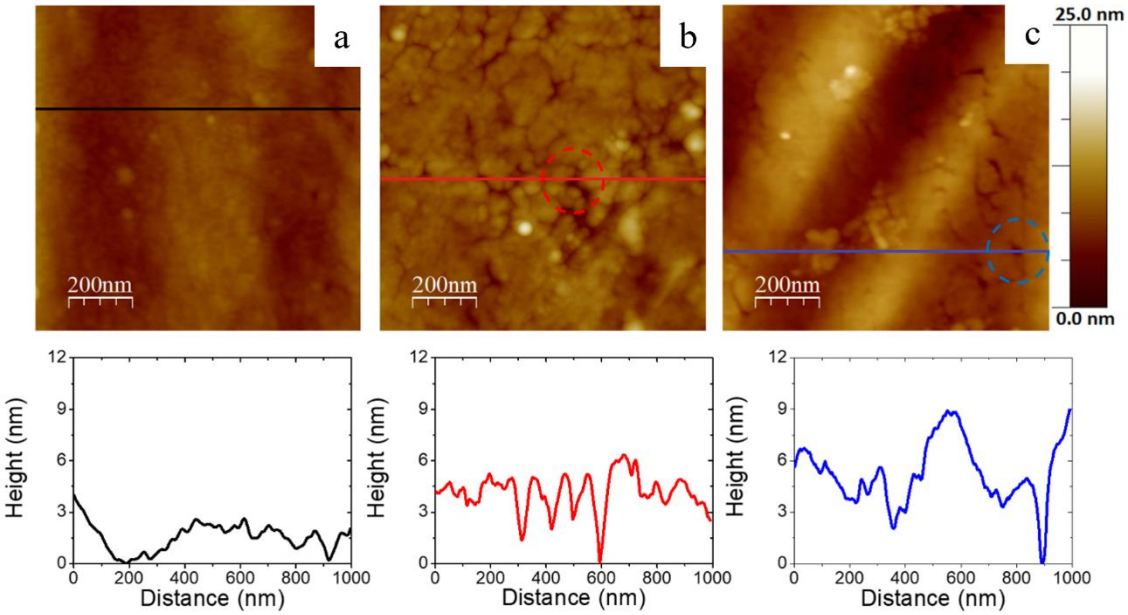

Figure 4-5: AFM images (1.0 x 1.0 µm²) of DC04 steel samples subjected to various surface conditioning processes. Polishing and subsequent immersion in a 25 g/L NaOH-containing aqueous solution for 1 min a); modification with BTSE for 5 s b), and modification with BTSE:Zn for 5 s c) (top panel). The bottom panel displays representative cross-sectional profiles, illustrating the dimensions of the corresponding BTSE deposits. Based on [258].

In this context, Figure 4-6 illustrates the topographic details associated with clusters of rounded particles, measuring 3-8 nm in height and 20-50nm in width, as depicted in the cross-section profile of Figure 4-5a. These particles display a clear negative phase contrast (attractive interaction) in contrast to the positive phase difference (repulsive interaction) exhibited by the organosilane layer component, as observed in Figure 4-6a and 4-6b, along with their respective cross-section profiles. Notably, these particles, absent in the BTSE layer, can be identified as ZnO particles.

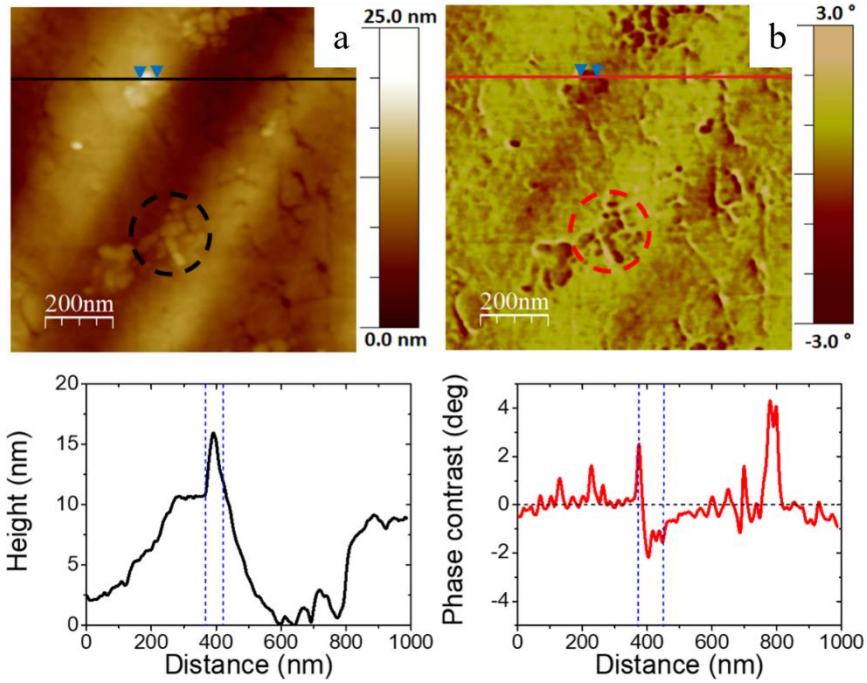

Figure 4-6: 1.0 x 1.0 µm^2 AFM images of DC04 steel samples modified with a BTSE: Zn layer for 5 s: topographic image a), and its corresponding phase contrast image b). Black and red circles depicted in the images identify a cluster of rounded particles exhibiting a negative phase contrast in comparison to the surrounding BTSE layer (positive phase values). Based on [258].

The electrochemical deposition of BTSE and BTSE: Zn layers for 5s can be also carried out onto aluminum, EN-AW-1050A surfaces. SEM and AFM imaging was performed to unveil their characteristic topographic features. Figure 4-7 shows SEM images registered for aluminum,EN-AW-1050 H111 substrates after solvent cleaning and pickling. Characteristic topographic element of the solvent-cleaned aluminum substrates such as major polishing lines, defects and featureless roughness coming from the manufacturing process can be easily identified in Figure 4-7a. After pickling, submicrometric concave void-like domains appears homogeneously distributed over the surface (see Figure 4-7b).

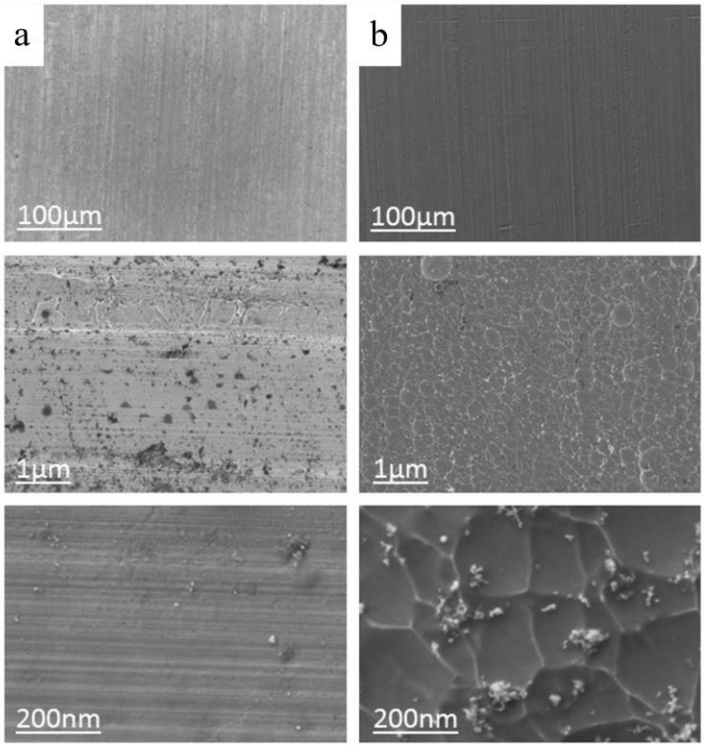

Figure 4-7: SEM images of EN-AW-1050 H111 aluminum samples with different surface conditioning processes: solvent cleaning a), and pickling b). Based on [258].

Further detailed topographic information analogous to AFM images of EN-AW-1050 H111 aluminum samples with different surface conditioning can be acquired. As anticipated, aluminum surfaces of solvent-cleaned EN-AW-1050 H111 exhibit polishing lines, defects, and undefined nanostructured roughness, clearly visible in Figure 4-8b. Following the pickling process, submicrometric concave domains emerge, displaying height variations between peaks and valleys of 30-80 nm (refer to cross-section profiles in Figure 4-8). AFM analysis reveals a local increase in the RMS roughness from 15.3 to 22.5 nm, as depicted in the insets of Figure 4-8. As previously indicated by Grundmeier et al., a significant reduction in the thickness of the aluminum oxide layer from 3.8 to 2.1 nm has been observed after the pickling surface treatment [10].

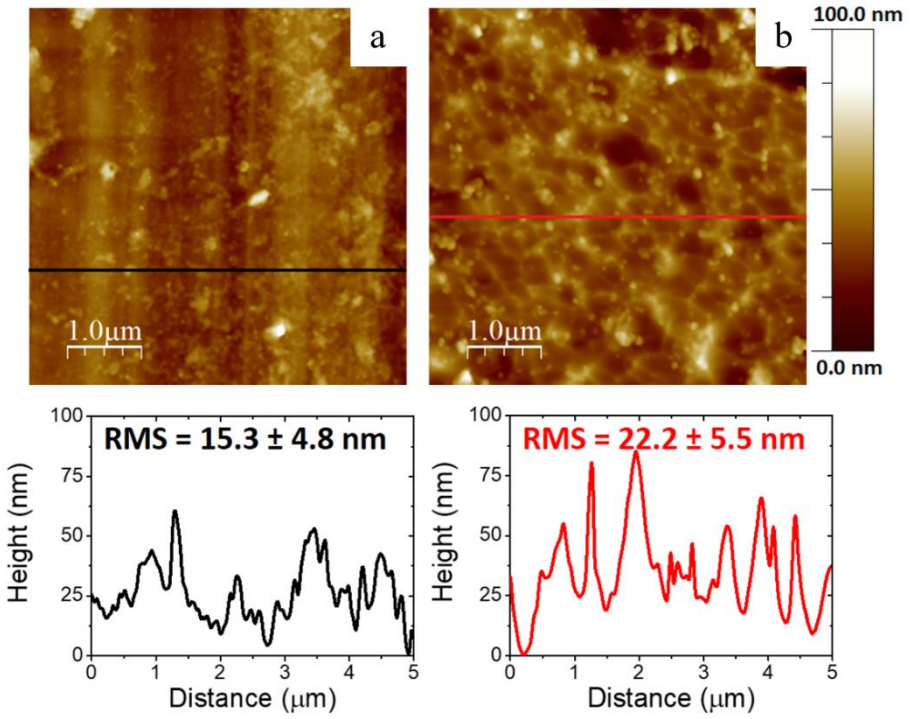

Figure 4-8: 5.0 x 5.0 µm^2 AFM images of EN-AW-1050 H111 aluminum samples with different surface conditioning processes: solvent cleaning a), and pickling b). Based on [258].

Electrochemical deposition of BTSE and BTSE:Zn layers for 5 s was also conducted on aluminum EN-AW-1050A surfaces, and AFM imaging was utilized to reveal their characteristic topographic features. The deposited thin films exhibited morphological profiles similar to those observed on DC04 samples, forming pancake-like islands that uniformly covered the aluminum substrate, as depicted in Figure S1 in the Supporting Information (SI). As previously mentioned, cracks and defects allowed for the quantification of the xerogel layer thickness. Cross-section profiles through the cracks estimated a thickness range of 20 to 35 nm. Interestingly, for the same deposition time of 5 s, the BTSE layers deposited on EN-AW-1050A surfaces were noticeably thicker than those obtained for DC04 samples, with values ranging from 3 to 6 nm. The deposition of the BTSE film resulted in a significant decrease in the average RMS roughness from 22.2 to 14.6 nm. It is noteworthy that Hu et al. have previously reported effective APTES and BTSE-based electrochemical deposition onto Al alloys [89].

However, upon the deposition of the BTSE:Zn layer, a rougher film incorporating round-shaped particles, 5 to 10 nm high and 30 to 60 nm wide, randomly distributed over the

surface, formed, as observed in Figure 4-8c. The thickness of the BTSE:Zn layer, deduced from the cross-section profile and the fracture identified with a blue circle, is expected to be in the same range as that obtained for the BTSE layer in the absence of Zn.

To gather insightful details regarding the chemical composition of the steel surfaces modified with BTSE, XPS measurements were conducted on the pristine substrates before and after the application of the sol-gel film, with or without Zn^{2+}. The results obtained from the quantitative analysis of the corresponding survey spectra are succinctly presented in Table 4-1. These findings corroborate the observations made through SEM and AFM analyses, confirming the successful modification of DC04 substrates with the BTSE and BTSE:Zn composite films. Notably, the electrochemically induced deposition of the sol-gel revealed the presence of BTSE or BTSE:Zn layers, as indicated by the emergence of the respective Si 2p or Si 2p and Zn $2p_{3/2}$ signals.

Table 4-1. XPS surface composition analysis of DC04 steel substrates following various surface treatments (sequential solvent cleaning, 120 grit size grinding, and NaOH activation for steel, and solvent cleaning and pickling for aluminum), as well as after BTSE and BTSE:Zn thin film deposition coupled with thermal annealing at 120 °C for 15 minutes. The data is presented in atomic percentage (at. %) for different surface states, with the corresponding XPS survey spectra illustrated in Figure S2 in the (SI).

Sample	**Element (at. %)**					
	C	**O**	**Si**	**Zn**	**Fe**	**Al**
DC04	26.2	37.7	-	-	35.1	-
DC04 - BTSE (*t = 5s*)	27.2	38.9	23.3	-	10.6	-
DC04 - BTSE:Zn (*t = 5s*)	23.2	37.5	24.9	1.6	12.8	-

A deeper analysis of the surface chemistry of the as-prepared BTSE-modified substrates was conducted by evaluating high-resolution core-level spectra, specifically focusing on C 1s, Si 2p, and Zn $2p_{3/2}$ as illustrated in Figure 4-9. The presence of C-Si, C-O-Si, and Si-O-Si bonds indicates the successful functionalization of the DC04 surface with the thin organosilane film. Only trace amounts of nitrogen were detected, suggesting the effective removal of $Zn(NO_3)_2$ and $NaNO_3$ residues through successive rinsing in ethanol and Milli-Q water. The C1s peak was fitted into three components at 284.6, 286.1, and 288.5 eV (Figure 5-9a). These components were attributed to C-Si, C-C, and C-H groups (284.6 eV), C-OH, C-O-Si, and C-O-C (286.1 eV), and finally C=O or O-C=O groups (288.5 eV), respectively. The contributions from adventitious carbon and the deposition of the BTSE film likely account for these components [210, 220].

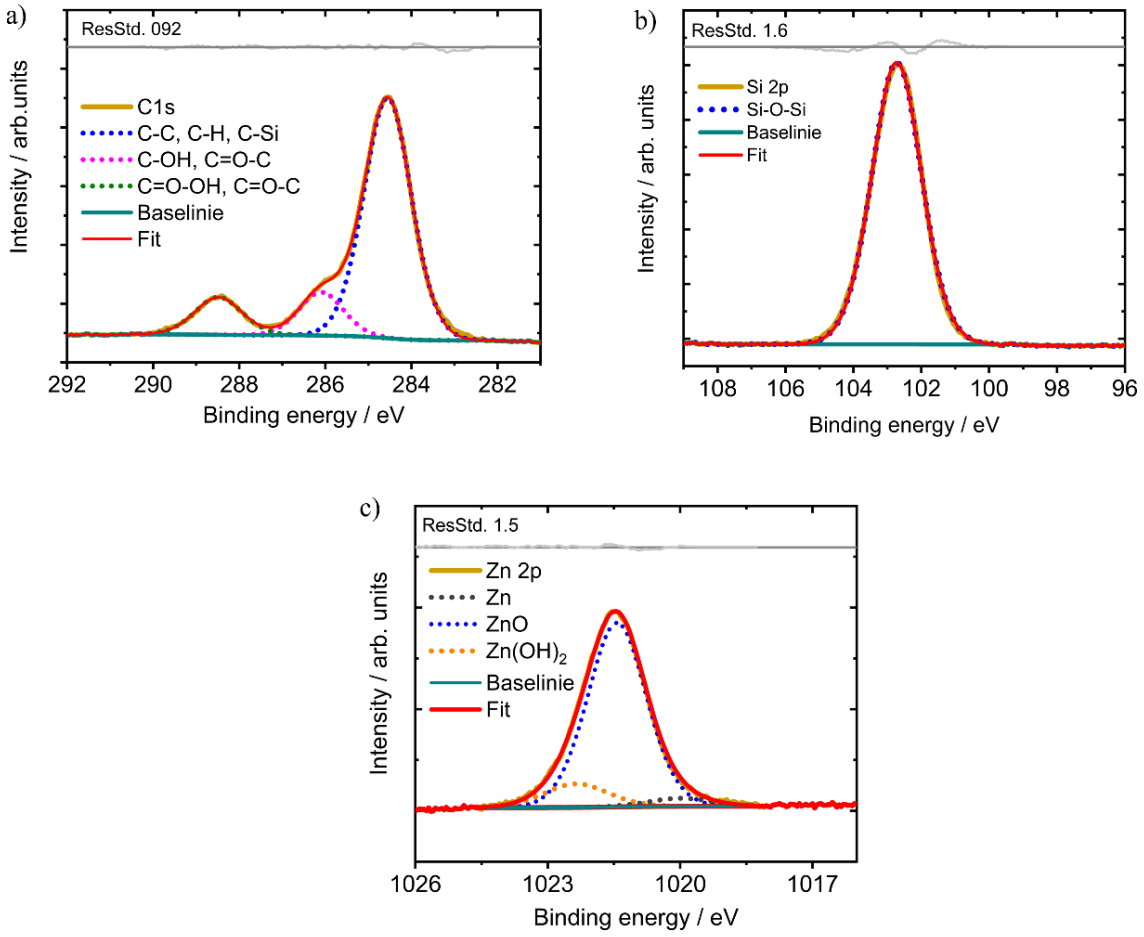

Figure 4-9: High resolution core-level spectra of BTSE:Zn layers deposited at -1.2 V (vs. Ag/ AgCl) for 5 s on $DC0_4$ steel substrates: C1s a); Si2p b), and $Zn2p_{3/2}$ c). Based on [258].

As evident in the high-resolution spectrum illustrated in Figure 4-9c, the Zn $2p_{3/2}$ peaks are centred at 1021.5 eV, predominantly associated with ZnO [223]. Notably, a minor contribution at 1020.2 eV was identified, attributed to metallic Zn. This confirms the co-deposition of metallic Zn during the thin-film formation process and subsequent oxidation to ZnO under ambient conditions [223]. Similar findings have been reported by Wu et al. in the co-deposition of BTSE and Zn on cold-rolled steel surfaces [219]. Analyzing the results from the survey spectra summarized in Table 1, only reduced amounts of co-deposited ZnO particles are obtained for short deposition times of 5 s, approximately 1-2%. The analysis of the fractional surface coverage of 3D-aggregates of ZnO particles extracted from AFM images (Figure 4-5c) reveals an approximate coverage of 5-10%. As expected, for longer deposition times (60 s), the Zn at. % increases to about 4% refer to Figure 4-6.

Additionally, a PM-IRRAS analysis was conducted on DC04 steel samples modified with the nanocomposite films.

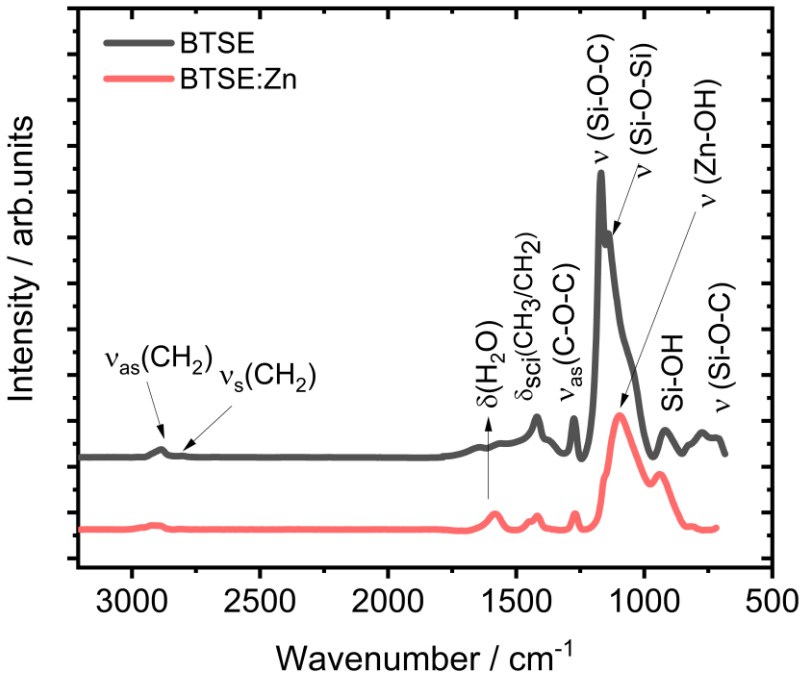

Figure 4-10: PM-IRRAS spectra registered for a DC04 steel substrate modified with BTSE (red line), and BTSE:Zn (gray) at -1.2 V (vs. Ag/ AgCl) for 5 s. Based on [258].

The PM-IRRAS results for BTSE and BTSE:Zn films, prepared with a deposition time of 5s, are depicted in Figure 4-10. The peaks at 2860 and 2916 cm^{-1} correspond to the symmetric and asymmetric C-H vibration modes, respectively, arising from -CH_2 groups in the aliphatic backbone of the BTSE molecule [221,222]. The peak at 1280 cm^{-1} is linked to Si-C symmetric bending [224]. Peaks at 916 and 1127 cm^{-1} are assigned to silanol (Si-OH) and Si-O-Si groups within the film [225]. The presence of silanol is crucial for promoting the formation of Si–O–Al bonds in Cold pressure welding (CPW) processes with aluminum counterparts, while Si-O-Si contributes to successful cross-linking within the silicone-like matrix during the curing process (15 minutes at 120 ºC). For BTSE:Zn, a partial overlap between the Si-O-Si and Zn-OH peaks was detected, causing a shift of the maximum peak to lower wavenumbers, i.e.,1088cm^{-1}[223].

Considering the results mentioned above, the electrografting mechanism of the BTSE-based film can be outlined as follows. The initial stage involves the hydrolysis of methoxy groups to form silanol groups (Si-OH), a process catalyzed in slightly acidic water-ethanol solutions. These silanols interact with the hydroxyl-rich oxide-covered steel surface through hydrogen bonding (I). When a negative potential is applied, the reduction of nitrate to nitrite groups, and/or H+ or dissolved oxygen, leads to the generation of hydroxyl anions, causing a localized increase in pH near the electrode. Consequently, a condensation reaction occurs, facilitating the electrografting of the film onto the steel surface (II). These stages are illustrated in Figure 4-11.

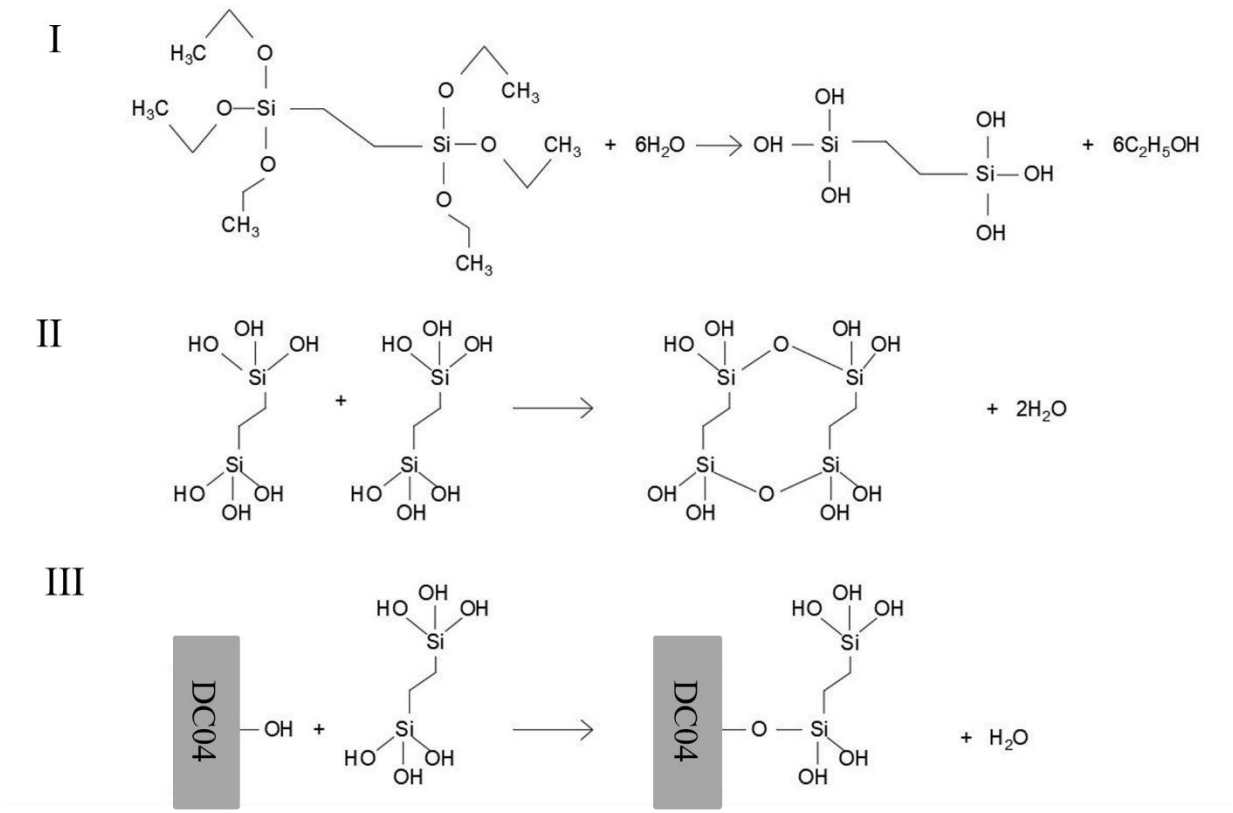

Figure 4-11: Scheme presenting different steps involved in the electrografting of the BTSE-based sol-gel thin film. Based on [258].

The subsequent curing process, involving water removal, promotes cross-linking (III). Furthermore, Si-O-Me bond formation is more like to be formed when the water activity at the interface is diminished during the curing process. If the electrochemically induced condensation reaction occurs in a Zn^{2+}-containing electrolyte, there is also the potential for the co-deposition of small metallic Zn particles, which rapidly oxidize to ZnO under ambient conditions (IV), as illustrated in the following Figure 4-12.

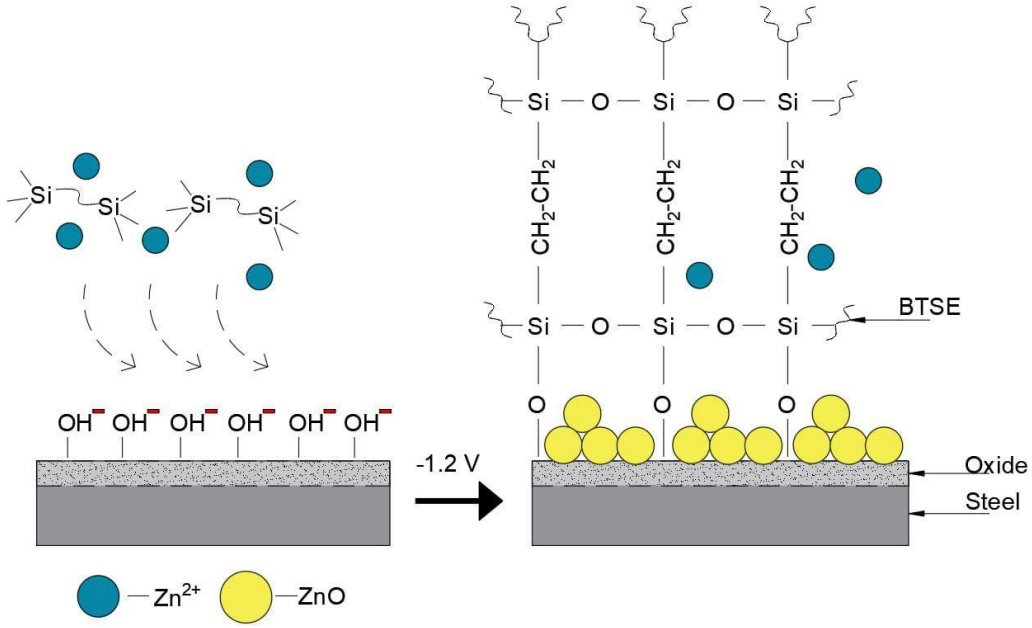

Figure 4-12: Different steps involved in the electrografting of the BTSE:Zn based sol-gel thin film.

4.1.3 Electrochemical characterization of BTSE / BTSE:Zn thin films

The charge transfer barrier properties exhibited by the BTSE and BTSE:Zn thin films were evaluated by recording cyclic voltammograms in the presence of an electrochemical redox probe, specifically 2,4,6-triphenylthiopyrylium in acetonitrile (ACN). This probe has previously been utilized by Daasbjerg and colleagues to investigate the charge transfer characteristics of polyphenylene-based thin films prepared through the electroreduction of aryldiazonium salts on steel surfaces [225]. Figure 4-13 illustrates the current density-potential (i-E) curves obtained for bare DC04, BTSE, and BTSE:Zn thin films deposited on DC04 steel substrates (post-curing for 15 minutes at 120 ºC). The two-peaked quasi-reversible and diffusion-controlled electrochemical profile exhibited by the former can be ascribed to the oxidation/reduction reactions of the electrochemical redox probe, displaying a peak-to-peak separation of approximately 200 mV. Following the electrochemically assisted deposition of BTSE and BTSE:Zn films for 5 s (red and blue voltammograms in Figure 4-13a, respectively), a notable increase in peak-to-peak separation, coupled with a decrease in measured current densities, is evident in the cyclic voltammograms of the latter. This overall effect can be explained by the restricted diffusion of the electrochemical redox probe through the as-prepared sol-gel films. Interestingly, this phenomenon is more pronounced for BTSE:Zn thin films, indicating the formation of a denser and more compact sol-gel layer when the Zn^{2+}-containing working electrolyte is employed, potentially due to catalysis of the

sol-gel process by Zn^{2+} ions and/or the co-deposition of Zn metallic particles. As depicted in Figure 4-13b, with longer deposition times (i.e., 60 s), the charge-transfer blocking properties of BTSE and BTSE:Zn films are significantly enhanced.

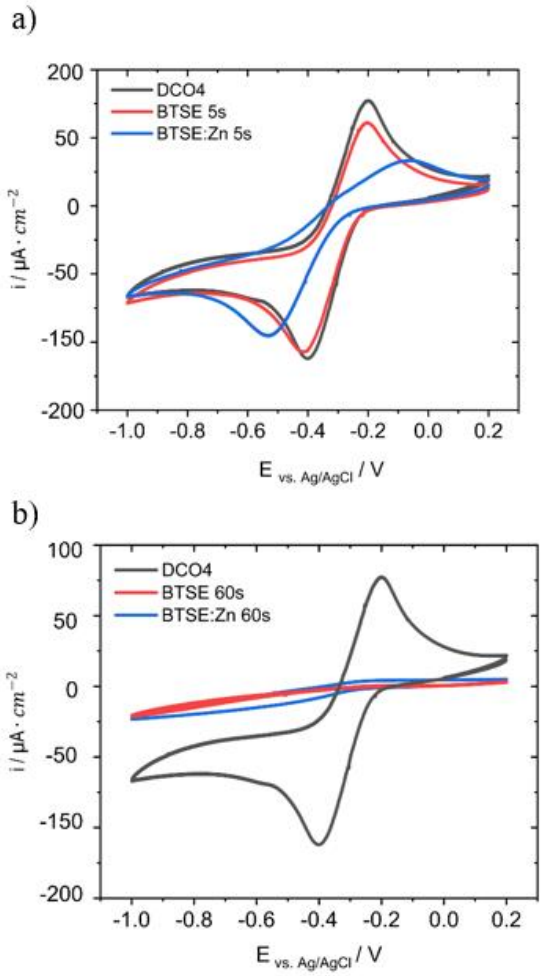

Figure 4-13: Cyclic voltammograms recorded for brushed unmodified DC04 (black line); modified with BTSE (red) and BTSE:Zn (blue) in a 2 mM 2,4,6 triphenylthiopyrylium-containing 0.1 M Bu_4NBF_4/ACN at a scan rate of 0.05 $V \cdot s^{-1}$ for deposition times of 5 s a) and b) 60 *s*. Based on [258].

Consequently, higher peak-to-peak separations and lower current densities are observed, attributed to the formation of thicker films with a lower density of defects and pinholes. Potentiodynamic polarization curves were acquired to further characterize the electrochemical properties of the BTSE and BTSE:Zn films. The data are presented in Figure 4-14. The E_{corr} values observed for substrates covered with BTSE films, prepared at different deposition times (5s and 60 s), are shifted towards more negative potentials compared to those of the bare DC04. This observation aligns with previous findings by Wu et al. and can be explained by the increased overpotentials necessary for the occurrence of the oxygen reduction reaction (ORR) [219].

As anticipated, extended deposition times result in decreased corrosion current densities, indicating the formation of a thicker film with a reduced density of defects or pinholes, as illustrated by the blue curve in Figure 4-14.

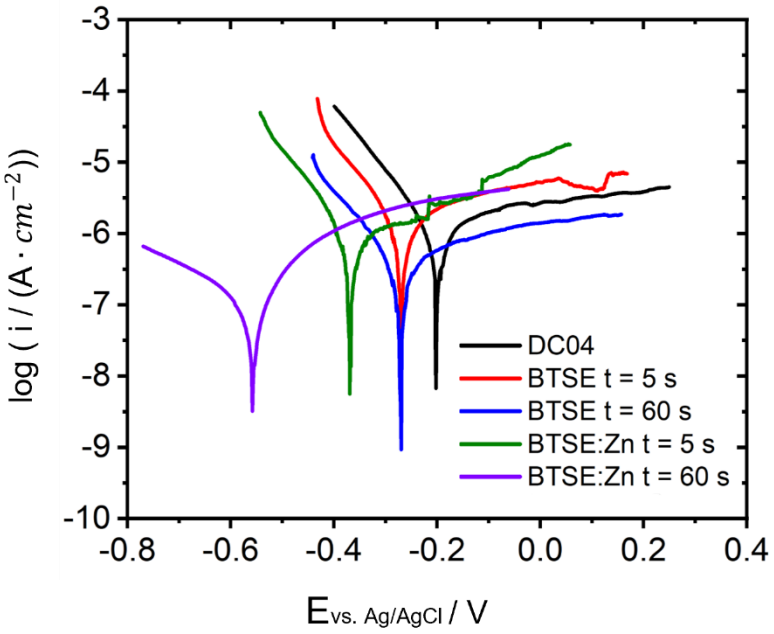

Figure. 4-14: Potentiodynamic polarization curves recorded in an aerated buffer solution (pH 8.4) at 2 $mV \cdot s^{-1}$ for the brushed, unmodified (black curve); BTSE modified (red for 5 s and blue for 60 s, and BTSE:Zn modified DC04 samples (green for 5 s and purple for 60 s). Based on [258].

When Zn/ZnO particles are introduced, as seen in the green and purple curves in Figure 4-14, the OCP values shift to even more negative values, indicating cathodic protection due to their sacrificial anode behaviour (green curve).

Consequently, lower exchange current densities are observed when thicker and less defective films are obtained for longer deposition times (blue curve). The corresponding values recorded for E_{corr} and i_{corr} are presented in Table 4-2.

Table 4-2. E_{corr} and i_{corr} estimated from the potentiodynamic polarization curves displayed in Figure 4-14 by extrapolation of Tafel plots.

Sample	E_{corr} **vs. Ag/AgCl / V**	i_{corr} **/ mA·cm^{-2}**
DC04	-0.204	-0.97
BTSE (*t = 5 s*)	-0.271	-0.53
BTSE (*t = 60 s*)	-0.271	-1.48
BTSE:Zn (*t = 5 s*)	-0.368	-3.47
BTSE:Zn (*t = 60 s*)	-0.556	-1.07

The corrosion protection properties of the BTSE-based films were assessed through EIS measurements conducted over various immersion times in an aerated borate buffer electrolyte solution. The corresponding Bode plots and low-frequency impedance modulus versus time plots for both BTSE and BTSE:Zn thin films at different deposition times (5 and 60 s) are presented in Figures S3 and S4 in the SI, respectively. In all cases, the impedance values recorded for the bare substrates were lower than those for the steel substrates coated with the nanocomposite film, indicating the corrosion inhibition effect arising from the barrier properties of the siloxane film. The gradual increase in the impedance modulus with immersion times can be attributed to the formation of a robust three-dimensional crosslinked Si-O-Si matrix firmly adhered to the DC04 steel surface, along with the generation of corrosion products that impede electrolyte diffusion. Notably, these values are further elevated when ZnO nanoparticles are incorporated into the film, providing additional protection.

4.1.4 Interfacial bonding and tensile shear test

For the tensile tests, specifically the measurement of shear strength in welded specimens, a low alloy steel, DC04, was utilized due to its favourable mechanical properties. The DC04 steel samples underwent modification with BTSE and BTSE:Zn thin layers prepared through chronoamperometry (CA) with various deposition times.

To activate the specimens for welding, the DC04 samples were ground for two minutes after which electropolymerization was performed. This process also served to eliminate the native oxide layer and enhance roughness at the nano and microscale, a critical factor for weldability. Similarly, aluminum samples (AW-EN-1050 H111) underwent pickling in NaOH to achieve the same objective.

Subsequently, the BTSE-activated steel and aluminum samples were welded through incremental rolling with a constant reduction ratio of 0.67, following the scheme outlined in Figure 4-15.

The shear strengths of the resulting joints were then determined using a tensile tester, as illustrated in Figure 4-15.

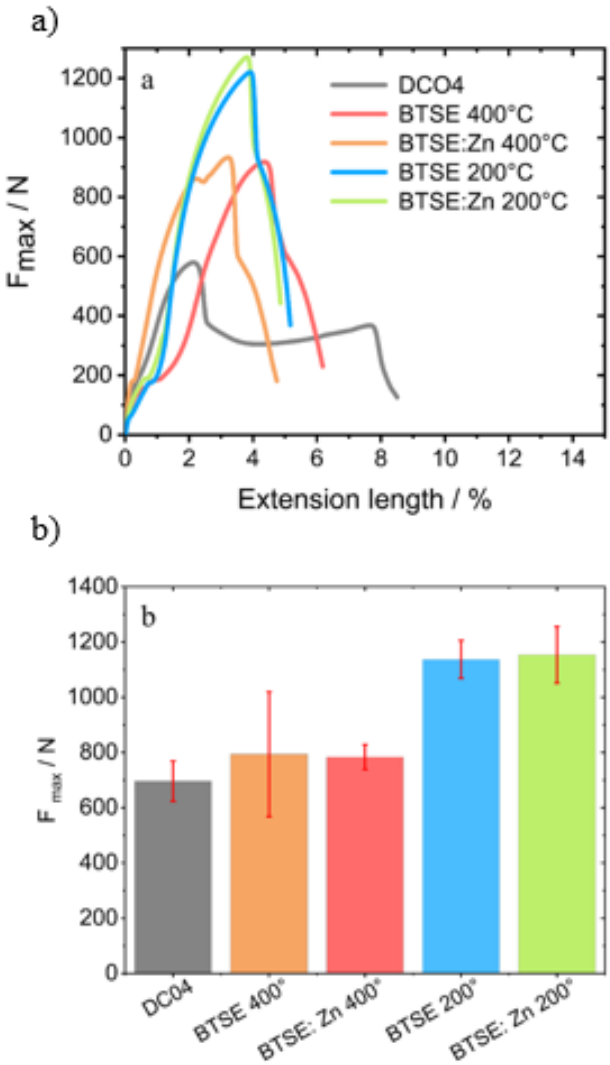

Figure 4-15: Results of shear test measurements a) and b) histograms showing the averaged maximum shear force recorded for joining specimens welded by CPW between pickled AW1050A H111, and unmodified DC04, as well as DC04 modified with BTSE and BTSE:Zn films, at either 200 ºC or 400 ºC (with a thickness reduction of 75%). Based on [258].

Figure 4-15a illustrates the characteristic tensile shear curves obtained from various combinations of welded specimens, namely DC04/BTSE-based thin film/ aluminum EN-AW-1050A , collected in this study and subjected to different heating treatments.

The averaged values corresponding to the maximum shear force recorded for the as-prepared welded specimens are presented in Figure 4-15b. In the reference case, where DC04 steel substrates (ground to P120 grit size paper) were welded to pickled EN-AW-1050A aluminum, maximum shear forces were observed in the range of 700 N and 705 N for specimens heated at 200 °C (DC04 200 °C). No significant differences in weld strength were observed for the reference specimens before and after thermal treatments at 200 ºC or 400 ºC The maximum shear force values recorded for joinings using BTSE and BTSE:Zn-modified DC04 specimens were not statistically distinct from the reference when no thermal treatment was applied (Figure S5 SI). Importantly, the results depicted in Figure 4-15 clearly indicate that BTSE-based coatings exhibit significantly increased shear strength values (1225 ± 100N) compared to the reference samples (700 ± 70N) after the thermal treatment at 200 ºC.

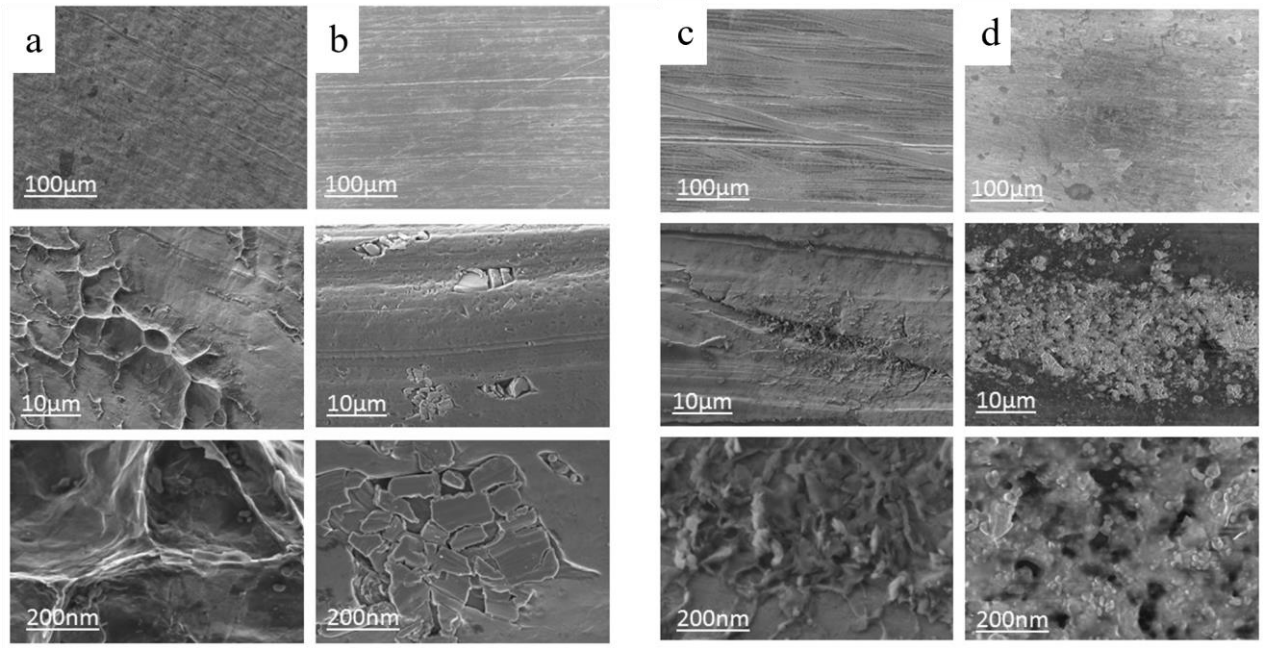

Figure 4-16: SEM images of DCO4 steel modified with BTSE a); pickeld AL-EN-AW-1050 H111 aluminum b); DCO4 steel modified with BTSE:Zn c), and pickled Al-EN-AW-1050 H111 aluminum d) after fracture by tensile test. Based on [258].

However, there were no drastic differences in weld strength between BTSE and BTSE:Zn coatings, just slightly elevated values were noted when Zn metallic particles were incorporated into the nanocomposite film. It is noteworthy that, contrary to the argument by Gandhi et al. [11] regarding the irreversible formation of siloxane bridges with hydroxyl groups at oxide surfaces at temperatures ≥400 ºC, the optimal results in this study were achieved at

200 ºC which aligns with findings by Hoppe et al. for a MPTS SAM interlayer in copper-aluminum joinings [10].

In this context, Grundmeier and co-workers had showed that higher applied temperatures dropped weld strengths in the joining between steel and aluminum via CPW [44].

Next, investigation into the plastic deformation process occurring at the interface between steel and aluminum specimens as a result of cold pressure welding (CPW) was undertaken. For this purpose, SEM and EDX measurements were conducted following tensile shear testing. Figure 4-16 presents the surfaces of DC04 steel and EN-AW-1050 H111 aluminum after tensile tests at various magnifications. On both aluminum and steel surfaces, the deformation of polishing lines resulting from induced stress and plastic deformations at the interface after CPW and the tensile test is evident. Additionally, a distinct increase in surface roughness, marked by the formation of new structures due to the deformation and cracking of the BTSE and BTSE:Zn thin layers, can be observed. Vein-like structures newly formed on DC04 steel surfaces (Figure 4-16a, 10 µm) can be observed at various spots on the steel surface. In contrast, the aluminum surface (Figure 4-16b) appears smoother compared to the steel surface, with no apparent vein-like structures.For the BTSE:Zn-deposited steel surface, the vein-like structures are more densely packed and deformed. The aluminum surface displays holes and pores resulting from fracture after the tensile test. A detailed EDX-mapping analysis of the DC04 steel substrates, conducted after tensile shear testing, is presented in Figure 4-17, indicating a noticeable presence of transferred aluminum oxide patches.

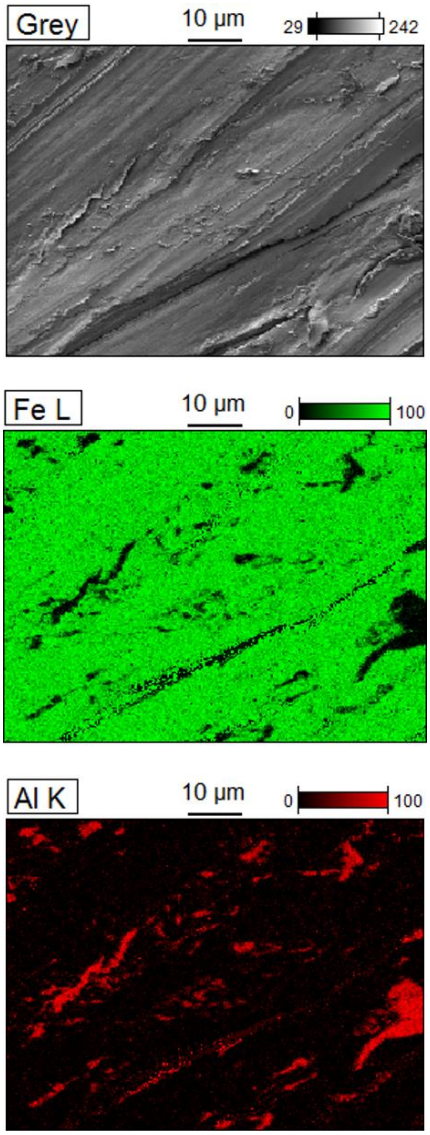

Figure 4-17: FE-SEM and EDX mapping of a DC04 surface after welding, heat treatment at 200 ºC, and tensile testing; the Al/ Fe at. % ratio for this sample is: 0.24 ± 0.08.

This bears resemblance to the characteristic topographical features produced after pickling, as depicted in Figures 4-17 and 4-18. The latter features were found to be considerably less prominent on the untreated specimens, as seen in Figure 4-17. This underscores the effective bonding support provided by the electrografted BTSE film.

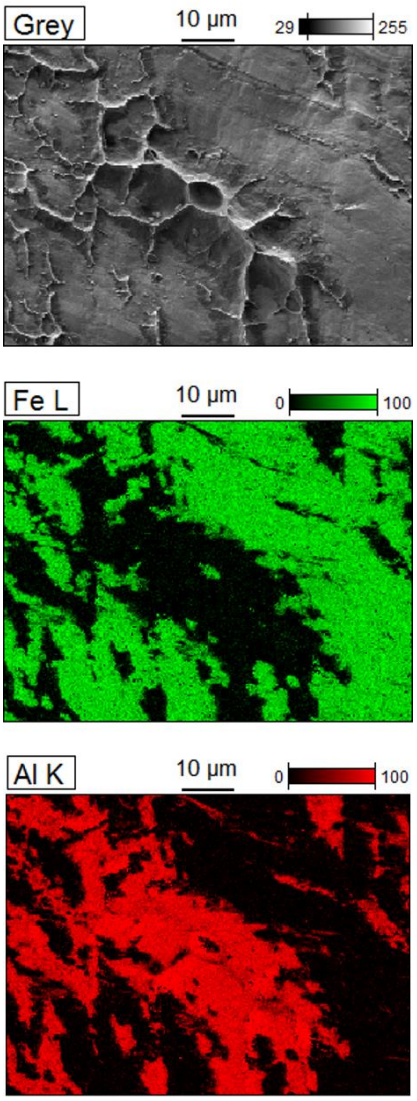

Figure 4-18: FE-SEM and EDX mapping of a DC04 surface previously modified with BTSE (for 5s) after welding; heat treatment at 200 ºC, and tensile testing; the transfer of broad patches of aluminum oxide to the steel surface is shown; the Al/ Fe at. % ratio for this sample is: 0.98 ± 0.27.

The noticeable presence of transferred aluminum oxide patches on the surface of DC04 steel samples after could be explained with the consideration that the stress concentration at pickled aluminum side causes cracking of the oxide layer during the CPW. Since aluminum oxide layer is more brittle than the thin steel oxide layer covered with BTSE based thin films it undergoes more cracking during CPW and allows aluminum in the interface to extrude through the microcracks by forming metal to metal bond.

4.1.5 Conclusions

The enhancement of interfacial bonding observed in this study can be elucidated through the following steps:

I. During CPW of DC04 steel and EN-AW1050A H111 aluminum counterparts, metal-to-metal bonds are formed by the extrusion of virgin metallic material through cracked oxide layers via plastic deformation.
II. Electrografting of a composite thin film, covalently linked to the steel surface, occurs through electrochemically assisted condensation between sol-gel silanol groups and hydroxyl groups at the metal oxide interface.
III. After curing, polycondensation of Si-O-Si groups within the films takes place.
IV. When BTSE-modified steel substrates are welded to aluminum counterparts by CPW, remaining silanol groups on the siloxane layer surface react with the hydroxyl-rich aluminum oxide surface, facilitated by thermal annealing at 200 ºC.

This results in a bifunctional BTSE-based layer covalently bound to both metal oxide surfaces, reinforcing the interfacial bonding in the joint as summarized in Figure 4-19. It depicted the plastic deformation of pristine metallic material through thin cracked oxide layers, leading to the formation of metal-to-metal bonds. Within the interstitial space between opposing metallic oxide layers, the bonding is strengthened through the presence of the bifunctional BTSE/ BTSE:Zn composite matrix, covalently tethered to both hydroxyl-rich metal oxide surfaces. It's noteworthy that the generation of intermetallic particles, such as Fe-Zn in galvanized steel at elevated temperatures, has been demonstrated to enhance the shear forces of welded joints [227,228].

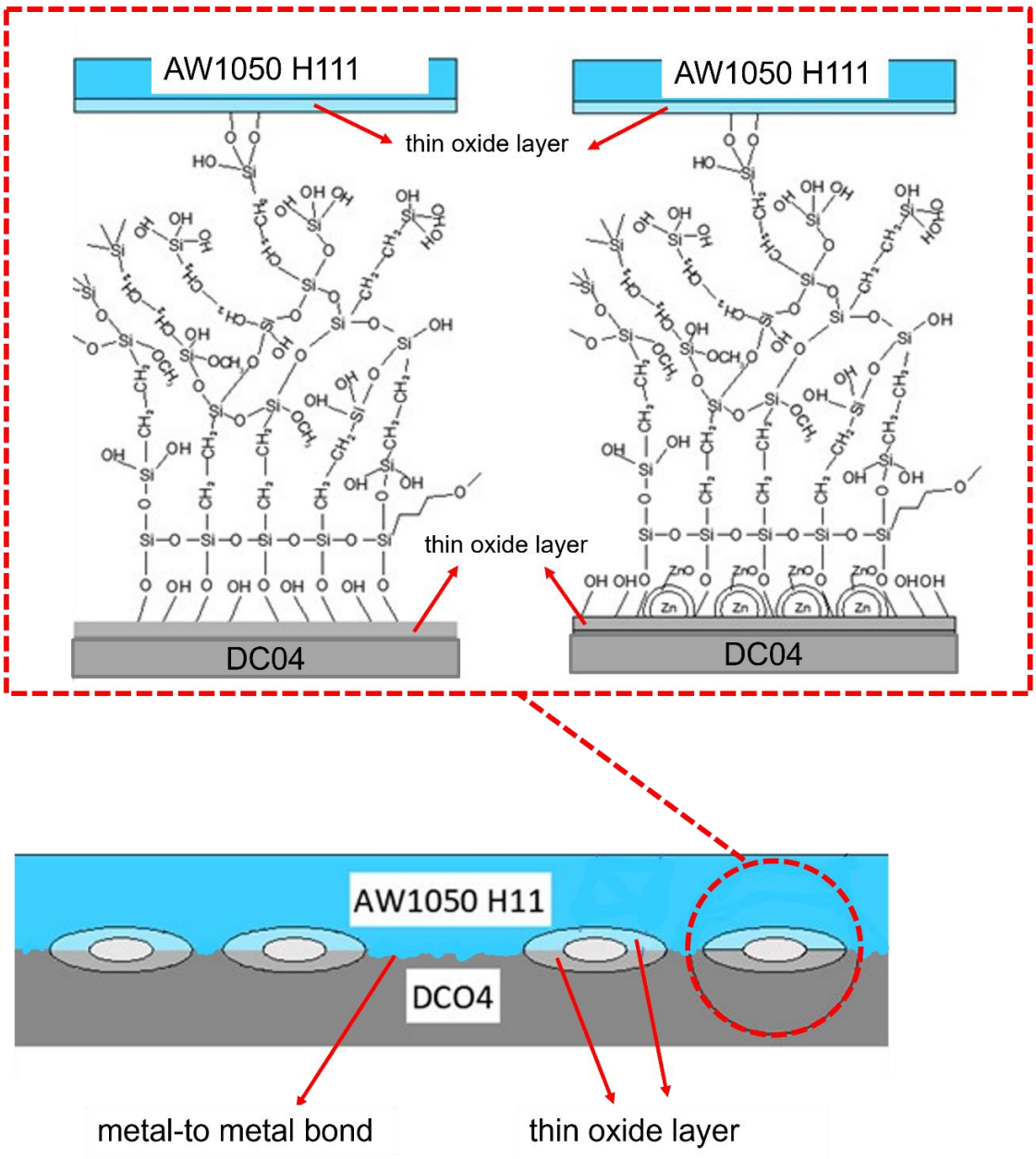

Figure 4-19: Illustration depicting the plastic deformation after CPW of steel-aluminum, with steel surface beeing modified with BTSE/ BTSE:Zn thin films. Based on [258].

The examination of FIB cross sections through FE-SEM, as illustrated in Figure S6 in SI along with the corresponding Energy Dispersive X-ray (EDX) profiles Figure 4-19, reveals the absence of intermetallic Fe-Al phases following the thermal treatment at 200 ºC.

This provides confirmation that the adhesive properties of the initially deposited BTSE-based nanocomposite thin films primarily contribute to the observed improvement in the maximum shear force values, as depicted in Figure 4-15. However, the slightly elevated results recorded for BTSE:Zn films compared to BTSE may tentatively be attributed to the potential formation of intermetallic Fe-Zn at the interface of solid oxides.

It's noteworthy to highlight that cold pressure welding relies on the extrusion of virgin metal material through cracked native oxide layers via plastic deformation, creating metallic bonds between the welded surfaces, as illustrated in Figure 4-19. Additionally, the development of ultrathin organic layers with appropriate functional groups can enhance the bonding between two metallic components. In this thesis, a BTSE-based thin film was applied to steel samples to offer support to the spaces between metal-bound areas through the covalent grafting of silanol groups present in the organic matrix, connecting to both hydroxyl-rich metal oxide surfaces.

4.2 Electrografting of poly acrylic acid (PAA)

4.2.1 Specific experimental approach

The cathodic polarization of steel samples was utilized for the electrografting and polymerization of acrylic acid (AA) in a solution with a pH of 6.

The aqueous solution included:

I. 2.0 M acrylic acid with methoxyphenone,
II. 0.2 M zinc chloride, and
III. 0.04 M N,N'-methylenebisacrylamide (bisacrylamide).

In this setup, Zn^{+2} ions acted as electroinitiators, bisacrylamide served as a cross-linker, and methoxyphenone played the role of an inhibitor. The presence or formation of AA-Zn^{+2} complexes in the solution played a crucial role in the polymerization reaction [31, 33].

Figure 4-20 illustrates cyclic voltammograms recorded for a DC04 sample cleaned with solvent in the operating aqueous solution.

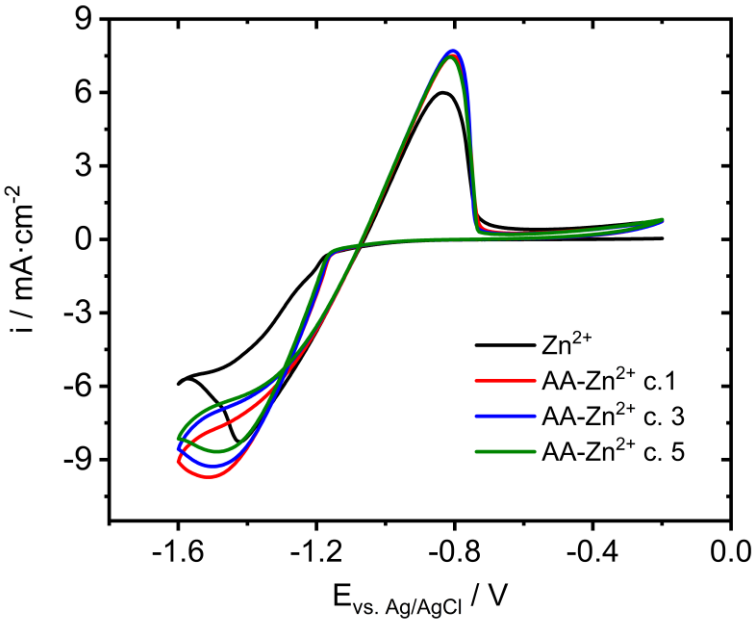

Figure 4-20: Cyclic voltammograms recorded for an untreated, solvent cleaned and brushed DC04 substrate at -0.1 and -1.6 V (vs. Ag/ AgCl) with a scan rate of 0.050 $V \cdot s^{-1}$, immersed in a deoxygenated 0.2 M $ZnCl_2$ aqueous solution at pH 6. The cycles were conducted in the absence (black line) or presence of 2.0 M AA + 0.4 M bisacrylamide: cycle 1 (red-); cycle 3 (blue-), and cycle 5 (green line). Based on [259].

The observed quasi-reversible electrochemical profile closely resembles the expected electrochemical features of Zn-based electrodes, specifically the electrochemical reduction of Zn^{2+} ions to metallic Zn at -1.45 V (vs. Ag/ AgCl) preceding the hydrogen evolution reaction (HER) and its subsequent reoxidation at more positive potentials, i.e., -0.85 V (vs. Ag/ AgCl). Notably, there are no distinct faradaic processes related to the electroreduction of AA monomers that can be readily identified in the voltammograms. For comparison, the electrochemical response recorded for a similar DC04 electrode in the same electrolyte solution, but lacking AA is included in Figure 4-20. Interestingly, when the cyclovoltammograms are obtained in the AA-containing solution, the current maximum corresponding to the reduction wave appears at slightly more cathodic potentials. This effect has been attributed by Cassasas and co-workers to the formation of AA-Zn^{2+} complexes in solution [229]. The PAA-based films on DC04 steel substrates were generated through chronoamperometry (CA). In this method, a constant DC potential of -1.4 V (vs. Ag/ AgCl) was applied to the working electrode in the working solution for various deposition times, as depicted in Figure 4-21. The selection of this cathodic potential aimed to strike a balance between achieving the very negative potentials necessary for the deposition of a dense PAA organic layer and minimizing the influence of the hydrogen evolution reaction (HER) [22, 212]. PAA-based coatings were generated on DC04 steel substrates using chronoamperometry (CA). In this method, a consistent potential of -1.4 V (vs. Ag/ AgCl) was employed on the working electrode/ DC04 sample in the working solution over various deposition times. The results are presented in Figure 4-21. The choice of this cathodic potential was a deliberate compromise, aiming to achieve the negative potentials essential for depositing a dense PAA organic layer while minimizing the influence of the hydrogen evolution reaction (HER)[22, 212].

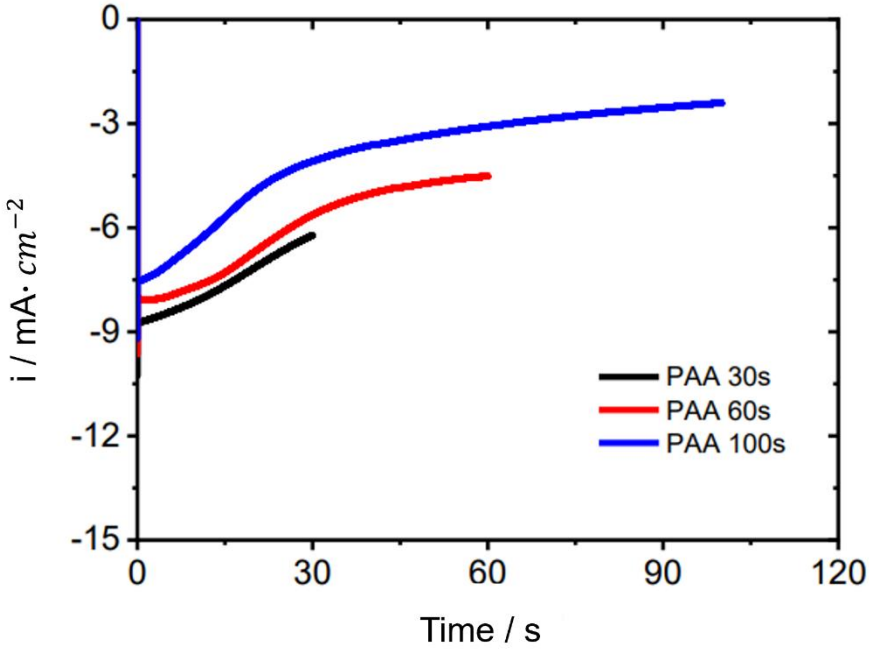

Figure 4-21: Chronoamperometric profiles recorded by applying a polarization potential of -1.4 V (vs. Ag/ AgCl) to bare, solvent cleaned and brushed DC04 substrates immersed in a deoxygenated aqueous solution containing 2.0 M AA, 0.2 M $ZnCl_2$, and 0.4 M bisacrylamide for varying deposition times: 30 s (black line); 60 s (red); and 100 s (blue). Based on [259].

The chronoamperometry curves depicted in Figure 4-21 demonstrate the expected pattern for electrochemical metal deposition. A peak of nucleation, marked by a minimum in current density for very short deposition times, signifies the formation of metallic Zn nuclei on the surface. Subsequently, a gradual decline in current follows, characteristic of a diffusion-controlled regime (Cottrell) [218, 230].

4.2.2 Surface thin film characterisation

AFM imaging, presented in Figure 4-22, was conducted on a solvent-cleaned low-alloy DC04 steel substrate under various conditions; brushing, solvent cleaning and after 100 s of cathodic polarization at -1.4 V (vs. Ag/ AgCl) in an AA-Zn^{2+} containing aqueous solution, and the latter after thorough rinsing in a 0.01 M HCl aqueous solution (refer to Figure 4-22a-c).

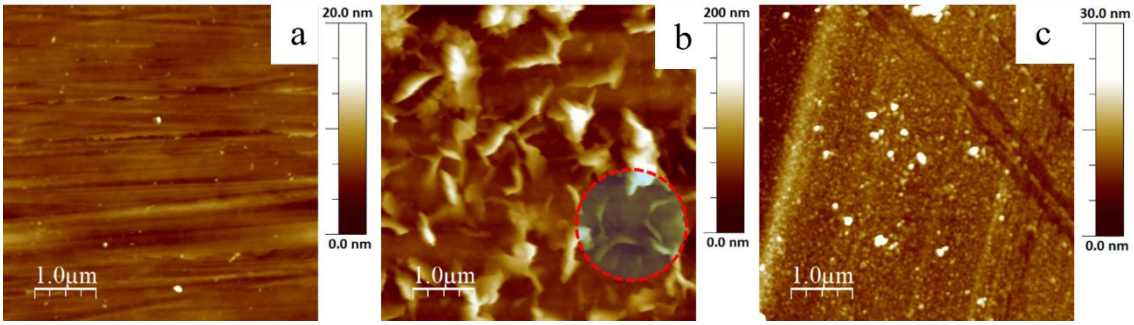

Figure 4-22: AFM images of a bare steel surface after brushing and solvent cleaning a); after 100 s of cathodic polarization at -1.4 V (vs. Ag/ AgCl) b), and the latter after thorough rinsing in 0.01 M HCl aqueous solution c). The dashed red circle highlights the presence of Zn crystalline structures surrounded by a dense PAA film. Based on [259].

As depicted in Figure 4-22a, the characteristic features of solvent-cleaned mirror-polished steel substrates, such as polishing lines, scratches, and indistinct defects and particles, are evident. After applying a potential of -1.4 V (vs. Ag/ AgCl) for 100 s in an AA-Zn^{2+} containing aqueous solution, a composite deposit consisting of PAA patches and platelet-like Zn crystalline structures is visible in Figure 4-22b. Notably, the red dashed circle suggests the formation of PAA domains surrounding the Zn particles. These observations affirm that PAA chains initiate formation primarily in the proximity of Zn(0) nuclei, underscoring the role of the AA-Zn^{2+} complex in the electrochemically induced AA polymerization process. Subsequent rinsing in dilute HCl solution selectively dissolves Zn structures, revealing a metal-free nanostructured and grain-shaped PAA film in Figure 4-22c.

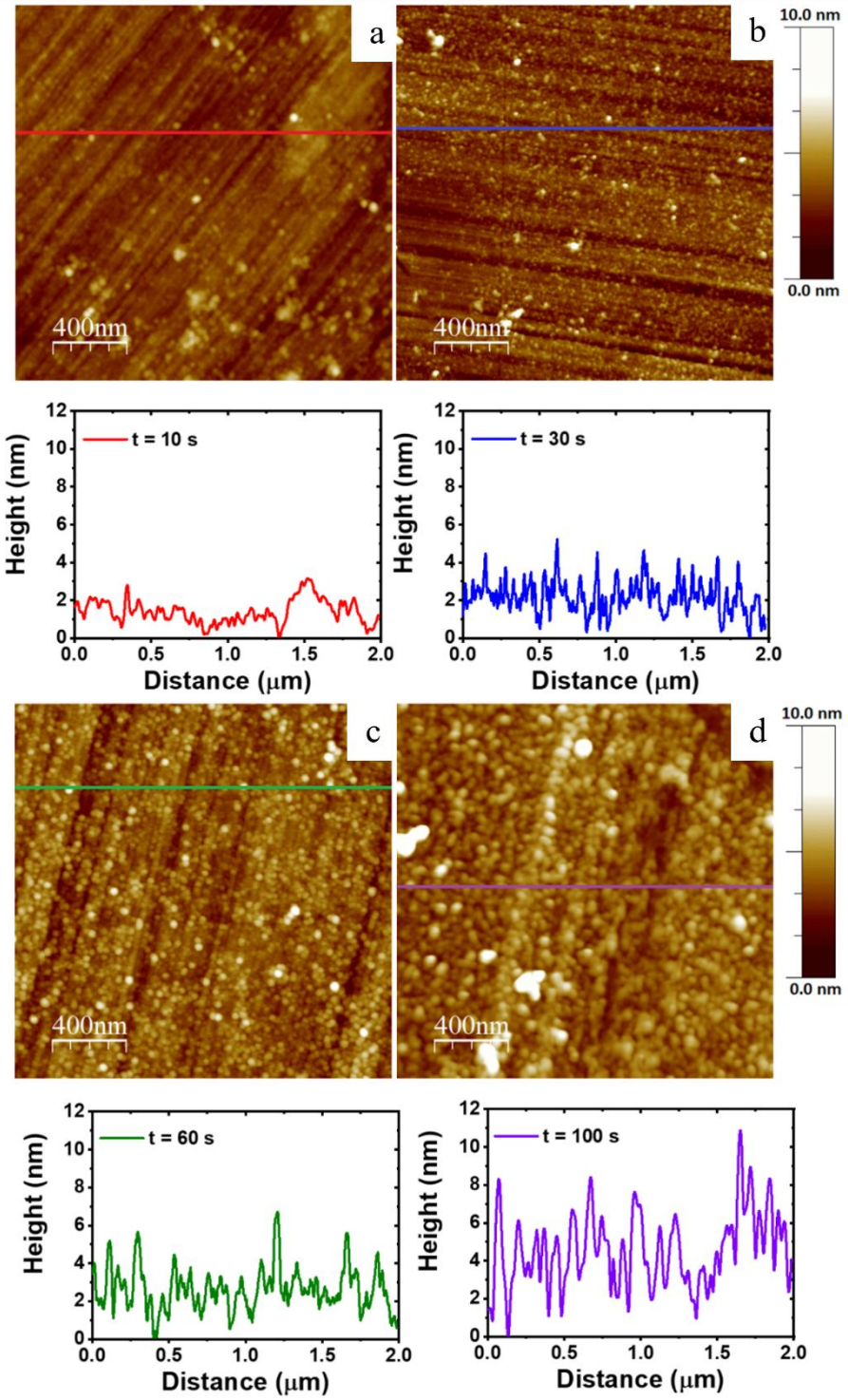

Figure 4-23: AFM images (2.0 x 2.0 µm2) of DC04 following cathodic polarization at -1.4 V (vs. Ag/ AgCl) for 10-100 s in a deoxygenated 2.0 M AA, 0.2 M Zn^{2+}, and 0.4 M bisacrylamide aqueous solution at pH 6. After thorough rinsing in 0.01 M HCl solution (upper panels), the images correspond to varying deposition times: 10 s a); 30 s b); 60 s c), and 100 s d). The lower panels display the corresponding cross-sectional profiles, illustrating the dimensions of the prepared PAA-based films. Based on [259].

AFM measurements were also conducted on various PAA films after rinsing in 0.01 M HCl, as depicted in Figure 4-23. As anticipated, cross-section profiles (lower panels in Figure 5-23) reveal an increase in particle size (10-40 nm diameter) and roughness of the PAA layer with longer deposition times. The PAA deposits, compact and granular, ranging from 2-10 nm in thickness, consist of small particles (bright PAA rounded nanoparticles) gradually covering the steel substrate. Adjusting the deposition time between 10-100 s yields variations in the PAA layer's morphology. For very short deposition times (10 s), Figure 4-24a shows minor defects, such as pinholes, allowing the estimation of the layer's thickness to be around 2 nm based on cross-section profiles. Similarly, scratches observed in areas of films prepared for longer deposition times (e.g., 100 s), as illustrated in Figure 4-24b, were used to quantify the layer thickness, falling in the range of 8-10 nm.

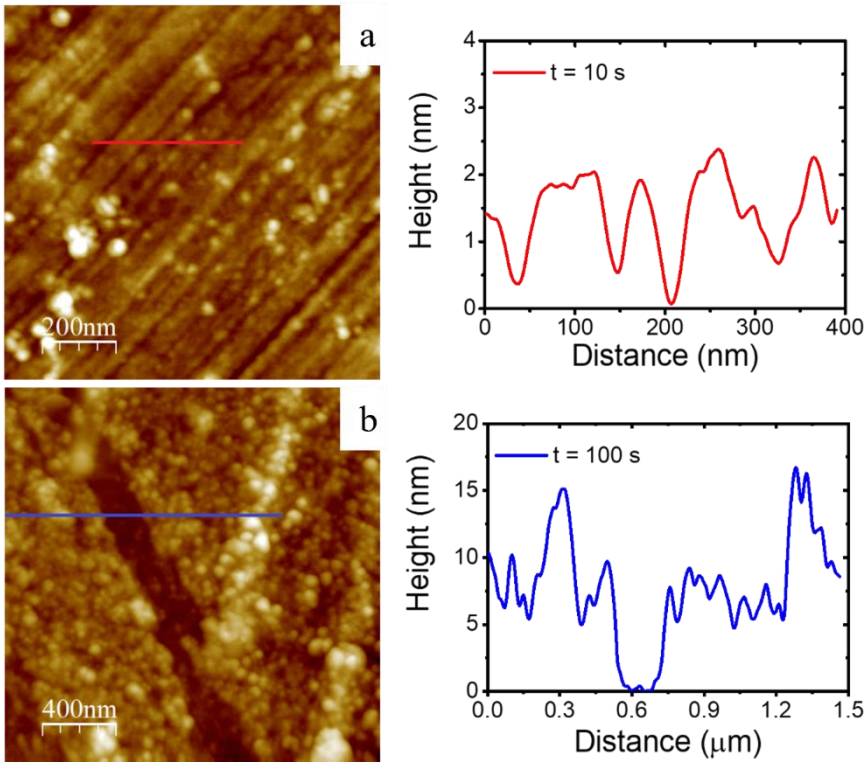

Figure 4-24: AFM images of a brushed and solvent cleaned DC04 after cathodic polarization at -1.4 V (vs. Ag/AgCl) in a deoxygenated 2.0 M AA, 0.2 M Zn^{+2}, and 0.4 M bisacrylamide aqueous solution at pH 6 for 10 s a), and 100 s b). The images on the left panel depict the samples after thorough rinsing in 0.01 M HCl aqueous solution, while the right panel shows cross-section profiles illustrating the dimensions of the resulting PAA-based films. Based on [259].

Figure 4-25 presents the PM-IRRA spectra acquired for PAA thin films prepared by chronoamperometry for 30s and 100s. The spectra demonstrated the characteristic spectroscopic features associated with PAA [22, 212, 231,232].

The broad band within the range of 3600 to 3000 cm^{-1} is linked to the stretching modes of hydroxide and amine (from bisacrylamide). The peaks in the 3000-2800 cm^{-1} range are attributed to the stretching mode of C-H in the hydrocarbon backbone.

The peak observed at 1720 cm^{-1} corresponds to the carbonyl group from free COOH moieties. Notably, a shift of this peak to lower wavenumbers (approximately 1700-1705 cm^{-1}) has been associated with adsorption through hydrogen bonds to metal oxide surfaces [28], a discussion on which will follow later. The broad band within the range of 1700-1500 cm^{-1} includes a predominant contribution centred at 1590 cm^{-1}, mainly attributed to the asymmetric stretching vibration of carboxylate groups coordinated to zinc ions, specifically AA-Zn^{2+} complexes [233]. The contributions in the range of 1640-1610 cm^{-1} can be attributed to the bending mode of water, along with the asymmetric carboxylate stretching. The peak at 1540 cm^{-1} is ascribed to the symmetric stretch of carboxylate groups [234]. Peaks at 1455 and 1420 cm^{-1} are linked to the bending mode of C-H in CH_2 groups present in the polymer chain, while the band at 1250 cm^{-1} corresponds to the stretch of C-O bonds [231]. The disappearance, after rinsing in dilute HCl aqueous solution, of the vibration bands at 1070 and 1360 cm^{-1} present in the black spectrum indicates the efficient removal of metallic Zn/ZnO particles. Additionally, PM-IRRAS spectra collected for PAA films after Zn removal for 30 and 100 s suggest that AA-Zn^{2+} complexes remain in the PAA organic matrix. It is noteworthy to mention that the ability of PAA thin films to trap metallic ions from aqueous solutions has been reported in previous studies [97, 235].

Interestingly, no significant alterations in the PM-IRRAS spectra were observed after immersing the initially prepared PAA thin films in a 0.05 M NaCl aqueous solution for 1 hour, involving stirring and subsequent ultrasound treatment in water/ethanol. Consequently, the electrodeposited PAA films demonstrated notable stability and resistance to water-ethanol, suggesting the prevalence of robust bonds at the PAA/steel interface. The increase in characteristic vibration modes of PAA, such as the -OH and the -COO^-/C=O bands, with the deposition time aligns well with the results depicted by AFM (indicating growing film thickness and roughness) and is consistent with contributions reported by Bauer et al. and Meinderink et al. [22, 212].

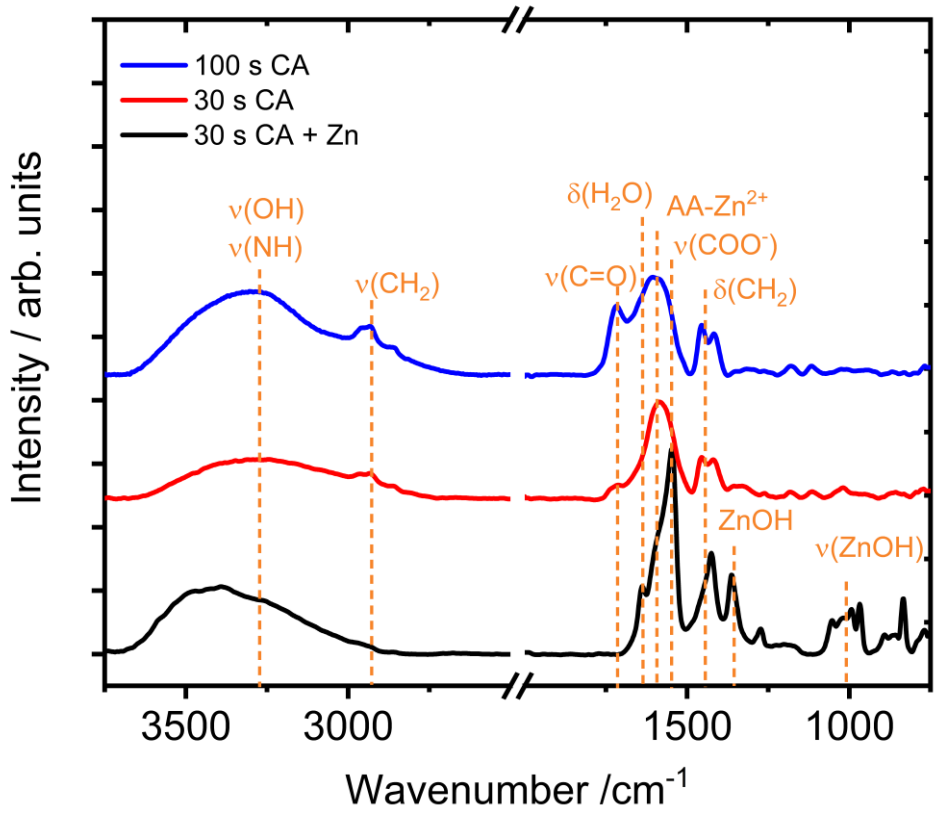

Figure 4-25: PM-IRRAS spectra obtained for PAA thin films synthesized through chronoamperometry (CA) at -1.4 V (vs. Ag/AgCl) for 30 s before (black line) and after rinsing in 0.01 M HCl for 30 s (red) and 100 s (blue). Based on [259].

To elucidate the surface chemistry of the PAA:Zn films produced through chronoamperometry (CA) or cyclic voltammetry (CV), XPS measurements were conducted. The XPS survey spectra acquired for the PAA-Zn films obtained by CA for 2 and 10 s are presented in Figure S7 in the SI. The spectrum exhibits characteristic peaks attributed to Fe, Zn, Cl, O, N, and C, aligning with the anticipated elements.

The atomic percentage of the different elements present in the PAA and in the PAA:Zn films obtained from the survey spectra presented in Figure S7 in SI are displayed in Table 4-3.

Table 4-3. Results of XPS elemental analysis in atomic percentage (at. %) for PAA and PAA-Zn films.

Sample	Element (at. %)					
	C	**O**	**N**	**Cl**	**Fe**	**Zn**
DC04	33.5	50.0	0.2	0.2	15.9	0.1
DC04 - PAA (*t = 2s*)	35.7	49.8	0.5	0.5	13.1	0.4
DC04-PAA *(t=10s)*	45.6	45.6	0.8	0.7	12.1	0.6
DC04 - BTSE:Zn (*t = 10s*)	46.4	46.4	0.7	0.7	0.1	10.7

As inferred from Table 4-3, an increase in deposition time correlates with higher levels of C and N content, accompanied by a subsequent decrease in Fe contribution. This decline suggests the development of a uniform and condensed PAA film cross-linked by bisacrylamide molecules, as previously observed in AFM and PM-IRRAS measurements. Following the rinsing of PAA:Zn samples in a 0.01 M HCl aqueous solution, metallic Zn particles dissolve. The remaining Zn content identified in the PAA films is then attributed to Zn^{2+} ions coordinatively bound to the PAA organic matrix, as supported by previous studies [22, 212, 233].

High-resolution XPS spectra for the core levels C1s, N1s, and Zn2p were recorded for a PAA film with a deposition time of 2 seconds. These spectra are illustrated in Figure 4-26 and S8 in the SI, respectively.

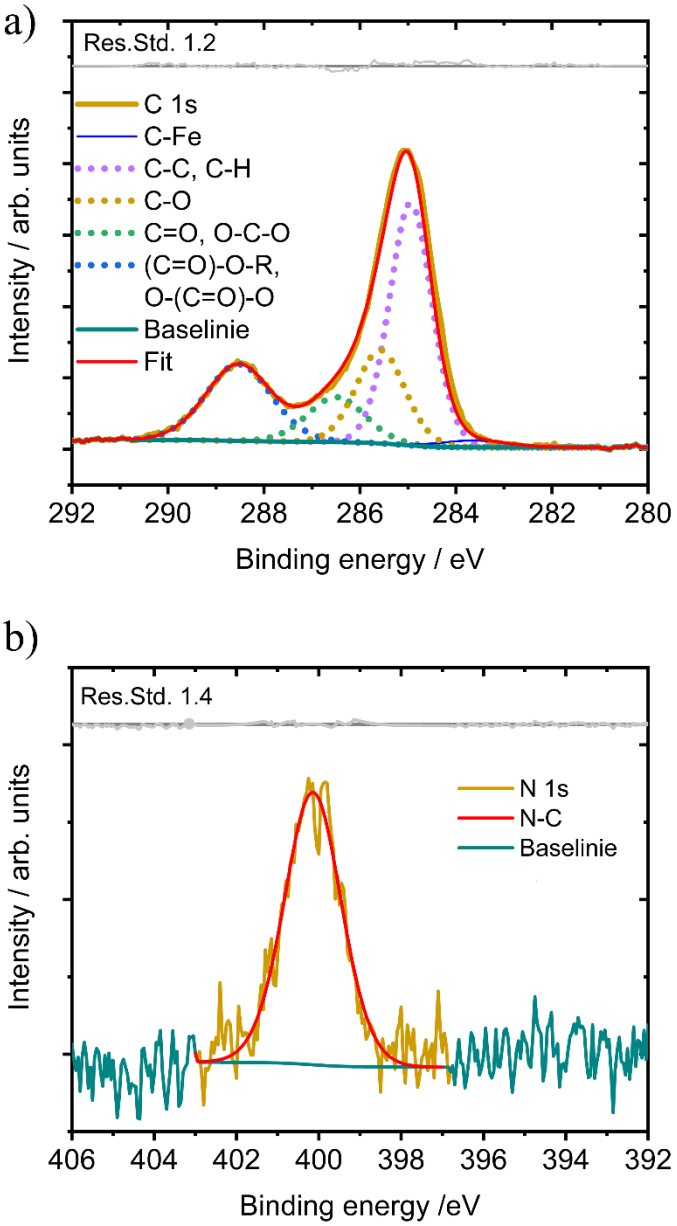

Figure 4-26: High resolution elemental spectra of C1s a) and N1s b) regions registered for an electrodeposited PAA film (*for 2 s*) onto a 120 ground DC04 substrate. Based on [259].

The C1s core level spectrum was analyzed using four distinct contributions as outlined by De Giglio et al. [30]. These components, detailed in the legend of Figure 5-26a, can be attributed to C−C/ C−H, C−C=O, C−O, COO−, and O−C=O contributions [28]. These findings align with the formation of a thin PAA layer on the steel substrate [236]. Despite its minor size, an additional contribution at 283.5 eV must be considered to adequately fit the C1s spectrum.

This has commonly been associated with metal carbide bonds, a component previously identified by Palacin and colleagues in the C1s core level spectrum resulting from the electrografting of acrylates on nickel surfaces [27]. In this instance, the nickel electrodes underwent electrochemical treatment to diminish the native oxide layer before the electrografting procedure. Pinson and colleagues also noted the presence of this 283.5 eV contribution during the electrografting of aryl diazonium salts on freshly polished iron surfaces [237]. The authors suggested that the formation of Fe-C bonds represented the most probable grafting mode for the as-deposited (poly)phenylene layer. It is important to highlight that the combination of grinding to 120 grit and the highly negative potentials (i.e., -1.4 V vs. Ag/AgCl) required for the electrografting process leads to the removal and reduction of the native iron oxide layer on the DC04 steel surface, respectively. These findings strongly suggest the formation of Fe-C bonds under these experimental conditions, providing evidence for the electrografting of acrylamide (AA) monomers onto the steel surface. However, it should be noted that considering the subtle contribution detected at 283.5 eV, the possibility of AA grafting onto iron oxide species, specifically Fe-O-C bonds, cannot be ruled out.

The N1s signal presented in Figure 4-26b was fitted to a single component at 400.7 eV, corresponding to amide groups within the bisacrylamide molecules utilized as a molecular cross-linker during synthesis [238]. Simultaneously, the Zn2p spectrum (Figure S4 in the SI) exhibited a peak centred at 122.7 eV. While commonly associated with Zn oxide, it could alternatively be linked to Zn-O complexes [239, 240]. The absence of notable contributions at 398.5 eV [241] and 1023.1 eV [240], however, allows the exclusion of Zn-N complexes (from bisacrylamide) formation. Furthermore, comparable profiles were observed in the C1s, N1s, and Zn2p regions for PAA films prepared via CA for 10 s (see Figure S9 in the SI), except for the absence of the component attributed to iron carbide. This absence is anticipated as an extensive PAA polymer would conceal the underlying polymer-metal interface. Furthermore, high-resolution XPS spectra were conducted for the PAA-Zn film with a deposition time of 10 seconds. Specifically, significant attention was devoted to the $Zn2_{p3/2}$ region, as illustrated in Figure S10a in the SI. The $Zn2p_{3/2}$ core level was meticulously fitted to three distinct contributions at 1020.2, 1022.1, and 1023.0 eV, corresponding to metallic zinc, oxidized zinc species (Zn^{2+}), and zinc hydroxides, respectively [241,242]. Additionally, the Auger Zn-LMM region (see Figure S10b in the SI) also displayed contributions indicative of metallic Zn [243].

These findings affirm the presence of nanostructured deposits based on metallic Zn, as previously revealed in the AFM image presented in Figure 4 -24b, showcasing a zinc oxyhydroxide outermost layer in the PAA films.

4.2.3 Electrochemical characterization of PAA /PAA:Zn thin films

Densely packed PAA thin films with strong covalent bonding are expected to serve as an organic barrier layer, potentially isolating the low-alloy steel substrate from the electrolyte medium. While low-alloy DC04 steel substrates are optimal for plastic deformation, they are more susceptible to corrosion reactions. Considering this, we conducted a characterization of the electrochemical properties exhibited by the freshly prepared PAA films using potentiodynamic polarization and electrochemical impedance spectroscopy [242, 243]. It is important to highlight that notable differences in electrochemical performance were observed between PAA and PAA-Zn films. Potentiodynamic polarization curves for a freshly polished bare low-alloy DC04 steel substrate, a PAA film prepared by CA with a deposition time of 10 s, and a PAA-Zn film for a desposition time of 10 s are presented in Figure 4-27.

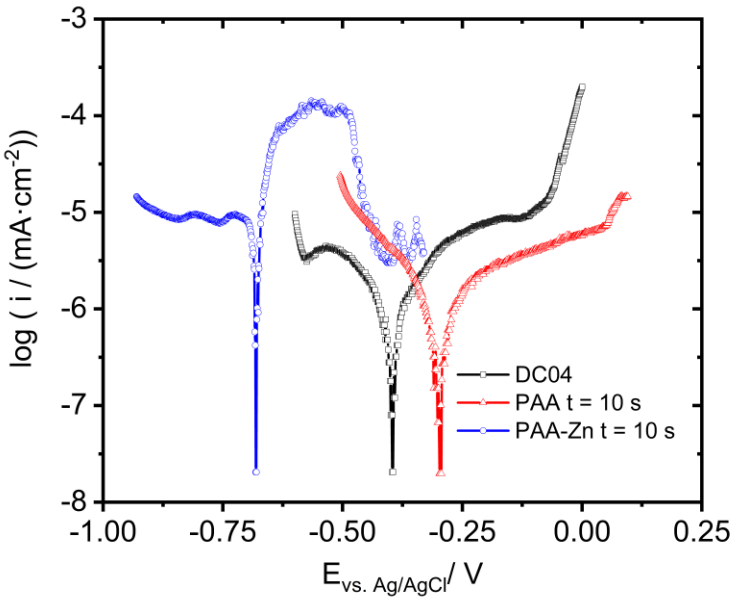

Figure 4-27: Potentiodynamic curves registered in 0.1 M borate buffer (containing 50 mM NaCl) at pH 8.3 for bare solvent cleaned DC04 substrate (black cure); with PAA for 10 s (red curve), and with PAA:Zn for 10 s (blue curve). The scan rate was 0.2 mV·s^{-1}. Based on [259].

A positive shift in the corrosion potential, E_{corr}, is evident for the PAA-modified DC04 electrode (for 10 s), as indicated by the red line in Figure 4-27, compared to the bare DC04 substrate, represented by the black line. This shift signifies protection of the DC04 surface by impeding anodic dissolution. Notably, the corrosion current density, i_{corr}, derived from the Tafel extrapolation of the anodic and cathodic branches [244], is lower than that observed for the reference material. This reduction can be attributed to the presence of a chemisorbed PAA layer, acting as a hindrance to the diffusion of electrolyte towards the electrode surface (acting as a physical barrier). Furthermore, the pit nucleation potential for the bare steel surfaces shifts towards more positive potentials in the presence of the PAA film. The corresponding values for Ecorr and icorr are summarized in Table 4-4.

Table 4-4. E_{corr} *and* i_{corr} estimated from the potentiodynamic polarization curves displayed in Figure 4-27 by extrapolation of Tafel plots.

Sample	E_{corr} **vs. Ag/AgCl / V**	i_{corr} **/ mA·cm^{-2}**
DC04	-0.40	-0.98
PAA (*t = 10 s*)	-0.29	-0.79
PAA:Zn (*t = 10 s*)	-0.68	-6.01

Remarkably, in the presence of Zn deposits alongside PAA, a shift to negative potentials in E_{corr} is observed (as depicted by the blue curve in Figure 10). This effect is attributed to cathodic protection facilitated by Zn metallic particles [245]. Consequently, higher values for i_{corr} have been observed. A limit current in the cathodic regime of PAA-Zn curves indicates a diffusion-controlled reaction, specifically driven by oxygen diffusion due to the oxygen reduction reaction (ORR) on the metal surface. Anodic polarization curves reveal the formation of a ZnO passive region, characteristic of metallic Zn electrodeposits in aerated NaCl-containing aqueous solutions within this pH range [246, 247]. FE-SEM images of PAA and PAA-Zn films prepared by CA for 10 s on freshly polished DC04 substrates are presented in Figure S11 in the SI. The (slightly) brighter spots in the former indicate a PAA thin film covering the DC04 surface, where polishing lines are still distinguishable. Meanwhile, the noticeable increase in roughness observed in the latter is attributed to the presence of Zn metallic co-deposits.

The Bode plots recorded for the passivated DC04 and the PAA film, represented by black and red lines, respectively, as shown in Figure S12 in the SI, exhibit capacitive behavior within the frequency range of 1-300 Hz. Although two-time constants are evident in the phase plots illustrated in Figure S12 in the SI, the one at lower frequencies is poorly defined. As a result, the time constant at higher medium frequencies, characterized by a relatively broad plateau, is considered for analysis. Impedance values measured at low frequencies, primarily reflecting the charge transfer resistance related to the rate of corrosion reactions at the equilibrium (passive) potential, show a slight difference between the PAA-modified surface (depicted by the red curve) and the bare DC04 steel substrate (depicted by the black curve). Notably, enhanced impedance values are observed for the 10 second PAA film. Consequently, the occurrence of corrosion reactions on the DC04 substrate is partially impeded, with the PAA film serving as a protective layer that restricts the diffusion of the corrosive solution to the steel substrate.

It is important to note that the formation of stable complexes between PAA and Fe cations [235] resulting from the anodic reaction, has been proposed by Sanei et al. as the probable reason for hindering the anodic dissolution of the iron underneath [239].

For the PAA-Zn film, a single time constant is identified in a narrower frequency range, indicative of a characteristic corrosion process controlled by charge transfer [243]. The region attributed to the resistances to charge transfer and the uncompensated electrolyte appears at higher frequencies than for the bare substrate and the one modified with only PAA. This is attributed to the electron transfer reaction of metallic Zn deposits well-connected to the buried steel surface, confirming the behavior of the PAA-Zn film as a sacrificial anode [246].

Conversely, in the case of PAA thin films applied to DC04 steel substrates, the formation of dense and tightly packed films is essential to serve as an effective polymeric layer that promotes adhesion. Therefore, our investigation focused on assessing the charge transfer capabilities exhibited by PAA films deposited onto DC04 steel substrates, serving as an indirect method to examine their surface coverage.

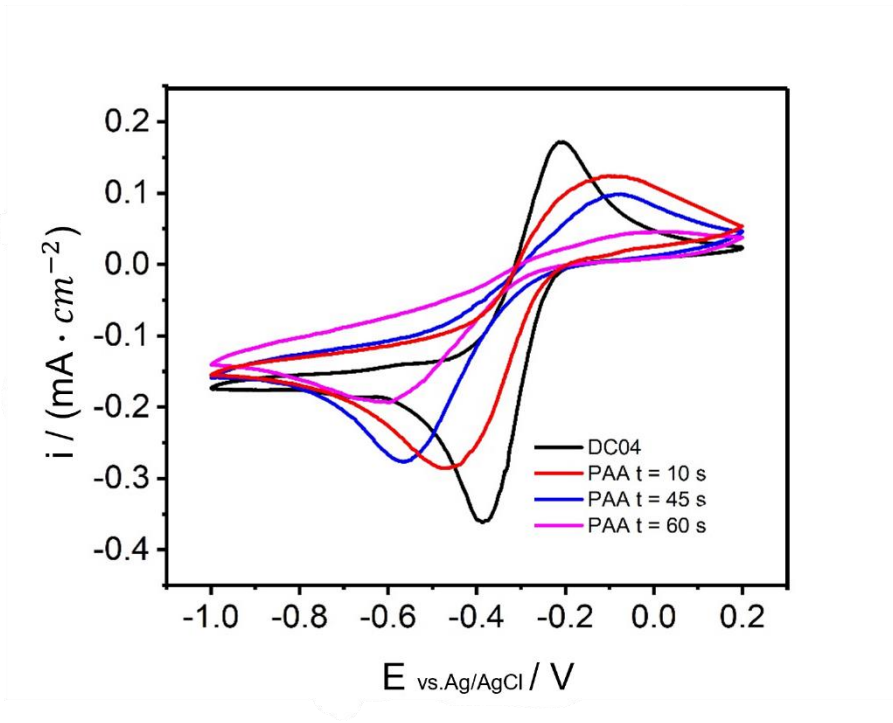

Figure 4-28: Cyclic voltammograms registered for a brushed and solvent cleaned DC04 steel substrate (black line) modified with PAA films by CA for 10 s (red); 45 s (blue), and 60 s (magenta) in a deoxygenated 2 mM 2,4,6-triphenylthiopyrylium redox probe in 0.1 M TTBAFB/ ACN at a scan rate of 0.2 $V \cdot s^{-1}$. Based on [259].

In pursuit of this objective, cyclic voltammograms were conducted in the presence of a redox probe, namely 2,4,6-triphenylthiopyrylium, and are presented in Figure 4-28 [246]. The DC04 steel surface, after brushing and solvent cleaning, displayed a characteristic diffusion-controlled quasi-reversible electrochemical profile (depicted by the black line) with a peak-to-peak separation (ΔEp) of 180 ± 12 mV. As anticipated, the electrochemical response observed for PAA films deposited on steel became progressively more irreversible, featuring increasing ΔEp values and decreasing current densities. This trend suggests the gradual development of a thicker and compact PAA layer, exhibiting fewer defects and pinholes, firmly bonded to the electrode. Such characteristics hinder the access of redox probe molecules to the metal surface. The series of PAA films prepared by CA, ranging from 10 s to 60 s, effectively illustrates this phenomenon, as depicted in Figure 4-30.

4.2.4 Interfacial bonding and tensile shear test

In conducting the tensile tests, specifically the measurement of shear strength for the welded specimens, we utilized a low-alloy steel, specifically DC04, chosen for its favorable mechanical properties, as previously mentioned. For these assessments, the DC04 steel samples underwent modification with PAA layers prepared by chemical activation with varying deposition times. The PAA-activated steel and EN-AW-1050A aluminum samples were subjected to welding through incremental rolling, maintaining a constant reduction ratio of 0.67. Subsequently, the shear strengths of the joints were determined using a tensile tester, as illustrated in Figure S13 in the SI. In this context, thin films of PAA with different thicknesses serve as an active layer, facilitating the bond formation between these dissimilar metal substrates. Post-heating treatments are recognized for their effectiveness in further enhancing the established bonding [20].

In this study, heating is confined to 200 ºC to prevent thermal degradation of PAA. Representative tensile test curves recorded for joint specimens prepared at various deposition times by chemical activation (CA) are displayed in Figure S7 in the SI. These results reveal a notable increase in the maximum shear force for samples modified with PAA compared to the references. It's noteworthy that only very thin PAA layers, specifically for the ones formed by electrografting for 5, 10, 15, and 30 s, yielded meaningful results, as thicker layers exhibited shear force values lower than those observed in the non-modified reference. Histograms illustrating the averaged maximum shear force are presented in Figure 4-29. Notably, the highest adhesion value was attained after electrografting for 10 s. However, for thicker PAA layers, the values gradually decreased. This observed trend might be attributed to the reduction in roughness occurring at the nanoscale as thicker PAA organic layers fill defects and valleys between polishing ridges, leading to a subsequent decrease in the occurrence of metal-to-metal bonds due to the thickness of the polymeric film.

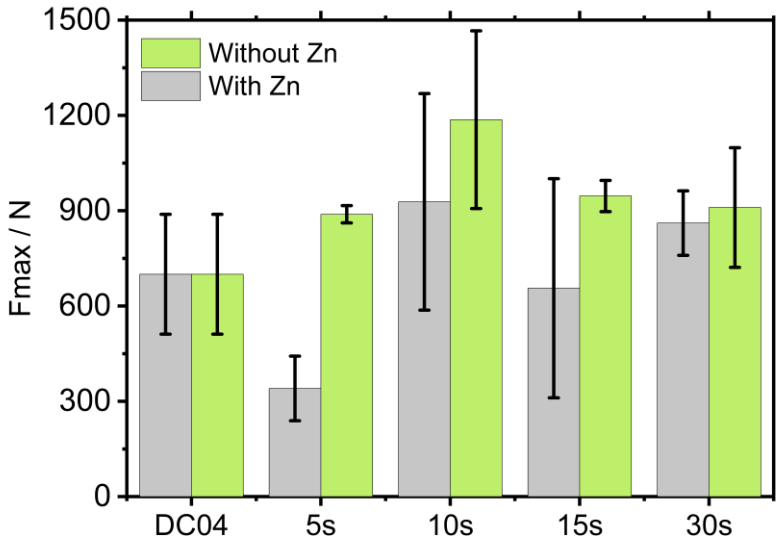

Figure 4-29: Histograms showing the averaged maximum shear force registered for the result of the CPW of pickled EN-AW-1050A and freshly polished DC04 and DC04 modified with PAA by CA for 5 s; 10 s;15 s, and 30 s with (blue bars) and without Zn particles (red). Based on [259].

Notably, higher maximum shear force values are achieved for PAA films when there are no Zn metallic deposits present in the organic layer, as evident from Figure 5-31 when comparing the blue and red bars for the same deposition time.

Crucially, when these welded specimens are subjected to heating up to 200 ºC in a N_2 atmosphere, the opposite occurs—PAA films containing Zn particles exhibit the highest maximum shear force values for the same deposition time, as illustrated in the histograms presented in Figure 4-30.

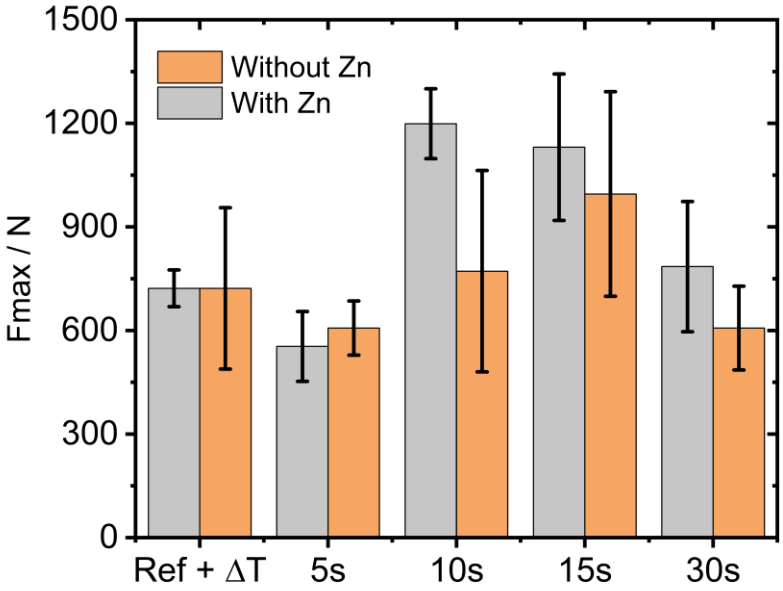

Figure 4-30. Histograms showing the maximum shear force values obtained for welded specimens from pickled EN-AW-1050A and 120 ground DC04 (reference) or DC04 substrates after modification with PAA films prepared by CA for 5;10; 15, and 30 s with (blue bars) and without Zn particles (red), after being heated up to 200 ºC in N_2 atmosphere. Based on [259].

This phenomenon can tentatively be ascribed to the high-temperature formation of intermetallic Zn-Fe phases at the bonding interface, as recently demonstrated by Hordych et al. [226].

The plastic deformation occurring at the steel/aluminum interface during cold-pressure welding (CPW) was investigated through FE-SEM imaging and EDX measurements conducted on the low-alloy DC04 steel surface after fracture during tensile testing.

The FE-SEM images presented in Figure 4-33 depict deformation of the polishing lines attributed to the stress and plastic deformation experienced at the bonding interface. Al EDX mappings, as shown in Figures 4-33c (collected for a reference bare low-alloy DC04 surface after tensile testing) and 4-33f (registered for a DC04 surface modified with PAA for 10 s) revealed the presence of transferred Al oxide patches only when DC04 surfaces were previously coated with PAA. This indicates successful support for metal-to-metal bonds due to the PAA thin film connected to both metallic oxide layers.

A significant increase in tensile strength, specifically 70% compared to the corresponding blank references, was observed for steel/aluminum substrates modified with PAA-Zn thin films prepared by chemical activation (CA) for 10 s, as shown in Figure 4-30, after thermal annealing at 200 ºC. The enhancement in bonding strength is comparable with the results obtained from the modification of steel/aluminum specimens with a layer of BTSE after post-heat treatment at 200 ºC. Notably, a significant increase in weld strengths, i.e., 65% compared to the corresponding blank references, was achieved even at room temperature by using a PAA thin film prepared by CA for 10 s, as illustrated in Figure 4-30.

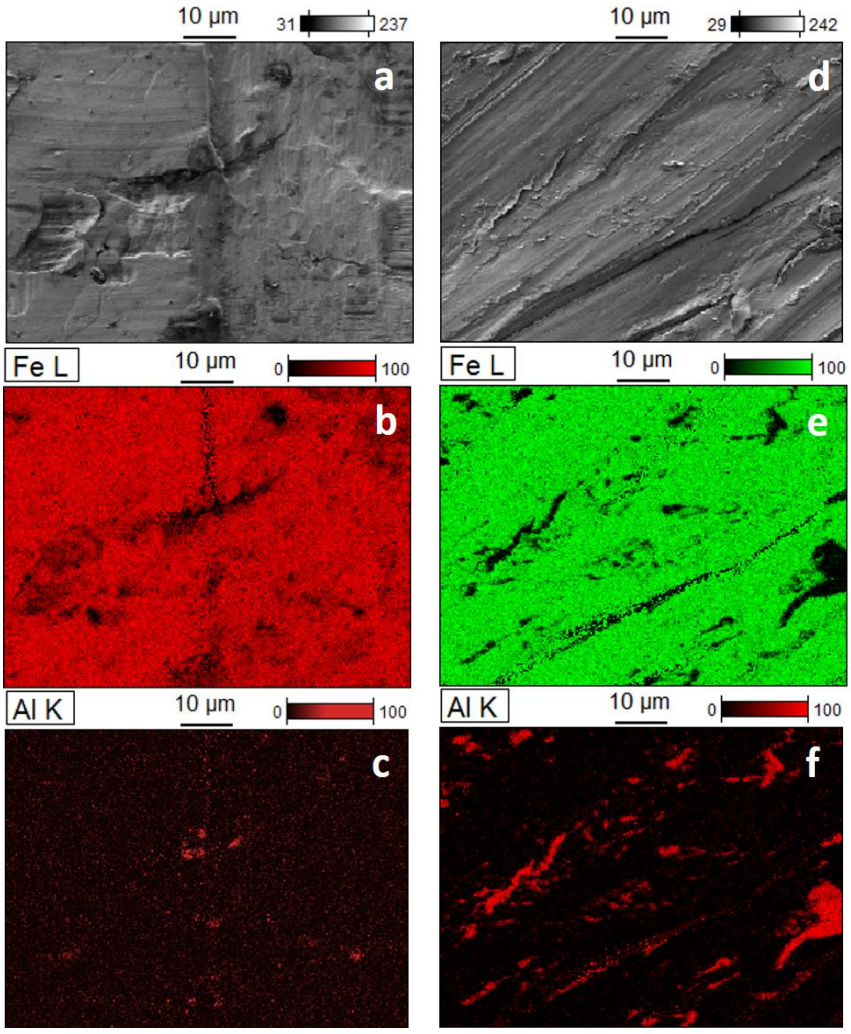

Figure 4-33: FE-SEM (a, d) and EDX mappings of a DC04 surface before (left panel) and after being modified with PAA by CA for 10 s (right) after tensile test: steel (b, e), and aluminum (c, f). Based on [259].

4.2.5 Peel-test measurements

It has also been thoroughly explored the adhesion promoting capabilities of these PAA thin films grafted, in this case, onto stainless steel 316 L versus a model epoxy amine resin used elsewhere [212]. In this case, we have prepared several strips of this resin which were cured on top of the PAA-modified steel samples. By means of peel test at 90º the adhesion promoting capabilities of these PAA layer could be quantified. Figure 4-34 shows the histograms with the averaged values of peel-off forces registered for the solvent cleaned 316L reference and the steel modified with PAA thin films prepared by CA and CV.

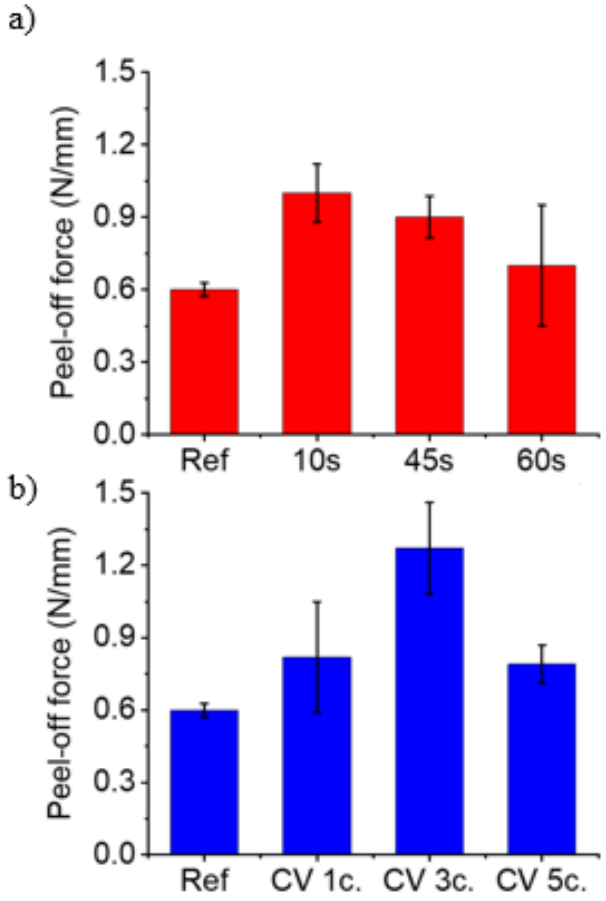

Figure 4-34: Histograms showing the averaged peel-off forces of the solvent cleaned 316L stainless steel before (reference) and after being modified with PAA thin films by CA for 10; 45, and 60 s (red bars a)), and by CV for 1, 3, and 5 cycles (blue b)). Based on [259].

These results exhibited a similar trend to that previously observed by Meinderink et al [212]. Essentially, better bonding values were registered for thin PAA films prepared by CA when compared to the thicker ones, with a maximum for 10 seconds as previously observed in the

CPW experiences. Once again, films prepared by CV, exhibited the same trend, but with a slightly better performance in terms of their enhanced interfacial adhesion.

The high peel-off forces registered for PAA modified steel surfaces are indicative of enhanced interfacial interactions between the cured epoxy-amine resin and the surface due to the presence of the grafted PAA film. In this regard, the bonding process might consequently involve strong interactions between the carboxylate groups belonging to the PAA organic layer and the epoxy-amine resin upper strips. A cross-linking process giving rise a robust entangled interfacial network taking place during the epoxy-amine curing reaction appears as the most likely binding mechanism. Additionally, epoxide and amine and groups present in the model resin used herein could get bound to carboxylate groups of PAA film according to different possible reaction mechanisms including ring opening and Schiff base formation, respectively [258].

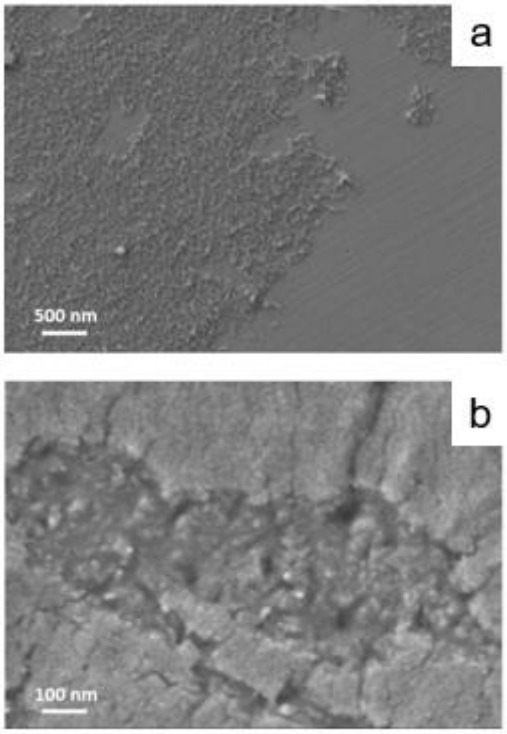

Figure 4-35: FE-SEM images of a 316 L substrate modified with PAA by CA for 10 s after test a) and the corresponding resin strip b). Based on [259].

SEM imaging of peeled bare steel 316L surfaces and the epoxy amine resin strips after peel off testing, Figure 4-35, have showed that only when steel surfaces are modified with PAA films, a significant number of patches of epoxy resin have been transferred to the latter.

This is indicative of (i) a strong interaction steel-(grafted)PAA film-resin strip, and (ii) the occurrence of a partial cohesive failure of the epoxy resin layer much more likely than for the PAA film.

4.2.6 Conclusions

Considering the results mentioned above, the electrografting mechanism of the poly acrylic acid (PAA)-based film can be outlined as follows. The deposition mechanism for PAA thin films involves an electrografting-based surface-initiated cathodic electropolymerization. This electrografting process has been extensively detailed in the comprehensive work by Pinson and colleagues [72], with Palacin et al. and Gabriel et al. specifically addressing the electrografting of acrylic moieties [27, 18]. The procedure entails applying an extremely negative potential to the surface of the electrode, leading to the generation of radical species from the acrylic monomer near the electrode. These radicals undergo immediate covalent modification by the monomers, and the reaction extends to incorporate new acrylic monomers in solution, resulting in an extended polymer covalently bound to the metallic surface.

In our specific case, a covalently bound PAA organic matrix is formed, consisting of PAA chains interconnected by bisacrylamide linking chains, and most likely, Zn-carboxylate complexes, as inferred from AFM, PM-IRRAS, and XPS measurements. Notably, in the absence of Zn^{2+} ions, no film is obtained. The electropolymerization is initiated by the reduction of AA-Zn^{2+} complexes, indicating that direct reduction of the AA monomers does not occur unless the window range potential is in proximity to the formal redox potential for the electrochemical reduction of Zn^{2+} ions. Furthermore, the as-prepared PAA coatings exhibit strong grafting to the surface, as evidenced by their resistance to removal from the steel substrate even after extended ultrasonic treatment in good solvents for the polymer. This resistance has significant implications for potential applications as a primer layer for adhesion-promoting purposes.

The mechanism underlying electrografting and subsequent polymerization is not fully comprehended at this stage, but a tentative explanation can be proposed as follows:

- Zn^{2+} ions form coordination complexes with acrylate ions in solution (AA-Zn^{2+} complexes) and are adsorbed onto the surface under cathodic polarization [22, 212, 245-247]. A double layer structure composed of these AA-Zn^{2+} complexes, similar to that

suggested by Gabriel et al., Bauer et al., and Cécius et al., can be anticipated here [18, 22, 19].

- Application of cathodic potentials to the electrode results in the reduction of these AA-Zn^{2+} complexed ions on the steel surface, activating the Zn-acrylate complex through electron transfer to the double bonds of the vinylic monomers. This generates covalently bound acrylate radicals [27, 31].
- Simultaneously, direct reduction of Zn^{2+} ions occur, leading to the accumulation of metallic Zn particles on the surface.
- The radical acrylates attached to the surface continue reacting with nearby AA monomers in solution through a vinylic-radical polymerization process.
- While it is expected that most hydrogen radicals produce hydrogen molecules, it cannot be excluded that a very small fraction may initiate radical polymerization as well [15]. Due to the extremely short lifetime of these hydrogen radicals, they would predominantly react in the vicinity of the electrode.
- In the early stages of polymerization, the concentration of inhibitors (methoxyphenone and residual O_2) at the substrate's surface is high, limiting chain growth. Once inhibitors are completely depleted at the surrounding interface, chain propagation commences, leading to an increase in the thickness of the polymer layer [22].

This grafting process involves a charge transfer process solely for the grafting step, not for the subsequent growth of the polymer (vinylic-radical polymerization reaction).

The improved interfacial bonding observed in Figures 4-36 and 4-37 is attributed to plastic deformation occurring during the cold-pressure welding (CPW) process, causing the extrusion of virgin metallic regions through the corresponding brittle metallic oxide layers forming Fe/ Al metal-to-metal bonds.

The electrochemical process facilitates the electropolymerization and grafting of acrylate (AA), resulting in the formation of PAA-Zn thin films connected to the metal/metal oxide surface of the DC04 steel. These films expose -COOH/-COO- groups at the interface. When a PAA-modified steel specimen is welded by CPW to aluminum, these groups interact with the hydroxyl-rich aluminum oxide surface [248-250].

The interaction between PAA and metal oxide surfaces has been extensively investigated by Meinderink et al., Schwiderek et al., and Nesslinger et al. [250, 255, 257].

Upon heating, there is potential for additional strengthening of established bonds, coupled with the formation of intermetallic Fe-Zn and Al-Zn phases at high temperatures [253].

This results in an active PAA-Zn composite thin film bound to both metal surfaces, significantly contributing to the interfacial bonding in the weld. The entire process is schematically summarized in Figure 4-36 and 4-37.

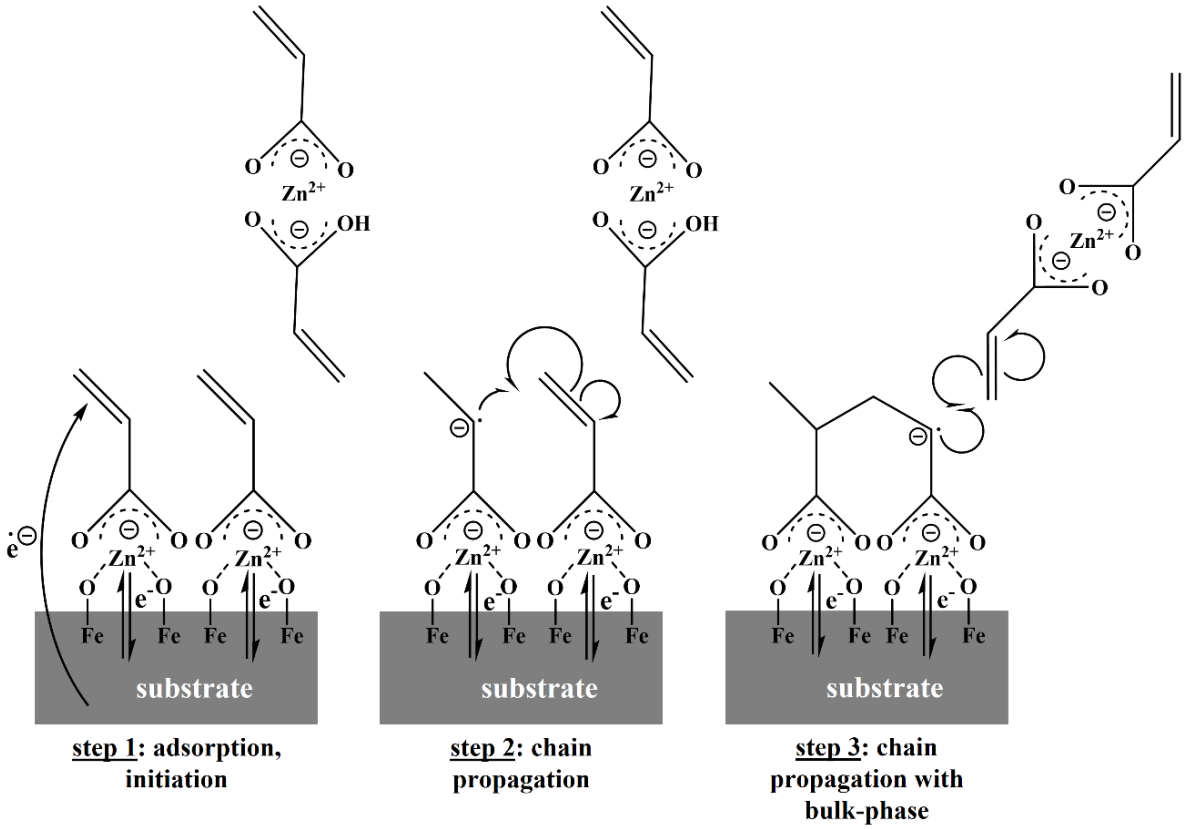

Figure 4-36: Scheme summarizing the different steps (electrochemical and purely chemical) involved in the electrografting and polymerization of AA monomers on steel substrates. Based on [259].

Analogue to the findings discussed in the initial study, the improvement in interfacial bonding can be explained as follows. During the CPW process involving DC04 and AW1050A H111, the formation of metal-to-metal bonds occurs as pristine metallic material is extruded, penetrating cracked oxide layers through plastic deformation. In cases where steel substrates are modified with PAA and joined with aluminum counterparts through CPW, the PAA layer contributes to the adhesion between steel and aluminum at the interface by interacting with the hydroxyl-rich aluminum surface as illustrated in Figure 5-37.

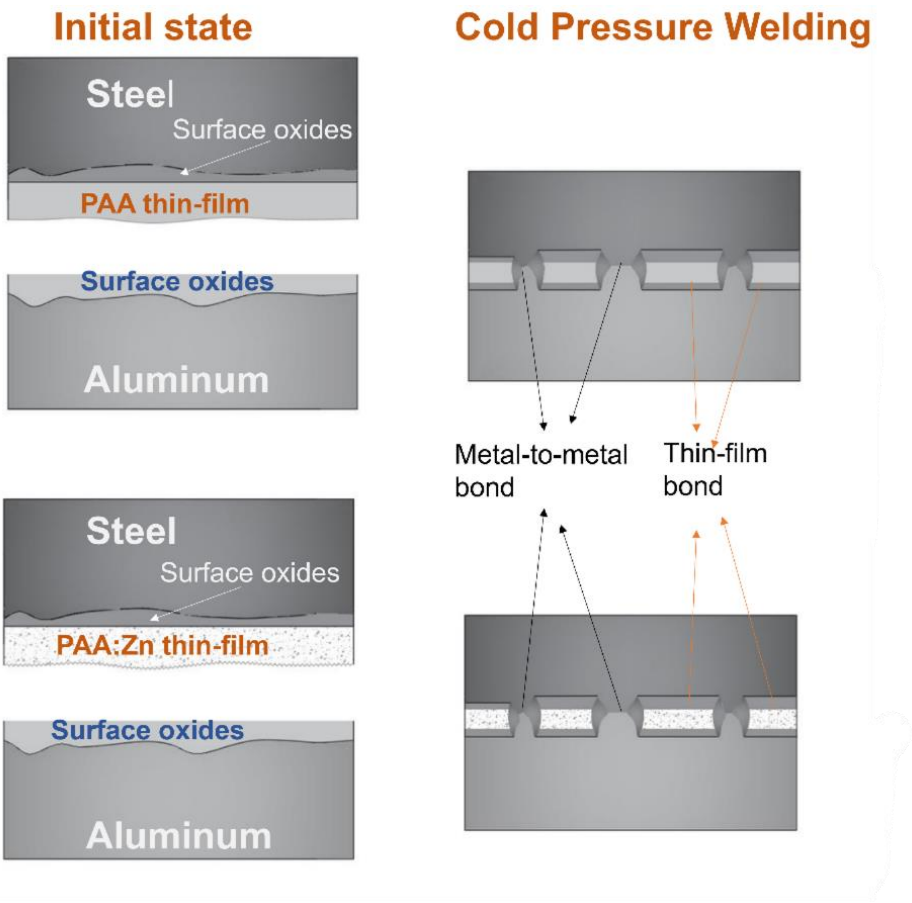

Figure 4-37: Schematic representation of the tentative mechanism proposed for the enhanced interfacial adhesion registered for the specimens obtained after welding of pickled aluminum EN-AW-1050A and DC04 surfaces modified with PAA thin films. Based on [259].

5

Overall Conclusions

In the study of electrografting of bis-1,2-(triethoxysilyl) ethane (BTSE) and BTSE: Zn films for advanced joining by plastic deformation, the impact of electrochemical conditioning and a combination of mechanical and electrochemical surface modification procedures was explored on steel specimens to enhance the binding to aluminum after cold pressure welding (CPW).

Successful surface modification was demonstrated through the electrochemical deposition of BTSE-based thin films for varying deposition times, as confirmed by various spectroscopic and electrochemical methods. XPS and PM-IRRAS spectra data exhibited consistent results, confirming the formation of BTSE-based thin layers on the steel surface.

Electrochemical Open Circuit Potential (OCP) measurements revealed a noticeable shift to more negative values when steel substrates were modified with the BTSE:Zn layer. This shift was attributed to the corrosion protection resulting from the presence of the Zn component in the BTSE:Zn composite layer.

AFM measurements on a bare 120-ground DC04 substrate displayed characteristic topographic features, showcasing a featureless, nanostructured surface. For lower deposition times of 5 s AFM images illustrated the formation of a granular BTSE-based electrodeposit with smooth grain-like polymer structures that uniformly covered the steel substrate.

Tin BTSE coatings (deposition time 5 s) on steel surfaces after welding with pickled aluminum were found to enhance binding after CPW compared to samples without BTSE coatings. Tensile tests indicated a significant increase in tensile forces, reaching a 75% improvement compared to the blank.

SEM and EDX measurements revealed the extrusion of virgin material through cracks in the oxyhydroxide layers, facilitated by plastic deformation, leading to the formation of metallic-bound areas.

Additionally, EIS results demonstrated enhanced corrosion resistance for DC04 samples modified with the organosilane layer, attributing this improvement to the barrier role played by the latter.

In the second study of electrografting of poly acrylic acid (PAA) and PAA: Zn films for advanced joining by plastic deformation, the impact of the electrochemical modification with PAA was analyzed on the weld strength of two dissimilar metals, namely low-alloy DC04 steel and EN-AW-1050A aluminum specimens, joined by plastic deformation by means of CPW. The successful electropolymerization and grafting of AA onto low-alloy DC04 steel surfaces is substantiated through a range of spectroscopic and electrochemical techniques. The surface's chemical state and the characteristics of the produced PAA thin films have been examined utilizing diverse methods such as AFM, FE-SEM, PM-IRRAS, and XPS, showing the formation of dense and tightly packed PAA films firmly attached to the steel surface, whose thicknesses are dependent on the reaction time.

The electrochemical characterization of the PAA thin films confirms the formation of non-conductive and thin, but compact, organic layers which can also incorporate nanostructured Zn particles. These PAA-based thin films consequently exhibit a moderate behavior as corrosion protection layer. This is straightforwardly related to the hindered diffusion of oxygen and the electrolyte to the metallic surface due to the presence of an adsorbed tightly packed PAA layer, i.e., an organic-inorganic hybrid composite.

The tensile shear testing assessments of steel/ aluminum joints reveal an enhancement in the bonding strength of these joints. This improvement can be attributed to the interaction between the carboxylate groups of PAA chains and the hydroxyl-rich aluminum oxide surface. The highest weld strengths were achieved by PAA films when Zn metallic deposits are not present in the organic layer. Conversely, by heating at 200 ºC in N_2 atmosphere, specimens bearing Zn particles showed increased values of shear strength.

It's important to emphasize at this point (refer to Figure 5-1) that, both studies underscore the reliance of cold pressure welding on extruding virgin metal material through cracked native oxide layers via plastic deformation.

This process results in the creation of metallic bonds between the welded surfaces. Moreover, the bonding has been further enhanced by developing ultrathin layers with appropriate functional groups, such as BTSE and PAA thin films.

These films contribute to strengthening the bonds between two metallic components by supporting the spaces between metal-bound areas through the covalent grafting of BTSE and PAA thin films present in the organic matrix. This grafting connects to both hydroxyl-rich metal oxide surfaces, potentially leading to the formation of intermetallic Fe-Zn at the interface of solid oxide within the case of BTSE:Zn and PAA:Zn coatings.

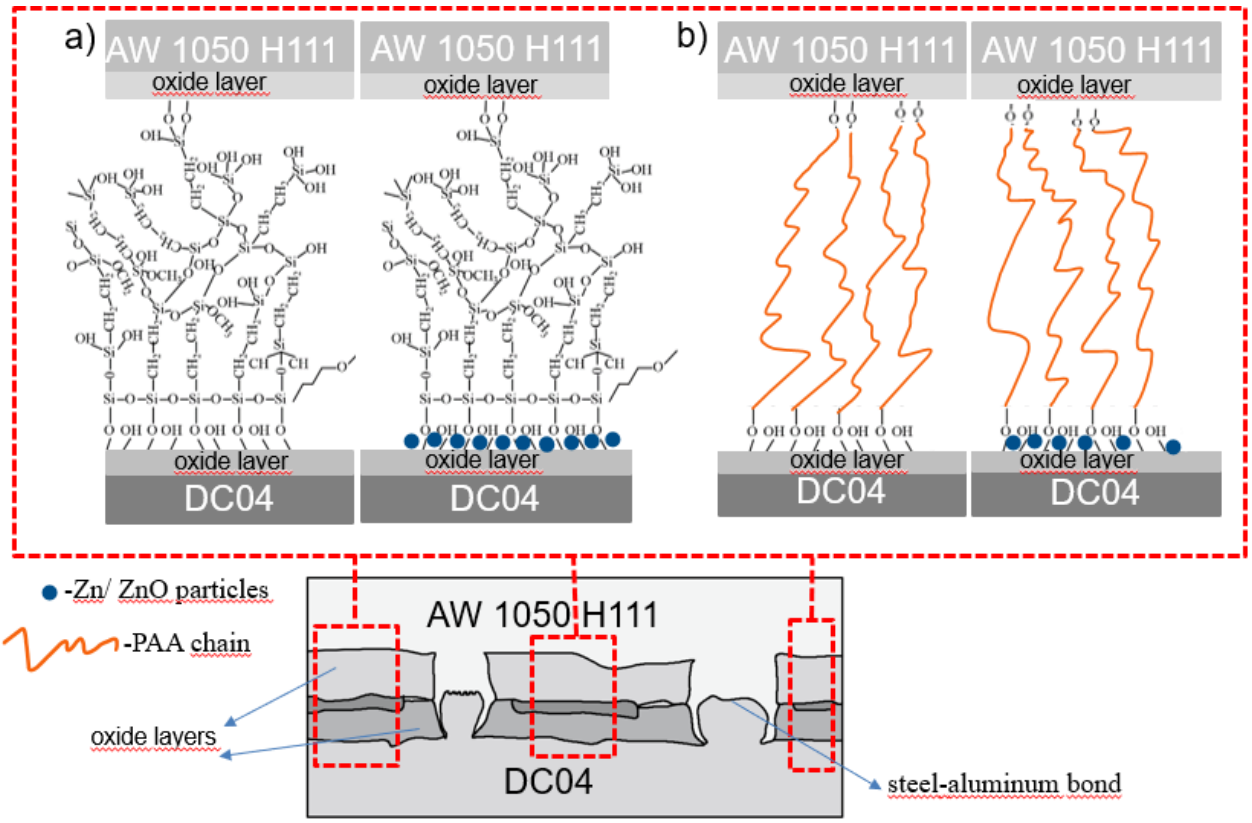

Figure 5-1. Illustration of interface deformation and bonding after CPW, with DC04 steel surface beeing modified with a) BTSE/ BTSE:Zn; and b) PAA/PAA:Zn thin films.

In conclusion, the application of electrochemical surface technologies, exemplified by the electrodeposition of thin based coatings of BTSE and PAA, not only showcased the substantial potential of activation strategies for press welding but also paves the way for integrating these strategies into various manufacturing processes, where innovation and efficiency play a pivotal role.

6

Outlook

Organosilane-based layer have been shown to exhibit effective adhesion-promoting capabilities for cold pressure welding purposes, especially for the case of low-alloy steels and aluminum substrates, based on the covalent grafting of silanol distal moieties present in the 1,2-bis (triethoxysilyl) ethane (BTSE) matrix to hydroxyl-rich metallic counterparts. In this regard, by taking advantage of the vast chemistry/ versatility of silane-based molecules which can thus incorporate different functional groups, which would stay exposed to the interface, different approaches should be further explored. Firstly, the deposition of mixtures of BTSE and 3-Aminopropyl- triethoxysilane (APTES) which would also provide the silane matrix with amine groups exposed to the interfaces, together with silanol groups. By means of a catalyzed amide condensation reaction, 6-phosphonohexanoic molecules could then be covalently attached to the previously formed silane deposits. Phosphonate groups are very well known to form very stable self-assembled monolayers on both steel and aluminum surfaces. A similar approach could also be considered based on the modification of steel samples with BTSE/ APTES ultrathin layers by electrochemical methods and the aluminum substrates with 6-phosphonohexanoic molecules by self-assembly. Thermal amide condensation should be promoted by heating at 120-200 ° C. On the other hand, over the last few years some seminal reports have addressed the modification of steel and aluminum samples by means of the electroreduction of diazonium salts. The latter has been presented as a very versatile electrochemical methodology which would account for the formation of very thin organic layers incorporating a considerably vast variety of different functional groups as potential metal adhesion promoters.

Building upon the knowledge obtained from the second study, in which DC04 underwent modification with poly acrylic acid (PAA) and PAA:Zn thin films, potentially raising sustainability concerns, there is an intriguing opportunity to explore the utilization of biopolymer coatings applied to DC04 for advanced joining processes. Specifically, polydopamine and polydopamine-iron compounds are under consideration, with the objective of evaluating the influence of bio-nanocomposite coatings on the cold pressure welding of steel and aluminum sheets through incremental forming.

7

Supporting Information

7.1 AFM characterization of BTSE and BTSE: Zn thin films

AFM imaging has been carried out in order to assess the topographic features associated with the result of the electrochemical deposition of BTSE and BTSE/ Zn layers for t = 5 s onto-EN-AW-1050 H111 aluminum surfaces. The BTSE films deposited on EN-AW-1050 H111 substrates exhibit similar morphological profiles to that previously observed for DC04 samples, namely the formation of flake-like islands which homogeneously covers the aluminum substrate, see Figure 5.8b. As previously mentioned, the occurrence of cracks and defects allows for the accurate quantification of the BTSE layer thickness. By carrying out cross section profiles through the cracks, a thickness range of 20-35 nm could be estimated. Consequently, the deposition of the BTSE film is responsible for a noticeable decrease in the average RMS roughness, namely from 22.2 to 14.6 nm. Interestingly, for the same deposition time, i.e. t = 5 s, the BTSE layers deposited onto EN-AW-1050 H111 surfaces are noticeable thicker than those obtained for DC04 samples, i.e. 5-7 nm. In this regard, Hu et al. has already reported efficient APTES and BTSE-based electrochemical deposition onto Al alloys [89].

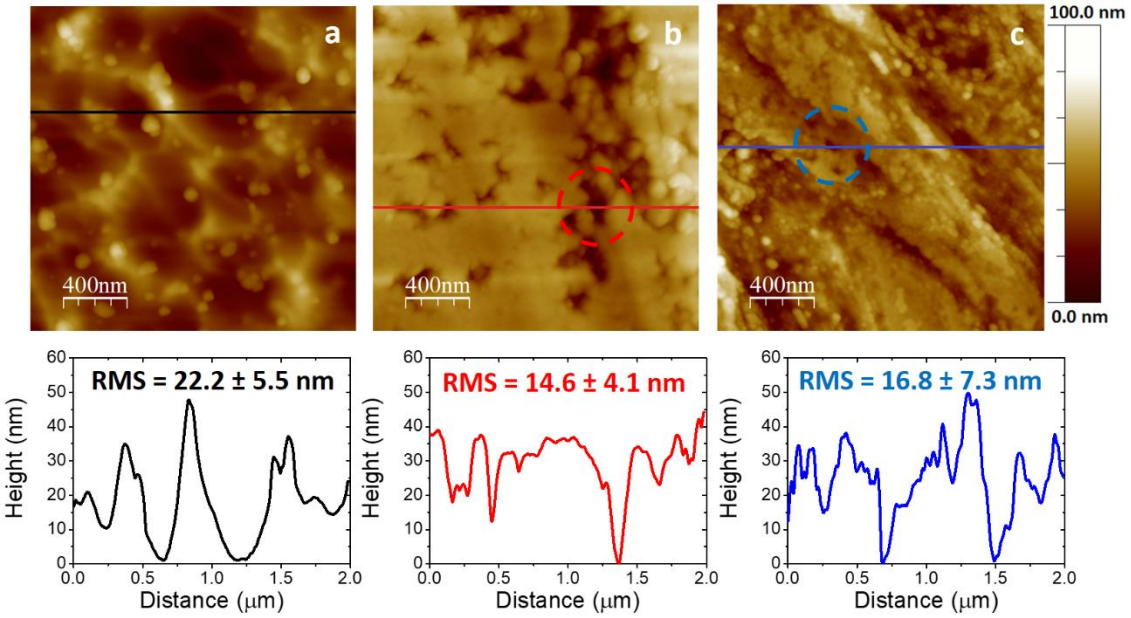

Figure S1: 2.0 x 2.0 μm^2 AFM images of EN-AW 1050 H111 samples with different surface conditioning processes: pickling a), modification with BTSE for 5 s b) and modification with BTSE: Zn for 5 s c). Representative cross section profiles showing the dimensions of the corresponding BTSE deposits. Red and blue circles are showing some specific defects in the organic layer allowing to quantify the thicknesses of the corresponding organic layers.

Following the deposition of the BTSE:Zn layer, an increased roughness is evident, featuring some rounded particles that are 5-10 nm high and 30-60 nm wide, randomly dispersed across the surface, as illustrated in Figure S1c. The thickness of the BTSE:Zn layer, determined from the cross-section profile and highlighting the fracture with a blue circle, is expected to be comparable to that of the BTSE layer in the absence of Zn Figure S1b.

7.2 XPS Characterization of BTSE/ BTSE:Zn Films

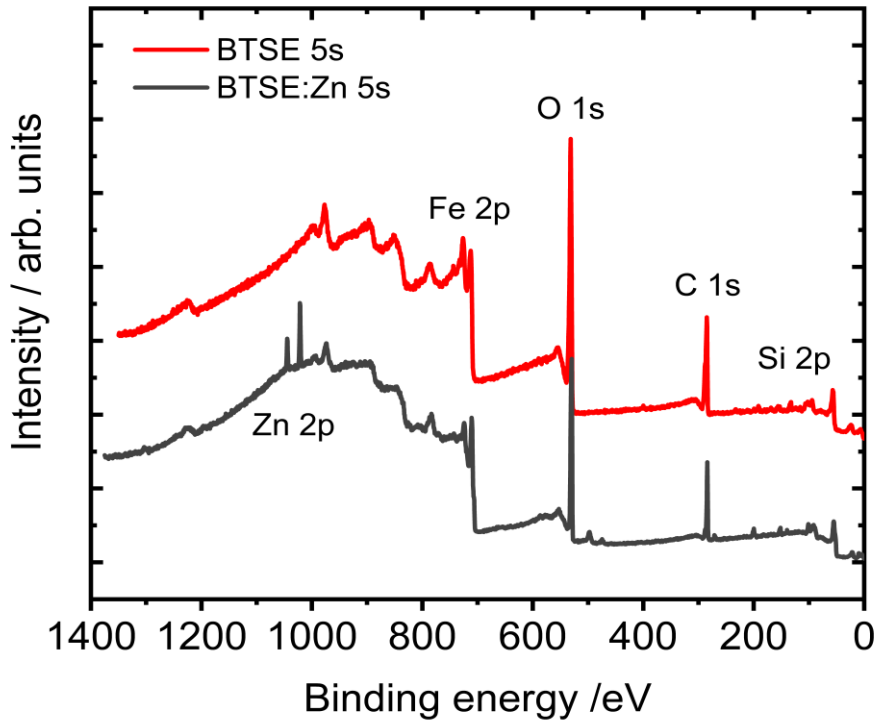

Figure S2: XP survey spectrum and the corresponding at. (%) concentrations collected for a DC04 steel sample after modification with BTSE:Zn for 60 s.

7.3 Electrochemical characterisation

As described in detail in the Results and Discussion chapter 5., Figure S3 and S4 display the Bode diagrams for the different studied films obtained by EIS. The impedance values measured for the bare substrates were lower than those of the film-coated steel substrates, suggesting an increase in the corrosion protection due to the barrier properties of the BTSE-based film. Prolongated immersion times induced an increase in the impedance modulus, accounting for the appearance of a synergy effect between the formed three dimensionally crosslinked Si-O-Si matrix firmly attached to the steel surface and the corrosion products, generating an inhibition of the electrolyte diffusion. These values were higher when ZnO nanoparticles were present in the film.

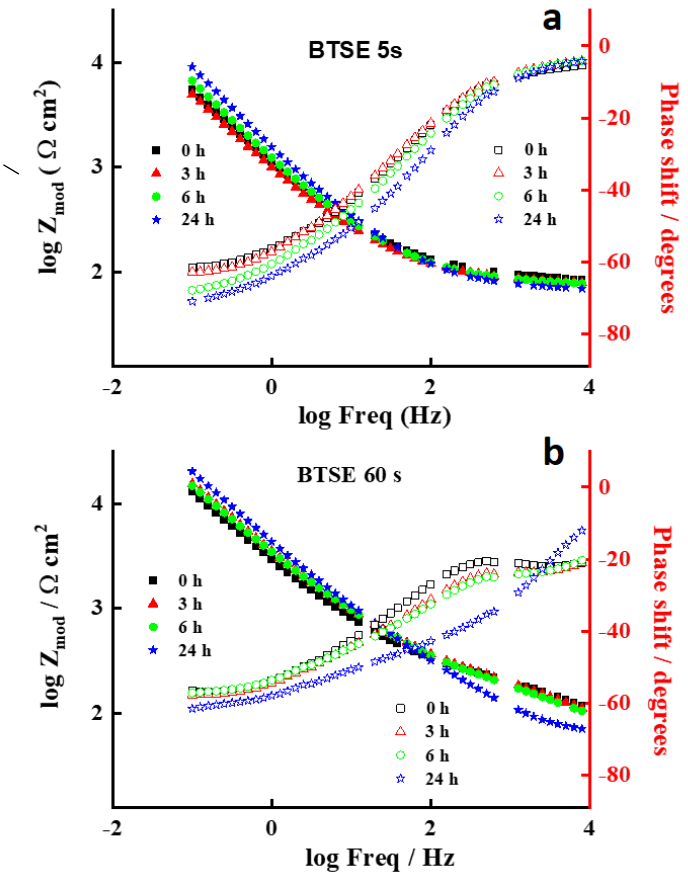

Figure S3: EIS measurements collected in aerated buffer solution (pH 8.4) at OCP for DC04 modified with BTSE films for t = 5 s a) and t = 60 s b) for different immersion times (0-24 h).

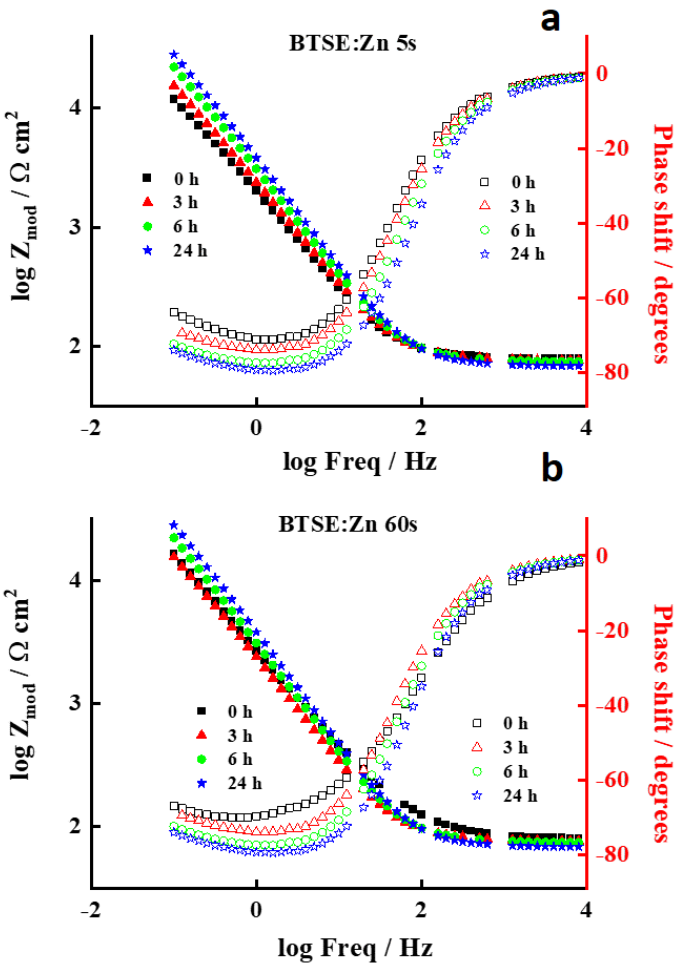

Figure S4: EIS measurements collected in aerated buffer solution (pH 8.4) at OCP for DC04 modified with BTSE:Zn films for t = 5 s (a) and t = 60 s (b) for different immersion times (0-24 h).

7.4 FIB imaging of metal-to-metal interface

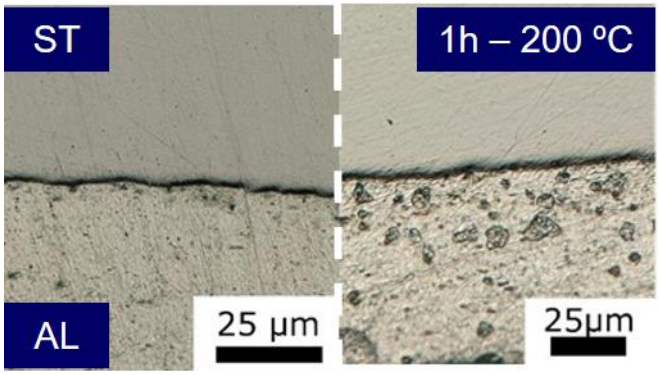

Figure S5: FE-SEM image showing the interfaces of the welded specimens before and after the heating treatment at 200 °C for 1 h in N_2 atmosphere.

7.5 Tensile test

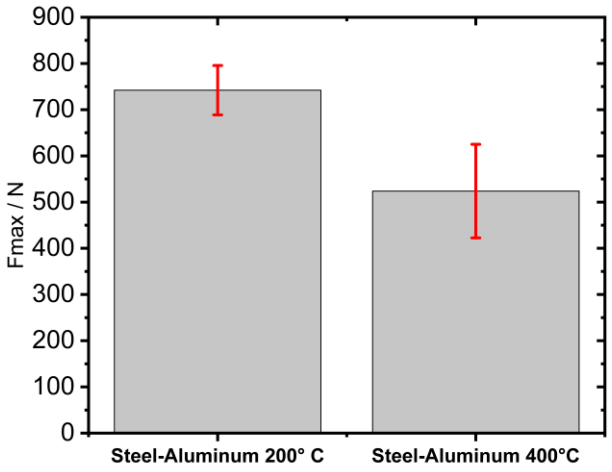

Figure S6: Histograms showing the maximum shear force values obtained for welded specimens from pickled aluminum EN AW-1050A H11 and 120 ground DC04 (reference) after being heated up to 200 °C and 400° C in N_2 atmosphere.

7.6 XPS Characterization of PAA/ PAA:Zn Films

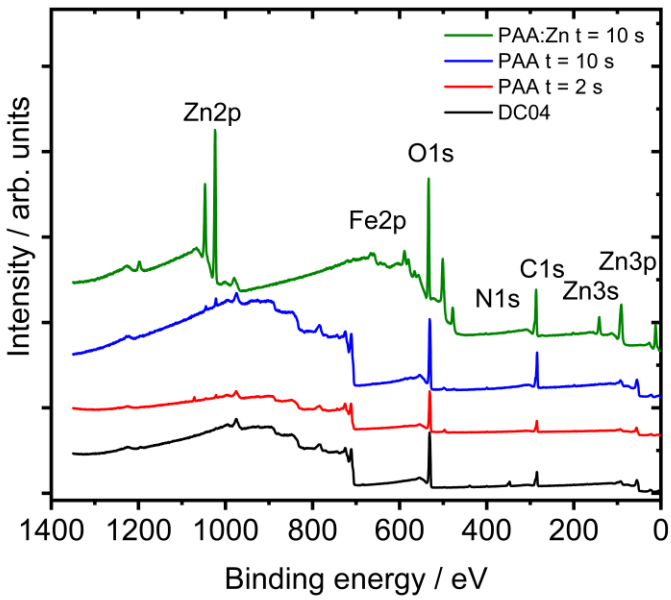

Figure S7: XPS survey spectra of 120 ground DC04 steel substrates before (black line) and after modification with PAA by CA at -1.4 V (vs. Ag/ AgCl) for 10 s before (green) and after rinsing in 0.01 M HCl aqueous solution for 2 (red); and 10 s (blue).

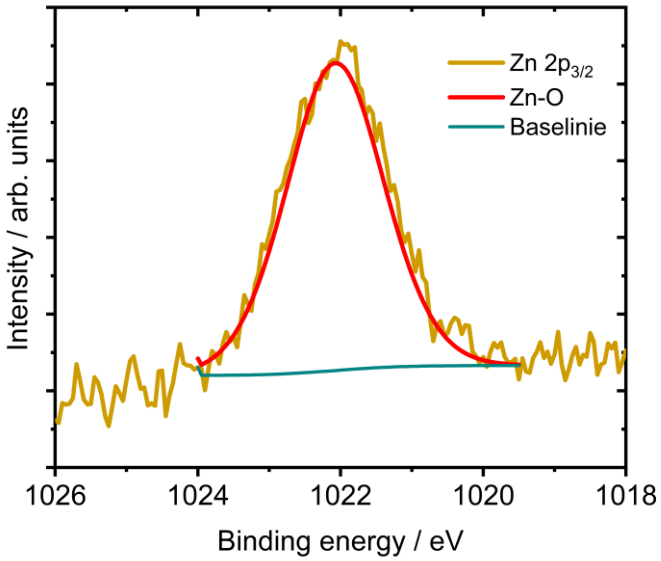

Figure S8: High resolution elemental spectra of Zn2p region registered for an electrodeposited PAA.

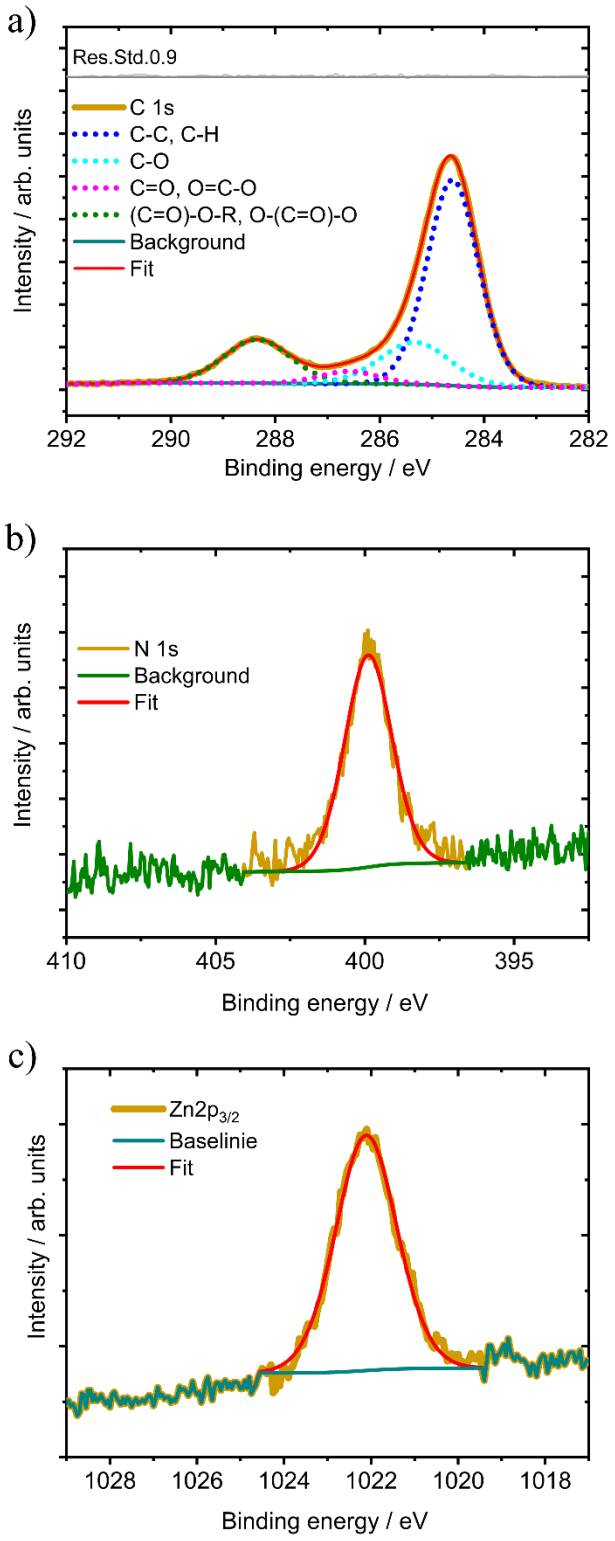

Figure S9: High resolution XP spectra of C1s a); N1s b); and Zn2p c) registered for an electrodeposited PAA film for 10 s onto a ground DC04 substrate.

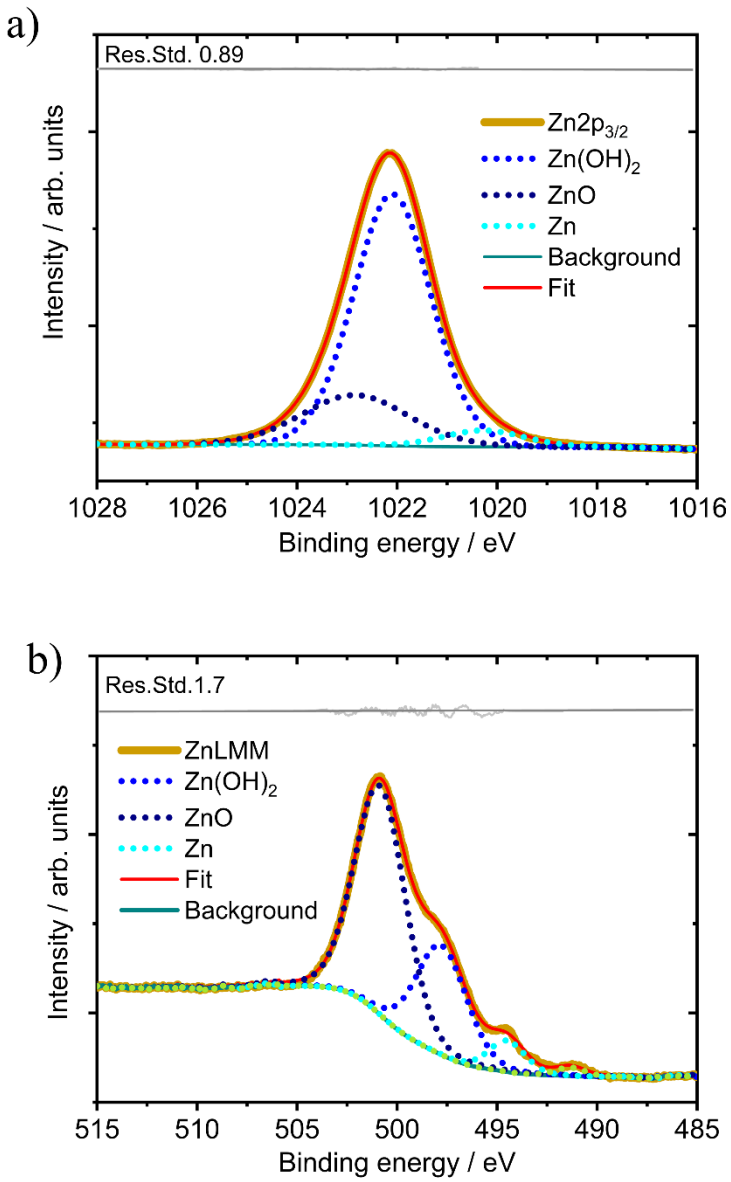

Figure S10: Zn2p high-resolution XPS a) and Zn LMM spectra b) registered for an electrodeposited PAA film (t = 10 s) onto a ground DC04 substrate.

7.7 FE-SEM images of PAA and PAA-Zn films prepared by CA for t = 10 s on low-alloy DC04 steel substrates

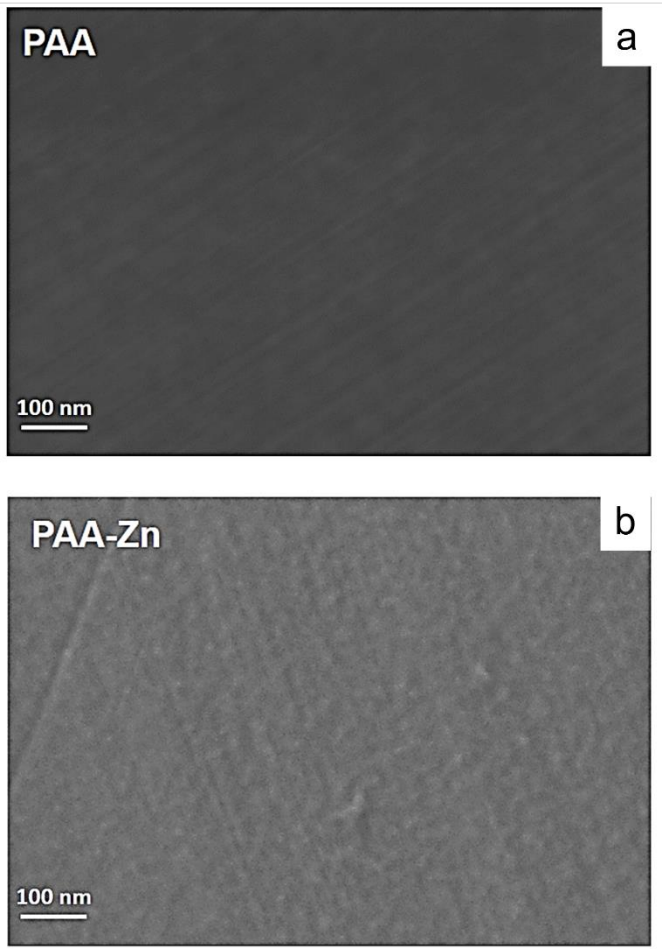

Figure S11: FE-SEM images of freshly polished (120 ground) DC04 steel substrates modified by CA for 10 s before a); and after gentle rinsing in 0.01 M HCl b), i.e., PAA (10 s) a) and PAA:Zn (10 s) b), respectively.

7.8 EIS of Low-alloy DC04 steel substrates modified by PAA and PAA-Zn films prepared by CA for 10 seconds

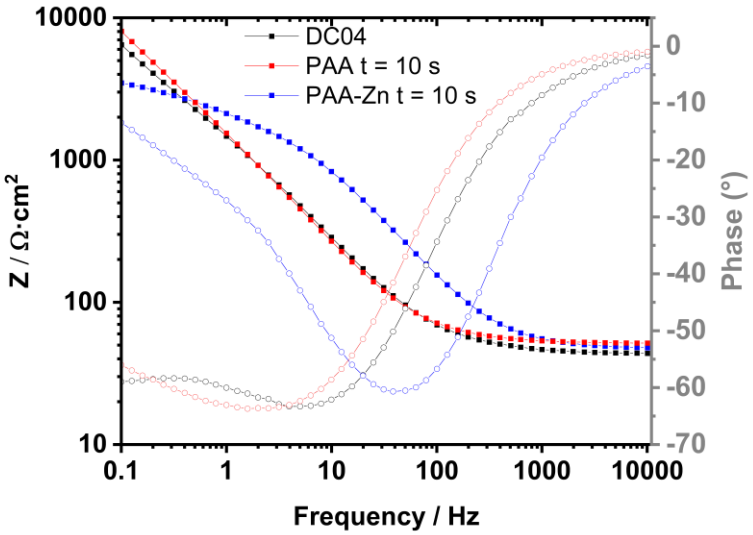

Figure S12: EIS collected for freshly polished DC04 steel substrates (black line) modified by CA for 10 s before (red) and after gentle rinsing in 0.01 M HCl (blue), i.e., PAA 10 s (red) and PAA-Zn 10 s (blue), respectively, in an aerated 50 mM NaCl containing 0.1 M borate buffer aqueous solution.

7.9 Shear force curves registered for the steel references and PAA films

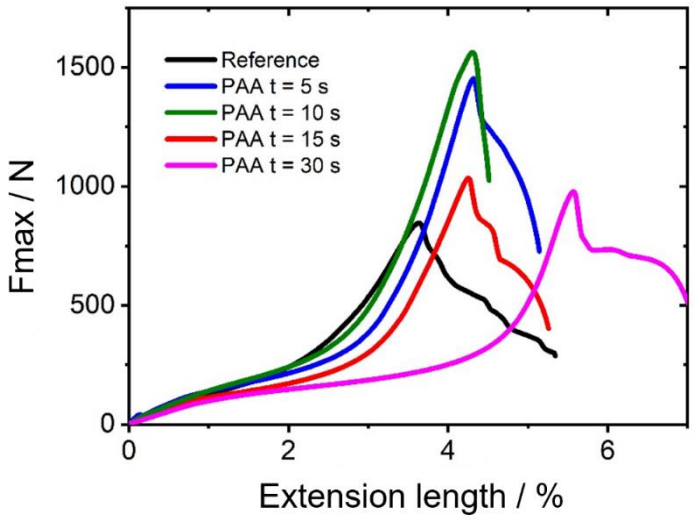

Figure S13: Representative shear force vs. strain curves registered for welded samples from pickled AW EN 1050 and ground DC04 (black line) specimens and DC04 after modification with PAA films prepared by CA for 5 (blue); 10 (green);15 (red), and 30 s (magenta).

8

List of references

[1] R. Grothe, S. Knust, D. Meinderink, M. Voigt, A.G. Orive, G. Grundmeier, Spray pyrolysis of thin adhesion-promoting ZnO films on ZnMgAl coated steel. Surface and Coatings Technology 2020; 394;125869.
[2] S. Knust, A. Kuhlmann, A.G. Orive, T. de los Arcos, G. Grundmeier, Influence of dielectric barrier plasma treatment of ZnMgAl alloy-coated steel on the adsorption of organophosphonic acid monolayers. Surface and Interface Analysis 2020;52:1077-1082.
[3] H. C. Barshilia, A. Ananth, J. Khan and G. Srinivas, Ar + H-2 plasma etching for improved adhesion of PVD coatings on steel substrates. Vacuum, 2012;86:1165-1173.
[4] O. Ozcan, K. Pohl, B. Ozkaya, G. Grundmeier, Molecular Studies of Adhesion and De- Adhesion on ZnO Nanorod Film-Covered Metals. The Journal of Adhesion 2013; 89:128-139.
[5] R. Toledano, D. Mandler, Electrochemical Codeposition of Thin Gold Nanoparticles/Sol−Gel Nanocomposite Films. Chemistry of Materials 2010;22:3943-3951.
[6] A. Goux, M. Etienne, E. Aubert, C. Lecomte, J. Ghanbaja, A. Walcarius, Oriented Mesoporous Silica Films Obtained by Electro-Assisted Self-Assembly (EASA). Chemistry of Materials 2009;21: 731-741.
[7] M.M. Collinson, A.R. Howells, Peer Reviewed: Sol–Gels and Electrochemistry: Research at the Intersection. Analytical Chemistry 2000; 72:702-709.
[8] B. Ikjoo, W.C. Anthony, K. Beomjoon, Transfer of thin Au films to polydimethylsiloxane (PDMS) with reliable bonding using (3-mercaptopropyl)trimethoxysilane (MPTMS) as a molecular adhesive. Journal of Micromechanics and Microengineering 2013;23;085016.
[9] J. Huser, S. Bistac, M. Brogly, C. Delaite, T. Lasuye, B. Stasik, Investigation on the Adsorption of Alkoxysilanes on Stainless Steel. Applied Spectroscopy 2013;67:1308-1314.
[10] C. Hoppe, C. Ebbert, M. Voigt, H.C. Schmidt, D. Rodman, W. Homberg, H.J. Maier, G. Grundmeier, Molecular Engineering of Aluminum–Copper Interfaces for Joining by Plastic Deformation. Advanced Engineering Materials 2016;18:1066-1074.
[11] D.D. Gandhi, M. Lane, Y. Zhou, A.P. Singh, S. Nayak, U. Tisch, M. Eizenberg, G. Ramanath, Annealing-induced interfacial toughening using a molecular nanolayer, Nature 447 (2007) 299.
[12] R. Shacham, D. Avnir, D. Mandler, Electrodeposition of Methylated Sol-Gel Films on Conducting Surfaces.Advanced Materials 1999;11:384-388.
[13] S. Sayen, A. Walcarius, Electro-assisted generation of functionalized silica films on gold. Electrochemistry Communications 2003;5:341-348.
[14] F. Luna-Vera, D. Dong, R. Hamze, S. Liu, M.M. Collinson, Electroassisted Fabrication of Free-Standing Silica Structures of Micrometer Size. Chemistry of Materials 2012;24:2265-2273.

[15] A. Ghorbal , F. Grisotto, J. Charlier, S. Palacin, C. Goyer, C. Demaille, Localized Electrografting of Vinylic Monomers on a Conducting Substrate by Means of an Integrated Electrochemical AFM Probe. Physical Chemistry 2009;10:1053-1057.
[16] C. Fredriksson, R. Lazzaroni, J.L. Brédas, M. Mertens, R. Jérôme, A combined theoretical and experimental study of the electrochemically induced chemisorption of acrylonitrile on nickel, copper, and zinc. Chemical Physics Letters 1996;258:356-362.
[17] A. Charlot, S. Gabriel, C. Detrembleur, R. Jerome, C. Jerome, Combination of electrografting and layer-by-layer deposition: an efficient way to tailor polymer coatings of (semi)-conductors. Chemical Communications 2007:4656-4658.
[18] S. Gabriel, R. Jérôme, C. Jérôme, Cathodic electrografting of acrylics: From fundamentals to functional coatings. Progress in Polymer Science 2010; 35:113-140.
[19] M. Cécius, R. Jérôme, C. Jérôme, New Monomers Tailored for Direct Electrografting onto Carbon in Water. Macromolecular Rapid Communications 2007; 28:948-954.
[20] H.C. Schmidt, W. Homberg, A.G. Orive, G. Grundmeier, B. Duderija, I. Hordych, S. Herbst, F. Nürnberger, H.J. Maier, Joining of blanks by cold pressure welding : Incremental rolling and strategies for surface activation and heat treatment. Materialwissenschaft und Werkstofftechnik 2019; 50:924-939.
[21] H.C. Schmidt, W. Homberg, A.G. Orive, G. Grundmeier, I. Hordych, H.J. Maier, Cold pressure welding of aluminium-steel blanks: Manufacturing process and electrochemical surface preparation. AIP Conference Proceedings 2018;1960;050007.
[22] A. Bauer, D. Meinderink, I. Giner, H. Steger, J. Weitl, G. Grundmeier, Electropolymerization of acrylic acid on carbon fibers for improved epoxy/fiber adhesion. Surface and Coatings Technology, 2017;321:128-135.
[23] G. Deniau, L. Azoulay, L. Bougerolles, S. Palacin, Surface Electroinitiated Emulsion Polymerization: Grafted Organic Coatings from Aqueous Solutions. Chemistry of Materials, 2006;18:5421-5428.
[24] L. Tessier, G. Deniau, B. Charleux, S. Palacin, Surface Electroinitiated Emulsion Polymerization (SEEP): A Mechanistic Approach. Chemistry of Materials 2009; 21:4261-4274.
[25] G. Deniau, L. Azoulay, P. Jégou, G. Le Chevallier, S. Palacin, Carbon-to-metal bonds: Electrochemical reduction of 2-butenenitrile. Surface Science 2006;600:675-684.
[26] X.T. Le, P. Viel, A. Sorin, P. Jegou, S. Palacin, Electrochemical behaviour of polyacrylic acid coated gold electrodes: An application to remove heavy metal ions from wastewater. Electrochimica Acta 2009; 54:6089-6093.
[27] S. Palacin, C. Bureau, J. Charlier, G. Deniau, B. Mouanda, P. Viel, Molecule-to-Metal Bonds: Electrografting Polymers on Conducting Surfaces. ChemPhysChem, 2004;5:1468-1481.
[28] S. Pletincx, K. Marcoen, L. Trotochaud, L.-L. Fockaert, J.M.C. Mol, A.R. Head, O. Karslioğlu, H. Bluhm, H. Terryn, T. Hauffman, Unravelling the Chemical Influence of Water on the PMMA/Aluminum Oxide Hybrid Interface In Situ. Scientific Reports 2017; 7;13341.
[29] S. Pletincx, J.M.C. Mol, H. Terryn, A. Hubin, T. Hauffman, An in situ spectro-electrochemical monitoring of aqueous effects on polymer/metal oxide interfaces. Journal of Electroanalytical Chemistry 2019;848;113311.
[30] E. De Giglio, S. Cometa, N. Cioffi, L. Torsi, L. Sabbatini, Analytical investigations of poly(acrylic acid) coatings electrodeposited on titanium-based implants: a versatile approach to biocompatibility enhancement. Analytical and Bioanalytical Chemistry 2007; 389:2055-2063.
[31] E. Katz, A.L. de Lacey, V.M. Fernandez, Covalent binding of viologen to electrode surfaces coated with poly(acrylic acid) prepared by electropolymerization of acrylate ions: II. Effect of the ionization state of the polymeric coating on the formal potential of viologen. Journal of Electroanalytical Chemistry 1993; 358:261-272.

[32] S. Hernández, J.K. Papp, D. Bhattacharyya, Iron-Based Redox Polymerization of Acrylic Acid for Direct Synthesis of Hydrogel/Membranes and Metal Nanoparticles for Water Treatment. Industrial & Engineering Chemistry Research2014; 53:1130-1142.
[33] L. Sheeney-Haj-Ichia, Z. Cheglakov, I. Willner, Electroswitchable Photoelectrochemistry by Cu2+−Polyacrylic Acid/CdS-Nanoparticle Assemblies. The Journal of Physical Chemistry B 2004; 108:11-15.
[34] M. Abdul Karim, Y.-D. Park, A Review on Welding of Dissimilar Metals in Car Body Manufacturing. Journal of Welding and Joining 2020; 38:8–23.
[35] W. Sobek, Ultra-lightweight construction. International Journal of Space Structures 2016; 31:74–80.
[36] N. Bay, Cold pressure welding —The Mechanisms Governing Bonding. Journal of Engineering for Industry1979;101:121-127.
[37] N. Bay, Mechanisms Producing Metallic Bonds in Cold Welding. Welding Journal 1983; 2;137.
[38] N. Bay, C. Clemensen, O. Juelstorp, T. Wanheim, Bond Strength in Cold Roll Bonding, CIRP Annals, 1985;34:221-224.
[39] G. Meschut, M. Merklein, A. Brosius, D. Drummer, L. Fratini, U. Füssel, M. Gude, W. Homberg, P.A.F. Martins, M. Bobbert, M. Lechner, R. Kupfer, B. Gröger, D. Han, J. Kalich, F. Kappe, T. Kleffel, D. Köhler, C.M. Kuball, J. Popp, D. Römisch, J. Troschitz, C. Wischer, S. Wituschek, M. Wolf, Review on mechanical joining by plastic deformation. Journal of Advanced Joining Processes,2022; 5;100113.
[40] C. Ebbert, H.C. Schmidt, D. Rodman, F. Nürnberger, W. Homberg, H.J. Maier, G. Grundmeier, Joining with electrochemical support (ECUF): Cold pressure welding of copper. Journal of Materials Processing Technology 2014; 214:2179-2187.
[41] G. W. Critchlow, D.M Brewis, Review of surface pretreatments for aluminium alloys. International Journal of Adhesion and Adhesives 1996;16:255–275.
[42] E.M Liston, Plasma Treatment for Improved Bonding: A Review. The Journal of Adhesion 1989;30:199–218.
[43] P.K Mallick, Joining for lightweight vehicles. In Materials, design and manufacturing for lightweight vehicles. Woodhead Publishing in materials CRC Press 2010:275–308.
[44] C. Hoppe, C. Ebbert, R. Grothe, H.C. Schmidt, I. Hordych, W. Homberg, H.J. Maier, G. Grundmeier, Influence of the Surface and Heat Treatment on the Bond Strength of Galvanized Steel/Aluminum Composites Joined by Plastic Deformation. Advanced Engineering Materials 2016;18:1371-1380.
[45] H.C. Schmidt, W. Homberg, C. Hoppe, G. Grundmeier, I. Hordych, H.J. Maier, Cold pressure welding by incremental rolling: Deformation zone analysis. AIP Conference Proceedings, 2016;1769;100013.
[46] I. Hordych, D. Rodman, F. Nürnberger, C. Hoppe, H.C. Schmidt, G. Grundmeier, W. Homberg, H.J. Maier, Effect of Pre-Rolling Heat Treatments on the Bond Strength of Cladded Galvanized Steels in a Cold Roll Bonding Process. Steel research international 2016; 87:1619-1626.
[47] I. Hordych, D. Rodman, F. Nürnberger, H.C. Schmidt, A.G. Orive, W. Homberg, G. Grundmeier, H.J. Maier, Influence of heat-pretreatments on the microstructural and mechanical properties of galfan-coated metal bonds. AIP Conference Proceedings 2018; 1960;040007.
[48] H.C. Schmidt, Ein Beitrag zum stoffschlüssigen Fügen durch plastische Deformation: partielles Kaltpressschweißen durch inkrementelles Walzen. Dr.-Ing. Dissertation, in, University of Paderborn, 2018.
[49] I. Hordych, S. Herbst, F. Nürnberger, H.C. Schmidt, A.G. Orive, W. Homberg, G. Grundmeier, H.J. Maier, The role of heat-treatments performed before and after a cold roll bonding process of galvanized steel sheets. AIP Conference Proceedings 2019; 2113;050017.

[50] S.Ed. Ebnesajjad, Handbook of Adhesives and Surface Preparation: Plastics Design Library; William Andrew Publishing, 2011.
[51] G. Habenicht, Kleben:Grundlagen, Technologie, Anwendungen, 2., völlig neubearb. und erw. Aufl.; Springer, 1990.
[52] L.-H. Lee. Fundamentals of Adhesion; Springer US, 1991.
[53] Z. Fritah, C. Drouet, C. Thouron, M. Aufray, Direct evidence of amine-metal reaction in epoxy systems: An in-situ calorimetry study of the interphase formation. Progress in Organic Coatings 2020; 148;105769.
[54] L.-H. Lee, Fundamentals of adhesion; Plenum Press, 1991.
[55] P. W. Atkins, J. de. Paula, Physikalische Chemie, 4., vollst. überarb. Aufl.; Wiley-VCH, 2006.
[56] H.-J. Butt, M.Kapple, Surface and interfacial forces; Physics textbook; Wiley-VCH Verlag GmbH & Co, 2010.
[57] H.-J. Butt, K.Graf, M.Kappl, Physics and chemistry of interfaces, 1. ed.; Physics textbook; Wiley-VCH, 2003.
[58] C. Bockenheimer, B. Valeske, W. Possart, Network structure in epoxy aluminium bonds after mechanical treatment. International Journal of Adhesion and Adhesives 2002; 22:349–356.
[59] D.G. Shchukin, E. Skorb, V. Belova, H. Möhwald, Ultrasonic cavitation at solid surfaces. Advanced Materials 2011; 23:1922–1934.
[60] A. Brotchie, D. Borisova, V. Belova, H. Möhwald, D. Shchukin, Ultrasonic Modification of Aluminum Surfaces: Comparison between Thermal and Ultrasonic Effects. Journal of Physical Chemistry 2012; 116:7952–7956.
[61] B.B. Johnsen, F. Lapique, A. Bjørgum, J. Walmsley, B.S. Tanem, T. Luksepp, The effect of pre-bond moisture on epoxy-bonded sulphuric acid anodised aluminium. International Journal of Adhesion and Adhesives 2004; 24:183–191.
[62] A. Baldan, Adhesively bonded joints and repairs in metallic alloys, polymers and composite materials: Adhesives, adhesion theories and surface pretreatment. Journal of Materal Science 2004; 39:1–49.
[63] J.D. Venables, D.K. McNamara, J.M. Chen, T.S. Sun, R. L. Hopping, Oxide morphologies on aluminum prepared for adhesive bonding. Applications of Surface Science 1979; 3:88–98.
[64] L. B. Hunt, Gold Bull. 1973; 6:16–27.
[65] C. Raub, In Metal Plating and Patination: Cultural, Technical and Historical Developments; La-Niece, S., Ed.; Butterworth-Heinemann, 1993.
[66] G. Zangari, Fundamentals of Electrodeposition, Elsevier 2018.
[67] G. Inzelt, A. Lewenstam, F. Scholz, Handbook of Reference Electrodes, Springer: Berlin, 2013.
[68] A. Behr, D. W. Agar und J. Jörissen. Einführung in die Technische Chemie. Heidelberg: Spektrum Akademischer Verlag, 2010. isbn: 978-3-8274-2073-2.
[69] P. Najafisayar, M.E. Bahrololoom, The effect of pulse electropolymerization on the electrochemical properties of polythiophene films. Electrochimica Acta 2013; 114:462–473.
[70] W. Su, J.O. Iroh, Electropolymerization of pyrrole on steel substrate in the presence of oxalic acid and amines. Electrochimica Acta 1999; 44:2173–2184
[71] S. Wencheng, J.O. Iroh, Effects of electrochemical process parameters on the synthesis and properties of polypyrrole coatings on steel. Synthetic Metals 1998; 95:159–167.
[72] D. Bélanger, J. Pinson, Electrografting: a powerful method for surface modification. Chemical Society reviews 2011; 40:3995–4048.
[73] E. Giglio, S. Cometa, M.A.Ricci, L. Sabbatini, Biocompatibility of Poly(Acrylic Acid) Thin Coatings Electro-synthesized onto TiAlV-based Implants. Journal of Bioactive and Compatible Polymers 2010; 25:374-391.
[74] A. A. Pasa, Electrodeposition. Encyclopedia of Chemical Processing 2006;821-832.

[75] E.P. Plueddemann,General Concepts. In Silane Coupling Agents, Springer: Boston, 1991:1-29.
[76] N. Asadi, R. Naderi, Nanoparticles Incorporated in Silane Sol-Gel Coatings. Elsevier 2020:451–471.
[77] D.E Packham, Silane adhesion promotors. In Handbook of Adhesion, 2nd ed.; John Wiley & Sons:2005.
[78] A. Fanquet, C. Le Pen, H.Terryn, J. Vereecken, Effect of bath concentration and curing time on the structure of non-functional thin organosilane layers on aluminium. Electrochemica Acta 2003; 48:1245–1255.
[79] H. Wang, R. Akid, Encapsulated cerium nitrate inhibitors to provide high-performance anti-corrosion sol–gel coatings on mild steel. Corrosion Science 2008; 50:1142–1148.
[80] M.J. Tsapakos, K.E.;Wetterhahn, The interaction of chromium with nucleic acids. Chem. Biol. Interact. 1983; 46:265–277.
[81] W. J Van Ooij, D.Zhu, Electrochemical impedance spectroscopy of bis-[triethoxysilypropyl] tetrasulfide on Al 2024-T3 substrates. Corrosion Sience 2001; 57:413–427.
[82] U. Eduok, O.Faye, J.Szpunar, Recent developments and applications of protective silicone coatings: A review of PDMS functional materials. Prog. Org. Coat. 2017; 111:124–163.
[83] M. Montemor, A. Rosqvist, H. Fagerholm, M.G.S. Ferreira,The early corrosion behavior of hot dip galvanised steel pre-treated with bis-1, 2-(triethoxysilyl) ethane. Prog. Org. Coat. 2004;51:188–194.
[84] A. K Singh, M.Quraishi, Investigation of the effect of disulfiram on corrosion of mild steel in hydrochloric acid solution. Corrosion Science 2011;53:1288–1297.
[85] H. Woo, P.J. Reucroft, R.J. Jacob, Electrodeposition of organofunctional silanes and its influence on structural adhesive bonding. Journal of Adhesion Science Technology, 1993;7;681.
[86] E. Tourwé, M. Biesemans, R. Willem, H. Terryn, Silane solution stability and film morphology of water-based bis-1,2-(triethoxysilyl)ethane for thin-film deposition on aluminium. Progress in Organic Coatings 2008;63:38-42.
[87] M. Sheffer, A. Groysman, D. Mandler, Electrodeposition of sol–gel films on Al for corrosion protection. Corrosion Science 2003; 45;2893.
[88] J.S. Gandhi, W.J. van Ooij, Improved corrosion protection of aluminum alloys by electrodeposited silanes. Journal of Material Engineering Performance 2004;13;475.
[89] J.M. Hu, L. Liu, J.Q. Zhang, C.N. Cao, Effects of electrodeposition potential on the corrosion properties of bis-1,2-[triethoxysilyl] ethane films on aluminum alloy. Electrochimica Acta 2006; 51;3944.
[90] J.M. Hu, L. Liu, J.Q. Zhang, C.N. Cao, Effect of heat treatment processing on the microstructure and properties of hot extrusion deformed FGH95 alloy. Jorunal of Chemistry 2006;27;1121.
[91] W.M. Zhang, J.M. Hu, Cathodically electrochemical-assisted deposition and protective properties of silane films. Acta Metallurgica Sinica 2006;42;295.
[92] A.E Danks, S.R. Hall, Z. Schnepp, The evolution of ‘sol-gel’chemistry as a technique for materials synthesis. Material Horizon 2016;3:91–112.
[93] B.Borup, K. Weissenbach, Silane Coupling Agents, John Wiley & Sons: Hoboken, NJ, USA, 2010; 61–90.
[94] Z. Pu, W. Van Ooij, J. Mark, Hydrolysis kinetics and stability of bis (triethoxysilyl) ethane in water-ethanol solution by FTIR spectroscopy. Journal of Adhesion Science Technology 1997;11:29–47.
[95] Y. Uyama, K.Kato,Y. Ikada, Surface Modification of Polymers by Grafting. In Grafting/Characterization Techniques/Kinetic Modeling; Galina, H., Ikada, Y., Kato, K., Kitamaru, R., Lechowicz, J., Uyama, Y., Wu, C., Eds.; Springer Berlin Heidelberg, 1998;1– 39.
[96] F. Barroso-Bujans, R. Serna, E. Sow, J.L.G Fierro, M. Veith, Grafting of poly(acrylic acid) onto an aluminum surface. Langmuir: the ACS journal of surfaces and colloids 2009; 25:9094–9100

[97] E . Katz, A .L . de Lacey and V.M. Fernandez, Covalent binding of viologen to electrode surfaces coated with poly(acrylic acid) prepared by electropolymerization of acrylate ions: II. Effect of the ionization state of the polymeric coating on the formal potential of viologen. Jorunal of Electroanalytical Chemistry 1993;358:261-272.
[98] V. I. Chegel, O.A. Raitman, O.Lioubashevski, O. Shirshov, E. Katz, I. Willner, Redox Switching of Electrorefractive, Electrochromic, and Conductivity Functions of Cu2+/Polyacrylic Acid Films Associated with Electrodes. Advanced Materials 2002; 14:1549–1553.
[99] M.D. Lechner, K. Gehrke, E.H. Nordmeier, Makromolekulare Chemie: Ein Lehrbuch für Chemiker, Physiker, Materialwissenschaftler und Verfahrenstechniker, 5. Aufl.; Springer Spektrum, 2014.
[100] C.Decker, R. Vataj, A. Louati, A. Synthesis of acrylic polymer networks by electroinitiated polymerization. Progress in Organic Coatings 2004;50:263–268.
[101] S.Sadki, N. Brodie, G.Sabouraud, the mechanisms of pyrrole electropolymerization. Chemical Society reviews 2000;29:283–293.
[102] D. Wei, C. Kvarnström, T. Lindfors, L.Kronberg, R.Sjöholm, A.Ivaska, Electropolymerization mechanism of N-methylaniline. Synthetic Metals 2006;156:541–548.
[103] G.L. Collins, N.W Thomas, Mechanism of coating by electropolymerization on metal cathodes from zinc chloride solutions of acrylamide. Journal of Polymer Science: Polymer Chemistry Edition 1977;15:1819–1831.
[104] S. Schreijäg, D. Kaufmann, M. Wenk, O. Kraft, R. Mönig Size and microstructural effects in the mechanical response of α-Fe and low alloyed steel, Acta Materialia 2015;97:94-104.
[105] W. Bleck, B. Engl, A. Frehn, D. Nicklas, and G. Steinbeck, Ermittlung von Berechnungskennwerten an Karosseriewerkstoffen, Bericht über ein Gemeinschaftsprojekt der Stahl- und Automobilindustrie. Materialwissenschaft und Werkstofftechnik. 35;8:483-494.
[106] C. Jasinski, A. Kocanda, Ł. Morawinski, S. Świllo, A new approach to experimental testing of sheet metal formability for automotive industry. Arch. Metall. Mater. 2019;64:1231-1238.
[107] C. Vargel, Corrosion of aluminium, Elsevier, 2004.
[108] J. P. Magrinho, M.B. Silva, L.R. Paulo A. F. Martins, Formability Limits, Fractography and Fracture Toughness in Sheet Metal Forming. Materials 2019;12:1493.
[109] M. Lewandowska, T. Wejrzanowski, K.J. Kurzydłowski, Grain growth in ultrafine grained aluminium processed by hydrostatic extrusion, Journal of Material Science 2008;43:7495–7500.
[110] H. Jazaeri H, F.J. Humphreys, The transition from discontinuous to continuous recrystallization in some aluminium alloys: I–the deformed state. Acta Materialia 2004;52:3251.
[111] M.Ferry, N.E. Hamilton, F.J. Humphreys, Continuous and discontinuous grain coarsening in a fine-grained particle.containing Al.Sc alloy. Acta Materialia 2005;53:1097.
[112] J.R. Bowen, O.V. Mishin, P.B. Prangnell PB, D.J. Jensen, Orientation correlations in aluminum deformed by ECAE, Scr.Mater (2002) 16:289.
[113] J. Zhu, L. H. Hihara. Corrosion Science 2010;52: 406.
[114] K. F. Lorking. Journal of Applied Chemistry 1960;10:449.
[115] K. Sotoudeh, T. H. Nguyen, R. T. Foley, B. F. Brown. Corrosion 1981;37:358.
[116] K.Mori, N. Bay, L.Fratini, F. Micari, A. E. Tekkaya, Joining by plastic deformation, CIRP Annals 2013;62:673-694.
[117] L. Li, K. Nagai, F. Yin, Progress in Roll Bonding of Metals. Science and Technology of Advanced Materials 2008; 9(2):1–11.
[118] R.F. Tylecote, The Solid Phase Welding of Metals, Edward Arnold Ltd., London 1968.
[119] D.R.Milner, G.W Rowe, Fundamentals of Solid Phase Welding. Metallurgical Reviews 1962;7(28):433–480. Advanced Materials 9(2):1–11.

[120] N. Bay, T.J. Lienert, S.S. Babu, T.A. Siewert, Cold Welding of Metals. Handbook Welding Fundamentals and Processes 2011;6A:711–716.
[121] W. Zhang. „Bond formation in cold welding of metals“. Dissertation. Lyngby: Technical University of Denmark, 1994.
[122] G. Durst. „A New Development In Metal Cladding“, JOM-J. Met. 8 1956.
[123] W. Hofmann und J. Ruge. „Versuche über die Kalt-Preßschweißung von Metallen“, Z. Metallkd. 5 1952.
[124] C. Pabst und P. Groche. „Electromagnetic Pulse Welding: Process Insights by High-Speed Imaging and Numerical Simulation“. In: Proceedings of the 6th International Conference on High-Speed Forming 77-78.
[125] Y. Lu, J. Y. Huang, C. Wang, S. Sun und J. Lou. „Cold welding of ultrathin gold nanowires“, Natural Nanotechnology 2010;5.3;218–224.
[126] N. Bay. „Friction and Adhesion in Metal Forming and Cold Welding“. PhD Thesis. Dänemark: Technical University of Denmark, 1985.
[127] P. A. Taylor, J. S. Nelson und B. W. Dodson. „Adhesion between atomically flat metallic surfaces“, Phys. Rev. B: Condens. Matter 44.11 1991:5834–5841.
[128] H. Conrad und L. Rice. „The cohesion of previously fractured Fcc metals in ultrahigh vacuum“, Metall Trans. November.1 1970.
[129] M. Schmidtchen, Hrsg. Technologie der Werkstoffverbundherstellung durch Umformen: MEFORM 2004; 08. - 09. März 2004; Tagungsband. Freiberg: Technische Univ. Bergakad, 2004. isbn: 3860122215.
[130] H. G. Bauer und W. Schadt, Hrsg. Walzen von Flachprodukten. Berlin, Heidelberg: Springer Berlin Heidelberg, 2017. isbn: 9783662480915.
[131] Dynamic Materials Corporation. Explosion Welding Process. 2018.
[132] Wickeder Westfalenstahl GmbH. Werkstoffdatenblatt CU-AL-CU: Plattierte Werkstoffe. Hrsg. von Wickeder Westfalenstahl GmbH. 2016.
[133] E. Roos und K. Maile. Werkstoffkunde für Ingenieure: Grundlagen, Anwendung, Prüfung. 5. Aufl. 2015. Springer-Lehrbuch. Berlin, Heidelberg: Springer Berlin Heidelberg, 2015. isbn: 9783642549892.
[134] EMS Clad. Overlay Clad Materials. Hrsg. von Wickeder Westfalenstahl GmbH. 2016.
[135] M. Köhler. „Plattiertes Stahlblech“, Stahlanwendungen: Merkblätter Merkblatt 383 (2006)1–18.
[136] K. Lange. Massivumformung. 2., völlig neubearb. Aufl. Bd. Handbuch für Industrie und Wissenschaft /Kurt Lange Hrsg. ; Bd. 2. Umformtechnik. Berlin: Springer, 1988.
[137] Wickeder Westfalenstahl GmbH. Innovative Plattierdesigns. 2018.
[138] A. Knauscher, Hrsg. Oberflächenveredeln und Plattieren von Metallen. 1. Auflage. Leizpig: VEB Deutscher Verlag für Grundstoffindustrie, 1978.
[139] M. Kleiner, W. Homberg, R. Krux, B. Rauscher, M. Trompeter, H. Karbasian, M. Gösling, M. Köhler, T. Langhammer, F.-J. Lenze und S. Schwarz. Forschungsbericht P565: Fertigung innovativer IHU-Stahlbauteile auf Basis neuartiger, partiell plattierter Blechhalbzeuge. Hrsg. von Foschungsvereinigung Stahlanwendung. Düsseldorf, 2006.
[140] SA Rubanox. Technologie: Expandal-Technologie. Hrsg. von Rubanox SA. 2016.
[141] G.A. Steinlage, K.J.Bowman and K.P.Trumble, A comparison of three mechanical models for cold roll bonding metal laminates, Journal of Adhesive Science Technology 1996;10:199-229.
[142] On the Properties of Things: John Trevisa's Translation of Bartholomaeus Anglicus, De Proprietatibus Rerum: A Critical Text, Vol. 2, Oxford University Press, 1975.
[143] K. Bobzin, Oberflächentechnik für den Maschinenbau, 1. Aufl. Weinheim: Wiley-VCH, 2013. isbn: 9783527330188.

[144] A. R. Birkert, S. Haage und M. Straub, Hrsg. Umformtechnische Herstellung komplexer Karosserieteile: Auslegung von Ziehanlagen. Springer Berlin Heidelberg, 2013. isbn: 9783642346705.
[145] K. E. Petersen und C. R. Guarnieri, Young's modulus measurements of thin films using micromechanics. Journal of Applied Physycs 1979; 50: 6761–6766.
[146] J. A. Schey, Hrsg. Metal Deformation Processes: Friction and Lubrication. New York: Marcel Dekker Inc., 1970.
[147] S. H. Carpenter und R. H. Wittman. „Explosion Welding", Annu. Rev. Mater. Sci. 5.1 1975:177–199.
[148] K. Siegert und J. Ulmer. „Influencing the Friction in Metal Forming Processes by Superimposing Ultrasonic Waves", CIRP Ann.-Manuf. Techn. 50.1 2001:195–200.
[149] P. L. Threadgill, A. J. Leonard, H. R. Shercliff und P. J. Withers. „Friction stir welding of aluminium alloys", Int. Mater. Rev. 54.2 2013:49–93.
[150] E. P. S. Tan, Y. Zhu, T. Yu, L. Dai, C. H. Sow, V. B. C. Tan und C. T. Lim. „Crystallinity and surface effects on Young's modulus of CuO nanowires", Appl. Phys. Lett. 90.16 2007:163112.
[151] L. R. Vaidyanath und D. R. Milner. „Significance of Surface Preparation in Cold pressure welding ", Brit. Weld. J. 7;1960:1–6.
[152] V. P. Lugin und G. V. Nedzvetskii. „Cold Welding of Transistor Bodies", Welding Prod+ 14.2 1967;65–67.
[153] K. K. Khrenov, P. I. Gurksii und V. A. Dubolazov, The Cold Welding of Copper to Kovar Alloy in the Sealing of Semiconductor Devices .Automat. Weld+ 23.5 1970;46–49.
[154] C. Clemensen, O. Juelstorp und N. Bay. „Cold Welding - Part 3 - Influence of surface preparation on bond strength", Met. Constr.-Brit. Weld. 18.10:1986;625–629.
[155] Y. Onodera, T. Fujita und M. Koike, Automatic Cold pressure welding Equipment Applied to Sealing Electronic Devices. NEC research and development: technical journal of Nippon Electric Co., Ltd. 53; 1979:80–86.
[156] J. Verstraete, W. De Waele und K. Faes, Mangetic pulse welding: lessons to be learned from explosive welding". In: Sustainable construction and design. Hrsg. von J. van Wittenberghe. Bd. 2. Ghent University, Laboratory Soete, 2011:458–464. isbn: 9789490726010.
[156] E. Vinaricky, Hrsg. Elektrische Kontakte, Werkstoffe und Anwendungen: Grundlagen, Technologien, Prüfverfahren. 3. Auflage. Berlin und Heidelberg: Springer Vieweg, 2016. isbn: 978-3-642-45427-1.
[157] S.-H. Lee und D. N. Lee, Analysis of roll bonding of silver clad phosphor bronze sheets, Mater. Sci. Tech. Ser. 7.11 1991.
[158] N. Bay, W. Zhang und S. S. Jensen, The application of strategic surface coatings to improve bonding in solid phase welding. International Journal for the Joining of Materials 6.2 (1994).
[159] H. A. Mohamed und J. Washburn, Mechanism of Solid-State Pressure Welding, Welding Research Supplement September 1975:302-310.
[160]REM/FIB-https://chemie.uni-paderborn.de/arbeitskreise/technischechemie/cmp/ausstattung/fib/.
[161] H. R. Verma, in Atomic and nuclear analytical methods. XRF, Moessbauer, XPS, NAA and ion-beam spectroscopic techniques (Ed. P. Hoffmann), Springer, Berlin, Heidelberg, New York, 2007: 213.
[162] D. Briggs, J. T. Grant, IM Publ. Chichester 2003:11.
[163] L. Sabbatini, Surface characterization of advanced polymers; VCH, 1993.
[164] H. Bluhm, X-ray photoelectron spectroscopy (XPS) for in situ characterization of thin film growth. In In situ characterization of thin film growth; Koster, G., Rijnders, G., Eds.; Woodhead Publishing Series in Electronic and Optical Materials; Woodhead Pub, 2011; pp 75–98. DOI: 10.1533/9780857094957.2.75.

[165] C. Kunze, B. Torun, I. Giner, G. Grundmeier, Surface chemistry and nonadecanoic acid adsorbate layers on TiO2(100) surfaces prepared at ambient conditions. Surface Science 2012;606 :19-20.
[166] S. Hofmann, Auger- and X-Ray Photoelectron Spectroscopy in Materials Science:A User-Oriented Guide; Springer Series in Surface Sciences, Vol. 49; Springer, 2013.
[167] W. G. Golden, D. S. Dunn, J. Overend, A method for measuring infrared reflection Absorption spectra of molecules adsorbed on low-area surfaces at monolayer and submonolayer concentrations. Journal of Catalisis 1981;71:395.
[168] Y. J. Chabal, Surface infrared spectroscopy. Surface Science Reports 1988;8:211–357.
[169] T. Buffeteau, B. Desbat, J. M. Turlet, Polarization modulation FT-IR spectroscopy of surfaces and ultra-thin films: experimental procedure and quantitative analysis. Applied Spectroscopy 1991;45:380.
[170] G. Grundmeier, A. Keudell, T. de. los Arcos, Fundamentals and Applications of Reflection FTIR Spectroscopy for the Analysis of Plasma Processes at Materials Interfaces. Plasma Processes and Polymers 2015;12: 926–940.
[171] R. F. Egerton, Physical principles of electron microscopy: An introduction to TEM, SEM, and AEM; Springer, 2005.
[172] W. Zhou, Z. Wang, Fundamentals of Scanning Electron Microscopy Advanced Scanning Microscopy for Nanotechnology:Chapter 1; HEP Frontiers Online Higher Education Press, 2007
[173] M. Abd Mutalib, M.A. Rahman, M.H.D. Othman, A.F. Ismail, J. Jaafar, Scanning Electron Microscopy (SEM) and Energy-Dispersive X-Ray (EDX) Spectroscopy. Membrane Characterization; Elsevier, 2017:161–179, ISBN 9780444637765.
[174] K.S. Subramanian, G.J. Janavi, S.Marimuthu, M. Kannan, K. Raja, S. Haripriya, D. Jeya Sundara Sharmila, P. Sathya Moorthy, P. Textbook on Fundamentals and Applications of Nanotechnology. Daya Pub. House 2018.
[175] P. Eaton and P. West, Atomic force microscopy, 2010 (Oxford university press).
[176] T. R. Albrecht, C. F. Quate, Noncontact Atomic Force Microscopy for Atomic-Scale Characterization of Material SurfacesJ. Vac. Sci. Technol., A 1988; 6:271.
[177] H. C. van der Mei, H. J. Busscher, R. Bos, Atomic Force Microscopy, a Powerful Tool in Microbiology. Journal of Biophysics 2000;78:2668.
[178] T. R. Albrecht, S. Akamine, T. E. Carver, C. F. Quate, Microfabrication of cantilever styli for the atomic force microscope, J. Vac. Sci. Technol., A 1990;8:3386.
[179] Y. Martin, C.C. Williams. H.K. Wickramasinghe H K, Atomic force microscope–force mapping and profiling on a sub 100-Å scale, Journal of Applied Physics 1987; 61:4723–9.
[180] Y. Seo W. Jhe Atomic force microscopy and spectroscopy , 2008 Rep. Prog. Phys. 71 16101.
[181] A.J. Bard, L.R. Faulkner Electrochemical methods, 2nd edn. Wiley, (2001), New York, pp 156–180.
[182] G.Inzelt, Kinetics of electrochemical reactions. In: Scholz F (ed) Electroanalytical methods, Springer, Berlin 2nd edn. 2010:33–56.
[183]G. Inzelt, Chronocoulometry. Electroanalytical methods. Springer, Berlin 2nd edn. 2010:147–158.
[184] H.B. Oldham, J.C. Myland, Fundamentals of electrochemical science. Academic San Diego 1994.

[185] R. Bento, L. Mascaro, Analysis of the initial stages of electrocrystallization of Fe, Co and Fe-Co alloys in chloride solutions. J. Braz. Chem. Soc. 2002; 13:502–509.
[186] X. Zhou, Y. Wang, L. Zhipeng, H.Jin, Electrochemical Deposition and Nucleation/Growth Mechanism of Ni–Co–Y_2O^3 Multiple Coatings. Materials 2018; 11:1124.
[187] A. J. Bard, L. R. Faulkner, and H. S. White, Electrochemical Methods: Fundamentals and Applications (3rd ed.), John Wiley & Sons 2022.
[187] P. T. Kissinger and W. R. Heineman, Laboratory Techniques in Electroanalytical Chemistry (2nd ed.), Marcel Dekker, New York 1996.
[189] T. Osakai, K. Kano, and S. Kuwabata, Basic Electrochemistry, Kagakudojin, Kyoto 2000.
[190] J. O. M. Bockris and A. K. Reddy, Modern Electrochemistry 1: Ionics (2nd ed.), Kluwer Academic/Plenum Publishers, New York 1998.
[191] C.H. Hamann, W. Vielstich, Elektrochemie, 4th ed.; WILEY-VCH Verlag GmbH & Co. KGaA: Weinheim, 2005.
[192] H. Dennis, M. Evans-Kathleen, A. O'Connell-Ralph, A. Petersen/Michael, J. Kelly. Cyclic voltammetry. Journal of Chemical Education 1983, 60.
[193] G.A. Mabbott, An introduction to cyclic voltammetry. Journal of Chemical Education 1983, 60, 697–702
[193] G. Bontempelli , R. Toniolo, Linear sweep and cyclic voltammetry, Encyclopedia of Analytical Science, London: Elsevier.2nd edn., vol. 9, pp. 2005: 188–197.
[194] P. Lang, Y. Liu, Soft Matter at Aqueous Interfaces; Springer International Publishing: Cham, 2016, ISBN 978-3-319-24500-3.
[195] R. Guidelli, R.G. Compton, J.M. Feliu, E. Gileadi, J. Lipkowski, W. Schmickler, S.Trasatti, Defining the transfer coefficient in electrochemistry: An assessment (IUPAC Technical Report). Pure and Applied Chemistry 2014, 86, 245–258, doi:10.1515/pac-2014-5026.
[197] P. Delahay, New Instrumental Methods in Electrochemistry. Wiley Interscience, New York (1954).
[198] A. J. Bard and L. R. Faulkner, Electrochemical Methods: Fundamental and Applications (2nd ed.), John Wiley, New York (2001).
[199] M. Sluyters-Rehbach, Pure Appl. Chem., 66, 1831 (1994). 4. A. Lasia, Electrochemical Impedance Spectroscopy and Its Applications, Springer (2014)
[200] A.R.C Bredar, A.L. Chown, A.R. Burton, B.H Farnum. Electrochemical Impedance Spectroscopy of Metal Oxide Electrodes for Energy Applications. ACS Appl. Energy Mater. 2020, 3, 66–98, doi:10.1021/acsaem.9b01965.
[201] H. Herrera Hernández, A.M. Ruiz Reynoso, J.C. Trinidad González, C.O González Morán, J.G. Miranda Hernández, A. Mandujano Ruiz, J. Morales Hernández, R.Orozco Cruz, Electrochemical Impedance Spectroscopy (EIS): A Review Study of Basic Aspects of the Corrosion Mechanism Applied to Steels 2020.
[203] A. D. Crocombe, R. D. Adams, Peel Analysis Using the Finite Element Method. The Journal of Adhesion 1981; 12 (2):127–139.
[204] L. Zhang, J. Wang, A generalized cohesive zone model of the peel test for pressure sensitive adhesives. International Journal of Adhesion and Adhesives 2009;29 (3):217–224.
[205] R.D.Adams, A. Comyn, W.C. Wake, Structural Adhesive Joints in Engineering, second edition,
New test methods for the prediction of the environmental resistance of adhesive bonded joints', Proceedings Bicentennial of Materials Progress 21, Society for the Advancement of Material and Process Engineering, USA, 581–691.
[206] V.C.Beber, N. Wolter, B.Schneider and K. Koschek, Experimental investigation and numerical prediction of static strength and fracture behaviour of notched epoxy-based structural adhesives,Proc IMechE Part E: J Process Mechanical Engineering 2020;0:1-8.

[207] A. D. Crocombe R. D. Adams, Peel Analysis Using the Finite Element Method. The Journal of Adhesion 1981;12 (2): 127–139.
[208] M. Gharagozlou, R. Naderi, Z. Baradaran, Effect of synthesized NiFe2O4-silica nanocomposite on the performance of an ecofriendly silane sol–gel coating. Progress in Organic Coatings 2016; 90:407-413.
[209] N. Parhizkar, B. Ramezanzadeh, T. Shahrabi, Corrosion protection and adhesion properties of the epoxy coating applied on the steel substrate pre-treated by a sol-gel based silane coating filled with amino and isocyanate silane functionalized graphene oxide nanosheets. Applied Surface Science 2018;439:45-59.
[210] N. Parhizkar, T. Shahrabi, B. Ramezanzadeh, A new approach for enhancement of the corrosion protection properties and interfacial adhesion bonds between the epoxy coating and steel substrate through surface treatment by covalently modified amino functionalized graphene oxide film. Corrosion Science 2017;123:55-75.
[211] D. Meinderink, C. Kielar, O. Sobol, L. Ruhm, F. Rieker, K. Nolkemper, A.G. Orive, O. Ozcan, G. Grundmeier, Effect of PAA-induced surface etching on the adhesion properties of ZnO nanostructured films. International Journal of Adhesion and Adhesives 2021; 106:102812.
[212] D. Meinderink, A.G. Orive, G.G Grundmeier, Electrodeposition of poly(acrylic acid) on stainless steel with enhanced adhesion properties. Surface and Interface Analysis 2018;50:1224-9.
[213] K.A. Yasakau, I. Giner, C. Vree, O. Ozcan, R. Grothe, A. Oliveira, G. Grundmeier, M.G.S. Ferreira, M.L. Zheludkevich, Influence of stripping and cooling atmospheres on surface properties and corrosion of zinc galvanizing coatings. Applied Surface Science 2016; 389:144-156.
[214] V. Jovancicevic, R. C. Kainthla, Z. Tang, B. Yang, and J. O'M. Bockris, Mechanismus der Sauerstoffreduktion an Eisen in neutralen wässrigen Lösungen: Sauerstoff-Chemisorptionsmodell, Langmuir 1987:3- 388.
[215] I. Díez-Pérez, P. Gorostiza, F. Sanz, C. Müller, First Stages of Electrochemical Growth of the Passive Film on Iron. Journal of The Electrochemical Society 2001;148(8): 307-313.
[216] N. Ait Ahmed, M. Eyraud, H. Hammache, F. Vacandio, S. Sam, N. Gabouze, P. Knauth, K. Pelzer, T. Djenizian, New insight into the mechanism of cathodic electrodeposition of zinc oxide thin films onto vitreous carbon. Electrochimica Acta 2013;94:238-244.
[217] J. Vazquez-Arenas, F. Sosa-Rodriguez, I. Lazaro, R. Cruz, Thermodynamic and electrochemistry analysis of the zinc electrodeposition in NH4Cl–NH3 electrolytes on Ti, Glassy Carbon and 316L Stainless Steel. Electrochimica Acta 2012; 79:109-116.
[218] L. Guo, G. Oskam, A. Radisic, P.M. Hoffmann, P.C. Searson, Island growth in electrodeposition. Journal of Physics D: Applied Physics 2011;44:443001.
[219] L.-K. Wu, J.-M. Hu, J.-Q. Zhang, Electrodeposition of zinc-doped silane films for corrosion protection of mild steels. Corrosion Science 2012;59:348-351.
[220] N. Graf, E. Yegen, T. Gross, A. Lippitz, W. Weigel, S. Krakert, A. Terfort, W.E.S. Unger, XPS and NEXAFS studies of aliphatic and aromatic amine species on functionalized surfaces. Surface Science 200);603:2849-2860.
[221] P.M. Dietrich, S. Glamsch, C. Ehlert, A. Lippitz, N. Kulak, W.E.S. Unger, Synchrotron-radiation XPS analysis of ultra-thin silane films: Specifying the organic silicon. Applied Surface Science 2016;363:406-411.
[222] M.P. Quiroga Argañaraz, J.M. Ramallo-López, G. Benítez, A. Rubert, E.D. Prieto, L.M. Gassa, R.C. Salvarezza, M.E. Vela, Optimization of the surface properties of nanostructured Ni–W alloys on steel by a mixed silane layer. Physical Chemistry Chemical Physics 2015;17(21):14201-14207.
[223] N. Fink, B. Wilson, G. Grundmeier, Formation of ultra-thin amorphous conversion films on zinc alloy coatings: Part 1. Composition and reactivity of native oxides on ZnAl (0.05%) coatings. Electrochimica Acta 2006; 51:2956-2963.

[224] J. Huser, S. Bistac, M. Brogly, C. Delaite, T. Lasuye, B. Stasik, Investigation on the Adsorption of Alkoxysilanes on Stainless Steel. Applied Spectroscopy 2013;67:1308-1314.
[225] M. Hinge, E.S. Gonçalves, S.U. Pedersen, K. Daasbjerg, On the electrografting of stainless steel from para-substituted aryldiazonium salts and the thermal stability of the grafted layer. Surface and Coatings Technology 2010; 205(3):820-827.
[226] I. Hordych, D. Rodman, F. Nürnberger, C. Hoppe, H.C. Schmidt, G. Grundmeier, W. Homberg, H.J. Maier, Effect of Pre-Rolling Heat Treatments on the Bond Strength of Cladded Galvanized Steels in a Cold Roll Bonding Process. Steel research international 2016;87:1619-1626.
[227] I. Hordych, D. Rodman, F. Nürnberger, H.C. Schmidt, A.G. Orive, W. Homberg, G. Grundmeier, H.J. Maier, Influence of heat-pretreatments on the microstructural and mechanical properties of galfan-coated metal bonds. AIP Conference Proceedings 2018; 1960(1):040007.
[228] I. Hordych, S. Herbst, F. Nürnberger, H.C. Schmidt, A.G. Orive, W. Homberg, G. Grundmeier, H.J. Maier, The role of heat-treatments performed before and after a cold roll bonding process of galvanized steel sheets. AIP Conference Proceedings 2019;2113(1):050017.
[229] J. Díaz-Cruz, R.Tauler, B.S. Grabarić, M. Esteban, E.Casassas, Application of multivariate curve resolution to voltammetric data. Part 1. Study of Zn(II) complexation with some polyelectrolytes. Journal of Electroanalytical Chemistry 1995;393:7-16.
[230] M. Skompska, K. Zarębska,Electrodeposition of ZnO Nanorod Arrays on Transparent Conducting Substrates–a Review. Electrochimica Acta 2014;127:467-88.
[231] L.J.Kirwan, P.D. Fawell, W. van Bronswijk, In Situ FTIR-ATR Examination of Poly(acrylic acid) Adsorbed onto Hematite at Low pH. Langmuir 2003;19:5802-7.
[232] L.J.Kirwan, P.D. Fawell, W. van Bronswijk, An in Situ FTIR-ATR Study of Polyacrylate Adsorbed onto Hematite at High pH and High Ionic Strength. Langmuir 2004;20:4093-100.
[233] J.J Hermans, L. Baij, M. Koenis, K. Keune, P.D. Iedema, S. Woutersen, 2D-IR spectroscopy for oil paint conservation: Elucidating the water-sensitive structure of zinc carboxylate clusters in ionomers. Science Advances 2019;5:eaaw3592.
[234] S. Liufu, H.Xiao H, Y.Li, Adsorption of poly(acrylic acid) onto the surface of titanium dioxide and the colloidal stability of aqueous suspension. Journal of Colloid and Interface Science 2005;281:155-63.
[235] Z. Wei, J. He, T. Liang, H. Oh H, J. Athas, Z. Tong, Autonomous self-healing of poly(acrylic acid) hydrogels induced by the migration of ferric ions. Polymer Chemistry 2013;4:4601-5.
[236] A.B. Ruiz-Muelle, R. Contreras-Cáceres, P. Oña-Burgos, A. Rodríguez-Dieguez, J.M. López-Romero, I.Fernández, Polyacrylic acid polymer brushes as substrates for the incorporation of anthraquinone derivatives. Unprecedented application of decorated polymer brushes on organocatalysis. Applied Surface Science 2018;428:566-78.
[237] A.Adenier, M.C. Bernard,M.M. Chehimi, E.Cabet-Deliry, B. Desbat, O.Fagebaume et al. Covalent Modification of Iron Surfaces by Electrochemical Reduction of Aryldiazonium Salts. Journal of the American Chemical Society 2001;123:4541-9.
[238] L.Bardini, M.Ceccato, M.Hinge, S.U. Pedersen, K. Daasbjerg, M.Marcaccio, Electrochemical Polymerization of Allylamine Copolymers. Langmuir 2013;29:3791-6.
[239] Z.Sanaei, T. Shahrabi, B. Ramezanzadeh, Synthesis and characterization of an effective green corrosion inhibitive hybrid pigment based on zinc acetate-Cichorium intybus L leaves extract (ZnA-CIL.L): Electrochemical investigations on the synergistic corrosion inhibition of mild steel in aqueous chloride solutions. Dyes and Pigments 2017;139:218-32.
[240] B. Ramezanzadeh, E. Ghasemi, F. Askari, M. Mahdavian, Synthesis and characterization of a new generation of inhibitive pigment based on zinc acetate/benzotriazole: Solution phase and coating phase studies. Dyes and Pigments 2015;122:331-45.

[241] O.Galmiz, M. Stupavska, H. Wulff, H. Kersten, A. Brablec, M.Cernak, Deposition of Zn-containing films using atmospheric pressure plasma jet. Open Chemistry2014.
[242] J.Izquierdo, C.Kranz, Electrochemical techniques for investigating redox active macromolecules. European Polymer Journal 2016;83:428-49.
[243] G.Grundmeier, C. Reinartz, M. Rohwerder, M. Stratmann, Corrosion properties of chemically modified metal surfaces. Electrochimica Acta 1998;43:165-74.
[244] E. McCafferty, Validation of corrosion rates measured by the Tafel extrapolation method. Corrosion Science 2005;47:3202-15.
[245] T.K. Ross, J. Wolstenholme, Anti-corrosion properties of zinc dust paints. Corrosion Science 1977;17:341-51.
[246] C.A.M Dutra, E.N Codaro, R.Z Nakazato, Electrochemical Behavior and Corrosion Study of Electrodeposits of Zn and Zn-Fe-Co on Steel. Materials Sciences and Applications 2012;3:348-54.
[247] J.A. Cabral-Miramontes, D.M Bastidas, M.A Baltazar, P. Zambrano-Robledo, J.M Bastidas, F.M. Almeraya-Calderón, et al. Corrosion behavior of Zn-TiO2 and Zn-ZnO Electrodeposited Coatings in 3.5% NaCl solution. International Journal of ELECTROCHEMICAL SCIENCE 2019:4226-39.
[248] M.Hinge, E.S Gonçalves, S.U Pedersen, K. Daasbjerg, On the electrografting of stainless steel from para-substituted aryldiazonium salts and the thermal stability of the grafted layer. Surface and Coatings Technology 2010;205:820-7.
[249] C.Kunze, M.Valtiner, R.Michels, K. Huber, G. Grundmeier, Self-localization of polyacrylic acid molecules on polar ZnO(0001)-Zn surfaces. Physical Chemistry Chemical Physics 2011;13:12959-67.
[250] D. Meinderink, A.G. Orive, S. Ewertowski, I. Giner, G. Grundmeier G. Dependance of Poly(acrylic acid) Interfacial Adhesion on the Nanostructure of Electrodeposited ZnO Films. ACS Applied Nano Materials 2019;2:831-43.
[251] M. Valtiner, G. Grundmeier, Single Molecules as Sensors for Local Molecular Adhesion Studies. Langmuir 2010;26:815-20.
[252] K.M.S Juhl, N. Bovet, T. Hassenkam, K. Dideriksen, C.S. Pedersen, C.M Jensen et al. , Change in Organic Molecule Adhesion on α-Alumina (Sapphire) with Change in NaCl and CaCl2 Solution Salinity. Langmuir 2014;30:8741-50.
[253] T. Bauer, T. Schmaltz, T.Lenz, M. Halik, B. Meyer , T. Clark, Phosphonate- and Carboxylate-Based Self-Assembled Monolayers for Organic Devices: A Theoretical Study of Surface Binding on Aluminum Oxide with Experimental Support. ACS Applied Materials & Interfaces 2013;5:6073-80.
[254] S.P. Pujari, L- Scheres, A.T.M Marcelis, H. Zuilhof, Covalent Surface Modification of Oxide Surfaces. Angewandte Chemie International Edition 2014;53:6322-56.
[255] S. Schwiderek, A.G. Orive, S. Karimi Aghda, J.M. Schneider, T. de los Arcos, G. Grundmeier, Single-Molecule Desorption Studies of Poly(acrylic acid) at Electrolyte/Oxide/TiAlN Interfaces. Langmuir 2020;36:9489-98.
[256] V. Neßlinger, A.G. Orive, D. Meinderink, G. Grundmeier, Combined in-situ attenuated total reflection-Fourier transform infrared spectroscopy and single molecule force studies of poly(acrylic acid) at electrolyte/oxide interfaces at acidic pH. Journal of Colloid and Interface Science 2022;615:563-76.
[257] K. Nishimoto, Y. Okumoto, T. Harano, K. Atagi, H. Fujii, S. Katayama, HR-TEM observation of laser pressure weld of galvannealed steel and pure aluminium. Welding International 2009;23:824-9.
[258] B. Duderija, A. González-Orive, H.C. Schmidt, J.C. Calderón, I. Hordych, H.J. Maier, W. Homberg, G. Grundmeier, Electrografting of BTSE: Zn films for advanced steel-aluminum joining by plastic deformation. Journal of Advanced Joining Processes 2022;7:1100137.

[259] B. Duderija, F. Sahin, D. Meinderik, J.C. Calderón, H.C. Schmidt, W. Homberg, G. Grundmeier, A. González-Orive, Electrografting of Acrylic acid on steel for enhanced joining by plastic deformation. Journal of Advanced Joining Processes 2024;9:100181.

9

Attachments

9.1 List of Figures

9.2 List of tables

9.3 Standards

[N1] DIN 8593-0:2003-09. Manufacturing processes joining - Part 0: General; Classification, subdivision, terms, and definitions.

[N2] DIN EN 10130: 2006 Cold rolled low carbon steel flat products for cold forming. Technical delivery conditions.

[N3] DIN EN 485-2:2016-08. Aluminium and aluminium alloys - Sheet, strip, and plate - Part 2: Mechanical properties.

[N4] DIN EN ISO 2080:2009-08. Metallic and other inorganic coatings.

[N5] DIN 8583-2:2003-09. Manufacturing processes forming under compressive conditions - Part 2: Rolling; Classification, subdivision, terms, and definitions.

9.4 List of abbreviations and acronyms

AA	Acrylic acid
AFM	Atomic Fore Microscopy
Ag	Silber
AgCl	Silber-chloride
AR-HR-XPS	Angle-Resolved High-Resolution X-ray Photoelectron Spectroscopy
BTSE	1,2-bis(triethoxysilyl)ethane (96 %) + $NaNO_3$
BTSE	1,2-bis(triethoxysilyl)ethane (96 %)
BTSE: Zn	1,2-bis(triethoxysilyl)ethane (96 %) + $Zn(NO_3)_2$
CH_3COOH	Acetic acid
CPW	Cold pressure welding
CV	Cyclovoltammetry
DCO_4	Commercial steel samples
DLVO	from Derjaguin, Landau, Verwey, Overbeek
EC	Elecrochemical
ECSA	Electrochemical Surface Area
ECUF	Electrochemically assisted joining
EDL	electric double layer
EDX	Energy Dispersive X-ray Spectrometry
EIS	Electrochemical Impedance Spectroscopy
EN-AW105 H11	Commercial aluminum samples
Fe	Iron
$Fe(OH)_2$	Iron-hydroxide
FTIR	Fourier-transformed infrared spectroscopy
HER	Hydrogen Evolution Reaction
HNO_3	Nitric acid
IEP	Isoelectric point
IHP	inner Helmholtz plane
IRRAS	Infrared Reflection Absorption Spectroscopy
KCl	Kalium-clorid
LSS_{nom}	The nominal lap-shear strength
MPTS	Metacryloxypropyltrimethoxysilane

N	Newton
N_2	Nitrogen
$Na_2B_4O_7 \cdot 10H_2O$	Natrium-borhydrid-decahydrat
NaCl	Natrium-chloride
$NaNO_3$	Natrium-nitrate
NaOH	Natrium-hidroxid
OCP	Open Circuit Potential
-OH	hydroxyl group
OHP	outer Helmholtz plane
PAA	Poly (acrylic acid)
PAA:Zn	Poly (acrylic acid) + Zn
PMA50	Photo-Elastic-Modulator 50
PM-IRRAS	Polarization modulation-infrared reflection-adsorption spectroscopy
PZC	Point of zero charge
RMS	Root Mean Square
SAM	Self -Assembly Monolayar
SEM	Scanning Electron Microscope
WE	Working Electrode
XPS	X-ray Photoelectron Spectroscopy
Zn	Zink
$Zn(NO_3)_2$	Zink-nitrate
ZnO	Zink-oxide

9.5 Permissions

Inclusion of the Figure 4.1 from the dissertation Thesis "*Microstructure and Mechanical Behavior of Deep Drawing DC04 Steel at Different Length Scales*" by Simone Schreijäg, in subchapter 2.3 of the Thesis, is premitted by CC-BY-NC-ND 3.0 DE license/ Open access.

Inclusion of the Figure 1. from the manuscript "*M. Lewandowska, T. Wejrzanowski, K.J. Kurzydłowski, Grain growth in ultrafine grained aluminium processed by hydrostatic extrusion, Journal of Material Science 2008;43:7495–7500.*" , in subchapter 2.3 of the Thesis, is permitted by Springer Nature (journalpermissions@springernature.com).

Inclusion of the results from manuscripts "*B. Duderija, A. González-Orive, H.C. Schmidt, J.C. Calderón, I. Hordych, H.J. Maier, W. Homberg, G. Grundmeier, Electrografting of BTSE: Zn films for advanced steel-aluminum joining by plastic deformation. Journal of Advanced Joining Processes 2022;7:1100137." and* "*B. Duderija, F. Sahin, D. Meinderik, J.C. Calderón, H.C. Schmidt, W. Homberg, G. Grundmeier, A. González-Orive, Electrografting of Acrylic acid on steel for enhanced joining by plastic deformation. Journal of Advanced Joining Processes 2024;9:100181."* , in subchapters 4.1 and 4.2 of the thesis, is permitted by the Journal of Advanced Joining Processes (https://www.elsevier.com/about/our-business/policies/copyright#Author-rights).